

Mechatronic Design,  
Dynamics, Controls, and Metrology of a  
Long-Stroke Linear Nano-Positioner

by

Ahmet Okyay

A thesis  
presented to the University of Waterloo  
in fulfillment of the  
thesis requirement for the degree of  
Doctor of Philosophy  
in  
Mechanical Engineering

Waterloo, Ontario, Canada, 2016

©Ahmet Okyay 2016

## **Author's Declaration**

I hereby declare that I am the sole author of this thesis. This is a true copy of the thesis, including any required final revisions, as accepted by my examiners.

I understand that my thesis may be made electronically available to the public.

Ahmet Okyay

## Abstract

Precision motion systems find a broad range of application in various fields such as micro/nano machining tools, lithography scanners, testing and metrology machines, micro-assembly, biotechnology, optics manufacturing, magnetic data-storage, and optical disk drives. In this thesis, an ultraprecision motion stage (nano-positioner) is designed and built based on the concept of a low-cost desktop precision micro machine tool. Linear positioning performance requirements of such a machine tool are used as design objectives.

The nano-positioner's mechatronic design is carried out in such a way to integrate different components towards high performance in terms of high dynamic range, high feedrate, servo accuracy, and geometric accuracy. A self-aligning air-bearing/bushing arrangement is employed for frictionless motion with infinite theoretical resolution, as well as reduced assembly costs and footprint. The air discharge from the air bearings/bushings are also utilized for assistance in the removal of heat dissipated from actuator coils. A voice coil actuator (VCA) is chosen for continuous, non-contact operation, and designed from scratch. A number of dimensional variables of the cylindrical VCA are set according to required forces, motion range, production/assembly tolerances, magnet availability, leakage flux, etc. The remainder of variables is determined according to two novel optimization objectives defined independent of the coil wire gauge, which separately aim for maximum stage acceleration capacity and minimum heat generation per generated force. The actuators are operated in a complementary double configuration for control simplicity which allows for a straightforward and robust design for controller stability.

Controller design is carried out at current control and position control levels. Current frequency response of the voice coil actuators is obtained, and they are observed to possess additional high frequency dynamics on top of the expected first order lumped resistance and inductance model. These are attributed to the eddy currents in the stator structure. A closed loop bandwidth of better than 907 [Hz] is achieved using the integrator plus lead current controller. The position controller is designed using the identified overall plant which includes the moving body, current dynamics and the force response. The lead-lag position controller is tuned at 450 [Hz] cross-over frequency and 40 [deg] phase margin. The control error during the tracking of a step trajectory filtered at 40 [Hz] is found to vary between  $\pm 5$  [nm], indicating a 4 million dynamic range over the 20 [mm] stroke length. Dynamic Error Budgeting (DEB) method has been used to resolve the components of the error, and

the largest contributor is found to be the sensor noise. The actual positioning error, which is an ideal signal excluding sensor noise is estimated using the same methodology and disturbance models, and it is found to be 0.680 [nm] root-mean-square (RMS). For the trajectory following case, experiments are carried out with and without a compensation scheme for encoder quadrature detection errors. The compensation is observed to reduce the  $\pm 45$  [nm] control error to  $\pm 15$  [nm].

For the assessment of stage performance and the verification of design choices, modal testing and laser interferometric metrology have been applied to the linear nano-positioner. For modal testing, two independent methods are used and their predictions are compared. In the first method, a graphical approach, namely the peak-picking method, is employed to identify modal parameters (natural frequency and damping ratio) and mode shapes. In the second method, a modal testing software package is used to identify the same using automated algorithms. The first mode, which is the most critical one for controller design, is identified at 65 [Hz] as a roll mode, followed by horizontal, vertical, and pitch modes at 450, 484, and 960 [Hz], respectively. The geometric errors of the system are identified using laser interferometric measurements, using various optical setups for linear and angular components. An error budget is formed using these results, together with the estimated thermal errors and servo errors. The accuracy of the stage is determined to be  $\pm 5.0$  [ $\mu\text{m}$ ], which had a  $\pm 1.1$  [ $\mu\text{m}$ ] non-repeatable component.

In the future, the controller structure can be enhanced with an additional pole beyond the crossover frequency, in order to suppress unnecessary oscillations of the control effort signal around the set point due to the encoder noise transmitted to the controller input. Using an estimation of air bearing pitch stiffness from the catalogue values for normal stiffness, the roll mode was predicted at 672 [Hz]. The much lower natural frequency for that mode identified in modal testing (65 [Hz]) can be attributed to the shortcomings of the estimation method, primarily the neglect of the distortion of the supporting air cushion at the bearing interface due to out of plane rotations. In the future, experimental data can be obtained to characterize the air bearing pitch stiffness more accurately. It was observed that the preferred compensation scheme for the encoder quadrature detection errors is unable to match third and fourth harmonics of the encoder measurement error sufficiently. In the future, better compensation methods can be investigated for an improved match. During laser interferometric measurements, measurement uncertainty due to laser beam misalignment and air turbulence were inferred to be high. In the future, better ways to align the laser with the optics, as well as methods for improved assessment and compensation of environmental effects can be investigated.

## **Acknowledgments**

I would like to express my deep gratitude to my research supervisors Dr. Kaan Erkorkmaz and Dr. Mir Behrad Khamesee for the support and motivation they have provided me throughout the years of my PhD study. They have been excellent mentors to me with their immense knowledge, utmost enthusiasm, patience and understanding.

I would also like to show gratitude to my committee members: Dr. Ehab El-Saadany, Dr. Steve Lambert, and Dr. Soo Jeon. I would also like to thank my external examiner Dr. René Mayer for attending my defence in person despite his busy schedule. They have asked many important questions during my defence and provided valuable feedback regarding my thesis.

I would like to thank Mr. Bjarni Tryggvason for the assistance in the conception of this research and his valuable inputs into the development of the nano-positioner.

My sincere thanks go to University of Waterloo technicians Mr. Robert Wagner and Mr. Neil Griffett for the assistance they have provided.

Many thanks to all my friends and family for their encouragement and support.

This research has been supported by the Natural Sciences and Engineering Research Council of Canada (NSERC) and QDAC Systems, Inc.

# Table of Contents

<b>Author's Declaration</b> .....	<b>ii</b>
<b>Abstract</b> .....	<b>iii</b>
<b>Acknowledgments</b> .....	<b>v</b>
<b>Table of Contents</b> .....	<b>vi</b>
<b>List of Figures</b> .....	<b>x</b>
<b>List of Tables</b> .....	<b>xiii</b>
<b>Chapter 1 Introduction</b> .....	<b>1</b>
1.1. Background .....	1
1.2. Thesis overview.....	2
<b>Chapter 2 Literature Review</b> .....	<b>4</b>
2.1. Introduction .....	4
2.2. Literature on the design of ultraprecision motion stages.....	4
2.2.1. Ultraprecision motion stage applications and performance requirements.....	4
2.2.2. Selected works from the literature.....	6
2.2.3. Summary of works in tabular form.....	10
2.3. Literature on voice coil actuators and their optimal design.....	20
2.3.1. Utilization of voice coil actuators in ultraprecision motion stages.....	20
2.3.2. Optimal design of voice coil actuators .....	20
2.4. Literature on performance assessment and verification methods.....	21
2.4.1. Dynamic Error Budgeting (DEB).....	21
2.4.2. Modal testing.....	22
2.4.3. Laser interferometric metrology .....	23
2.5. Conclusion and comparison of specifications .....	24
<b>Chapter 3 Mechatronic Design of the Positioning Stage</b> .....	<b>25</b>
3.1. Introduction .....	25
3.2. Low-cost desktop precision micro machine tool concept .....	26
3.3. Design features .....	28
3.4. Error budget at the design stage .....	34
3.4.1. Measurement errors .....	34
3.4.2. Geometric errors.....	35
3.4.3. Servo error.....	35
3.4.4. Predicted error budget .....	37

3.5. Predicted vibratory dynamics .....	37
3.6. Conclusion.....	41
<b>Chapter 4 Actuator Design and Optimization.....</b>	<b>42</b>
4.1. Introduction .....	42
4.2. Description of the voice coil actuator.....	42
4.2.1. Configuration options for the steel core .....	42
4.2.2. Design variables .....	44
4.2.3. Magnetic properties .....	45
4.3. Optimization.....	47
4.3.1. Optimization objectives.....	47
4.3.2. Determination of $\delta$ and $h_3$ .....	50
4.3.3. Performance topologies with $r_1$ and $p$ .....	50
4.3.4. Re-evaluation of the optimization objectives .....	53
4.4. Coil design and electrical characteristics.....	55
4.4.1. Number of coil wire turns.....	55
4.4.2. Coil inductance, resistance and time constant .....	56
4.4.3. Power supply .....	58
4.5. Experimental study of the voice coil actuator design.....	61
4.5.1. Verification of the magnetic analysis method .....	61
4.5.2. Verification of force and performance formulations .....	62
4.6. Conclusion.....	64
<b>Chapter 5 Control System .....</b>	<b>65</b>
5.1. Introduction .....	65
5.2. Overview of the control system.....	65
5.3. Design of the current controller.....	66
5.4. Design of the position controller .....	71
5.5. Positioning resolution analysis via Dynamic Error Budgeting .....	73
5.5.1. DEB calculations .....	74
5.5.2. DEB results and discussion .....	78
5.6. Trajectory following performance.....	81
5.6.1. Compensation of encoder quadrature detection errors .....	81
5.6.2. Cubic acceleration profile trajectory test.....	84
5.6.3. Alternative compensation scheme for the encoder quadrature detection errors.....	86
5.6. Conclusion.....	88

<b>Chapter 6 Modal Testing .....</b>	<b>90</b>
6.1. Introduction .....	90
6.2. Overview of the testing methods .....	90
6.3. Using method 1 (peak-picking) .....	92
6.3.1 Impact and measurement points .....	92
6.3.2. Method of analysis .....	92
6.4. Using method 2 (software package) .....	98
6.4.1. Impact and measurement points .....	98
6.4.2. Method of analysis .....	98
6.5. Comparative modal testing results and discussion .....	100
6.6. Conclusion .....	102
<b>Chapter 7 Laser Interferometric Metrology .....</b>	<b>103</b>
7.1. Introduction .....	103
7.2. Methodology of measurements .....	103
7.2.1. Experimental procedure .....	104
7.2.2. Experimental setups .....	106
7.2.3. Abbe errors .....	109
7.3. Metrology results .....	110
7.3.1. EXX results .....	111
7.3.2. EYX results .....	113
7.3.3. EZX results .....	114
7.3.4. EBX results .....	115
7.3.5. ECX results .....	116
7.4. Error budget .....	117
7.4.1. Geometric components .....	118
7.4.2. Thermal components .....	118
7.4.3. Final error budget .....	127
7.5. Discussion .....	128
7.6. Conclusion .....	129
<b>Chapter 8 Conclusions and Future Work .....</b>	<b>130</b>
8.1. Thesis conclusions .....	130
8.2. Thesis contributions .....	131
8.3. Future research .....	132
<b>References .....</b>	<b>133</b>



<b>Appendix A Current Amplifier Circuit Diagram.....</b>	<b>142</b>
<b>Appendix B Technical Drawing of the Main Shaft .....</b>	<b>144</b>
<b>Appendix C Frequency Response Functions for Modal Analysis .....</b>	<b>145</b>
<b>Appendix D Formulas Used to Calculate Accuracy .....</b>	<b>148</b>
<b>Appendix E Motion Errors in Standard Format.....</b>	<b>149</b>
<b>Appendix F Photographs of the Laser Interferometric Measurement Setups.....</b>	<b>155</b>
<b>Appendix G Estimated Deflections Due to Machining Forces .....</b>	<b>158</b>

## List of Figures

Fig. 2.1: Magnetically levitated stage [113].	6
Fig. 2.2 Linear motor driven aerostatic planar motion table	7
Fig. 2.3 Single-axis precision controlled stage [12].	8
Fig. 2.4 The 3-DOF piezo-stage	9
Fig. 2.5 Combined ball screw and voice coil motor system	9
Fig. 2.6 XY stage employing grid encoder [38].	10
Fig. 3.1 Preliminary design of a desktop precision micro machine tool.	26
Fig. 3.2 Exploded view and photograph of the long-stroke translational nano-positioner.	28
Fig. 3.3 Drawing of the main shaft.	29
Fig. 3.4 VCA alignment to the shaft.	30
Fig. 3.5 VCA core assembly	31
Fig. 3.6 VCA coil assembly.	32
Fig. 3.7 Signal outputs (A and B) from the encoder.	32
Fig. 3.8 Force factor vs. stroke position	33
Fig. 3.9 Tolerances on the shaft.	35
Fig. 3.10 Assumed motion profile.	36
Fig. 3.11 Air-bearing / air-bushing arrangement of the motion stage.	38
Fig. 3.12 Estimation of air bearing rotational stiffness.	39
Fig. 4.1 Overview of the cylindrical VCA.	43
Fig. 4.2 Permanent magnet materials, BH curves [37].	44
Fig. 4.3 VCA design variables and magnetic flux density distribution for a sample design.	45
Fig. 4.4 Magnetic equivalent circuit model of the VCA.	46
Fig. 4.5 Coil diagram related to space efficiency.	51
Fig. 4.6 COMSOL® FE analysis for the variable pair $\{ r_1 = 7 \text{ [mm]}, p = 1 \text{ [mm]} \}$ .	52
Fig. 4.7 Performance topologies.	53
Fig. 4.8 Performance topologies with re-evaluated optimization objectives.	55
Fig. 4.9 Magnetic energy and permeance vs. coil engagement.	57
Fig. 4.10 Power components in the AC case as a function of current frequency.	59
Fig. 4.11 Experimental measurement of flux densities.	61
Fig. 4.12 Experimental setup for force measurement.	62
Fig. 4.13 Force response of the VCA.	63

Fig. 4.14 Interactions of VCA properties .....	64
Fig. 5.1 Overview of the position control loop.....	65
Fig. 5.2 Detailed control block diagram. ....	66
Fig. 5.3 Experimentally measured and model predicted VCA electrical TF.....	68
Fig. 5.4 Current FRF simulation for the fully engaged (100%) VCA at 200 [Hz].....	69
Fig. 5.5 Current controller ( $C_c$ ) and loop TF ( $L_c$ ). ....	70
Fig. 5.6 Current control CLTF. ....	71
Fig. 5.7 Transfer functions related to position controller design.....	72
Fig. 5.8 Positioning results with the step trajectory. ....	74
Fig. 5.9 Control system block diagram with the disturbance and measurement noise signals.....	74
Fig. 5.10 Bode plots of transfer functions. ....	75
Fig. 5.11 CPS of encoder measurement at fixed position. ....	77
Fig. 5.12 Calculation of $CPS_e$ .....	79
Fig. 5.13 Calculation of $CPS_a$ .....	80
Fig. 5.14 Lissajous figure with recorded and fitted A' and B' signals.....	83
Fig. 5.15 Position measurement error in one signal period. ....	83
Fig. 5.16 Control block diagram showing sensor compensator. ....	84
Fig. 5.17 Jerk limited cubic acceleration profile trajectory. ....	85
Fig. 5.18 Trajectory following results. ....	85
Fig. 5.19 FFT of the control error.....	86
Fig. 5.20 Trajectory used to estimate measurement errors.....	87
Fig. 5.21 High-pass filtered encoder signal.....	87
Fig. 6.1 Impact and measurement locations for method 1 (peak-picking). ....	91
Fig. 6.2 The SDOF vibratory system.....	93
Fig. 6.3 Real and imaginary plots of a sample accelerance FRF.....	94
Fig. 6.4 Using imaginary peak/dip values to determine modal displacements. ....	97
Fig. 6.5 Impact and measurement points for method 2 (software package).....	98
Fig. 6.6 Comparative modal testing results .....	101
Fig. 7.1 Coordinate system and definitions for error motions .....	103
Fig. 7.2 Measurement trajectory.....	105
Fig. 7.3 EXX experimental setup. ....	106
Fig. 7.4 EYX and EZX experimental setup.....	107
Fig. 7.5 EBX and ECX experimental setup.....	108

Fig. 7.6 Formation of Abbe errors.....	109
Fig. 7.7 Determination of Abbe moment arm lengths.....	110
Fig. 7.8 EXX plots with the Abbe errors subtracted. ....	112
Fig. 7.9 EYX plots with the Abbe errors subtracted. ....	114
Fig. 7.10 EZX plots with the Abbe errors subtracted.....	115
Fig. 7.11 EBX plots.....	116
Fig. 7.12 ECX plots.....	117
Fig. 7.13 Schematic diagram of the positioning stage.....	119
Fig. 7.14 Heat transfer surfaces.....	122
Fig. 7.15 COMSOL® FEA simulation of the temperature distribution. ....	126
Fig. 7.16 Variations of the ambient temperature. ....	126
Fig. A.1 Simplified circuit diagram of the amplifier board [86]. ....	142
Fig. B.1 Technical drawing of the main shaft. ....	144
Fig. C.1 Bode, real - imaginary, and Nyquist plots of FRF's.....	147
Fig. F.1 Linear error (EXX) setup. ....	155
Fig. F.2 Straightness error (EYX and EZX) setup. ....	156
Fig. F.3 Angular error (EBX and ECX) setup.....	157
Fig. G.1 Forces due to milling operation.....	158
Fig. G.2 Control block diagram with cutting force disturbance.....	159
Fig. G.3 Receptances and total deflection due to cutting forces .....	160

## List of Tables

Table 2.1. Summary of performance goals and their relationship with applications. ....	6
Table 2.2. Summary of ultraprecision motion stage design literature.....	14
Table 3.1 Predicted error budget .....	37
Table 3.2 Air - bearing/bushing stiffness properties and dimensions. ....	39
Table 3.3 Inertia properties of the moving body. ....	39
Table 3.4 Calculation of the natural frequencies.....	40
Table 4.1. Summary of VCA design variables.....	45
Table 4.2. Expressions for magnetic circuit elements and sample values.....	47
Table 4.3. Electrical parameters for different wire gauges.....	56
Table 4.4. Comparison of FE and experimental flux densities.....	62
Table 5.1. Pole/zero/gain fitted to the VCA frequency response. ....	69
Table 5.2 Calculated and measured FFT's of sensor correction and error signals.....	84
Table 5.3 Least-squares fit to the approximate measurement error.....	88
Table 6.1. Comparison of the two independent methods used in modal testing. ....	91
Table 7.1 Measurement target positions.....	104
Table 7.2 Feed, acceleration, and jerk limits of the measurement trajectory. ....	105
Table 7.3 Values of Abbe moment arms. ....	110
Table 7.4 EXX summary.....	113
Table 7.5 EYX summary.....	114
Table 7.6 EZX summary. ....	115
Table 7.7 EBX summary. ....	116
Table 7.8 ECX summary. ....	117
Table 7.9 Summary of geometric accuracies.....	118
Table 7.10 Thermal sensitivities and parameters used in calculating them. ....	120
Table 7.11 Calculation of coefficients of convective heat transfer for Surfaces 1-4.....	123
Table 7.12 Definitions of variables used in the calculations of Table 7.11.....	124
Table 7.13 Properties of air .....	124
Table 7.14 Calculation of the forced convective heat transfer coefficient.....	125
Table 7.15. Ambient temperature data. ....	127
Table 7.16. Error budget.....	128
Table A.1 Implementation of the current controller configuration .....	143

Table C.1 Low and high frequency asymptotes of FRF's.....	145
Table D.1 Formulas used to calculate accuracy .....	148
Table E.1 Linear positioning error (EXX) results .....	150
Table E.2 Vertical straightness error (EYX) results.....	151
Table E.3 Horizontal straightness error (EZ $X$ ) results .....	152
Table E.4 Yaw error (EB $X$ ) results .....	153
Table E.5 Pitch error (EC $X$ ) results .....	154
Table G.1 Deflections due to cutting forces.....	161

# Chapter 1

## Introduction

### 1.1. Background

Mechatronics has evolved as a wide and multi-disciplinary design discipline in engineering, mainly as a result of developments in computers and information technology. Finding application in the areas of robotics, machining centers, vehicles, wafer scanners, metrology equipment and so on, it has gradually become evident that the discipline represents more than a combination of two existing fields. As W. Bolton states [8]:

“A mechatronic system is not just a marriage of electrical and mechanical systems and is more than just a control system; it is a complete integration of all of them.”

Furthermore, software and optics have also become an integral part of mechatronics. Among several distinct topics within mechatronics, the design of high precision motion systems has been the subject of significant interest. Precision motion systems find a broad range of application in micro/nano machining tools, lithography scanners, testing and metrology machines, micro-assembly, biotechnology, optics manufacturing, magnetic data-storage, optical disk drives, and so on. In precision manufacturing, ultraprecision refers to tolerances typically smaller than 50 [nm] [27]. In this thesis, an ultraprecision motion stage is designed and built based on the concept of a low-cost desktop precision micro machine tool [7], [94], [105].

The design of an ultraprecision motion stage reflects the characteristics of the mechatronic design discipline in terms of the requirement to combine components rooted in various disciplines in a holistic manner, recognizing their strong inter-dependency, to achieve high performance. For such a system, based on the application, a great variety of performance goals can be prescribed. Some of those relevant to micro-machining, which forms the basis for the stage designed in this thesis, can be listed as:

- Dynamic range, which is basically the stroke length (motion range) divided by the effective motion resolution. In the case of an ultraprecision motion system, it is often in the range of several millions.

- Accuracy, which can be effectively presented in an error budget [23]. It involves geometric accuracy of mechanical components, thermal expansion, servo accuracy, dynamic errors due to inertial forces, deflections due to machining forces, and so on [102].
- Speed, which is necessary for increased throughput. It is related to both the feedrate, which is the speed of positioning, and the acceleration, which dominates during short stroke movements. As ultraprecision stages are typically designed for smaller workpieces, the limited motion range requires high accelerations in order to reach the desired high feedrates within a fraction of the commanded displacement.
- Cost, which depends on numerous factors, and also weighs against the three other performance goals mentioned above. There can be many different ways, apart from sacrificing other performance goals, one can attempt to limit cost. In this thesis, the two main aspects of cost tackled in design are assembly costs and maintenance. Assembly costs can be limited by employing self-aligning bearing technologies and a simple design approach to limit the necessity of complex fabrication procedures and specialized fixtures. Maintenance costs can be limited by not requiring intensive environment control, or avoiding components which require extensive support systems like hydrostatic bearings which require pumps, filters, coolers, etc.

In this thesis, the mechatronic design of a long stroke linear nano-positioning stage has been carried out with respect to the performance goals listed above. The motion controller has also been designed, and positioning results have been obtained. Modal testing and laser interferometric metrology have been carried out to identify the vibratory dynamics and geometric accuracy of the system, respectively. These allow for the dynamic and accuracy limitations of the proposed motion stage to be experimentally characterized.

## **1.2. Thesis overview**

Following the literature review presented in Chapter 2, the main contents of this thesis comprises two main parts as ‘design’ and ‘evaluation’. Chapters 3, 4, 5 are related to the ‘design’ of the long-stroke linear nano-positioner. Chapters 6, 7 are related to its ‘evaluation’. Findings from these two main categories are combined where necessary. In Chapter 3, an overview of the mechatronic design of the stage is presented. Descriptions of the mechanical design, assembly, bearing structure, sensors, control system and actuators is provided. Instead of a tip-to-toe description of the stage, only the most prominent design features are discussed. Also, predictions of the motion accuracy and the vibratory dynamics at the design phase are made. In Chapter 4, optimal design of the voice coil actuators



(VCA) is presented. The definitions of two novel optimization objectives, which are independent of the coil wire gauge, are introduced. Performance topologies are plotted with respect to dimensional variables and the most feasible point is determined. This chapter also contains experimental results verifying the gap flux density and force response predictions. In Chapter 5, the control system of the stage is designed. Measured characteristics in the frequency domain, regarding the current control and position control systems, are presented. Where necessary, underlying physical principles of the observed characteristics are investigated, such as additional high frequency dynamics contributed by eddy currents. Positioning performance and tracking response are also reported. The positioning performance is analyzed using the Dynamic Error Budgeting (DEB) method [75]. In Chapter 6, modal testing of the stage is carried out using two independent methods. In the first method, ‘peak-picking’ is employed, which is closer to an educated layman’s approach and provides physical insight into dynamics of the system. In the second method, a standardized modal testing software package commonly applied in industry is used, which automates the identification and presentation steps. Results from the two methods are compared, and their implications for the overall performance of the system are discussed. In Chapter 7, laser interferometric metrology is used to identify geometric motion errors of the stage. Using these along with the estimation of thermal errors and measured servo errors, a final error budget of the precision motion stage is compiled which can be used as a reference in future ultraprecision actuator or machine development case studies. In Chapter 8, conclusions drawn from this thesis are summarized and suggestions for future work are presented.

## **Chapter 2**

### **Literature Review**

#### **2.1. Introduction**

There have been many studies on the design of ultraprecision motion stages, owing to their wide application in several branches of industry. Design of such systems involves the combination of knowledge pertaining to different fields, such as mechanical design, sensors, bearing systems and actuators. Several methods used in the design, analysis, and implementation of such systems also constitute major academic fields in their own right. These include methods for the investigation of control performance, vibratory dynamics, and motion errors. In this chapter, literature on the design as well as testing of ultraprecision motion stages is presented. In Section 2.2, previous designs are reported. In Section 2.3, studies on the optimal design of magnetic (voice coil) actuators are presented. In Section 2.4, the literature on various assessment and verification methods followed in this thesis, namely Dynamic Error Budgeting (DEB), modal testing, and laser interferometric metrology are presented. This chapter finishes with a comparison of the key specifications achieved by the proposed design with a number of other works.

#### **2.2. Literature on the design of ultraprecision motion stages**

In this section, a review of ultraprecision motion stage applications, and a discussion of up-to-date performance requirements are presented. Sample works from the literature are detailed, and also presented in tabulated form.

##### **2.2.1. Ultraprecision motion stage applications and performance requirements**

Precision positioning stages with accuracies in the order of several nanometers are an important building block for technologies developed in various fields. In the case of micro-manufacturing, ultraprecision motion systems are required for both lithography and non-lithography techniques. In photolithography, the recent introduction of extreme ultraviolet (EUV) lithography, which uses 13.5 [nm] radiation wavelength, is expected to achieve feature sizes that are less than 10 [nm] in semiconductor manufacturing. The existing technology, deep ultraviolet (DUV) lithography, uses 193 [nm] argon-fluoride lasers which can achieve down to 38 [nm] feature size with the use of special optics [111]. Hence, positioning resolutions of less than 10 [nm] are becoming a standard requirement for motion stages used in semiconductor manufacturing. Also, high acceleration and velocity are

generally desirable for increasing the throughput, by reducing the time spent between exposures. Both of these require the design of a high dynamic accuracy servo control system.

For micromachining operations (i.e., microdrilling, micromilling, microturning), ultraprecision machine tools, as well as their miniaturized versions, are used. Miniaturized micro-machine tools have the advantage of cost effectiveness, higher natural frequencies, and lower vibration amplitudes [14], [57]. Recently, a ‘nano-milling’ procedure has been developed which uses elliptical motions of a 10 [nm] radius atomic-force microscopy (AFM) tip to remove material by shearing [39]. The 3D piezoelectric nanopositioner used (Physik Instrumente P-611.3 NanoCube®) is capable of achieving 1 [nm] resolution with 5 [nm] root-mean-square (RMS) repeatability, in 100 [μm] range. As the cutting feed motion is provided by the nano-positioner (like in a conventional CNC), the nano-positioner’s positioning performance is a direct determinant of the achievable tolerance. Hence, positioning stages used in micro / nano - machining operations are similarly required to achieve less than 10 [nm] positioning resolution, in order to match the demands of emerging machining applications.

In precision positioning, another necessity which is becoming more emphasized is the ability to deliver extremely accurate motions over an extended motion range. This requirement is the motivation for the development of ultraprecision motion stages with long stroke lengths. The generation of nanometer-sized or toleranced features and patterns that extend to the millimeter scale is readily observable in applications such as semiconductor manufacturing, optical lens array dies, and nano-patterning for roll-to-roll production. Nano-metrology, which deals with the measurement of such parts, similarly requires high precision over extended motion ranges [71].

Performance goals for ultraprecision motion stages are determined from the recent developments as exemplified above, and summarized in Table 2.1. In addition to requirements on positioning resolution, positioning speed, and motion range, a final requirement on the capital and maintenance costs is introduced. In this thesis, the motion stage proposed is based on the concept of a low-cost desktop precision micro-milling machine tool, as presented in Chapter 3.

Table 2.1. Summary of performance goals and their relationship with applications.

Performance goal	Value	Use in application
Positioning resolution	< 10 [nm]	- Small feature sizes and higher tolerances in manufacturing.
Positioning speed	as high as possible	- Increased throughput.
Motion range	> 10 [mm]	- Micro features and patterns on macro - sized workpieces. - Increased throughput (e.g., semiconductor manufacturing, optical lens array dies, nano - patterning for roll - to - roll production).
Capital and maintenance costs	as low as possible	- Desktop sized fabrication systems.

### 2.2.2. Selected works from the literature

In this section, a number of important works on the design of ultraprecision motion stages, which constitute a representative set of recent and influential literature, is presented. Works with differing design choices regarding sensors, actuators, bearing system, and mechanical design are selected to provide a wide perspective. Although many more studies with similar importance have been found, those have been included into a summary in tabulated form in Section 2.2.3.

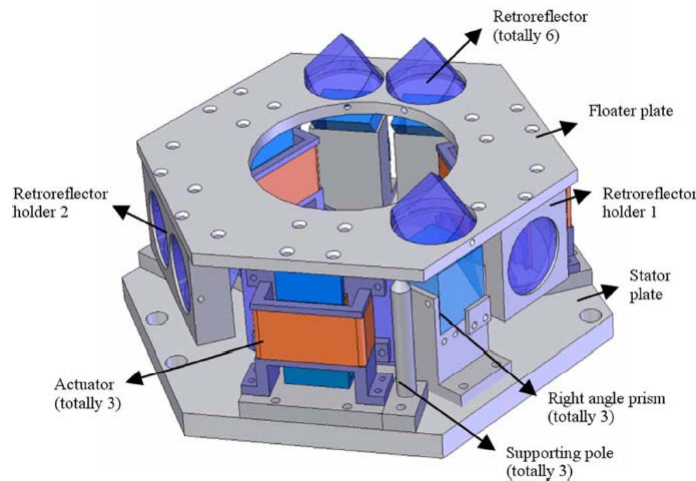


Fig. 2.1: Magnetically levitated stage [113].

Zhang and Menq [113] have built a six degrees-of-freedom (DOF) magnetically levitated stage, as shown in Fig. 2.1. They have used Lorentz force actuators to position and stabilize the system. The design has 2 [mm] stroke in linear axes and 4 [deg] in rotational axes. For feedback, laser interferometer sensors have been used. Static errors of positioning for X and Y axes are 1.1 [nm] root-mean-square (RMS), and 0.74 [nm] RMS, respectively.

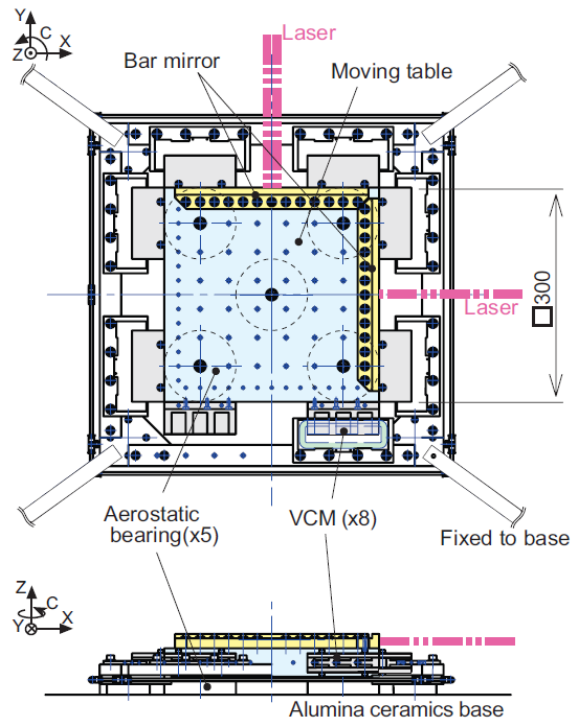


Fig. 2.2 Linear motor driven aerostatic planar motion table for nano-machining [99].

Shinno et al. [99] have developed a linear motor driven aerostatic planar motion table for nano-machining, as shown in Fig. 2.2. The table rests on aerostatic bearings and is actuated by 8 voice coil actuators (VCA) at the sides, in a coordinated manner to achieve X-Y- $\theta$  motions. Stroke lengths in linear axes are  $\pm 10$  [mm], while the rotational degree of freedom is more suited for alignment correction (actual range not reported). The table system can achieve tracking errors of less than 1 [nm] while tracing a 100 [nm] radius circle in the XY plane at 2 [Hz], without rotations in  $\theta$ . Disturbance (e.g. machining) force estimation is made from motion sensor outputs, relying on a mathematical model of the system. This estimation is fed back to the controller to improve tracking.

Buice et al. [12] have built a 50 [mm] range single axis positioning system by mounting a piezoelectric (PZT) driven flexure on top of a coarse motion stage. Schematic drawing of the system

is presented in Fig. 2.3. The stage is driven by feedscrew and Roh'lix® drives, alternatively. The latter is a friction based threadless drive. The controller bandwidth for the fine stage has been set as high as 2188 [Hz]. Over a 5 [mm] travel range with maximum 150 [ $\mu\text{m/s}$ ] feed rate, peak to peak errors of 21.5 [nm] and 111.8 [nm] have been obtained with feedscrew and Roh'lix® drives, respectively.

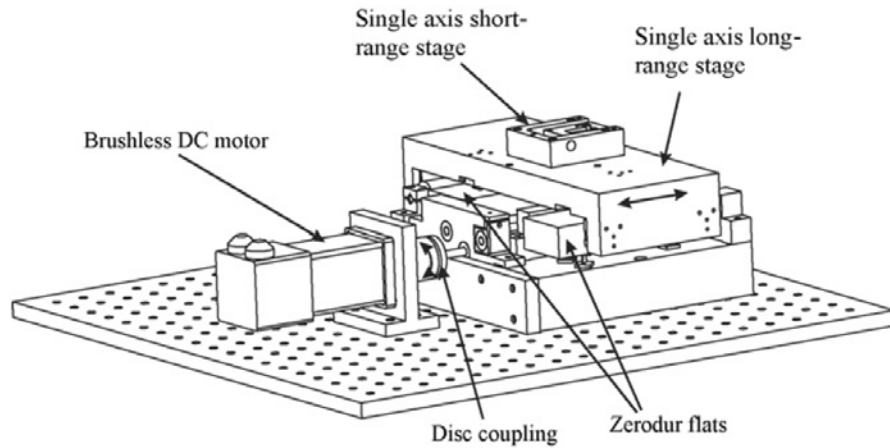


Fig. 2.3 Single-axis precision controlled stage [12].

Liu et al. [60] have developed a dual-axis long-traveling nano-positioning stage (DALTNPS). The system is composed of a stacked 2-DOF traditional ball screw and a 3-DOF piezo-stage mounted on top of it. The 3-DOF piezo-stage is shown in Fig. 2.4. Position measurements are obtained using two laser interferometers; a single beam for displacement in X, and a dual beam for displacement in Y and rotation in Z-axes. The system can run with errors less than 30 [nm] while tracing a 49.4 [mm] radius circle in the XY plane, but the feedrate is not reported.

Shinno et al. [100] have combined a ball screw drive with a voice coil motor to achieve 150 [mm] linear positioning range with sub-nanometer resolution. The schematic of the system is shown in Fig. 2.5. The secondary table, which is actuated by the ball screw, provides the coarse displacement. The light primary table, which is coupled to the secondary table by electromagnetic attraction and air bearing forces, provides the fine correction. The primary table is fitted with mirrors for laser interferometry. Aerostatic bearings, for their freedom from stick-slip type friction, have been used to reduce motion errors, and to have a thermally stable structure. The system responds with less than 10 [nm] error to a jerk-continuous reference input with 150 [mm] displacement, 100 [mm/s] feedrate, and 500 [ $\text{mm/s}^2$ ] acceleration limits.

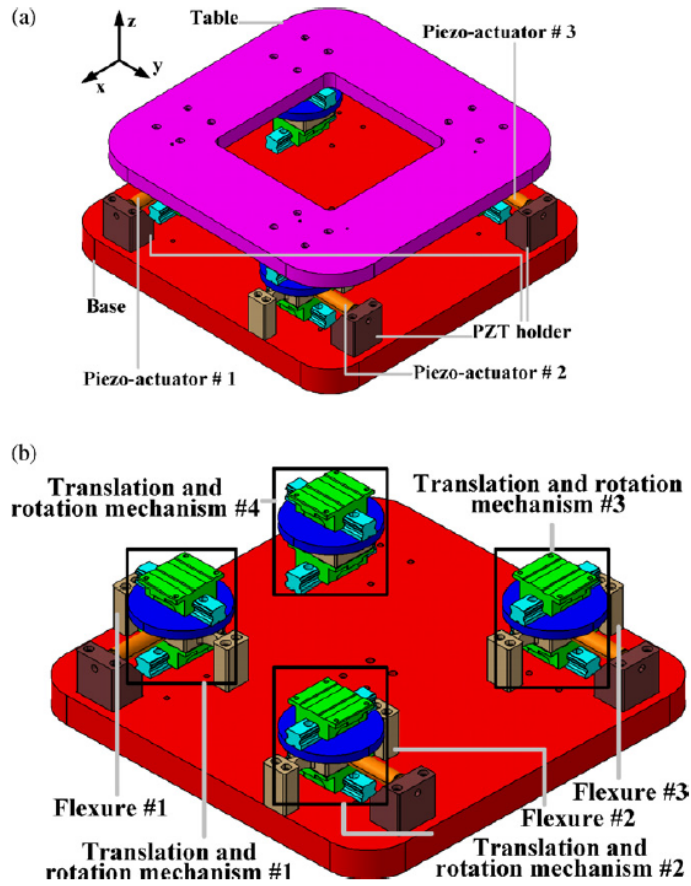


Fig. 2.4 The 3-DOF piezo-stage for dual-axis long-traveling nano-positioning stage [60].

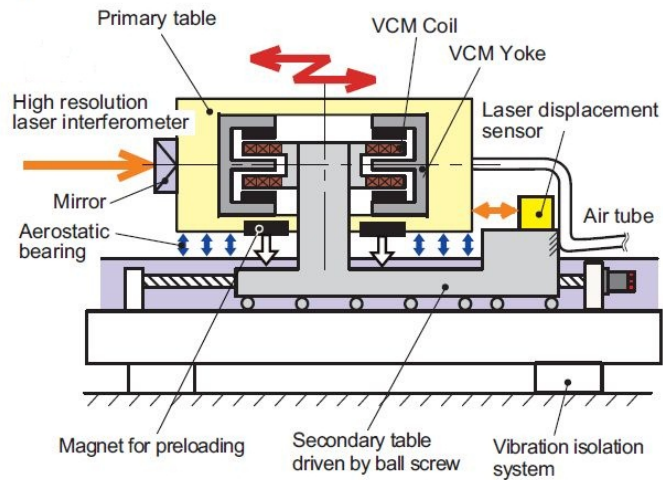


Fig. 2.5 Combined ball screw and voice coil motor system for nano-positioning [100].

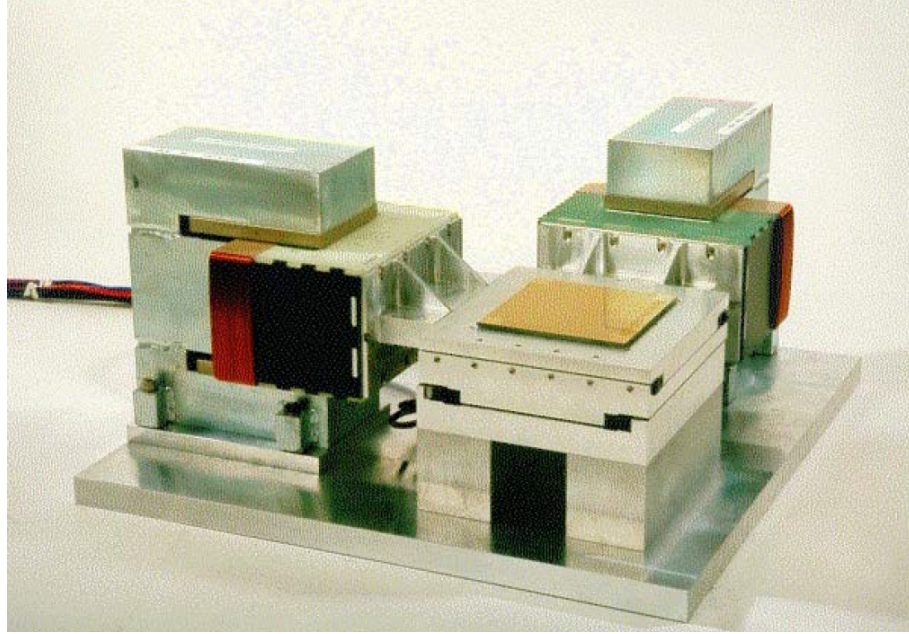


Fig. 2.6 XY stage employing grid encoder [38].

An ultraprecision motion stage with motions in X and Y axes was built by Heidenhain® and National Institute of Standards and Technology (NIST), using a grid encoder which provides position readings in both X and Y axes (Fig. 2.6). The stage has 50 [mm] x 50 [mm] motion range and utilizes VCA's for actuation [38].

### 2.2.3. Summary of works in tabular form

Several works in ultraprecision motion stage design, along with the works in Section 2.2.2, are compared in Table 2.2 according to their design features. Design features are grouped in 3 categories as: 'Axes', 'Positioning performance', and 'Technology', such that:

- The 'Axes' category is made up of 'Motion axes' and 'Motion range'. Under 'motion axes', linear motion axes are indicated by XYZ, and rotational axes are indicated by  $\alpha\beta\theta$ . Linear motion stages with unidirectional motion are indicated by a '+' sign, e.g. 'X+'. Where all six possible motion axes exist, it is briefly noted as '6 DOF'. The range of  $\theta$  in most XY $\theta$  stages is intended to provide small corrections to the stage alignment, but they are reported nevertheless.
- The 'Positioning performance' category is made up of 'Positioning resolution', 'Dynamic response', and 'Control bandwidth'. Under 'Positioning resolution', only the experimentally verified position holding resolution is reported. The nominal resolution of position sensors, if



reported, is not taken into account, as these can be several times better than the experimental case. Under ‘Dynamic response’, the response of the system to demanding high feedrate trajectories, such as a jerk continuous trajectory, sinusoidal motion, and circular contouring, is reported. The ‘Dynamic response’ is directly related to feedback ‘Control bandwidth’, which is reported for some works and constitute a more general measure. Higher bandwidth indicates wider responsive frequency range for accurately tracking the given motion commands, and rejecting the detrimental effects of disturbances.

- The ‘Technology’ category is made up of ‘Actuator’, ‘Bearing’, and ‘Position sensor’ sub-categories.
- Some of the works are stacked designs which combine a coarse stage with a fine one for improved motion resolution over a higher stroke length. For such systems, components for ‘coarse’ and ‘fine’ stages are reported separately.
- Sorting of the works is done according to the actuator type, as it is a primary determinant of the degrees of freedom of motion, motion range, positioning resolution, and dynamic response. As an electromagnetic Lorentz force based VCA is used in the design proposed in this thesis, ‘lorentz’ actuators are presented on top of the list. The order continues as ‘linear motors’, ‘electromagnetic reluctance’, ‘piezoelectric (PZT)’, and ‘stacked designs’. Some less common types of actuators are presented at the end as ‘ultrasonic motor’, and ‘electrostatic actuator’.
- For some of the works, properties of the system were reported in separate sources. For those systems, more than one publication has been cited.
- Information not available in the mentioned works are noted as ‘N/A’.

The compilation presented includes designs made for very different purposes. Therefore, a direct comparison based on numbers may not reflect all particulars of the systems. For example, the iterative learning controller (ILC) in [84] is optimized with respect to a certain repeating trajectory; hence accuracy is boosted by a highly specialized controller design. For other designs, a controller designed for more general purposes may have led to seemingly poorer results. In another case [74], the authors have designed a stage to reject atmospheric perturbation from a Very Large Telescope Interferometer (VLTI); hence results only for tracking a stochastic excitation resembling such perturbations is presented. Positioning resolution of the system is not reported, although it is likely to be in the nanometer range.

There were also other contributions that were quite specialized and fell outside the general scope of precision motion stages. These have not been included in the table. In [17], for example, a miniature ( $\phi 3$  [mm]) 6-DOF nanopositioner is built based on a parallel kinematic flexure mechanism design. This device can be used in applications like endoscopic scanners, integrated alignment mechanisms in micro-optic devices, and positioners that are used in Scanning Electron Microscopes (SEM). The system makes use of thermo-mechanical actuators (TMA). Due to the lack of micro-scale sensors for measurement in six axes, the device is operated in open loop in an envelope of  $3.0 \times 4.4 \times 3.0$  [ $\mu\text{m}$ ] and  $6.3 \times 6.3 \times 8.7$  [mrad], where its response properties are reasonably predictable.

Patterns observed in the list of works included in Table 2.2 reflect general trends in ultraprecision motion stage design. For example, stages with 6-DOF motions [51], [65], [66], [67], [113] mostly use electromagnetic levitation for bearing purposes, as bearing systems with mechanical contact inevitably constrain some DOF's. One shortcoming associated with these mentioned designs is the constantly produced heat by the actuator coils, even when the stage is at rest. In [65], [66], [67] a novel Lorentz actuator is used to position and levitate the stage which is made up of a Halbach array mover and a planar stator with coil windings fabricated as a printed circuit board (PCB). In [97], the need for bearing structure is eliminated altogether from the 6-DOF stage by using a walking - drive. A walking drive is made up of a series of PZT actuators which exert synchronized forces on the motion stage to change its position and orientation. There are a number of XY $\theta$  stages which use differential input from multiple linear actuators to generate rotations [16], [20], [31], [69]. The method results in lower rotational motion range compared to the linear range. A different approach is taken by [112], which involves a mechanism to amplify the rotation produced. Air bearings and flexure bearings are used in most of the designs, due to their theoretically infinite motion resolution. In the case of flexures, the bearing has to be large enough to deliver the required stroke length in the low stiffness region. Otherwise, actuators need to exert large forces at all times, which may lead to heating due to increased current demand. On the other hand, air bearings typically have lower stiffness and require tighter tolerances in the manufacturing of mating components. The alternative, sliding contact bearings are limited to 2 - 10 [ $\mu\text{m}$ ] motion resolution, due to stick-slip motion [102], hence they are not preferred. Stick-slip occurs due to the difference between static and dynamic coefficients of friction in such bearings, which results in an impact-like disturbance in the control system during motion reversal. Two examples defying this trend [21], [58] could be realized due to the unidirectional operation. Zschaeck et al. [114], on the other hand, used a Kalman filter to estimate friction disturbance and achieved high resolutions using sliding v-groove guides.

Although most electromagnetic actuators used are of Lorentz force type, there are also ones using electromagnetic reluctance [16], [63], [68]. Electromagnetic reluctance actuators provide much higher force density compared to Lorentz force actuators, but they are inherently non-linear. Therefore, their use requires more complex control and sensing schemes, or a special design to linearize their response [63]. Another common actuator type is PZT, whose range is inherently limited in bidirectional operation. In [21], [58], the PZT is operated in a uni-directional walking-drive configuration for theoretically infinite motion range. In [97] full 6 - DOF bidirectional motion is achieved using a walking-drive comprising 9 PZT actuators.

Control bandwidths higher than 1 [kHz] are reported by [12], [76]. As vibration modes can be a primary limiting factor of control bandwidth, both designs employ small and lightweight actuators in the main and stacked fine motion stages, respectively, which results in very high first natural frequency of the structure.

Motion stages using capacitive sensors are limited to 500 [ $\mu\text{m}$ ] stroke range, which coincides with the present range of such sensors [33], [82]. On the other hand, ranges up to 300 [mm] were reported by designs employing laser interferometers [60], [100], which is similar to ranges observed for optical encoders. Although the grating period of optical encoders are in the range of microns, output from optical encoders with sinusoidal measurement signals can be interpolated for fine measurement resolution. Regarding measurement systems used in precision positioning, the largest and increasing share is observed to belong to optical encoders, which is followed by laser interferometers and capacitive sensors [35]. Optical encoders are preferred for their low cost and operational robustness, especially when the strict environment control required for highly accurate laser interferometry is not achievable [55].

Table 2.2. Summary of ultraprecision motion stage design literature (continued on pages 15-19). Color coded for actuator type.

Work		Axes		Positioning performance			Technology		
Author	Brief title	Motion axes	Motion range	Positioning resolution	Dynamic response	Control band width	Actuator	Bearing	Position sensor
Choi et al. (2008) [20]	Nanoprecision XY $\theta$ scanner	XY $\theta$	XY:1 [mm] $\theta$ : N/A	20 [nm]	$\phi$ 400 [ $\mu$ m], 1 [Hz]: 0.15 [ $\mu$ m] error	85 [Hz]	lorentz	air bearing	laser interferometer
Kim et al. (2007) [51]	$\Delta$ -stage	6 DOF	0.3 [mm] and 3.5 [mrad]	$\pm$ 5 [nm] $\pm$ 300 [ $\mu$ rad]	N/A	50 [Hz]	lorentz	magnetic levitation	capacitive + laser interferometer
	Y - stage	6 DOF	5 [mm] and 3.5 [mrad]	$\pm$ 4 [nm] $\pm$ 100 [ $\mu$ rad]	N/A	109.5 [Hz]	lorentz	magnetic levitation	capacitive + laser interferometer
Maeda et al. (2006) [69]	XY nano-positioning table	XY $\theta$	XY: 10 [mm] $\theta$ : N/A	N/A	$\phi$ 200 [nm], 500 [Hz]: 7 [nm] error	N/A	lorentz	vacuum preloaded air bearing	laser interferometer
Mori et al. (2003) [76]	Linear actuator	X	N/A	17 [nm]	N/A	4 [kHz]	lorentz	air bearing	optical encoder
Parmar et al. (2014) [84]	Large dynamic range nanopositioning	X	8 [mm]	25 [nm]	4 [mm] amp., 2 [Hz] sine: 10 [nm] RMS error	85 [Hz]	lorentz	flexure	optical encoder

Work		Axes		Positioning performance			Technology		
Author	Brief title	Motion axes	Motion range	Positioning resolution	Dynamic response	Control band width	Actuator	Bearing	Position sensor
Shinno et al. (2007) [99] Hiroshi et al. (2012) [44]	X-Y motion table system	XY	18 [mm]	1 [nm]	$\phi$ 200 [nm], 2 [Hz]: 1 [nm] error	N/A	lorentz	air bearing	laser interferometer
Teo et al. (2015) [106]	Flexure-based re-configurable actuator	X	2 [mm]	$\pm$ 10 [nm]	N/A	N/A	lorentz	flexure	optical encoder
Zhang and Menq (2007) [113]	Six-axis magnetic levitation and motion	6 DOF	2 [mm] and 4 [deg]	XYZ: 7x5x20 [nm] $\alpha\beta\theta$ : 0.5x0.5x0.1 [μrad]	N/A	107 [Hz]	lorentz	magnetic levitation	laser interferometer
Lu and Usman (2012) [65] Lu et al. (2013) [66]	6D direct drive planar motion stage	6 DOF	X: 400 [mm] Y: 400 [mm] Z: 15 [mm]	< 1 [μm]	N/A	N/A	planar lorentz	magnetic levitation	stereo - vision

Work		Axes		Positioning performance			Technology		
Author	Brief title	Motion axes	Motion range	Positioning resolution	Dynamic response	Control band width	Actuator	Bearing	Position sensor
Lu et al. (2015) [67]	Magnetically levitated rotary table	6 DOF	XY: $\pm 200$ [ $\mu\text{m}$ ] Z: $\pm 150$ [ $\mu\text{m}$ ] $\alpha\beta$ : $\pm 0.54$ [deg] $\theta$ : Unlimited	XY: $\pm 20$ [nm] Z: $\pm 100$ [nm] $\alpha\beta$ : N/A $\theta$ : $\pm 0.5$ [ $\mu\text{rad}$ ]	N/A	100 [Hz]	planar lorenz	magnetic levitation	capacitive + optical encoder
Ruben (2010) [93] Fesperman et al. (2012) [31]	Multi-scale alignment and positioning system	XY $\theta$	XY: 10 [mm] $\theta$ : N/A	<1 [nm]	N/A	N/A	linear motor	air bearing	laser interferometer
Zschaeck et al. (2011) [114]	Decentralized high precision motion	XY	200 [mm]	N/A	max 1 [mm/s] smooth traj.: 15 [nm] RMS error	N/A	ironless linear motor	v-groove guide	laser interferometer
Chen et al. (2002) [16]	X - Y - $\theta$ stage	XY $\theta$	XY: $\pm 50$ [ $\mu\text{m}$ ] $\theta$ : $\pm 2.2$ [mrad]	50 [nm]	response at bandwidth verified	85 [Hz]	electro- magnetic reluctance	flexure	capacitive

Work		Axes		Positioning performance			Technology		
Author	Brief title	Motion axes	Motion range	Positioning resolution	Dynamic response	Control band width	Actuator	Bearing	Position sensor
Lu and Trumper (2005) [63]	Ultrafast tool servo	X	30 [ $\mu\text{m}$ ]	1.7 [nm] RMS	8 [ $\mu\text{m}$ ] amp., 3 [kHz] sine: 2.1 [nm] error	23 [kHz]	electro-magnetic reluctance	flexure	capacitive
MacKenzie (2015) [68]	High - accuracy variable reluctance actuator	X	N/A	N/A	N/A	150 [kHz]	electro - magnetic reluctance	air bearing	optical encoder
Shamoto et al. (2000) [97]	Walking drive 6 - axis table	6 DOF	XY: 60 [mm] $\theta$ : Unlimited Z: 2.3 [ $\mu\text{m}$ ] $\alpha$ : 5.5 [sec] $\beta$ : 7.9 [sec]	3 [nm]	N/A	N/A	PZT	none	laser interferometer + capacitive
Chu and Fan (2006) [21]	Long travel PZT stage	X+	unlimited in stepping	5 - 10 [nm]	N/A	N/A	PZT	cylindrical guide	laser interferometer
Liu et al. (2003) [58]	Spring mounted PZT table	X+	>310 [ $\mu\text{m}$ ]	N/A	N/A	N/A	PZT	v-groove guide	capacitive
Liu and Li (2016) [62]	3-axis precision positioning device	XYZ	N/A	N/A	$\phi$ 4[ $\mu\text{m}$ ], 200 [Hz] : < 30 [nm] error	N/A	PZT	flexure	capacitive

Work		Axes		Positioning performance			Technology		
Author	Brief title	Motion axes	Motion range	Positioning resolution	Dynamic response	Control band width	Actuator	Bearing	Position sensor
Wang and Zhang (2016) [112]	3-DOF nanopositioning platform	XY $\theta$	XY ~285 [ $\mu\text{m}$ ] $\theta$ : 9 [mrad]	X: 5.5 [nm] Y: 5.9 [nm] $\theta$ : 1 [ $\mu\text{rad}$ ]	$\phi$ 50 [ $\mu\text{m}$ ], 8 [ $\mu\text{m/s}$ ] < 5 [nm] error	N/A	PZT	flexure	capacitive
Buice et al. (2009) [12]	Single-axis precision controlled stage	X	50 [mm]	N/A	330 [ $\mu\text{m/s}$ ] feedrate: 12 [nm] RMS error	2188 [Hz]	coarse: i. Roh'lix® ii. feed-screw fine: PZT	coarse: linear guide fine: flexure	laser interferometer
Liu et al. (2010) [60]	Long-travelling nano-positioning stage	XY	300 [mm]	$\pm$ 10 [nm]	N/A	N/A	coarse: ball screw fine: PZT	coarse: linear guide fine: flexure	laser interferometer
Michellod et al. (2006) [74]	Dual-stage nano-positioning system	X	70 [mm]	N/A	200 [Hz] stochastic: 8 [nm] RMS error	PZT: 300 [Hz]	coarse: stepper motor fine: PZT	flexure	laser interferometer
Shinno et al. (2011) [100]	Long range positioning with sub-nanometer resolution	X	300 [mm]	1 [nm]	jerk cont., 100 [mm/s]: 5 [nm] error	N/A	coarse: ball screw fine: lorentz	air bearing	laser interferometer



Work		Axes		Positioning performance			Technology		
Author	Brief title	Motion axes	Motion range	Positioning resolution	Dynamic response	Control band width	Actuator	Bearing	Position sensor
Cheng et al. (2012) [18]	Ultrasonic motor	X	15 [mm]	5 [nm]	N/A	N/A	ultrasonic motor	N/A	linear diffraction grating interferometer
Ghazaly and Sato (2013) [36]	Multilayer thin electrostatic actuator	X	500 [ $\mu\text{m}$ ]	30 [nm]	N/A	N/A	multilayer thin electrostatic actuator	oil immersion	capacitive

### **2.3. Literature on voice coil actuators and their optimal design**

Voice coil actuators (VCA) are a class of electromagnetic devices which work on the principle of Lorentz forces to generate actuation within stroke lengths that are proportional to their own length. Their name derives from their common use in loudspeakers. VCA's are particularly useful in precision motion applications, for they are free from mechanical hysteresis, force or torque ripple, and backlash, due to their non-contact and continuous operation [10], [102]. Their simple design and cog-free motion makes them feasible, although their stroke length is typically shorter than multi-phase electromagnetic linear motors. However, they can be a very suitable form of actuation particularly in miniaturized fabrication systems. In this section, examples of the utilization of VCA in precision motion stages and the literature on their optimal design are presented.

#### **2.3.1. Utilization of voice coil actuators in ultraprecision motion stages**

Owing to the large versatility in the design of VCA's regarding size, shape, stroke length, configuration and capacity, several different uses of them in precision motion systems have emerged [4], [5], [24], [59], [76], [84], [88], [99], [100], [113]. Depending on the design requirements, VCA's can be made to directly actuate a stage resting on some type of support structure, like an air bearing [76], [99], [100] or a platform with a ground V-groove [59]. Also, they can be used to provide the lifting force for a system made to be levitated, while simultaneously providing the differential forces for maneuvering [113]. For reasons of preloading the system and providing a motion guide/bearing, VCA's can be designed to operate indirectly by means of a flexure mechanism [5], [24], [84], [88]. It is possible to couple VCA's in parallel with other types of actuators to enhance the positioning performance [4], [24], [59], [100]. In [100], the VCA driven stage is mounted on a ball-screw driven stage to provide fine motion. In contrast, VCA's provide the coarse motion for PZT actuators in [24], [59], while PZT motion is further refined by a thermal actuator in [4]. Although being largely dependent on the skill of the designer and the performance of other components as well, motion systems employing only VCA's for actuation have demonstrated excellent positioning accuracy. The tracking system for a magnetic recording system developed by Mori et al. [76] has 0.5 [nm] positioning accuracy after the 8 [nm] sensor noise is filtered out. The planar motion table with  $\pm 10$  [mm] range [99] has 1 [nm] positioning resolution on each axis. The single axis nano-positioning system [84] could achieve tracking with 10 [nm] RMS error.

#### **2.3.2. Optimal design of voice coil actuators**

Optimization of VCA's has been investigated in several studies [29], [50], [52], [56], [61], with the overall shape and structure of the VCA varying according to the applications, such as a high-precision

motion stage [50], [61], an optical disk drive [52], or just studying the optimal design of VCA's on its own [29], [56]. In [50], the only requirement from the VCA is the ability to actuate the system with regard to the forces demanded by the flexure bearing. The requirement to limit heat dissipation is handled indirectly through constraints. In [61], the optimization cost function is a combination of dynamic response, acceleration and heat dissipation, while in [52] it is aimed to minimize the vibratory disturbances on the system. For the evaluation of magnetic fields, finite element (FE) analysis [52], [56], magnetic equivalent circuit (MEC) method [50], [61], or a combination of the two [29], have been used. The method of optimization also differs among different works, such as manifold-mapping [29], sequential quadratic programming (SQP) [50], genetic algorithms (GA) [61], the level set (LS) method [56] and the design of experiments (DOE) [52]. Predictions of the physical properties of the design are verified in experiments in [50], [52], [61].

In this thesis, VCA's have been designed using two novel optimization objectives, which are independent of the coil wire gauge. In the earlier VCA optimization studies, wire gauge of the coil was either a preset, or it appeared as a variable inside the optimization problem, or was eliminated by combining different criteria (i.e., new cost functions derived in a way to eliminate the wire gauge variable). In this thesis, the coil design is achieved separately, according to desired electrical characteristics without impacting the optimality of the VCA from a standpoint of the chosen performance criteria, which are maximum stage acceleration, and minimum thermal output.

#### **2.4. Literature on performance assessment and verification methods**

In this section, descriptions and relevant literature regarding the motion stage performance assessment and verification methods used in this thesis are presented.

##### **2.4.1. Dynamic Error Budgeting (DEB)**

Error budgets [23] are frequently used in the design of precision machines, in order to assess the contributions of different factors such as parasitic motions, thermal expansion, and servo accuracy, on the positioning accuracy of a machine. Dynamic Error Budgeting (DEB) or 'Spectral Analysis' extends this concept to the realm of feedback control. Recognizing that the controller can provide only a finite attenuation of disturbance signals interfering with the servo, DEB provides a methodology for predicting the cumulative effect of such signals on the control error as a function of their spectral (frequency) content. The method can be used to predict the control accuracy of a system implemented using a set of certain devices under certain conditions before it is realized. Furthermore, as it is formulated in the frequency domain, it can be used to optimize the controller design as well,

typically leading to an  $H_2$  - optimal control framework. In DEB, the disturbance signals are modeled with their power spectral density (PSD), assuming that they are stationary stochastic processes which are not correlated with each other. Then, these PSD's are transmitted to the performance goal, most often the positioning error, using linear time invariant (LTI) system theory. The transmitted PSD's are summed up into the variance of the performance goal, which constitutes a comparative measure of performance. Most importantly, the influence of different dynamic factors and disturbance sources, which have the greatest impact on the achievable performance (e.g., accuracy) can be easily spotted and improved, through this kind of analysis. An approach similar to DEB was followed to decompose the contribution of different noise sources on the hard disk position error in [1], [2], [45]. DEB has been used to assess the performance of a geophone and a vibration isolation system in [75]. Jabben [49] has used DEB in the mechatronic design of a magnetically suspended rotating platform. Aguirre et al. [3] have analyzed the performance of active aerostatic thrust bearings using DEB.

In this thesis, DEB is used to decompose the control error and the actual positioning error signals, recorded during positioning with a step trajectory, into their constituent factors. These factors are given as the servo tracking error, sensor noise and the digital to analogue converter (DAC) quantization noise. This way, individual effects of these factors on the overall positioning performance is identified, and the most critical ones are determined. This serves as both a verification of already implemented design choices regarding the control system, and a guideline for future practices.

#### **2.4.2. Modal testing**

Modal testing refers to a broad family of methods pertaining to the measurement and evaluation of vibratory dynamics of mechanical systems. Its realization involves the utilization of knowledge in the fields of linear systems, signal analysis, sensors, and optimization. The practice of modal testing is achieved by exciting the system under study (e.g., car body, turbine shaft, machine tool spindle) using a specially designed device. In impact testing used in this thesis, a hammer fitted with a force sensor at its tip is used. A shaker can also be used which provides a sinusoidal excitation sweeping the frequency range of interest. The response of the system is sensed using transducers, like accelerometers which measure the acceleration, laser vibrometers which measure the velocity, and linear variable differential transformers (LVDT) which measure the displacement. The frequency response function (FRF) between the excitation point and the measurement point is then calculated using a variety of estimators involving the auto - spectral and cross - spectral densities of the signals, each having their own robustness to different sources of noise. Using a variety of methods, both

manual like the ‘peak-picking’ method, and automated optimization and curve - fitting based like the ‘least-squares complex exponential’ (LSCE) method, the FRF is fitted a dynamic model. The model consists of pole natural frequencies and damping ratios, as well as participation factors (i.e., gains) representing the contribution of each vibration mode on the observed response. By comparing the FRF’s obtained from different measurement points, the modal vibration shapes of the system can be determined. Modal testing results can be used for a variety of purposes, like determining the first natural frequency of a system which might interfere with the servo control, assessing the compliances in a structure for stability, or non-destructive testing [9], [30], [43], [70], [72].

In this thesis, modal testing is applied to the ultraprecision motion stage in the form of two sets of impact tests subject to two different modal analysis methods. Identified modal dynamics, in terms of system poles (natural frequencies and damping ratios) and vibratory motion patterns (mode shapes) are compared.

#### **2.4.3. Laser interferometric metrology**

The positioning accuracy of a machine tool, as obtained from the sensors used in feedback control, only reflects a partial picture of its performance. While moving in any of the desired translational or rotational directions, the stage inevitably undergoes motions in all five remaining degrees of freedom. Such geometric errors occur due to the bearing preloads, imperfections in the assembly of the stage, component dimensional errors, static deflections, etc., and are not necessarily detectable by the position sensors used in feedback [73], [102]. Furthermore, the position measurement from sensors themselves also has imperfections, causing periodic or non-periodic positioning errors [42], [64]. Therefore, means to measure the true positioning accuracy of machine tools have been established. Definitions and methods regarding the metrology of machine tools (motion stages) as well as the presentation of results have been compiled under a number of international standards [47], [48], [107]. In this thesis, the most often referenced standard is the one pertaining to the determination of accuracy and repeatability of positioning of numerically controlled axes (ISO, 2006) [47]. The standard by ASME (2005) [107] is used in conjunction with [47].

Laser interferometry is a practical and widely used method in determining a machine tool’s geometric errors. Laser interferometers have various types, such as polarization interferometer, dual-frequency interferometer, and Twyman - Green interferometer [25]. In this thesis, a homodyne polarization type laser interferometer has been used. For each error component measured, a specific set of optical elements are used to direct the laser beam in the required differential path. In the literature, geometric

errors measured using laser interferometry have been used in error budgets [23], which grade the overall accuracy of a machine.

In this thesis, laser interferometric metrology is used to determine the geometric errors of the ultraprecision motion stage. A subsequent error budget is formed using geometric errors, as well as other contributing error sources such as the servo error and the thermal error.

## **2.5. Conclusion and comparison of specifications**

This chapter has presented the review of literature related to ultraprecision motion stage designs, optimal design of voice coil actuators, and performance assessment and verification methods. The qualitative specifications of example precision stages ([12], [31], [60], [84], [99]) can be compared to the stage designed in this thesis for an overview. When a single stage design (as opposed to stacked design) is used, motion ranges reported are 10 [mm], 8 [mm], and 18 [mm] ([31], [84], [99]), compared to the 20 [mm] stroke length realized in the design proposed in this thesis. For stacked designs, motion ranges extend to 50 [mm] [12] and 300 [mm] [60]. The 20 [nm] and 25 [nm] ([60], [84]) peak-to-valley positioning resolutions reported are obtained using homodyne laser interferometer and optical encoder, respectively. In the design proposed in this thesis, 10 [nm] peak-to-valley positioning resolution is obtained using an optical encoder. In [31] and [99], positioning resolutions less than or equal to 1 [nm] are reported, both using heterodyne laser interferometers. Their higher resolution can be attributed to the superior accuracy in measuring frequency, which is employed in heterodyne laser interferometers, compared to measuring light intensity, which is employed in homodyne laser interferometers. The control bandwidths reported are 85 [Hz] [84] and 2188 [Hz] [12]. In the design presented in this thesis, the control bandwidth achieved is 450 [Hz]. In [12], the high bandwidth is achieved using a PZT actuator. The small motion range of the PZT is compensated by stacking it with a coarse motion stage, which is a feed-screw drive.

The following chapters present the details of mechatronic design (Chapter 3), actuator design (Chapter 4), controller design (Chapter 5), modal testing (Chapter 6), and laser interferometric metrology (Chapter 7).

## **Chapter 3**

### **Mechatronic Design of the Positioning Stage**

#### **3.1. Introduction**

Mechatronic design of a precision positioning stage is a multi-disciplinary problem involving several design choices. The main challenge involved is that obtaining high performance from such a system requires each and every component to function as desired, within a holistic framework. For example, if high positioning accuracy is desired, a voice coil actuator (VCA) can be preferred for continuous, ripple-free actuation over iron cored permanent magnet synchronous motors (PMSM). However, that would not suffice unless an aerostatic or hydrostatic bearing free from stick-slip motion is used, for which part tolerance requirements are tighter than slide or rolling element type bearings. Another alternative would be to use a flexure bearing; however that requires a constant force to be applied at the displaced stage position and would result in the heating of VCA even while holding a static displacement. Certain ceramics can be used in the stage to lower errors caused by thermal gradients, but that would increase stage inertia and lower positioning bandwidth. As can be seen, implementing the right combination of actuator - bearing - structural material requires considerable deliberation. Adding to these, the choice of sensors, assembly method, dimensions, actuator location and configuration, and considering a larger set of performance criteria including stroke length, vibratory dynamics, motion errors, difficulty of assembly, and overall cost, a more complete picture of the design process can be drawn.

In this chapter, the mechatronic design of the translational positioning stage is described, excluding the details of the voice coil actuators (VCA) which are presented in detail in Chapter 4. First, the preliminary design of a low-cost desktop precision micro machine tool is presented in Section 3.2. The ultraprecision motion stage designed and built in this thesis corresponds to the X axis positioning component of the machine tool, from which the design requirements are derived. In Section 3.3, the most prominent features of the stage are presented along with the reasoning behind the choices. In Section 3.4, the predicted error budget is presented. In Section 3.5, prediction of vibratory dynamics of the system is presented.

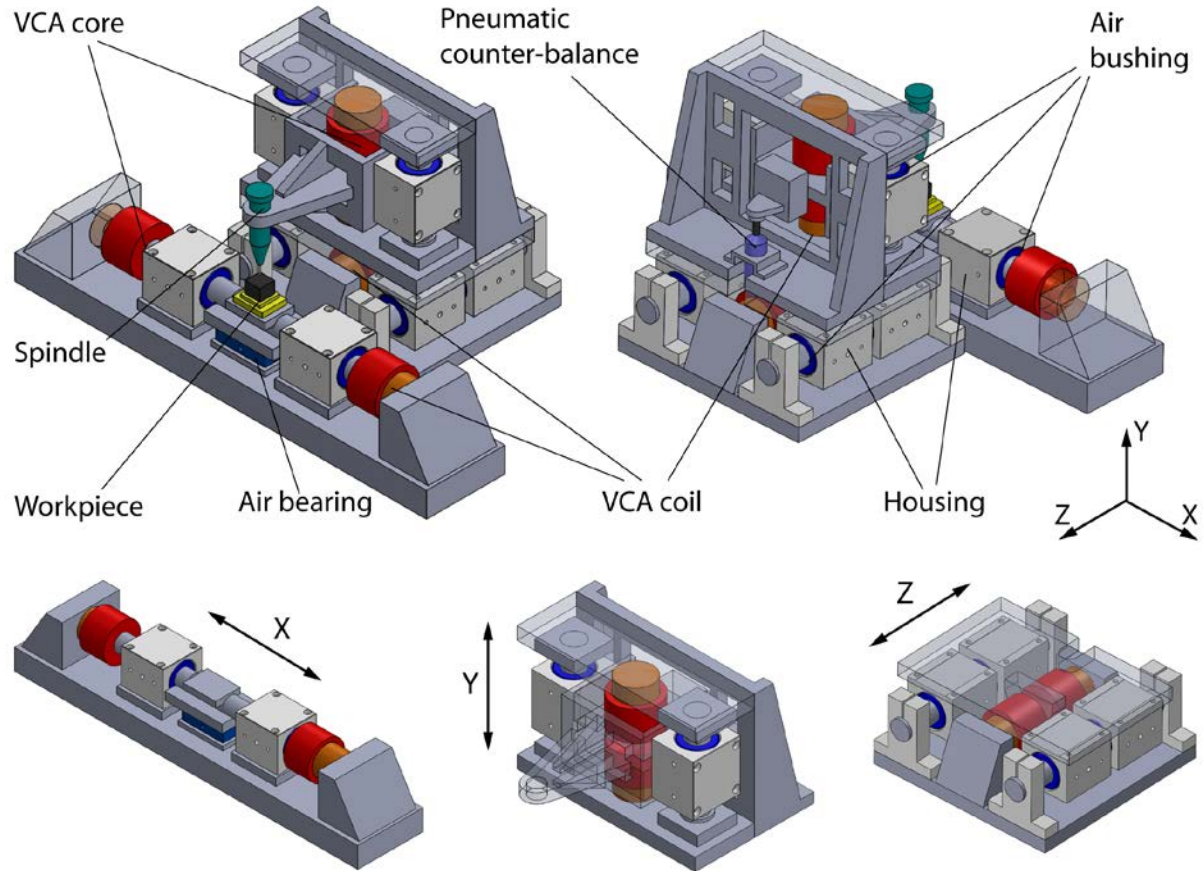


Fig. 3.1 Preliminary design of a desktop precision micro machine tool.

### 3.2. Low-cost desktop precision micro machine tool concept

Front and back views for the preliminary design of a desktop precision micro machine tool are presented in Fig. 3.1. Main components of the machine which provide motions in X, Y, and Z directions are also shown individually. The micro machine tool is designed for micro-cutting, more specifically for micro-milling. Micro-milling is used to generate features as small as a few microns on micro ( $<1000$  [ $\mu\text{m}$ ]) or macro sized workpieces. Example products manufactured using micro-milling are dental implants, biomedical devices, lab-on-a-chip, optical lens arrays, micro moulds, and injection nozzles. The general performance requirements for ultraprecision motion stages (Table 2.1) also apply to the positioning axes of the micro-milling machine. Micro-milling can be performed on a conventional CNC machine retro-fitted with a high speed spindle. On the other hand, a special machine tool designed for that purpose can exploit certain advantages of miniaturization. One such advantage is that the workpiece sizes are generally limited to 10-20 [mm], which allows machines to be built with similarly low stroke capacity. This allows the feedscrew and linear motor drives to be replaced by the more linear, lighter, and simpler to operate voice coil actuators [19].



The proposed concept employs air bushings, for easy and low-cost assembly. Air bushings, being fixed in the housings by O-rings, allow for self-alignment. Only in the X-axis, a rectangular air bearing is used to constrain the roll motion. This way, the common double shaft arrangement is avoided, and the overall size of the machine is reduced. Voice coil actuators in moving magnet mode, in complementary double configuration, are used for non-contact and continuous actuation with near uniform force response. The proposed design targets workpiece dimensions of 20 x 20 x 20 [mm]. Servo accuracy is intended to be a few nanometers, and overall part accuracy due to servo accuracy, thermal errors and tolerances on the mechanical components to be a few microns. A pneumatic counter-balance is built in to cancel out force due to gravity; hence, running a constant current on the vertically oriented actuator is avoided. This way, excessive heating of actuator coils is prevented. The translational positioning bed designed and built in this thesis corresponds to a prototype version of the X-axis positioning stage of such a machine tool. The X positioning axis presents an additional design challenge due to the replacement of the double guideway arrangement utilized in other axes in favor of the single shaft air-bearing design. The Y and Z axes are bulkier, but the desired control bandwidths are believed to be achievable by proper tuning of the controllers, and if required, by rescaling the actuators accordingly.

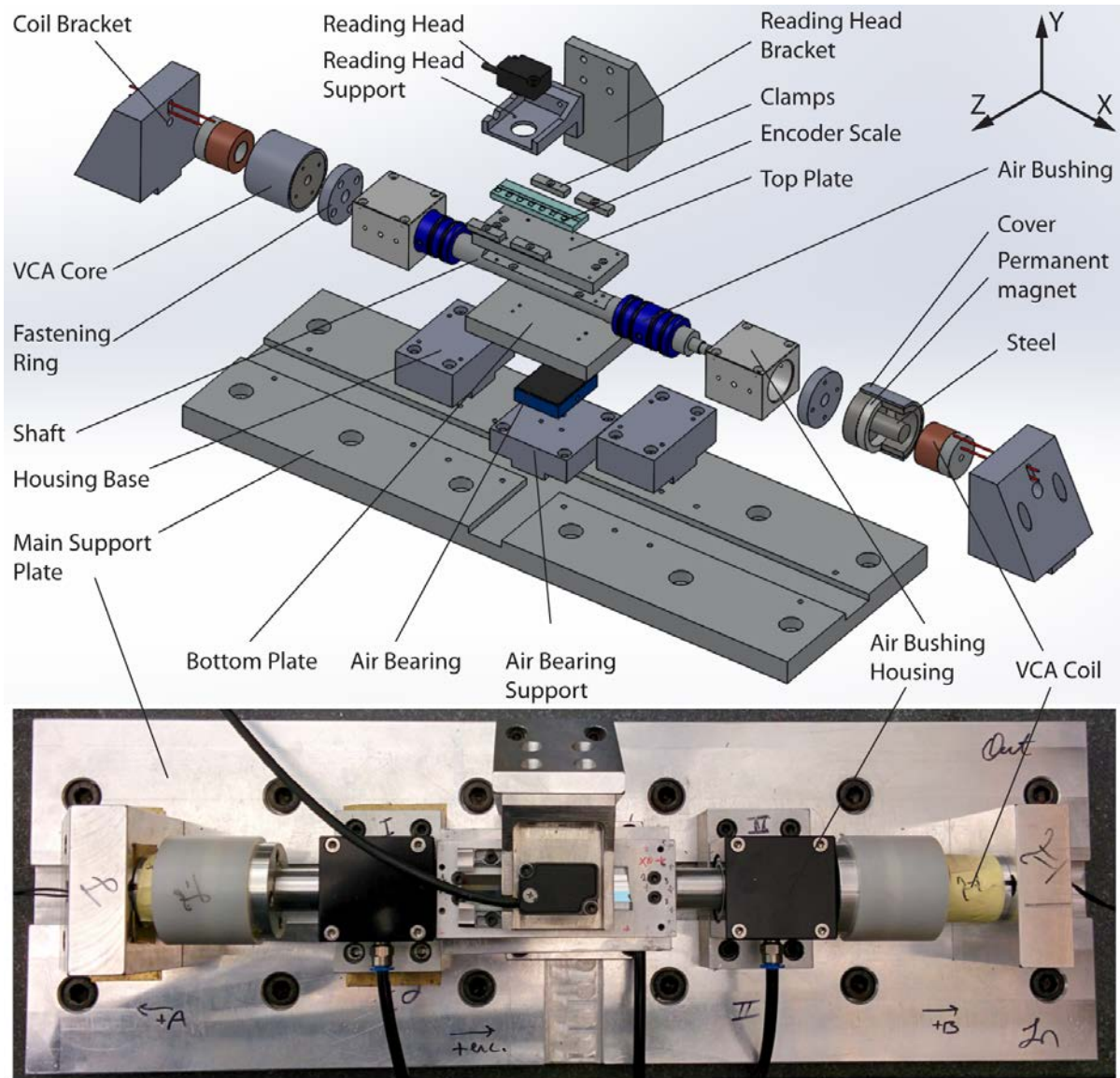


Fig. 3.2 Exploded view and photograph of the long-stroke translational nano-positioner.

### 3.3. Design features

An exploded view and photograph of the long-stroke translational nano-positioner is presented in Fig. 3.2. The design features and details are outlined in the proceeding:

- i. The shaft, top and bottom plates are made of Aluminum (6061) for reduced mass, corrosion resistance, and the prevention of electromagnetic interactions. Support structures in the setup are also made of the same material. A three dimensional rendering of the shaft is presented in Fig. 3.3. A detailed technical drawing of it is presented in Appendix B. The part is

manufactured by machining two parallel flat surfaces at the top and bottom of the  $\phi 20$  [mm] precision ground shaft. Grinding is preferred due to the tight tolerances and excellent surface quality required by the air bushings. Thread screws are machined, which engage to the VCA cores using the method described in the next bullet point.

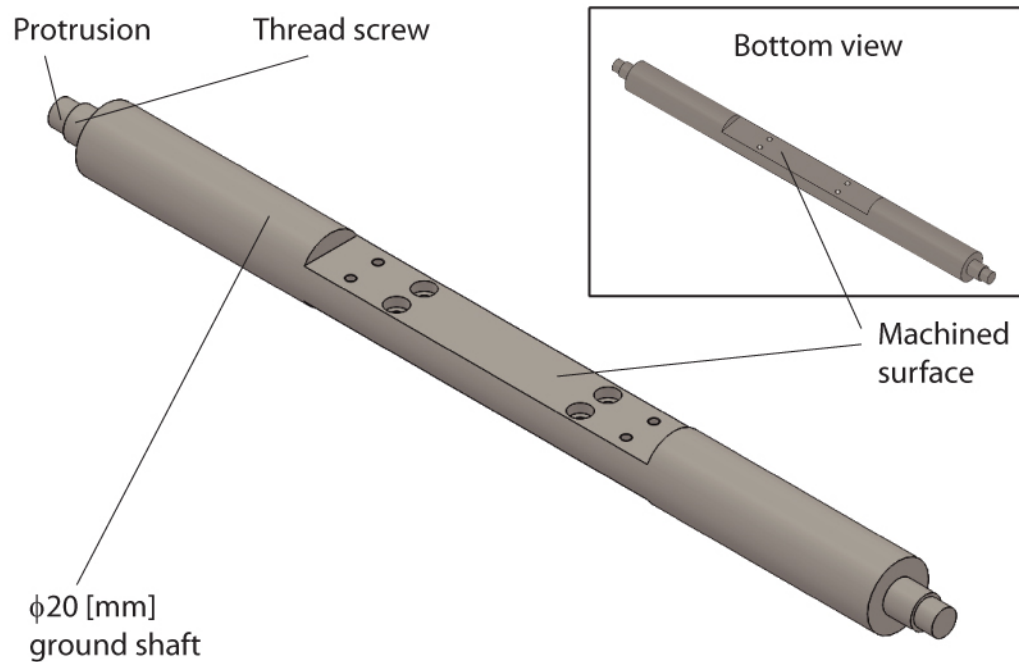


Fig. 3.3 Drawing of the main shaft.

- ii. The cylindrical VCA core (made of magnet and steel) is attached to the shaft using the thread screw and the fastening ring. The interface of the assembly is presented in Fig. 3.4. The fastening ring is tightened at the shoulder towards the shaft. A precision ground  $\phi 8 (+ 0, - 0.010)$  [mm] protrusion (6 [mm] long) of the shaft engages to an  $\phi 8 (+ 0.025, - 0)$  [mm] precision hole on the VCA core. When the M3 bolts are tightened, assembly is complete. Damage to the mating surfaces during assembly has to be minimized in order to prevent the relaxation of tolerances. During the operation of the nano-positioner, actuation forces act at the two ends of the main shaft, in the same direction. As the magnitudes of forces at the two ends are different, a moment can be generated if there is misalignment. Maximum difference in force magnitudes occurs at  $x = 0$  or 20 [mm] positions (Fig. 3.8) and it can be calculated as 2.99 [N]. The assembly tolerances shown allow a maximum of 17.5 [ $\mu\text{m}$ ] moment arm,

resulting in a moment of 0.052 [N.mm]. Using the stiffness values in yaw and pitch directions (as shown in Section 3.5), resulting angular deflections are calculated to be at the nano-radian level, making the stage practically free from quasi-static deflections due to actuation forces.

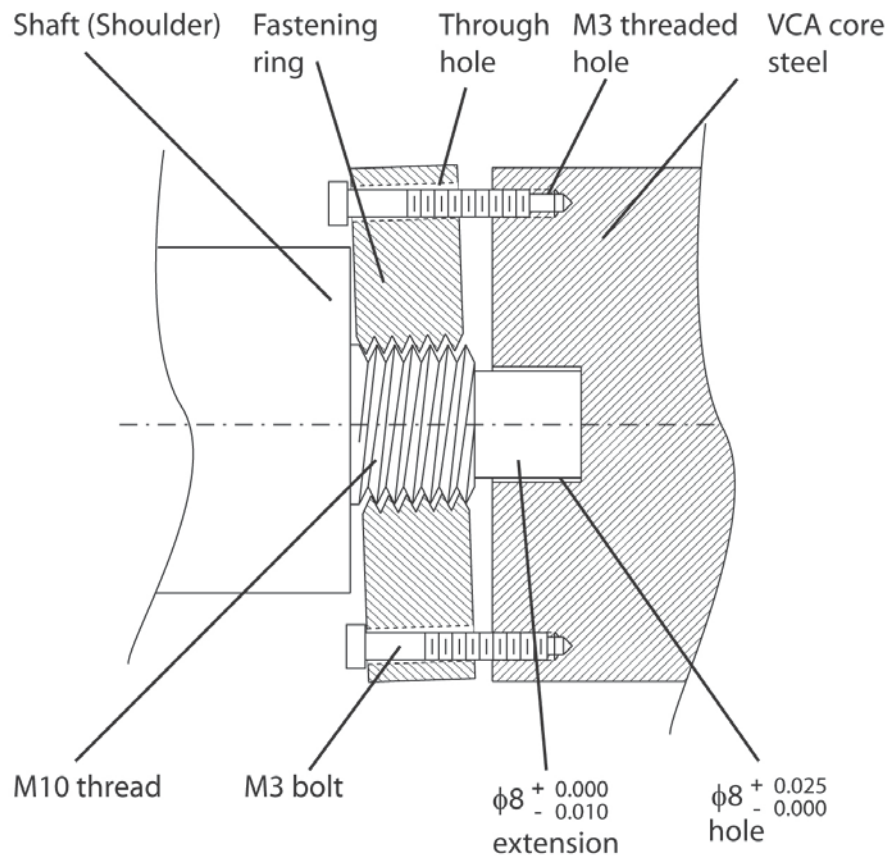


Fig. 3.4 VCA alignment to the shaft. Dimensions in [mm].

- iii. Air bushings are held in the housings using O-rings. O-rings provide some flexibility which allows for self-alignment. They also provide sealing for the air supply at the bushing-housing interface. After the guideways are self-aligned, under pneumatic pressure, an epoxy material can be injected into the cavity between the air bushings and the air bushing housings to achieve further stiffness in the radial direction [80][103].
- iv. The discharge of compressed air from the air bushings and bearings helps to remove heat, which is mainly produced by the actuator coils, from the stage.
- v. To minimize unwanted moment generation during actuation, the top and bottom plates are sized to align the axis of actuation with the center of mass, using CAD program calculations.

- vi. Voice coil actuators (VCA) are used in moving magnet mode. Although this increases the overall moving mass, it is considered a good trade-off from the moving coil configuration. This is due to the elimination of parasitic forces which may be introduced by lead cables. Technical drawings for the VCA core assembly and coil assembly are presented in Fig. 3.5 and 3.6. The VCA core is assembled in-house by removing a number of thin wooden plates one by one from the magnet/steel interface. Centering is done using the nylon cover. The coil assembly is fabricated by an external supplier, using solvent bonding to keep coil wires in place.

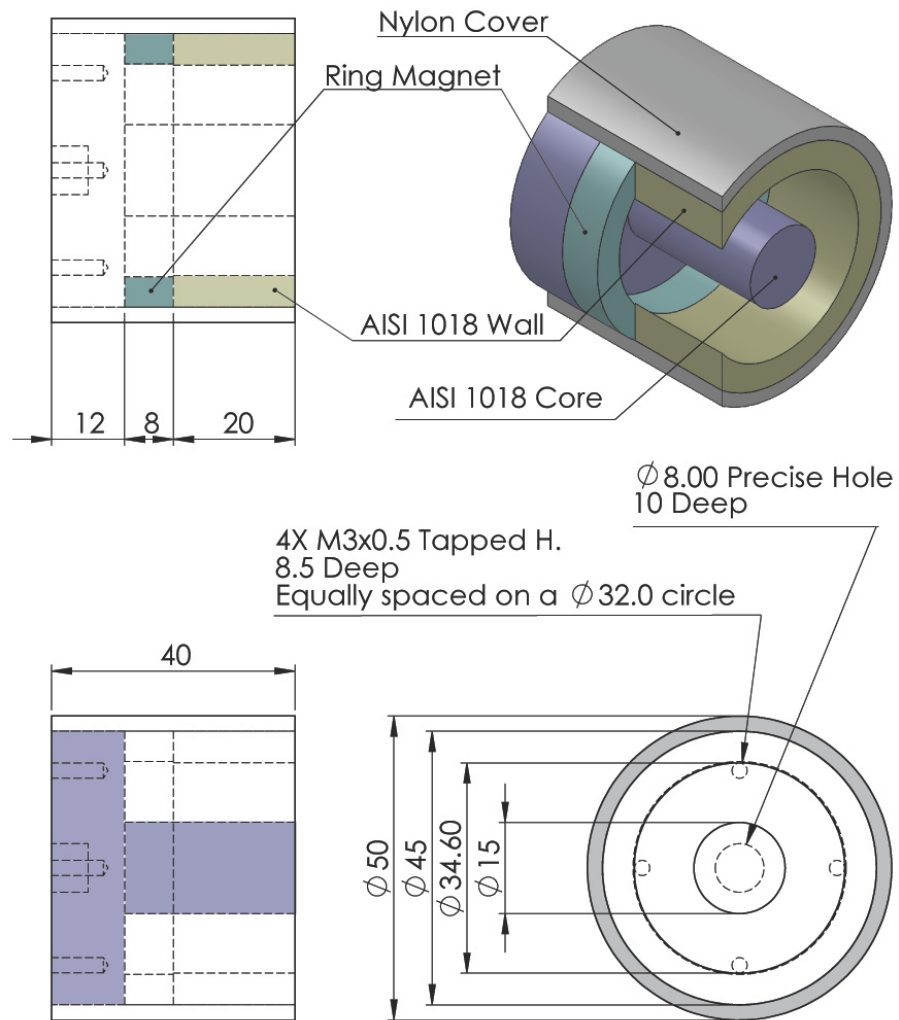


Fig. 3.5 VCA core assembly. Dimensions in [mm].

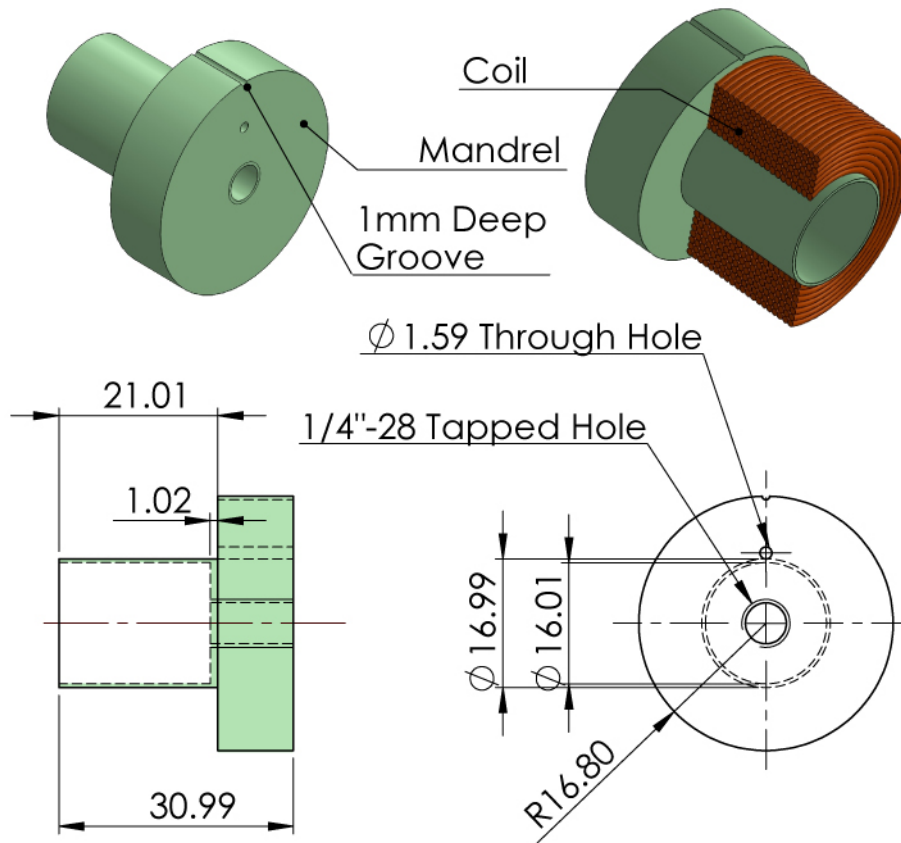


Fig. 3.6 VCA coil assembly. Dimensions in [mm].

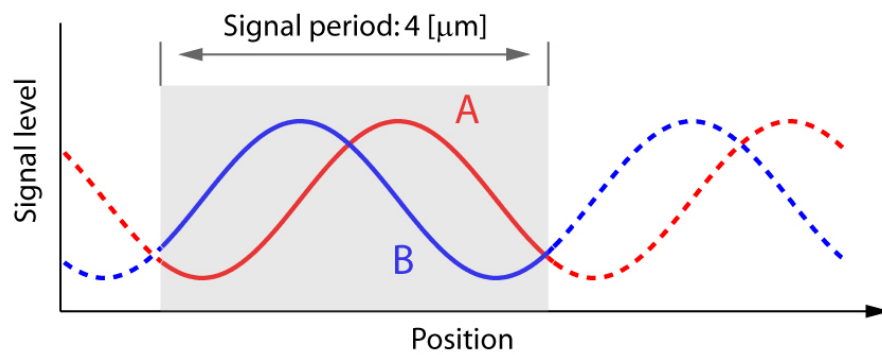


Fig. 3.7 Signal outputs (A and B) from the encoder.

- vii. The encoder scale (Heidenhain® LIP501 R) has 8 [μm] grating period and the encoder reading head (Heidenhain® LIP58) outputs two 90 [deg] phased measurement signals A and B, with 4 [μm] period due to integrated interpolation, as shown in Fig. 3.7 [28]. These sinusoidal signals can be further interpolated using arctangent formulation. The reading head support is made out of stainless steel for high stiffness, which has to be delivered within a compact volume.
- viii. The complementary double voice coil configuration has been used to provide near uniform force generation per supply current. Actuator force factor ( $K_f$ ) is simulated using COMSOL® finite element analysis (FEA) as shown in Fig. 3.8. This uniformity of response provides better linearization of the overall positioning system, hence allowing higher bandwidth control to be achieved without compromising stability margins, or requiring elaborate gain scheduling.

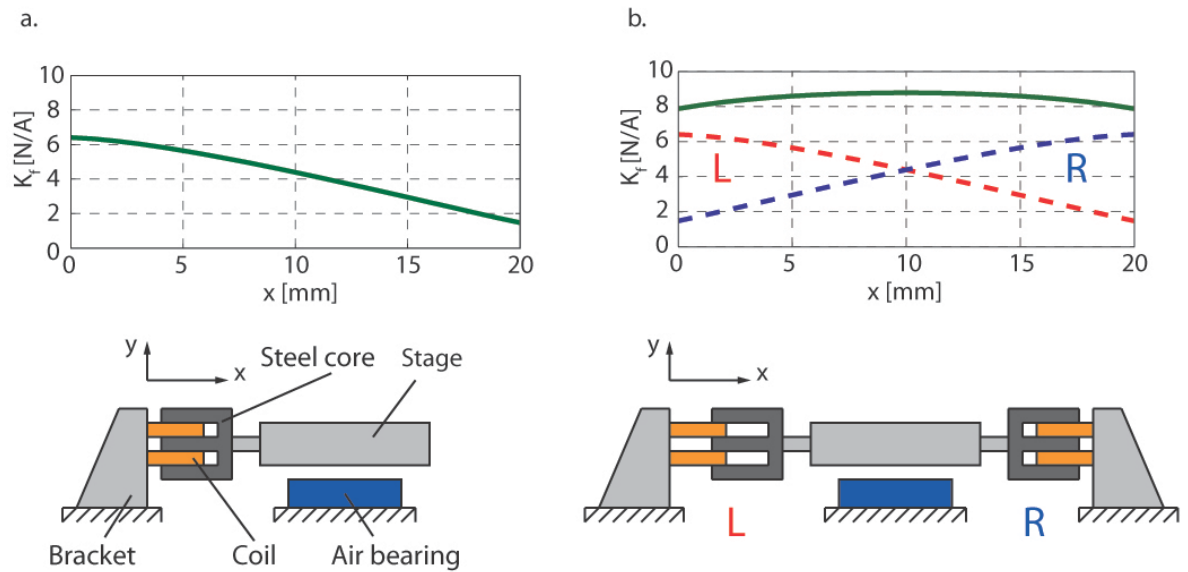


Fig. 3.8 Force factor vs. stroke position; a. single VCA, b. complementary double VCA.

- ix. Linear current amplifiers are used to power the VCA coils. A separate amplifier board is used for each coil, which is configured for the same controller. The circuit diagram of the amplifier board and the configuration of the controller are presented in Appendix A. A linear amplifier is preferred over a PWM amplifier due to better noise characteristics [104]. Also, due to the relatively low power requirements of the motion stage, lower efficiency and heating problems of linear amplifiers are manageable in the case of miniature-range actuators.

- x. The computer control is implemented using the DSpace® DS1005 controller running at 20 [kHz] sampling frequency. The closed loop bandwidth is typically selected as 20 times or less than the sampling frequency, which limits it to 1000 [Hz] in this thesis. The encoder is connected to the DS3002 encoder interface which allows 4096 times interpolation using arctangent formulation. The 4 [μm] signal period from the encoder can thus be interpolated to 0.97 [nm] measurement resolution. Voltage commanded to the amplifiers by the controller is transmitted via the DS2102 digital-to-analog converter (DAC) with ±10 [V] range and 16-bit resolution, corresponding to a least significant bit (LSB) of 0.305 [mV]. An analog-to-digital converter (ADC), DS2001 is used to gather fault and current measurement signals from the amplifier board. The ADC board has the same range and resolution specifications as the DAC board. It is also used to measure encoder A and B signals separately to initialize the encoder signal correction scheme described in Chapter 5.

### 3.4. Error budget at the design stage

Error budgets are used in precision machine design to determine the effect of various factors on the overall accuracy of a machine [23]. They can be used to evaluate design choices and identify bottlenecks. An error budget can be made before the machine is built, or can be compiled based on measurements on the actual machine to quantify its actual accuracy. In this section, an error budget is formed based on predictions at the design phase.

#### 3.4.1. Measurement errors

Linear errors in the motion axis (X) are related to the errors of the position sensor. These comprise the following:

- The interpolation of output from the encoder reading head by the encoder interface results in an effective sensor resolution and peak-to-valley (PV) error due to position uncertainty as,  $E_{res} = 0.97$  [nm].
- The linear encoder scale is manufactured to ±1 [μm] grating error. The calibration sheet provided suggests ±0.52 [μm] error for the specific scale used. Thus, the PV error due to encoder grating defects can be expressed as,  $E_{grating} = 1040$  [nm].



### 3.4.2. Geometric errors

Estimation of geometric errors is done according to the tolerances of the guideways. In the ultraprecision motion stage designed in this thesis (Fig. 3.2), the main shaft acts as the guideway. The  $\phi 20$  [mm] air bushings by New Way Air Bearings® require -7 g6 shaft tolerances, which means that the shaft radius varies between -3.5 to -10 [ $\mu\text{m}$ ] from the nominal radius, as shown in Fig. 3.9. An extra cylindricity tolerance is specified as 5 [ $\mu\text{m}$ ] for manufacturing, in order to reduce the variations. The axis of the shaft re-aligns itself with respect to the axis of the bushings in the face of dimensional variations, to come to force equilibrium. This effect roughly cancels half of the dimensional variations as reflected to the point of interest, which is assumed to be at the center of the top surface of the top plate. Therefore, PV errors of  $E_Y = 2.5$  [ $\mu\text{m}$ ] and  $E_Z = 2.5$  [ $\mu\text{m}$ ] can be predicted for errors in Y and Z directions, respectively. Dimensional variations can induce additional errors due to yaw and pitch rotations about the Y and Z axes, respectively. These are neglected assuming that the moment arms relating them to linear errors are small.

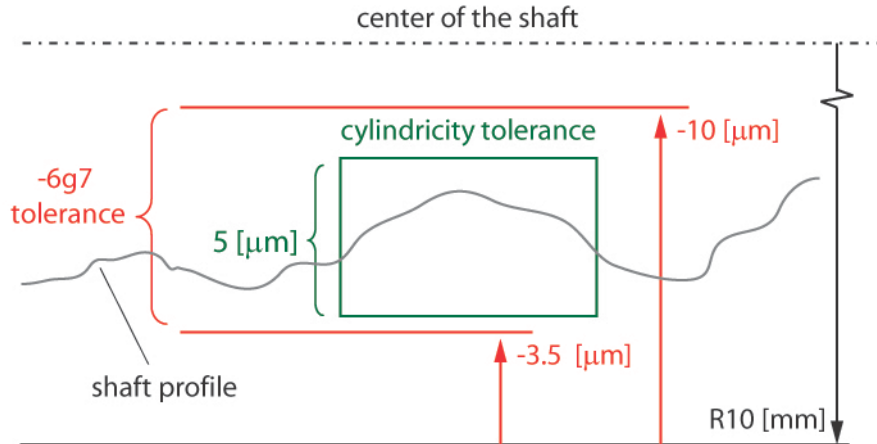


Fig. 3.9 Tolerances on the shaft.

### 3.4.3. Servo error

Due to the negligible viscous friction of air bushings, the positioning stage can be modeled as a pure mass given by,

$$G_p(s) = \frac{1}{ms^2}. \quad (3.1)$$

A proportional + derivative controller, which is the minimum requirement to stabilize the axis, can be assumed in the form:

$$C(s) = K_p + K_d s. \quad (3.2)$$

Then, the error transfer function can be derived as [34],

$$G_s(s) = \frac{e}{r} = \frac{ms^2}{ms^2 + K_d s + K_p} = \frac{s^2}{s^2 + 2\zeta\omega_n s + \omega_n^2}. \quad (3.3)$$

Above,  $G_s$  is the sensitivity transfer function,  $e$  is the positioning error,  $r$  is the reference input,  $\zeta$  is the closed loop damping ratio, and  $\omega_n$  is the closed loop natural frequency. Natural frequency of the system is set to the desired bandwidth during controller design as  $\omega_n = 2\pi \cdot 500$  [rad/s]. For the type 2 system formed (i.e., two integrators in the loop transfer function ( $L = CG_p$ )), the steady state error for a constant acceleration input is presented by [34],

$$E_{ss} = \frac{A}{\omega_n^2}, \quad (3.4)$$

where  $A$  is the acceleration. For the 20 [mm] stroke length, if a maximum feedrate of  $F = 10$  [mm/s] is assumed for the stage, a corresponding maximum acceleration command of  $A = 100$  [mm/s<sup>2</sup>] can be assumed as shown in Fig. 3.10. Then, the steady-state positioning error during constant acceleration becomes  $E_{ss} = 10$  [nm].

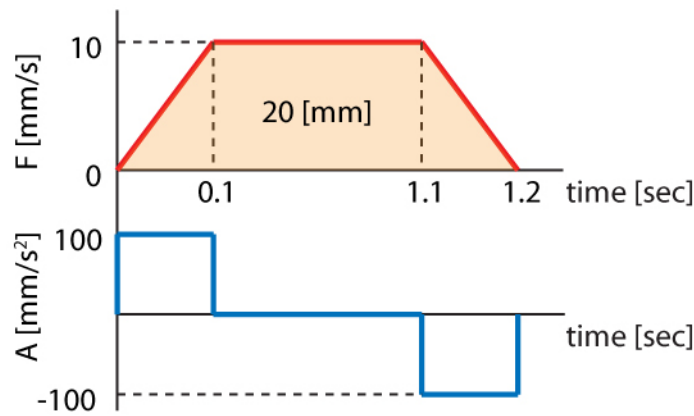


Fig. 3.10 Assumed motion profile.

### 3.4.4. Predicted error budget

The predicted error budget is presented in Table 3.1. The explanations for RMS sum and the usage of mean value of arithmetic and RMS sums can be found in Section 7.4. The 3.6 [μm] predicted PV sum can be interpreted as ±1.8 [μm] manufacturing tolerance, as the components of error are centered at zero. This value conforms to the tolerance range prescribed for micro-milling machines [11].

Table 3.1 Predicted error budget

Error components	PV magnitude [nm]
Position sensor resolution ( $E_{res}$ )	0.97
Position sensor grating error ( $E_{grating}$ )	1040
Servo error ( $E_{ss}$ )	10
Y straightness ( $E_Y$ )	2500
Z straightness ( $E_Z$ )	2500
<b>Arithmetic sum</b>	6051
<b>RMS sum</b>	1064
<b>Mean</b>	3557

### 3.5. Predicted vibratory dynamics

The air-bearing / air-bushing arrangement used in the proposed design of the precision motion stage is presented in Fig. 3.11. In the figure, the X-axis represents the direction of motion. All other degrees of freedom are constrained by the bearing arrangement. The bearings, on the other hand, can only provide a finite stiffness in the constrained axial and rotational directions, as reported in the manufacturer's catalogue [81]. Catalogue stiffness values of bushings/bearings and certain dimensions are presented in Table 3.2. Inertia values of the moving body are calculated using CAD program and presented in Table 3.3. Air bearings are usually not rated for their rotational stiffness. In Fig. 3.12, a simple model for the air bearing response to rotational loading is presented. When the matching structure is in its rotationally neutral position, the assumed distributed stiffness elements ( $w_k = k_{2y} / L$ ) are preloaded. The moment generated due to rotation of the supported body can be expressed as:

$$M_k = \int_{x=-L/2}^{x=L/2} (\theta x) \cdot x \cdot w_k \cdot dx = \frac{k_{2y} L^2 \theta}{12} = k_{2r} \theta, \quad (3.5)$$

where  $k_{2y}$  is the axial stiffness, and  $k_{2r}$  is the estimated rotational stiffness. The air bearing length ( $L$ ) is different along the X and Z axes ( $L_{2x}, L_{2z}$ ), which results in different estimations of roll and pitch stiffness of the air bearing.

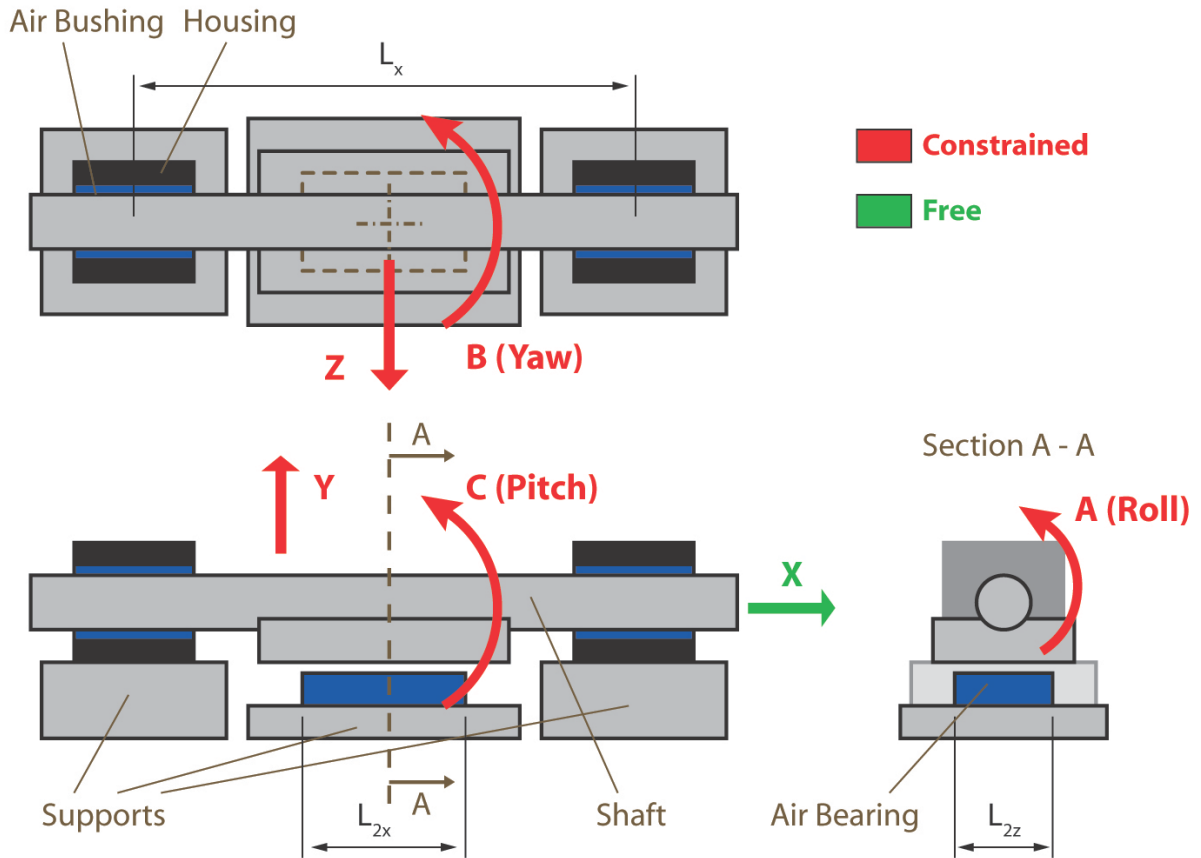


Fig. 3.11 Air-bearing / air-bushing arrangement of the motion stage.

Table 3.2 Air - bearing/bushing stiffness properties and dimensions.

Property	Symbol	Value
Air bushing axial stiffness	$k_{1yz}$	23 [N/ $\mu$ m]
Air bushing rotational stiffness	$k_{1bc}$	2.8 [Nm/mrad]
Air bearing axial stiffness	$k_{2y}$	35 [N/ $\mu$ m]
Air bearing roll stiffness (estimated)	$k_{2a}$	4.7 [Nm/mrad]
Air bearing pitch stiffness (estimated)	$k_{2c}$	7.3 [Nm/mrad]
Air bearing length along the X-axis	$L_{2x}$	50 [mm]
Air bearing length along the Z-axis	$L_{2z}$	40 [mm]
Distance between the middle of the air bushings along the X-axis	$L_x$	180 [mm]

Table 3.3 Inertia properties of the moving body.

Property	Symbol	Value
Mass	$m$	1.318 [kg]
Moment of inertia in A (Roll)	$I_a$	0.409 [kg.mm <sup>2</sup> ]
Moment of inertia in B (Yaw)	$I_b$	17.439 [kg.mm <sup>2</sup> ]
Moment of inertia in C (Pitch)	$I_c$	17.454 [kg.mm <sup>2</sup> ]

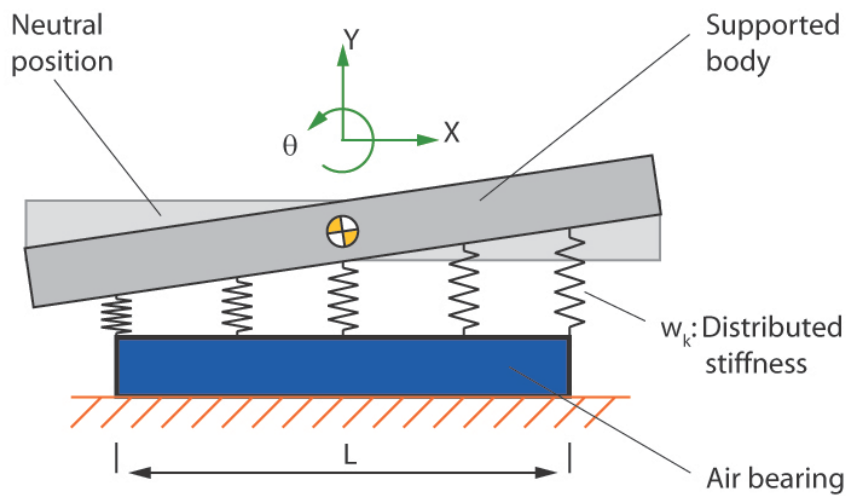


Fig. 3.12 Estimation of air bearing rotational stiffness.

Natural frequency predictions are presented in Table 3.4, assuming that the moving body is rigid and the compliances originate from the air bushings and bearing. For each motion axis, the natural frequency is found using the effective stiffness in that axis and mass or moment of inertia. In controller design, the lowest natural frequency is given the highest importance, as it is most likely to be excited by the controller. In the case of this analysis, it occurs in the roll direction as  $\omega_a = 672$  [Hz]. Whether this mode has the ability to interfere with the desired 500 [Hz] controller bandwidth needs to be tested in experiments. Experimental modal testing should also be carried out due to the following reasons:

- The simple method used to estimate the rotational stiffness of the air bearing may not be accurate, as it overlooks the distortion of the air cushion in the air bushing interface.
- The compliance of the aluminum shaft is expected to be coupled to the bearing compliances, resulting in shifts of the natural frequencies and increased complexity of the mode shapes.

Table 3.4 Calculation of the natural frequencies.

Direction	Expression	Value [Hz]
Y (Vertical)	$\omega_y = \sqrt{\frac{2k_{1yz} + k_{2y}}{m}}$	1248
Z (Horizontal)	$\omega_z = \sqrt{\frac{2k_{1yz}}{m}}$	940
A (Roll)	$\omega_a = \sqrt{\frac{2k_{2a}}{I_a}}$	672
B (Yaw)	$\omega_b = \sqrt{\frac{2k_{1bc} + 2\left(\frac{L_x}{2}\right)^2 k_{1yz}}{I_b}}$	741
C (Pitch)	$\omega_c = \sqrt{\frac{2k_{1bc} + 2\left(\frac{L_x}{2}\right)^2 k_{1yz} + k_{2c}}{I_c}}$	747

### **3.6. Conclusion**

In this chapter, the preliminary design of a low-cost desktop precision micro machine tool is presented. Performance requirements on the positioning axes constituting such a machine tool are described. Most prominent design features of the linear nano-positioner which corresponds to the X positioning axis of the machine are presented. The validity of design choices regarding the selection of sensors, configuration of the controller, components of the control system, guideways, bearings, and so on are evaluated in preliminary calculations. A positioning error budget is drawn and a positioning accuracy of  $\pm 1.8$  [ $\mu\text{m}$ ] is predicted. Vibratory dynamics of the designed stage are also estimated in preliminary calculations. The first harmonic (natural frequency) is found to be a roll mode located at 672 [Hz]. The mode is quite close to the desired 500 [Hz] bandwidth of the controller. The actual achievable control bandwidth, vibratory dynamics, and the motion accuracy of the system are experimentally verified in Chapters 5, 6, 7, respectively.

# Chapter 4

## Actuator Design and Optimization

### 4.1. Introduction

In this chapter, a voice coil actuator (VCA) is designed and built to be used in the precision translational motion stage. Instead of using a commercially available component, design is made from scratch with an involvement of several factors managed towards concrete performance goals. VCA's are highly suitable for precision motion systems due to their continuous and non-contact operation. In this thesis, attention is focused on the cylindrical VCA. In Section 4.2, a detailed description of the actuator is made in terms of the relative positions of steel and permanent magnet, design variables, and general magnetic properties. In Section 4.3, two different optimization objectives, 'acceleration per current density' and 'motor constant' are defined and maximized, for the goals of maximizing the stage acceleration capacity, and minimizing the heat dissipation from coils, respectively. Optimization is initially done for a general case, considering the force response of the VCA when the coil and steel core are fully engaged. Then, optimization criteria are modified according to the 'complementary double configuration' of dual VCA used in this thesis, and re-evaluated. As the optimization objectives are defined independent of coil wire gauge selection, coil design is carried out in a decoupled manner in Section 4.4. In Section 4.5, the VCA design is verified experimentally. Conclusions are presented in Section 4.6.

### 4.2. Description of the voice coil actuator

#### 4.2.1. Configuration options for the steel core

A cylindrical VCA comprises a steel core and an engaging coil as shown in Fig. 4.1. The equation of Lorentz force resulting from a current passing through a conductor of finite length is given as [46],

$$\vec{F} = \int_U I d\vec{u} \times \vec{B}, \quad (4.1)$$

where  $\vec{F}$  represents the Lorentz force,  $I$  represents the uniform current,  $U$  represents the conductor length,  $\vec{B}$  represents the magnetic flux density vector, and  $d\vec{u}$  is the variable of integration. For a coil, the length of the conductor is given by the total length of the wire wound to form the coil.



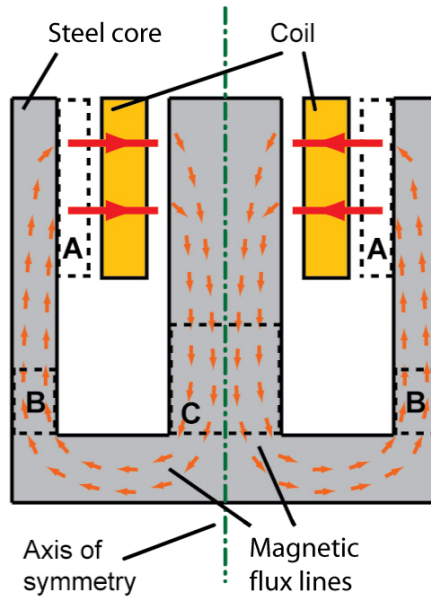


Fig. 4.1 Overview of the cylindrical VCA. A, B, C are possible locations for the permanent magnet.

In order to produce a Lorentz force in the direction of the axis of symmetry, component of the magnetic flux in the gap perpendicular to the coil axis, as indicated by the large arrows in Fig. 4.1, is needed. The overall path of the streamlines which would produce such a gap flux field is also presented. In this case, the permanent magnet can be placed in any of the locations marked as A, B or C. Each location corresponds to a different direction of magnetization and shape for the magnet. Location A requires a radially magnetized annular magnet. Such magnets are costly and difficult to procure. Approximating it with a circular array of separate magnets makes the assembly relatively more complicated. Location B requires an axially magnetized ring magnet, whereas Location C requires an axially magnetized cylindrical magnet. Being easy to obtain in both standard and custom sizes, magnets B and C have similar availability. The ring magnet of location B can be easily centered using the already available outer cover for the steel core manufactured to a tight tolerance. On the other hand, in order to align the cylindrical magnet of location C, a separate annular piece has to be produced with accurate dimensions in both inner and outer sides. For the sake of the practical assembly, location B has been chosen in this thesis.

Neodymium-iron-boron (NdFeB) magnets have higher remanence, coercivity, and energy product compared to Alnico, ceramic (ferrite), and rare earth cobalt magnets. This is the reason they are preferred in this thesis. Furthermore, as the demagnetization curve of NdFeB magnets in the second quadrant of the BH plane is mostly linear (Fig. 4.2) and their recoil permeability closely follows this as well, these magnets do not lose permanent magnetization during assembly or due to coil magnetic

fields. If an Alnico or ceramic (ferrite) magnet was used, the additional benefit of locations B and C would be to place the coil relatively distant to the magnet, thus preventing demagnetization due to coil magnetic fields [15], [87]. A shorted turn in the gap could have been considered to decrease inductance, regardless of the resulting reduction in gap length, but it would also result in additional heating. Presented possible configurations all suffer from reduction in thrust force as the coil disengages from the core, which is the reason complementary double VCA configuration is used in this thesis, as shown in Fig. 3.8.

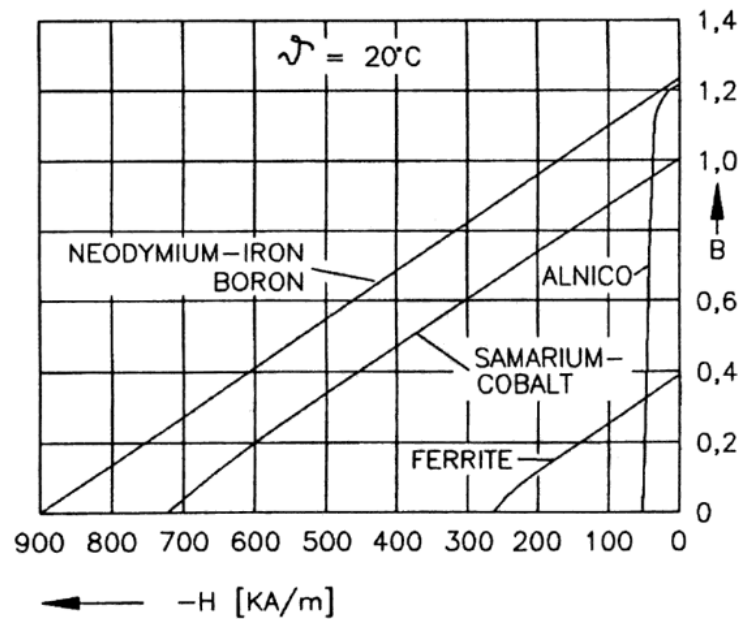


Fig. 4.2 Permanent magnet materials, BH curves [37].

#### 4.2.2. Design variables

Critical dimensions for the VCA design subject to the optimization problem are presented in Fig. 4.3. The left half of the figure shows the magnetic flux density distribution calculated in finite element analysis (FEA) for a sample design. A summary of design variables is presented in Table 4.1. Among these variables, some are preset to values arising from design limitations. Stroke length ( $h_1$ ) is determined from the desired range of motion. Scale of the VCA ( $r_3$ ) is determined with respect to the force requirements of the application. Its exact value is refined according to magnet availability. Dimensions,  $r_2$  and  $h_2$  follow from the chosen magnet. The remaining set of variables  $\{r_1, p, \delta, h_3\}$  are determined with respect to optimization objectives in Section 4.3.

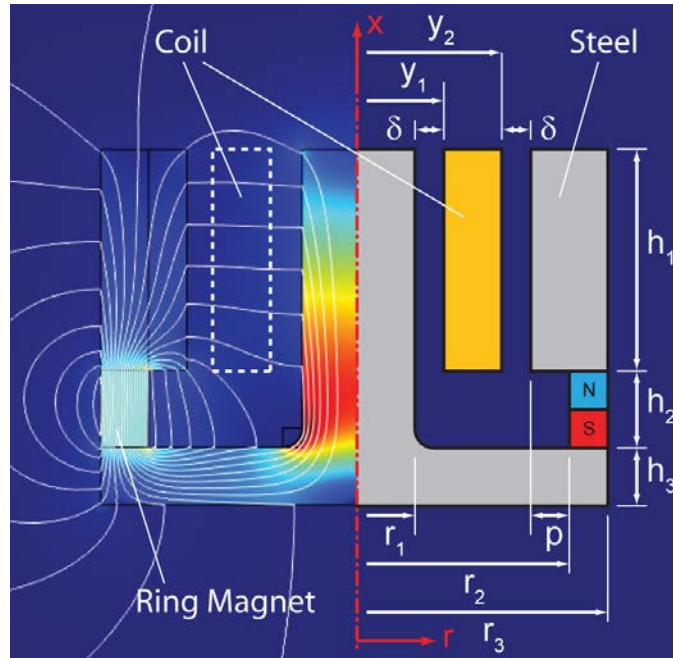


Fig. 4.3 VCA design variables and magnetic flux density distribution for a sample design.

Table 4.1. Summary of VCA design variables.

Symbol	Description	Value [mm]	Symbol	Description	Value [mm]
$h_1$	stroke length	20	$r_3$	magnet outer radius	22.5
$h_2$	magnet height	8	$p$	reduction in gap	-
$h_3$	core base height	-	$\delta$	clearance	-
$r_1$	core inner radius	-	$y_1$	coil inner radius	$r_1 + \delta$
$r_2$	magnet inner radius	17.5	$y_2$	coil outer radius	$r_2 - p - \delta$

#### 4.2.3. Magnetic properties

Magnetic equivalent circuit (MEC) is a method which allows analytical expressions for the magnetic flux densities to be derived for any point in a magnetic system, using approximations with lumped circuit elements. Where there are considerable leakage fluxes, these can be accounted for by estimating the permeance of probable flux paths using simply shaped volumes [53], [92]. With experience and by employing sufficient level of detail in approximations, satisfactory results can be obtained if the structure is not overly complicated. In this thesis, MEC analysis is carried out to demonstrate the relationship between magnetic field distributions and key design variables in the

VCA, while the main optimization results have been obtained by finite element analysis (FEA). Therefore, leakage fluxes are not considered in the MEC model, as shown in Fig. 4.4.

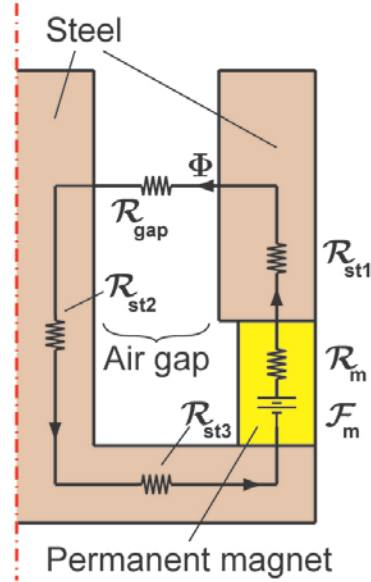


Fig. 4.4 Magnetic equivalent circuit model of the VCA.

The expressions for magnetic circuit elements on the flux path are calculated [32] and summarized in Table 4.2. Sample values for magnetic circuit elements with  $\{\delta = 0.5, h_3 = 6, r_1 = 10, p = 2\}$  are also given. The expression for the magnetic flux is given as,

$$\Phi = \frac{F_m}{R_m + R_{gap} + R_{st1} + R_{st2} + R_{st3}}, \quad (4.2)$$

where,  $F_m$  is the magnetomotive force (MMF) of the magnet,  $R_m$  is the equivalent source reluctance of the magnet,  $R_{gap}$  is the reluctance of the air gap and  $R_{st1...st3}$  are the reluctances of steel parts. Using this expression, the gap flux density at the middle of the gap is evaluated as,  $B = \Phi / A_{gap} = 0.385$  [T]. The value found from this MEC analysis should be taken only as a guideline since it does not take into account;

- i. fringing, which diverts the flux from its desired radial path,
- ii. losses from leakage fluxes.

Table 4.2. Expressions for magnetic circuit elements and sample values.

Variable	Expression	Value	Variable	Expression	Value
$B_r$	remance of permanent magnet (p.m.)	1.28 [T]	$R_m$	$\frac{h_2}{\mu_m \left[ \frac{\pi}{2} (r_3^2 - r_2^2) \right]}$	$18.42 \times 10^6$ [1/H]
$\mu_o$	permeability of air	$4\pi \times 10^{-7}$ [H/m]	$R_{gap}$	$\frac{1}{\mu_o \pi h_1} \ln \left( \frac{r_2 - p}{r_1} \right)$	$5.551 \times 10^6$ [1/H]
$\mu_m$	permeability of p.m.	$1.1 \times \mu_o$	$R_{st1}$	$\frac{h_1/2}{\mu_{st} \left[ \frac{\pi}{2} (r_3^2 - (r_2 - p)^2) \right]}$	4761 [1/H]
$\mu_{st}$	permeability of steel	$4000 \times \mu_o$	$R_{st2}$	$\frac{h_1/2 + h_2 + h_3/2}{\mu_{st} \left( \frac{\pi}{2} r_1^2 \right)}$	26597 [1/H]
$F_m$	$\frac{B_r h_2}{\mu_m}$	7408 [A.t]	$R_{st3}$	$\frac{1}{\mu_{st} \pi h_3} \ln \left( \frac{r_3}{r_1} \right)$	8559 [1/H]

It is seen in Table 4.2 that the largest reluctance originates from the air gap. The reluctance of the magnet is an imaginary one which approximates the BH-curve of NdFeB (Fig. 4.2). In order to increase the flux density in the gap, the gap length has to be minimized. However, the gap length also determines the volume of coil which can be accommodated inside the steel core, hence is directly proportional to the achievable force.

### 4.3. Optimization

The optimization problem can be stated as follows:

- i. Design variables  $\{r_1, h_3, p, \delta\}$  of the VCA have to be optimized,
- ii. such that ‘acceleration per current density’,  $\sigma_{acc}$  is maximized, and
- iii. ‘motor constant’,  $K_M$  is maximized.

The optimization objectives,  $\sigma_{acc}$  and  $K_M$  are derived and detailed in the following.

#### 4.3.1. Optimization objectives

##### 4.3.1.1. Acceleration per current density

Eq. (4.1) can be written for the volume of the conductor as follows,

$$F = \int_V \vec{J} \times \vec{B} dv, \quad (4.3)$$

where  $\vec{J}$  is the current density vector, and  $V$  is the volume of the conductor. Using the average value of the gap flux density in the radial direction ( $B_{gap}$ ) it can be rewritten as,

$$F = S V_c B_{gap} J, \quad (4.4)$$

where  $V_c$  is the bulk coil volume including non-conducting parts, and  $0 < S < 1$  is the space efficiency. If the VCA is operated in the ‘moving magnet’ mode, the mass of the iron cores add up to the moving mass as,

$$m_{tot} = m_{init} + n \times m_{core}, \quad (4.5)$$

where,  $m_{init}$  is the initial mass of the moving body,  $n$  is the number of VCA’s attached, and  $m_{tot}$  is the final mass. The equivalent mass per actuator can be calculated as,

$$\begin{aligned} m_{eq} &= m_{tot} / n, \\ &= m_{init} / n + m_{core}. \end{aligned} \quad (4.6)$$

As a sample case,  $m_{init} = 0.725$  [kg] and  $n = 2$  can be selected. Different values can be used for different applications. Using Eq. (4.4) and (4.6), acceleration per current density can be expressed as,

$$\sigma_{acc} = \frac{S V_c B_{gap}}{m_{eq}}. \quad (4.7)$$

Maximum current density for continuous operation can be set using the 700 [circ. mils/A] rule [41], which is equivalent to  $J_{max} = 2.819$  [A/mm<sup>2</sup>]. Hence, maximizing  $\sigma_{acc}$  maximizes the acceleration for all selections of coil wire gauge, as  $\max(F / m_{eq}) = \max(\sigma_{acc}) \times J_{max}$ . Thus, the optimized VCA design problem turns into two decoupled problems, consisting of magnetic circuit optimization and coil winding optimization.

#### 4.3.1.2. Motor constant

Heat dissipation of the coil is given as,

$$Q = I^2 R. \quad (4.8)$$

Total resistance of the wire can be expressed as,

$$R = \frac{\rho N l_t}{A}, \quad (4.9)$$

where,  $\rho$  is the resistivity,  $N$  is the number of coil turns,  $l_t$  is the average loop length, and  $A$  is the cross-sectional area of the conductor in the wire. The average loop length ( $l_t$ ) can also be expressed as,

$$l_t = \frac{S V_c}{N A}. \quad (4.10)$$

Using Eq. (4.10) in (4.9), the expression for wire resistance can be rewritten as,

$$R = \frac{\rho S V_c}{A^2}. \quad (4.11)$$

The standard definition of motor constant for rotary electric servomotors [102], can be reformulated to relate instantaneous force produced to the instantaneous heat generation as,

$$K_M = \frac{F}{\sqrt{Q}}. \quad (4.12)$$

Motor constant in  $(N/\sqrt{W})$  allows for current terms to be cancelled out, and gives an indication of how much force is produced per unit square root of heat dissipation rate. For the optimal case, it has to be maximized. Substituting Eq. (4.11) and the relationship,  $I = J \cdot A$ , in Eq. (4.8), and using the result in Eq. (4.12) together with Eq. (4.4), motor constant can be expressed as,

$$K_M = \sqrt{\frac{SV_c B_{gap}^2}{\rho}}. \quad (4.13)$$

### 4.3.2. Determination of $\delta$ and $h_3$

Large  $\delta$  reduces the available volume for the coil. It also increases the gap length, thereby reducing  $B_{gap}$ . Combined effect of these is the reduction of both optimization objectives. Thus,  $\delta$  should be set to a minimum.  $\delta = 0.5[\text{mm}]$  is set in this thesis. As  $\delta$  is related to thermal expansion of components, as much as the manufacturing/assembly errors, it has to be made proportionally bigger for designs with higher  $r_3$ .

The lumped reluctance term  $R_{st3}$  used in the MEC analysis, suggests that  $h_3$  should be increased in order to reduce reluctance and also to increase the magnetic flux in the circuit. However, it has been determined from FEA that increasing  $h_3$  reduces  $B_{gap}$  by diverting flux to the leakage paths. Increasing  $h_3$  also increases the mass of the iron core. However, if  $h_3$  is too small, saturation of the steel components occurs in the flux path. When the magnetic fields are as high as to cause saturation, the linear material magnetic models used in the FEA simulations become invalid. Hence, in the optimization process followed for this particular stage design, it has been set to  $h_3 = 6 [\text{mm}]$  with a margin for saturation through trial-and-error.

### 4.3.3. Performance topologies with $r_1$ and $p$

After the variables  $\delta$  and  $h_3$  are determined, the optimization procedure reduces to the search for an optimal pair  $\{r_1, p\}$  such that the linear combination of parameters  $\sigma_{acc}$  and  $K_M$ , as given in Eq.'s (4.7) and (4.13) respectively, are maximized. Instead of simply combining the two objectives with a weighting factor, the designer's engineering judgment also needs to be incorporated into the process. Therefore, a performance topology based approach has been followed, as detailed henceforth. The optimization objectives have to be evaluated for each candidate set of optimization variables.

The parameters which show up in the optimization objectives are set as follows:  $\rho$  is set to the resistivity of copper,  $V_c$  can be calculated from the varying coil dimensions, while  $m_{eq}$  can be calculated from steel core dimensions and material densities. The cross-section of the coil wire with layers of insulation and bonding material is shown in Fig. 4.5. Fig. 4.5 represents the most



conservative estimation, as the layers could be slightly shifted with respect to each other to improve packing.

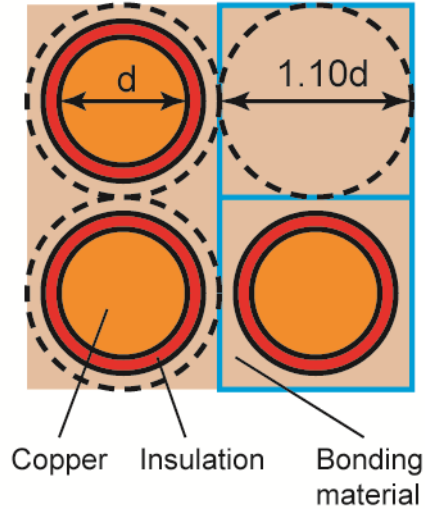


Fig. 4.5 Coil diagram related to space efficiency.

The average of standard minimum and maximum increase in the diameter of bare copper wire, due to single (type 1) and heavy (type 2) bonding, for wires AWG#18 to AWG#30 is found to be 10.8% (rounded to 10% in Fig. 4.5) [77]. The space efficiency corresponding to the 10% average increase in bare wire diameter can be calculated as,

$$S = \frac{N A l_t}{N [d(1+0.10)]^2 l_t} = \frac{\pi d^2 / 4}{[d(1+0.10)]^2} \approx 0.65. \quad (4.14)$$

Above,  $d$  is the diameter of the conducting wire. To obtain the value of  $B_{gap}$ , COMSOL® FE model is updated for each variable set and the magnetic flux densities are simulated. A screenshot from the FE analysis of the VCA for  $\{r_1 = 7 \text{ [mm]}, p = 1 \text{ [mm]}\}$  is shown in Fig. 4.6. Simulating the gap flux density and obtaining the resulting force response from analytical expressions is more preferable to simulating the force directly, as simulating the force requires modeling of the coil and the coil current. In this latter case, force values obtained for positive and negative current directions have to be averaged to cancel out coil demagnetization/magnetization effects, resulting in a two-step process.

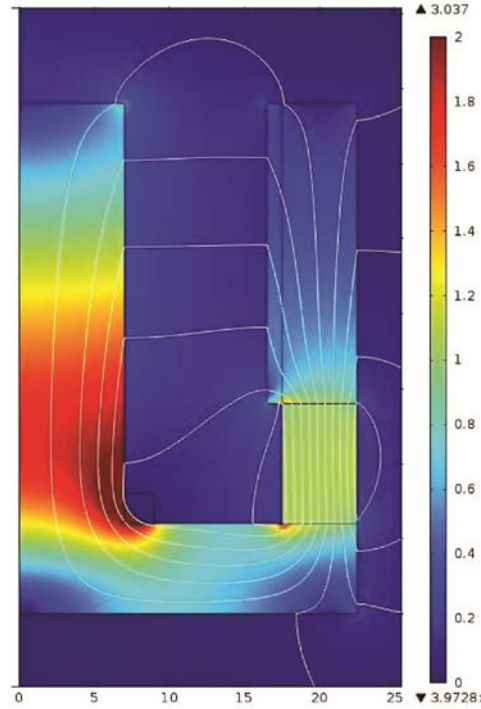


Fig. 4.6 COMSOL® FE analysis for the variable pair  $\{ r_1 = 7 \text{ [mm]}, p = 1 \text{ [mm]} \}$ .

Around 100 simulations have been conducted to map performance parameters to discrete values of  $r_1$  and  $p$ . The resulting performance topologies are charted in terms of the optimization objective functions as shown in Fig. 4.7. From the examination of the topology, the chosen design point is  $\{ r_1 = 7.5 \text{ [mm]}, p = 0.2 \text{ [mm]} \}$ .  $r_1 = 7.5 \text{ [mm]}$  is chosen, as it corresponds to a point with desirable balance between highest  $\sigma_{acc}$  and  $K_M$  points, horizontally. Performance topologies suggest the feature given by  $p$  to be eliminated altogether, but the small  $p = 0.2 \text{ [mm]}$  is chosen to keep that feature in case its effect on the reduction of leakage flux is underestimated in FEA.

In practice, the tolerance on  $p$  can be expected as  $\pm 0.050 \text{ [mm]}$  for all  $p$ , as it assumes the tolerance of the turning operation that produces the pole piece with  $r_2 - p$  inner radius. The design point  $\{ r_1 = 7.5 \text{ [mm]}, p = 0.2 \text{ [mm]} \}$  produces the values of  $\sigma_{acc} = 2.27 \text{ [N/kg.A/mm}^2\text{]}$  and  $K_M = 3.55 \text{ [N/\sqrt{W}]}$ . The slight advantage given to  $\sigma_{acc}$  is favorable, because motion bandwidth is generally more critical than heat dissipation. In the FEA results of the VCA with the final parameters, regions with  $B > 2.0 \text{ [T]}$  were observed to be minimal. If these regions were bigger, as might be observed for smaller  $r_1$ , FEA would have to be repeated using the full profile of the B–H curve,

which takes non-linearity and saturation into account that is present in steel after  $B \approx 2$  [T]. If this is not taken into account, the actual VCA magnetic fields would be realized lower than the FEA predictions.

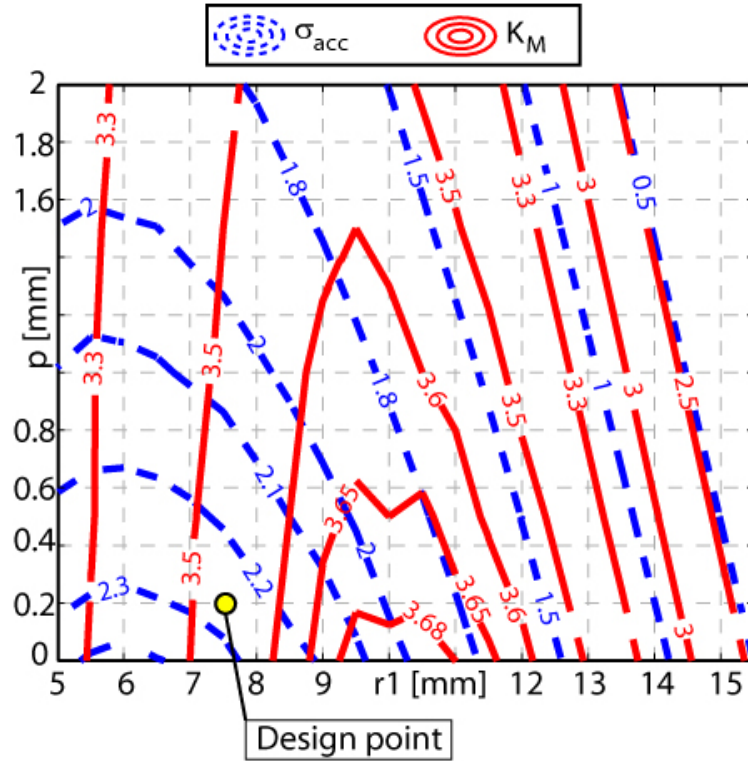


Fig. 4.7 Performance topologies.

#### 4.3.4. Re-evaluation of the optimization objectives

The approximation in Eq.(4.4) is valid only for the fully-engaged case where the coil current interacts with the orderly flux lines inside the gap and leakage flux has no effect. For the complementary double VCA case, the force response at partially engaged conditions, where leakage flux has significant contributions, also needs to be considered. Hence, the accuracy of the predictions can be further refined by fully simulating the actual force response in FEA instead of only the flux density. The optimization criteria can be re-derived in terms of the force response as,

$$\sigma_{acc} = \frac{F_0}{m_{eq} J}, \tag{4.15}$$

$$K_M = \frac{F_0}{\sqrt{Q}},$$

where  $F_0$  is the force response at  $x = 0$  [mm] corresponding to the fully-engaged VCA. For the dual VCA case, at each position forces from the two VCA's add up. Therefore, at  $x = 0$  [mm], force response is  $F_0 + F_{20}$ , where  $F_{20}$  corresponds to the force response of the fully-disengaged VCA at the opposite end. For the dual VCA case, a mean force response can be calculated from the aggregate responses at  $x = 0, 5, 10, 15, 20$  [mm] as,

$$F_m = \frac{(F_0 + F_{20}) + (F_5 + F_{15}) + (2F_{10})}{3}. \quad (4.16)$$

Then, optimization criteria for the complementary double VCA case can be re-derived as,

$$\sigma'_{acc} = \frac{F_m}{m_{tot} J}, \quad (4.17)$$

$$K'_M = \frac{F_m}{\sqrt{2Q}}.$$

Performance topologies with respect to the new criteria and the design point are presented in Fig. 4.8. The topology is computed using the average of response from positive and negative directions of the sample current. This way, demagnetization effect of coil electromagnetic fields on the permanent magnet is cancelled. Performance objectives are re-evaluated at the design point  $\{r_1 = 7.5$  [mm],  $p = 0.2$  [mm] $\}$  for the double VCA case as,  $\sigma'_{acc} = 1.48$  [N/kg.A/mm<sup>2</sup>], and  $K'_M = 3.27$  [N/ $\sqrt{W}$ ]. Contours are shaped by 3 main effects:

- i. Changes in the available volume of coil ( $V_c$ ),
- ii. Changes in the gap flux density ( $B_{gap}$ ) due to the changes in the gap length,
- iii. Variations in the leakage flux affecting the disengaged portions of the coil.

Effect (iii) is unique to the complementary double VCA analysis, as the engagement level is varying for both voice coils while the stage travels through its motion stroke.

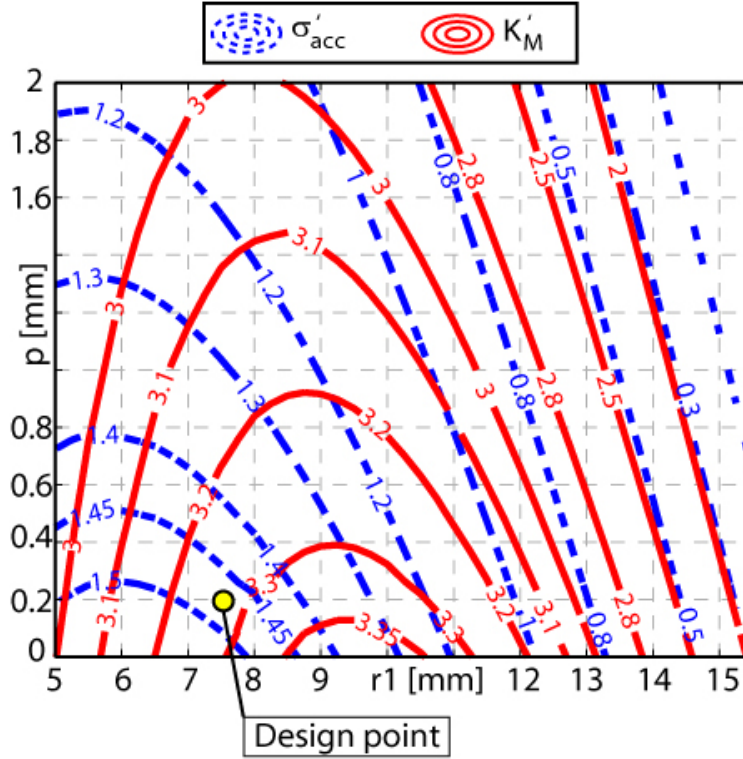


Fig. 4.8 Performance topologies with re-evaluated optimization objectives.

Comparing Fig. 4.7 and Fig. 4.8, the design point is observed to still remain as a good trade-off between the two optimal points for maximum  $\sigma_{acc}$  and maximum  $K_M$ . The slightly lower values obtained for the complementary double VCA case can be explained by the fact that the response from the two coils are averaged, which can never be as good as a single VCA at the fully engaged position. The topology curves of Fig. 4.8 are smoother than Fig. 4.7, due to the averaging operation.

#### 4.4. Coil design and electrical characteristics

##### 4.4.1. Number of coil wire turns

The number of coil wire turns can be expressed as,

$$N = \frac{4S(y_2 - y_1)h_1}{\pi d^2}, \quad (4.18)$$

where,  $d$  is the diameter of the conductor in the wire and  $S$  is the space efficiency.  $S$  is calculated from Eq. (4.14) as 61-69% for single (type 1) and 56-64% for heavy (type 2) bonding wires in the range AWG#18 - #30 [77]. In manufacturing, values can turn out to be slightly lower or higher,

depending on the quality of packing. The number of coil turns ( $N$ ) calculated for different wire gauges with  $S = 0.65$  are presented in Table 4.3. In the table,  $L_{50\%}$  refers to the inductance of the coil at the half-engaged position,  $R$  refers to the coil resistance,  $1/\tau$  is the first-order pole frequency,  $I_{max}$  is the maximum current,  $e_{DC}$  is the voltage supply required for generating the maximum constant force,  $P_{DC}$  is the power consumption corresponding to  $e_{DC}$ ,  $e_{250}$  is the voltage supply required for generating a sinusoidal force with maximum possible amplitude at 250 [Hz] frequency,  $P_{250}$  is the power consumption corresponding to  $e_{250}$ ,  $|K_v|$  is the back electromotive force (EMF) constant,  $e_v$  is the voltage supply required at maximum speed due to back EMF, and  $P_v$  is the power consumption corresponding to  $e_v$ . Calculation of these quantities is further elaborated in the proceeding subsections.

Table 4.3. Electrical parameters for different wire gauges.

AWG# (d) [mm]	N [turns]	$L_{50\%}$ [mH]	R [ $\Omega$ ]	$1/\tau$ [Hz]	$I_{max}$ [A]	$e_{DC}$ [V]	$P_{DC}$ [W]	$e_{250}$ [V]	$P_{250}$ [W]	$ K_v $ [V/(m/s)]	$e_v$ [V]	$P_v$ [W]
18 (1.024)	139	0.7	0.22	51	2.32	0.5	1.19	2.6	2.96	0.07	0.06	0.127
20 (0.813)	220	1.7	0.56		1.46	0.8		4.1		0.16	0.09	
22 (0.643)	353	4.4	1.42		0.91	1.3		6.5		0.42	0.14	
24 (0.511)	559	11.1	3.57		0.58	2.1		10.3		1.06	0.22	
27 (0.361)	1120	44.5	14.3		0.29	4.1		20.6		4.25	0.44	
30 (0.254)	2258	181	58.3		0.14	8.3		41.5		17.29	0.89	

#### 4.4.2. Coil inductance, resistance and time constant

The coil inductance is given as [15],

$$L = N^2 P, \quad (4.19)$$

where  $P$  is the overall permeance of the magnetic circuit around the coil. The magnetic energy stored in the inductor is given as [15],

$$W = \frac{1}{2}LI^2. \quad (4.20)$$

Using (4.19) in (4.20), the permeance of the magnetic circuit,  $P$ , can be found from magnetic energy as,

$$P = \frac{2W}{N^2I^2}. \quad (4.21)$$

The magnetic energy is simulated using FE software using an example coil with  $N = 100$  turns, considered to be running 1 [A] current. This is just a test case for the identification of the overall permeance of the magnetic circuit, which is independent of coil and current selection. Simulated magnetic energy and corresponding overall permeance values for varying levels of coil engagement to the core are given in Fig. 4.9.

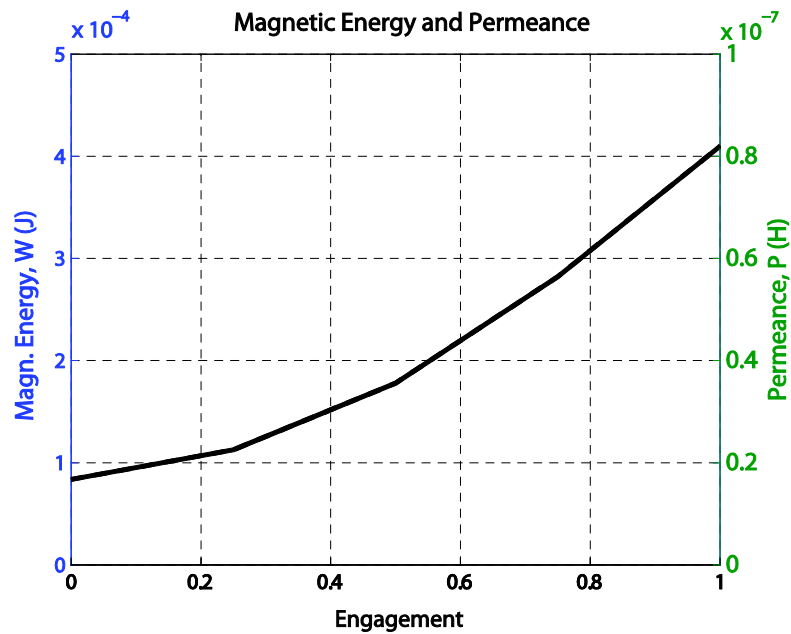


Fig. 4.9 Magnetic energy and permeance vs. coil engagement.  $N = 100$  turns.

Inductance values calculated using the overall permeance  $P$  at a nominal engagement of 50% are presented in Table 4.3. Resistance values calculated according to Eq. (4.9) are also presented in Table 4.3. Thus, the expected electrical time constant  $\tau$  can be expressed as,

$$\tau = \frac{L}{R} = \frac{SV_c P}{\rho I_t^2}. \quad (4.22)$$

Eq. (4.22) shows that the time constant is independent of the wire gauge. The value  $1/\tau$  corresponds to the pole of the first-order transfer function between the coil voltage input and the coil current. It varies according to the permeance of the equivalent magnetic circuit ( $P$ ) shown in Fig. 4.9. For the 50% engagement case, it is found as  $1/\tau = 51$  [Hz], as presented in Table 4.3. The parameter  $S = 0.65$  is the average space efficiency of wires in the wire gauge range of interest (AWG#18 - #30), as mentioned before.

#### 4.4.3. Power supply

The equation for the instantaneous voltage supply required for actuation is given as,

$$e = IR + \frac{dI}{dt}L + I \frac{dL}{dx} \frac{dx}{dt}. \quad (4.23)$$

The maximum current values, as presented in Table 4.3, are found by,

$$I_{max} = AJ_{max}. \quad (4.24)$$

##### 4.4.3.1. The DC case

For the DC case, the maximum voltage requirement and power consumption can be written as,

$$e_{DC} = I_{max} R = \frac{J_{max} \rho SV_c}{A}, \quad (4.25)$$

$$P_{DC} = I_{max}^2 R = J_{max}^2 \rho SV_c. \quad (4.26)$$

The corresponding values of  $e_{DC}$  for different wire gauges are presented in Table 3.  $P_{DC}$  is found to be 1.19 [W] for all wire gauges, as presented in Table 4.3.

##### 4.4.3.2. The AC case

When driving the VCA with a sinusoidal current,  $I(\omega) = I_{max} \cos(\omega t)$ , the amplitude of the voltage supply required is,



$$e_{AC}(\omega) = I_{max} \sqrt{R^2 + L^2 \omega^2}. \quad (4.27)$$

Above, value of the inductance at the 50% engagement level ( $L_{50\%}$ ) is used as  $L$ .  $e_{AC}$  at 250 [Hz] is presented in Table 3 as  $e_{250}$ . The 250 [Hz] sinusoidal current with maximum possible amplitude and the resulting actuation force correspond to a high force generation demand for an assumed positioning application with 500 [Hz] bandwidth. The complex power during AC operation can be expressed as [40],

$$P_{AC} = \frac{1}{2} I_{max}^2 R + j \omega \frac{1}{2} I_{max}^2 L = \frac{1}{2} J_{max}^2 \rho S V_c + j \frac{1}{2} \omega J_{max}^2 \frac{S^2 V_c^2}{l_t^2} P. \quad (4.28)$$

It can be observed from Eq. (4.28) that both real and reactive power components are independent of the wire gauge. Power components are plotted in Fig. 4.10 against  $\omega$ . The apparent power at 250 [Hz] is shown in Table 4.3 as  $P_{250} = 2.96$  [W]. Using the formula for complex internal impedance including the skin effect for solid round conductors [26], with a relative permeability of  $\mu_r = 1.0$  for copper, internal inductance at 1 [kHz] is observed to be less than 0.01 [mH] for the wire gauges in Table 4.3, along with less than 0.01% increase in resistance. Hence, the skin effect is neglected in calculations.

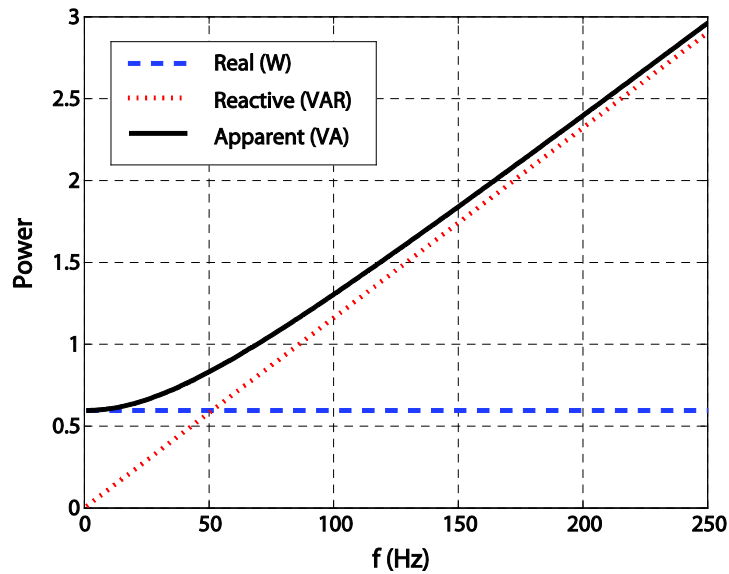


Fig. 4.10 Power components in the AC case as a function of current frequency.

#### 4.4.3.3. Effect of back - electromotive force

The voltage constant can be approximately defined as,  $K_v = \frac{dL}{dx}$ , by approximating the change in  $L$  using the two points of coil engagement, 25% and 75%, according to Eq. (4.19) as,

$$K_v = -N^2 \frac{P_{0.75} - P_{0.25}}{h_1 / 2}. \quad (4.29)$$

The actual  $K_v$  experienced during the operation of the VCA depends on the instantaneous  $\frac{dL}{dx}$  which depends on the position. The approximation in Eq. (4.29) is used as an average value to allow for the comparison of different coil wire gauges.  $K_v$  values calculated for the sample set of wires are given in Table 4.3.

The maximum acceleration achievable is given as,

$$a_{max} = \sigma_{acc} J_{max}. \quad (4.30)$$

The velocity limit (assuming a triangular velocity profile) follows as,

$$v_{max} = \sqrt{h_1 a_{max}} = 0.36 \text{ [m/s]}. \quad (4.31)$$

Additional voltage requirements ( $I_{max} |K_v| v_{max}$ ) for different wires are presented in Table 4.3. The maximum power demand due to back-EMF is given by,

$$P_v = I_{max}^2 |K_v| v_{max} = J_{max}^2 v_{max} \frac{S^2 V_c^2}{l_r^2} \left( \frac{P_{0.75} - P_{0.25}}{h_1 / 2} \right). \quad (4.32)$$

$P_v$  is found to be 0.127 [W] for all wire gauges, as shown in Table 4.3.

#### 4.4.3.4. Final design of the coil

From Table 4.3, the dominant voltage term is observed to be  $e_{250}$ . All voltage terms ( $e_{250}, e_{DC}, e_v$ ) can be reduced by selecting thicker wire gauge. However,  $I_{max}$  also increases with thicker wire and

can exceed the current available through the amplifier. For the experimental VCA, the power op-amp Texas Instruments® OPA549T used has enough voltage/current available to actuate all wire gauges considered in the sample set. The AWG #24 wire is chosen due to the availability of PB#1 (Polyvinyl Butyral) bondable wire by the supplier.

#### 4.5. Experimental study of the voice coil actuator design

The finalized VCA design was built in-house. The permanent magnet and steel parts were gradually brought to contact by removing a set of thin wooden plates one-by-one from the interface. The permanent magnet and the steel core were aligned using a nylon sleeve manufactured to a snug fit.

##### 4.5.1. Verification of the magnetic analysis method

Using a Lake Shore® 410 hand-held Gaussmeter, the gap flux density of the iron core was measured as shown in Fig. 4.11.

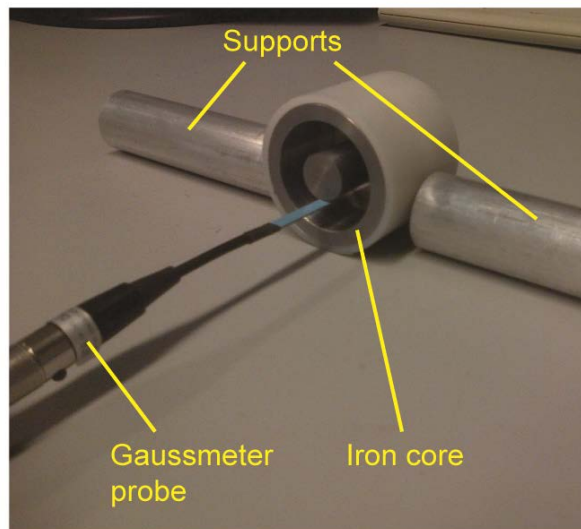


Fig. 4.11 Experimental measurement of flux densities.

COMSOL® FE prediction and measured values for different points along the radius of the iron core are compared in Table 4.4. While evaluating predictions of the FEA, half of the probe thickness,  $t/2 = 0.75$  [mm], is offset from the evaluation points on the inner and outer walls.

Table 4.4. Comparison of FE and experimental flux densities.

Loc.	FEA [T]	VCA 1		VCA 2	
		Exp. [T]	FEA Err. (%)	Exp. [T]	FEA Err. (%)
Inner wall	0.230	0.212	+8.5	0.213	+8.0
Outer wall	0.120	0.107	+12.1	0.107	+12.1
Middle	0.156	0.140	+11.4	0.142	+9.9

During FE simulation, the magnetic property of the core material (AISI 1018 steel) was approximated by the constant relative permeability,  $\mu_r = 4000$ . The NdFeB magnet with Grade 42 was modeled by a linear BH-curve of slope,  $\mu_r = 1.1$ , and remanent magnetic flux density of  $B_r = 1.28$  [T]. Deviations of the measurements from FEA results are an average 10%, which might have originated from the nonlinear magnetic properties of iron, mismatch of magnet properties, miscalculation of leakage fluxes, as well as manufacturing or measurement errors. For the practical application of the VCA, this discrepancy is acceptable.

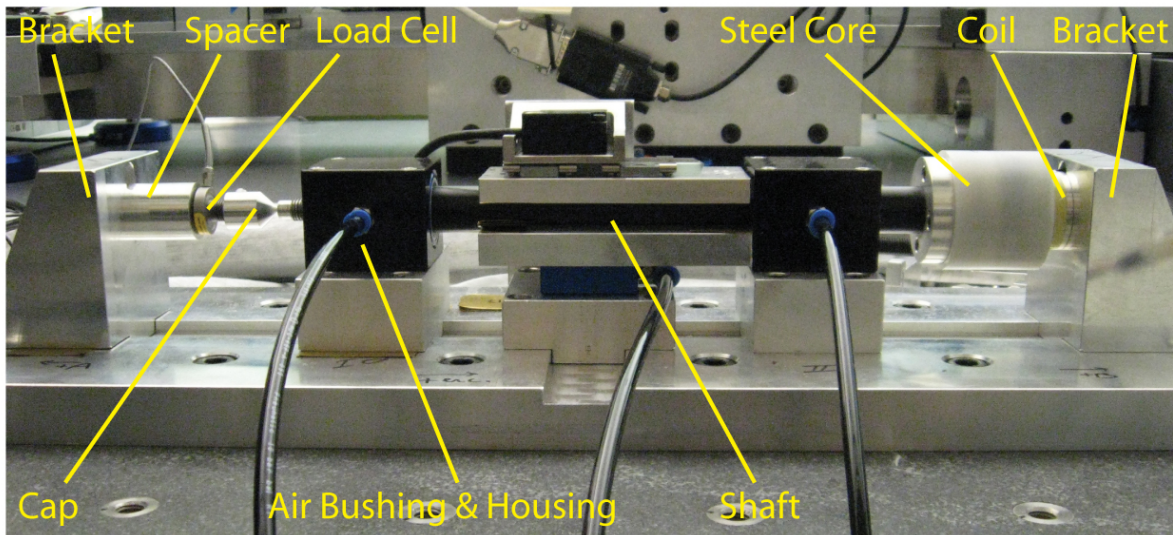


Fig. 4.12 Experimental setup for force measurement.

#### 4.5.2. Verification of force and performance formulations

The coils were built using AWG#24 ( $d = 0.511$  [mm]) NEMA standard MW-29C magnet wire with PB#1 (Polyvinyl Butyral) bond coat activated by alcohol (solvent bonding). A 0.5 [mm] aluminum

layer was used in the coil inner diameter to improve strength. Hence, the effective coil inner and outer radii became  $y_1 = 8.5$  [mm] and  $y_2 = 16.8$  [mm], respectively.

The VCA design was tested for the generated forces using the nano-positioner, as shown in Fig. 4.12. At one end of the shaft, the steel core is mounted. The coil is fixed on the mounting bracket and is fully engaged into the core. The other end of the shaft contacts a conical cap which is screwed onto the FUTEK® LCM200 load cell. When the coil is powered, the flat end of the shaft presses the load cell against the spacer, which is supported by the bracket. For force measurements, the coil is supplied a steady current via the Texas Instruments® OPA549T power amplifier and the response of the load cell is recorded. The measurement results are given in Fig. 4.13.

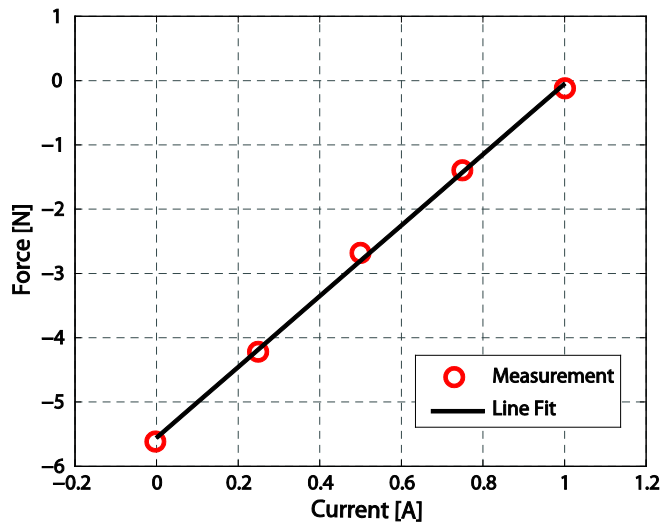


Fig. 4.13 Force response of the VCA.

The least-squares line fit in Fig. 4.13 indicates a measured force factor of  $K_f = 5.508$  [N/A]. Using the definition of current density in the force expression of Eq. (4.4), the analytical expression for force factor can be obtained as,

$$K_f = \frac{SV_c B_{gap}}{\pi d^2 / 4}. \quad (4.33)$$

Using the average of experimentally obtained gap flux densities at the middle of the gap from Table 5, as  $B_{gap} = 0.141$  [T], the corresponding expected force factor is found to be  $K_f = 5.907$  [N/A],

which is 7.2% greater than the measured one. This may have resulted from the actual space efficiency ( $S$ ) being lower than the predicted one, and possible measurement errors in registering the gap flux density. Nevertheless, there is good agreement between the predicted and actual force factors.

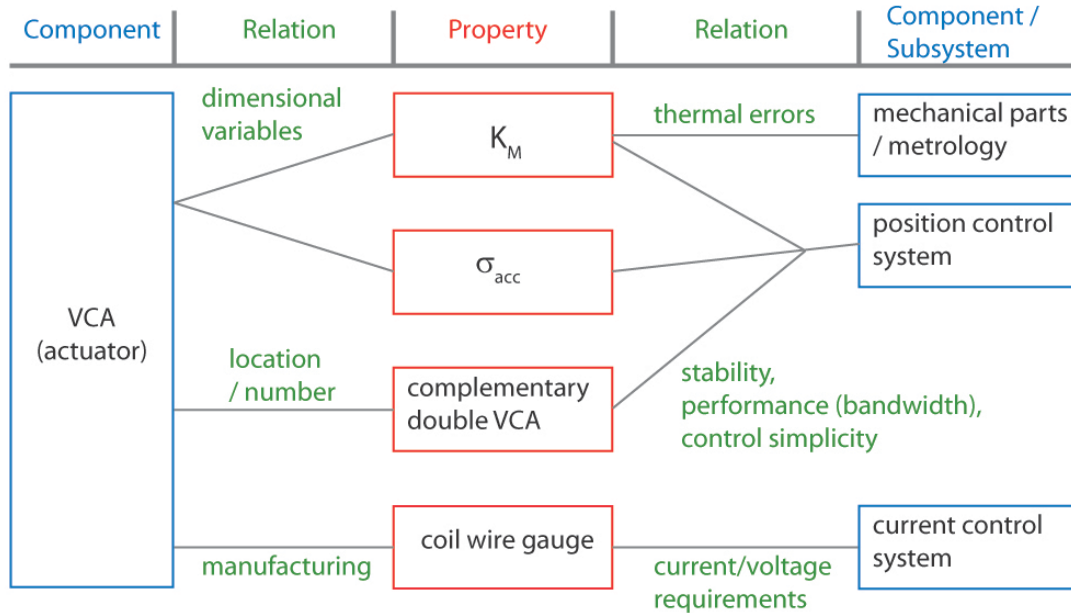


Fig. 4.14 Interactions of VCA properties with actuator design and other mechatronic components.

#### 4.6. Conclusion

In this chapter, a VCA has been designed, optimized, built, and tested for the translational nano-positioning stage. A detailed and systematic approach has been taken to relate the VCA specifications to the overall mechatronic design. A summary of these interactions mentioned at various preceding sections is presented in Fig. 4.14. Considering Fig. 4.14, the optimization objectives  $\sigma_{acc}$  and  $K_M$  are determined from the choice of VCA dimensional variables, and affect stability, performance and control simplicity.  $K_M$  is also related to the geometric accuracy (metrology) though thermal errors induced by heating. The chosen coil wire gauge affects the VCA manufacturing process in terms of winding and adhesive material, while also determining peak current and voltage demands on the current control system. The specific arrangement of VCA's in a complementary double VCA configuration improves the linearity of the force response, hence the position control stability, performance, and simplicity. It also affects the value of optimization objectives; however, such 'cross' interactions are not denoted in the figure. The diagram summarizes the multi-disciplinary approach taken in the optimal design of VCA's.

# Chapter 5

## Control System

### 5.1. Introduction

A stable control scheme with high positioning bandwidth is essential for the trajectory following and positioning accuracy of the nano-positioning stage. Controller design has to be based on as much information collected on the system as possible to avoid excessive corrections in the feedback, which would lower the overall accuracy. Also, the servo bandwidth has to be as high as possible to obtain the best tracking results. The goal of the design is to bring accuracy up as close as possible to the hardware limits, limiting servo errors to a few nanometers. In this chapter, details of the controller design, implementation, and experimental verification are presented. Two separate controllers are designed for current control and position control systems, based on observed and modeled system characteristics. The achieved control performance has been experimentally verified for both cases.

### 5.2. Overview of the control system

An overview of the position control loop is presented in simplified form in Fig. 5.1. The overall plant ( $G_p(s)$ ) is composed of the current controller ( $K_a$ ), voice coil actuator force response ( $K_f$ ), and the positioning stage. Positioning stage dynamics has a double integrator component, corresponding to a pure mass without friction. Additional dynamics ( $G^*(s)$ ) are also expected due to vibratory modes, and parasitic forces. A more detailed block diagram is presented in Fig. 5.2, showing the actual current control dynamics. Accordingly, the design of the current and position control loops are detailed in the proceeding Sections 5.3 and 5.4.

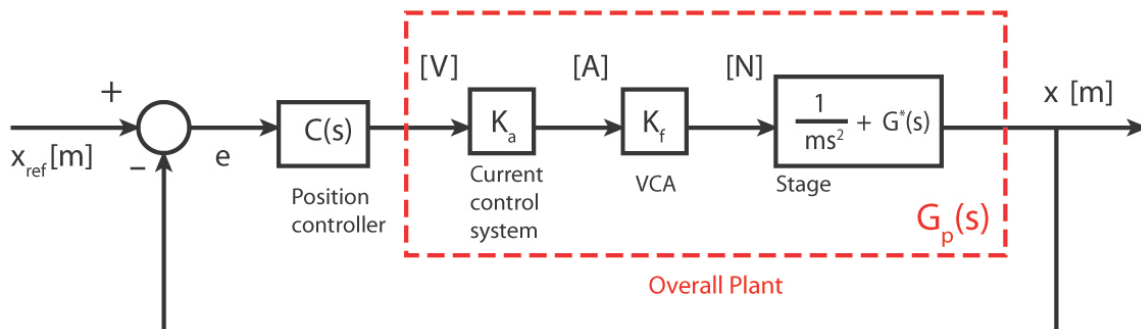


Fig. 5.1 Overview of the position control loop.

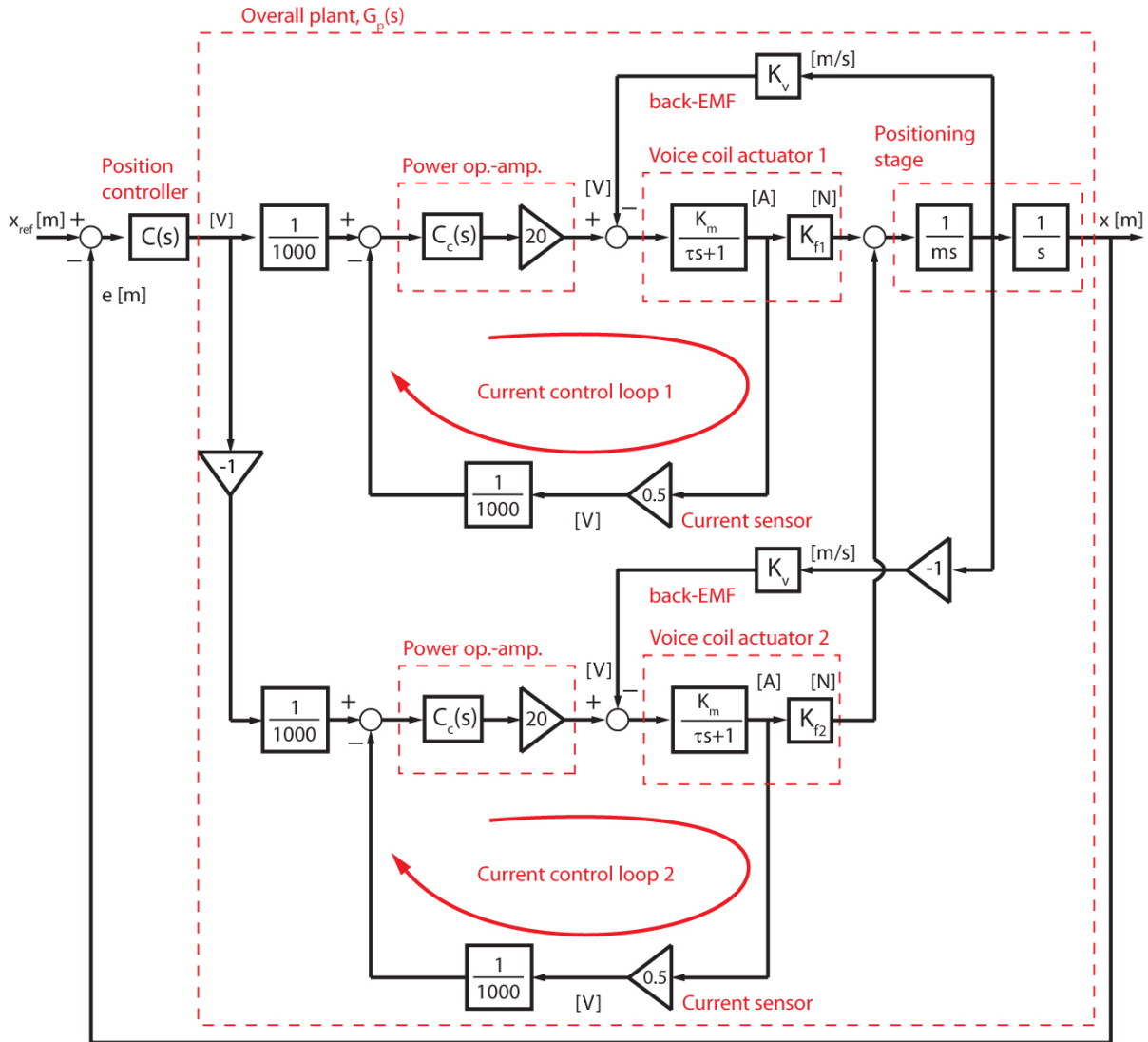


Fig. 5.2 Detailed control block diagram.

### 5.3. Design of the current controller

The current control loop is presented in detail alongside the position controller in Fig. 5.2. Two independent current control loops are implemented for actuators 1 and 2. For actuator 2, the current command is multiplied by -1 to accommodate the reversal of force direction with respect to the current. Similarly, the effect of back-EMF in terms of the sign of the generated voltage with respect to the motion direction is reversed. Individual force factors of the two actuators are expressed by  $K_{f1}$  and  $K_{f2}$ , which are dependent on the stroke position as was shown in Fig. 3.8. On the other hand, the combined force factor ( $K_f = K_{f1} + K_{f2}$ ) is almost uniform throughout the stroke length. As the position control loop is closed using the overall plant ( $G_p$ ) with  $K_f$ , benefits of this uniformity in



terms of simplicity of control in guaranteeing stability could be reaped, as presented in the next section. An alternative approach would be to use separate current commands for the two voice coils. In that case the force capacity would not change, as the present design can already provide the maximum force available at any stroke position by commanding the maximum current. On the other hand, this idea can be used in improving the energy efficiency during sub-maximum force generation. However, this option is discarded in favor of control simplicity. The simplified circuit diagram of the current control boards is presented in Appendix A. The current controller comprises an integrator and a lead filter, given by,

$$C_c(s) = K_c \frac{1}{s} \frac{T_c s + 1}{\alpha_c T_c s + 1}, \quad 0 < \alpha_c < 1, \quad (5.1)$$

The same controller design has been implemented for both actuators, using separate boards. The integrator enables high low-frequency gain, thus reducing the control error significantly within the bandwidth (BW) of the feedback system. The lead filter provides phase advance around the target cross-over frequency, in order to enable an acceptable stability margin. A current control bandwidth of 1000 [Hz] is targeted, in order to enable a positioning bandwidth of around 500 [Hz]. Also, phase lag of the current response has to be minimized to enable satisfactory positioning control performance. VCA electrical dynamics is indicated in the figure by the first-order transfer function,

$$G_m(s) = \frac{K_m}{\tau s + 1}, \quad (5.2)$$

where  $K_m = 1/R$  is the DC gain, and  $\tau = L/R$  is the time constant. The resistance of the coil is reported in Table 4.3 as  $R = 3.57$  [ $\Omega$ ]. The inductance at 100% and 0% engagement levels can be calculated from the simulated permeance values reported in Fig. 4.9 as,  $L_{100} = 25.6$  [mH] and  $L_0 = 5.2$  [mH], respectively. While this inductance ( $L$ ) + resistance ( $R$ ) model is widely accepted for coils, the system identification experiments consisting of frequency response measurements have revealed certain deviations from it. The identified  $G_m(s)$  for 100% and 0% coil-core engagement, corresponding to  $x = 0$  [mm] and  $x = 20$  [mm] positions, are shown in Fig. 5.3. Simulated frequency response functions (FRF) evaluated using COMSOL® finite element analysis (FEA), and the FRF corresponding to the  $L + R$  theoretical prediction are also plotted. The deviation from the ideal first

order plant (Eq.(5.2)) is due to eddy currents occurring in the aluminum components, such as the mandrel and the coil bracket, as can be observed from the screenshot from the finite element program (Fig. 5.4). The simulated FRF's have been fitted to a transfer function (TF) of the form,

$$G_m(s) = \frac{K(s + z_1)(s + z_2)}{(s + p_1)(s + p_2)(s + p_3)}, \quad (5.3)$$

Above,  $z_{1,2}$  are zeros,  $p_{1,2,3}$  are poles, and  $K$  is the gain. The identified pole/zero/gain for FE simulated FRF at 100% and 0% engagements are presented in Table 5.1. The TF fitting was achieved using Matlab® function 'lsqnonlin' in the Optimization Toolbox, which uses the 'trust-region-reflective' algorithm for nonlinear least-squares data-fitting [108]. It is observed that the fitted first pole's frequency is almost the same as the theoretical first-order pole ( $1/\tau$ ). This shows that the eddy current dynamics superpose on the existing coil dynamics and alter the high-frequency region.

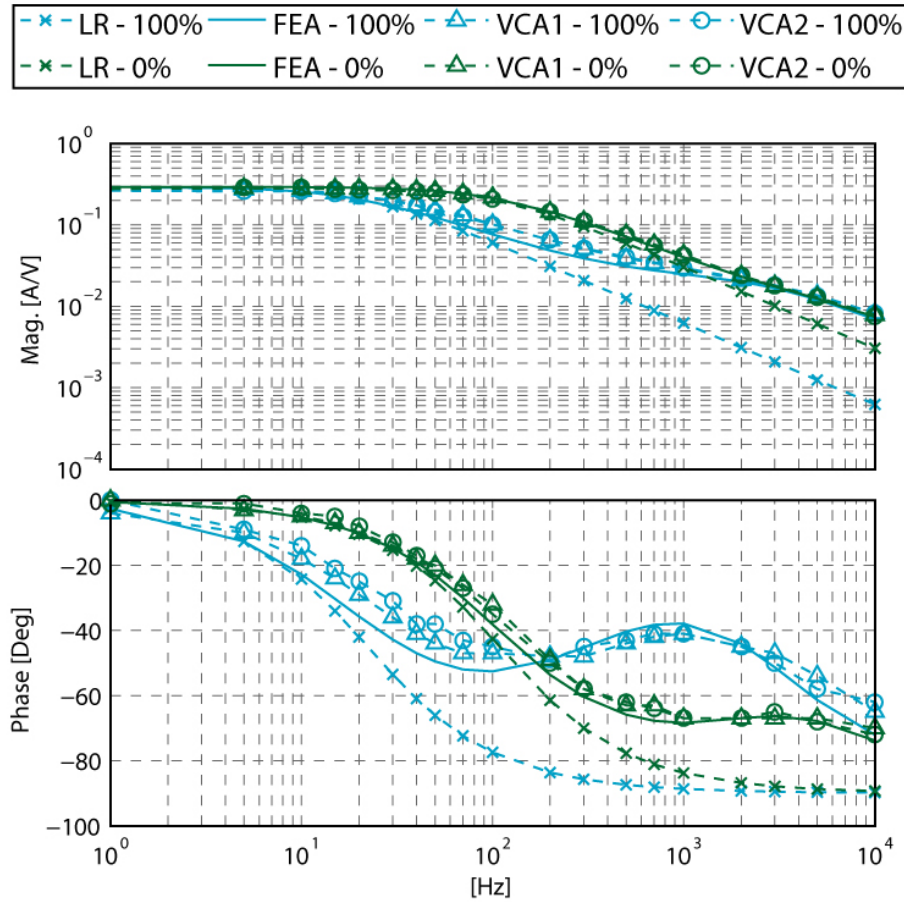


Fig. 5.3 Experimentally measured and model predicted VCA electrical TF ( $G_m(s)$ ). 'LR' stands for the first-order theoretical inductance-resistance model.

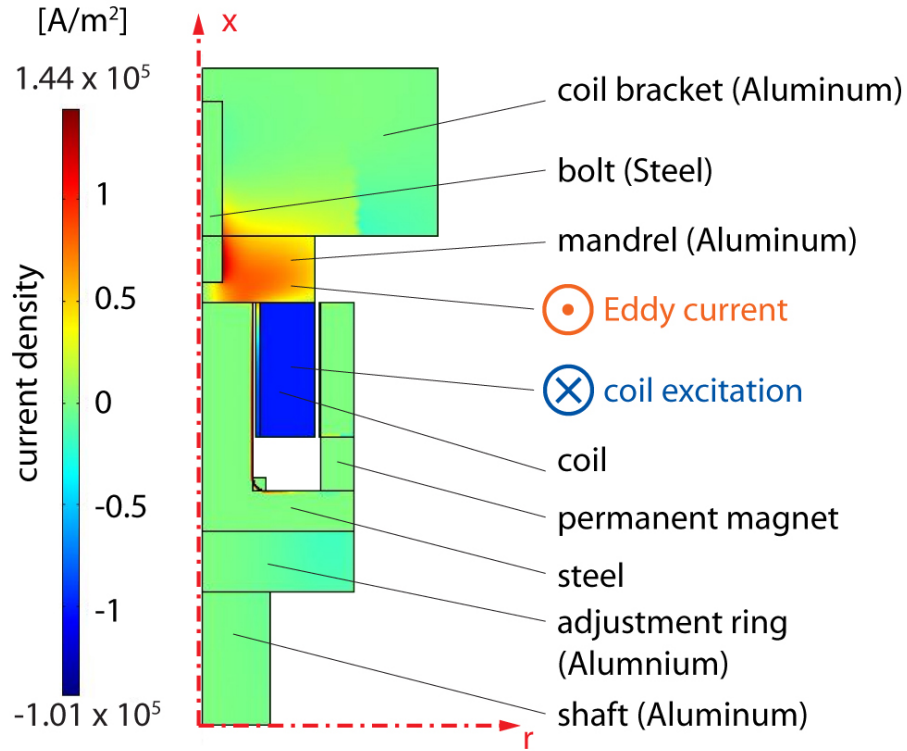


Fig. 5.4 Current FRF simulation for the fully engaged (100%) VCA at 200 [Hz].

Table 5.1. Pole/zero/gain fitted to the VCA frequency response.

engagement	$p_1$ [Hz]	$1/\tau$ [Hz]	$p_2$ [Hz]	$p_3$ [Hz]	$z_1$ [Hz]	$z_2$ [Hz]	K
100%	21	22	146	3010	84	434	452
0%	103	109	375	5494	287	2611	518

The current controller has been designed based on the measured  $G_m(s)$ , using the loop shaping procedure [34], [101]. A minimum crossover frequency of  $\omega_c = 1000$  [Hz] and a minimum phase margin of  $PM = 40$  [deg] was targeted. Controller parameters  $\{K_c, T_c, \alpha_c\}$  were implemented using equivalent resistors and capacitors in the analog current controller circuit which uses op-amps (Appendix A). The current controller ( $C_c$ ) and the current control loop TF ( $L_c = C_c G_p$ ) are plotted in Fig. 5.5. The common practice in loop-shaping controller design is to place the peak phase contribution of the lead filter at the cross-over frequency. However, due to the unexpected reversal of phase at high frequencies in the VCA transfer functions ( $G_m(s)$ ) of the 100% engagement case, their loop TF already possess enough PM when only the integrator is used. If more phase is added, their closed loop bandwidth falls below the 1000 [Hz] criterion. On the other hand, the disengaged case

still requires additional phase to match the  $PM = 40$  [deg] criterion. Hence, a lead filter with maximum 63 [deg] phase contribution at 122 [Hz] is designed which shapes  $L_c$ 's of both fully-engaged and fully-disengaged cases properly to match the design criteria (Fig. 5.5). The lowest cross-over frequencies are obtained for the fully-engaged cases at 1341 [Hz] and 1375 [Hz] for VCA's 1 and 2, respectively. Phase margin (PM) is 68 [deg] in both cases. For the fully-disengaged case, the cross-over frequencies are higher: 1595 [Hz] and 1593 [Hz] for VCA's 1 and 2, respectively. The PM is 41 [deg] for both VCA's, in that case.

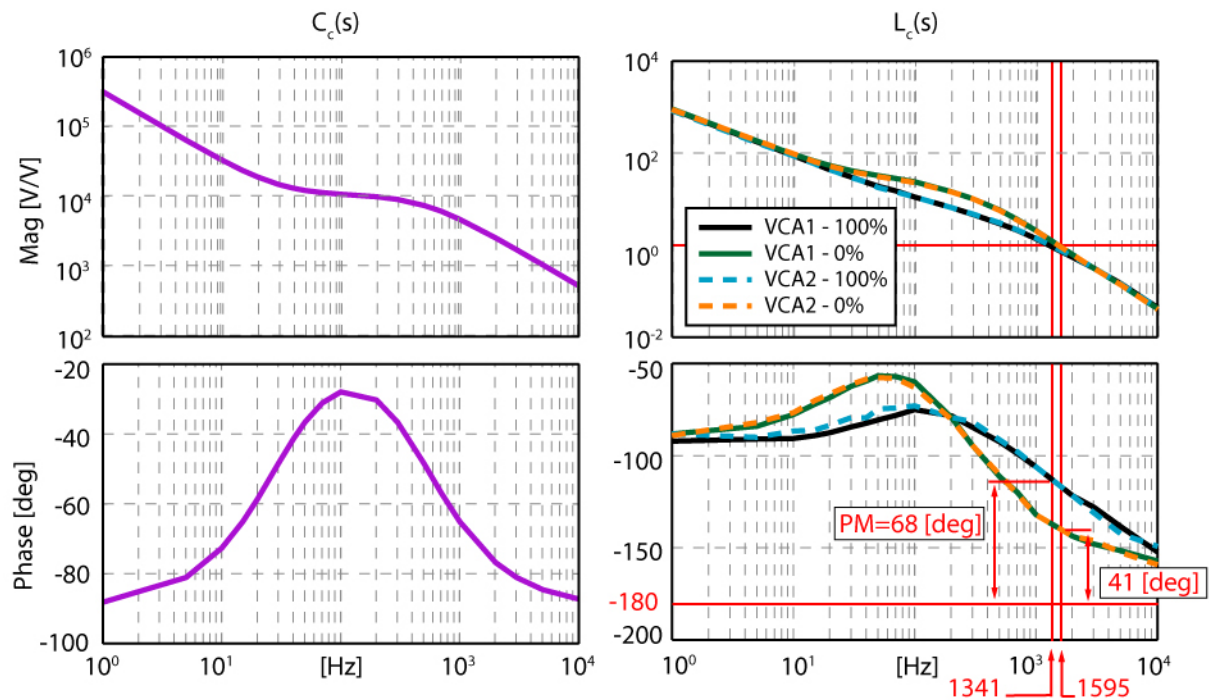


Fig. 5.5 Current controller ( $C_c$ ) and loop TF ( $L_c$ ).

The closed-loop transfer function (CLTF) has been identified using frequency response measurement for different levels of engagement, as presented in Fig. 5.6. For the 100% and 0% cases, predicted CLTF using the identified  $G_m(s)$  and the theoretical current controller have also been overlaid. The worst (lowest) current control bandwidths were measured at +3dB as 907 [Hz] and 915 [Hz], with phase losses of 61 [deg] and 62 [deg] for VCA's I and II, respectively. Both cases happen at the fully-disengaged case. The best (highest) bandwidths, in turn, were measured at -3dB as 1804 [Hz] and 1990 [Hz], with phase losses of -127 [deg] and -137 [deg] for VCA's I and II, respectively. The best cases are both for the fully-engaged case.

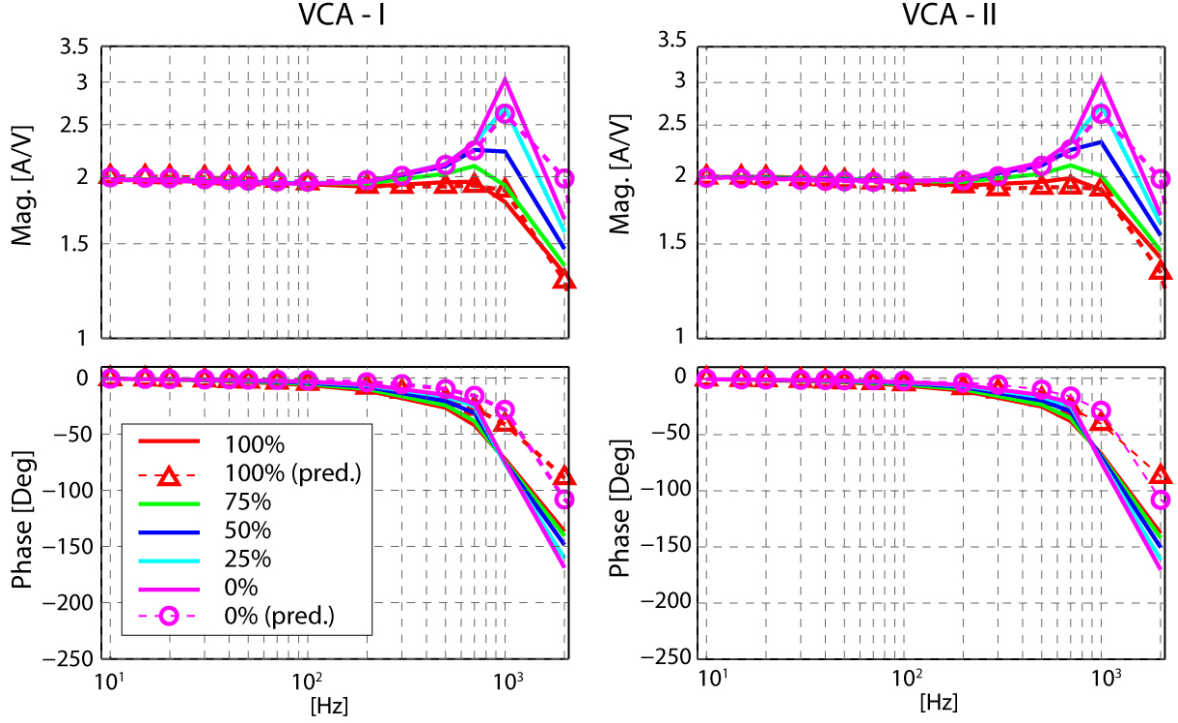


Fig. 5.6 Current control CLTF.

#### 5.4. Design of the position controller

The open loop positioning transfer function ( $G_p(s)$ ), which comprises dynamics of current control, the VCA force response, and stage mass, was measured for the 50% engagement case as presented in Fig. 5.7a, using the frequency response technique. The measured model behaves very similarly to a double integrator up to around 100 [Hz]. At higher frequencies, the phase starts rolling-off due to closed loop current control dynamics, as well as delays and filtering effects in the data acquisition system. Upon analyzing the plant frequency response, it was determined that a lead/lag type feedback controller would be suitable for achieving the desired positioning specifications. The structure of the lead/lag controller has the form:

$$C(s) = K_p \frac{T_a s + 1}{\alpha_a T_a s + 1} \frac{T_d s + 1}{\alpha_d T_d s + 1}, \quad 0 < \alpha_a < 1, \quad \alpha_d > 1. \quad (5.4)$$

The variables of lead ( $\alpha_a, T_a$ ) and lag ( $\alpha_d, T_d$ ) filters are determined using the loop-shaping controller design methodology, as for the current loop [34], [101]. In this approach, the controller is designed to satisfy certain criteria, such as the phase margin (PM), gain margin (GM), and maximum

sensitivity ( $S_{max}$ ). The control bandwidth is aimed as high as possible. The lag filter is used to lift the slope of the magnitude plot of the loop-transfer function ( $L$ ) at the low frequency region, which increases the tracking accuracy. It is designed to have its higher pole ( $1/\alpha_d T_d$ ) at least 10 times lower than the cross-over frequency ( $\omega_c$ ) not to affect stability. Assigning  $\alpha_d=0.01$  contributes 100 times amplification of  $L$  at 0 [Hz], which diminishes gradually towards  $\omega_c$ .

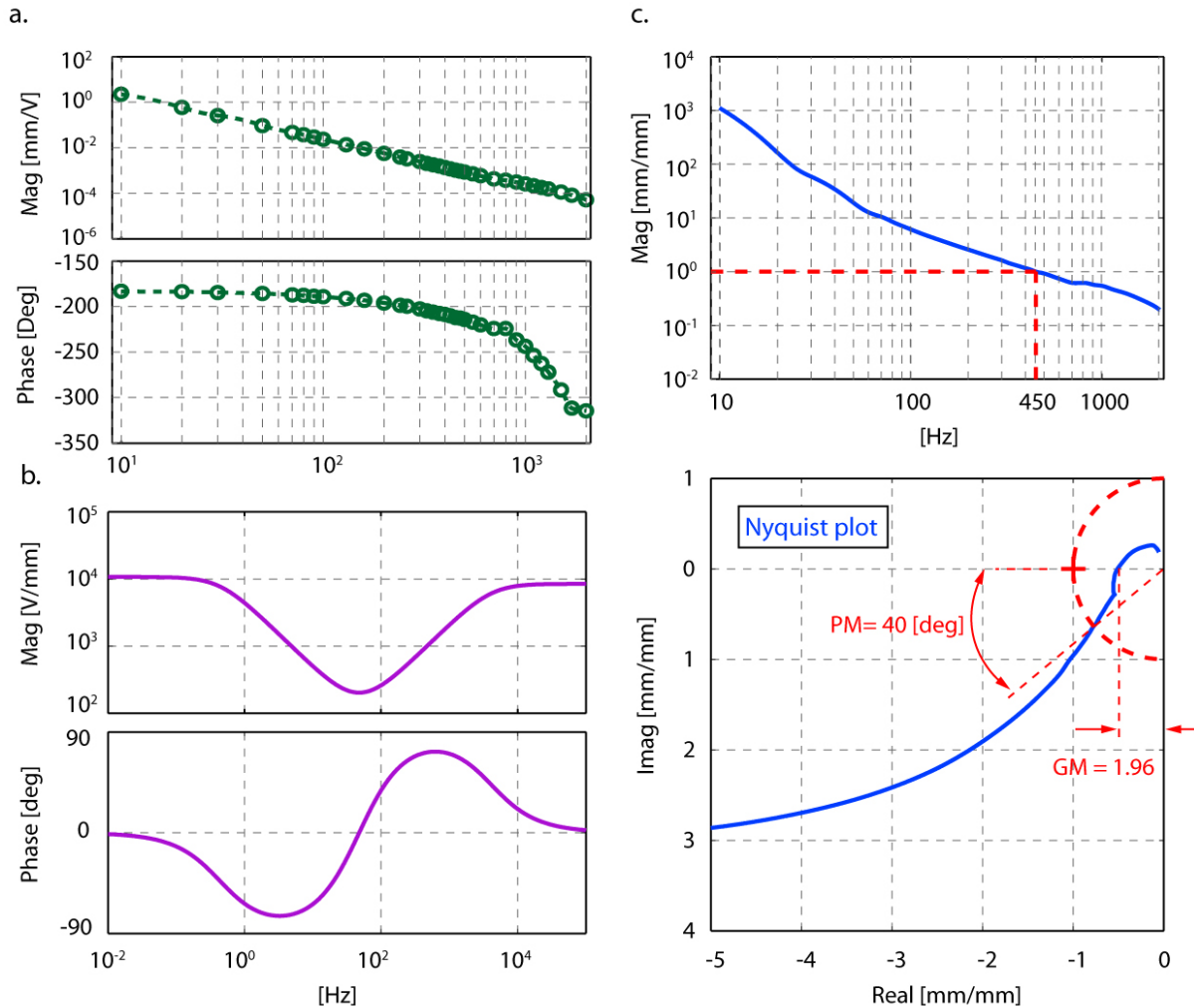


Fig. 5.7 Transfer functions related to position controller design; a. Measured  $G_p(s)$ , b. Controller ( $C(s)$ ), c. Positioning loop TF ( $L(s)$ ).

The lead filter design is made to match the stability requirements PM and GM, which are expressed by,

$$PM = 180[\text{deg}] + \angle L(\omega_c), \quad GM = 1/|L(\omega_{GM})|, \quad \angle L(\omega_{GM}) = 180[\text{deg}] \quad (5.5)$$

Variables  $(\alpha_a, T_a)$  are designed to provide the necessary phase advance at  $\omega_c$ . Finally,  $K_p$  is set as required to lift  $L$  such that its magnitude is exactly 1 at the desired  $\omega_c$ .

The controller Bode plot is presented in Fig. 5.7b. Bode magnitude and Nyquist plots for the loop transfer function,  $L = C G_p$ , are presented in Fig. 5.7c. The plots were obtained using the identified  $G_p(s)$  and the theoretical  $C(s)$ . The controller has 450 [Hz] cross-over frequency ( $\omega_c$ ), 40 [deg] phase margin (PM), and 1.96 gain margin (GM). With the same phase margin, up to 550 [Hz] cross-over frequency could be implemented. However, in this case the coil current was observed to widely exceed the 0.58 [A] limit for continuous operation, specified for AWG#24 cable from the 700 [circ.mils/A] rule [41]. The peak current demands were also observed to exceed 1 [A].

The digital position controller has been implemented at 20 [kHz] sampling frequency, using a DSpace® DS1005 system. The encoder signal is registered using the DS3002 encoder interface board which does 4096 times (12-bit) interpolation of the 4[ $\mu\text{m}$ ] measurement signal period for an effective position measurement resolution of 0.97 [nm]. The control voltage command to the power amplifiers is transmitted using the DS2102 digital-to-analog converter (DAC), which has  $\pm 10$  [V] range and 16-bit resolution.

### 5.5. Positioning resolution analysis via Dynamic Error Budgeting

Dynamic Error Budgeting (DEB) [75] has been used to predict and validate controller performance of ultraprecision motion systems by mapping individual disturbances modeled by their power spectral densities to a chosen performance goal (e.g. actual or measured positioning error). This method that has been established in the frequency domain allows for direct conclusions to be drawn and optimization to be carried out regarding the most significant contributions to positioning error. The predictions can be typically verified from the time history of the performance goal, using variance or standard deviation. In this section, DEB is used to analyze the positioning resolution of the linear motion stage, by predicting a ‘budget’ of contributions from different signals to the control error.

The positioning response of the system to a step trajectory with 200 [ $\mu\text{m}$ ] increments, low-pass filtered at 40 [Hz] using a second order filter with  $\zeta = 0.8$  is presented in Fig. 5.8. As shown in Fig.

5.8, closed loop positioning resolution was observed to be  $\pm 5$  [nm], compared to the 0.97 [nm] peak-to-valley resolution of the encoder signal.

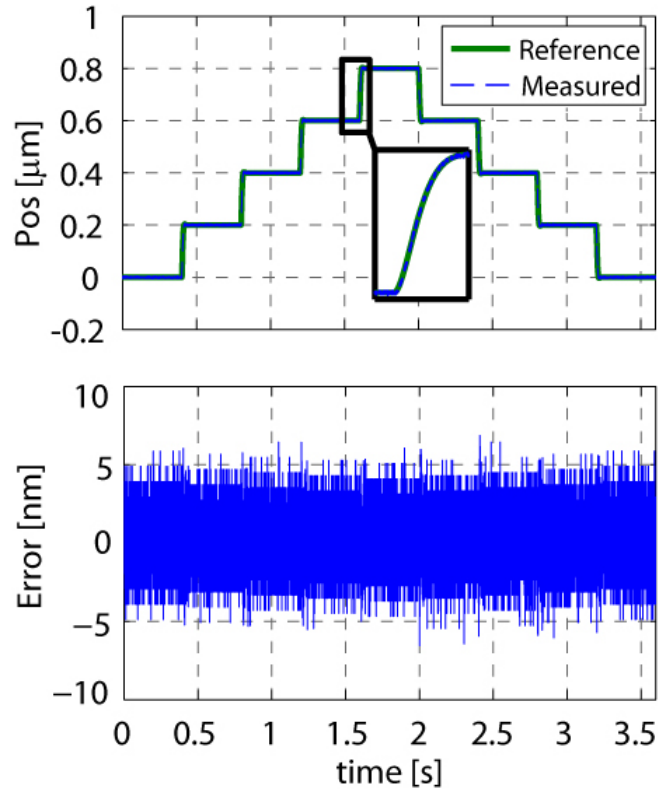


Fig. 5.8 Positioning results with the step trajectory.

### 5.5.1. DEB calculations

The block diagram of the control system with the disturbance and noise signals included is presented in Fig. 5.9 [34].

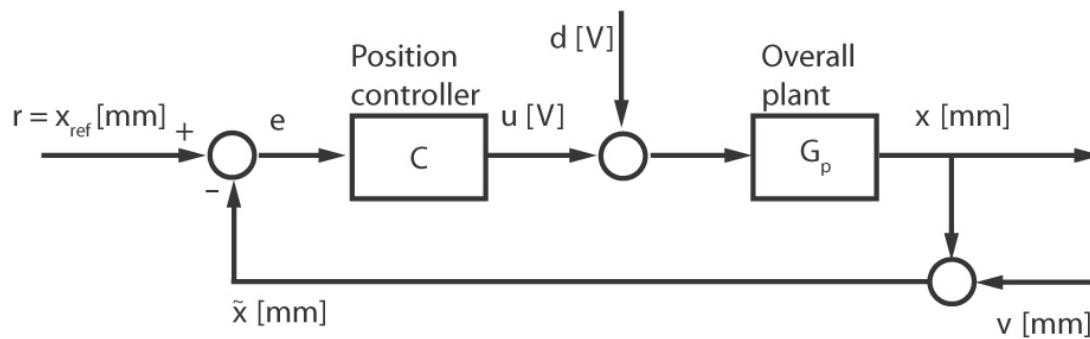


Fig. 5.9 Control system block diagram with the disturbance and measurement noise signals.



In Fig. 5.9,  $x_{ref}$  (generally denoted as  $r$ ) is the positioning reference input,  $e$  is the control error,  $u$  is the control effort,  $d$  is the plant input level disturbance,  $x$  is the actual position,  $v$  is the position measurement noise, and  $\tilde{x}$  is the measured position. To differentiate between the control error ( $e = x_{ref} - \tilde{x}$ ) and the actual error of positioning, the actual error can be denoted as  $a = x_{ref} - x$ . Then, the transfer functions relating key variables to each other can be expressed as,

$$\begin{aligned} e &= G_S r - G_S G_p d - G_S v, \\ a &= G_S r - G_S G_p d + G_T v. \end{aligned} \quad (5.6)$$

Above,  $G_S$  and  $G_T$  correspond to sensitivity, and complementary sensitivity functions, respectively, which can be expressed as,

$$G_S = \frac{1}{1 + C G_p}, \quad G_T = \frac{C G_p}{1 + C G_p} \quad (5.7)$$

Bode plots of  $G_S$ ,  $G_T$ , and  $G_S G_p$  are shown in Fig. 5.10.

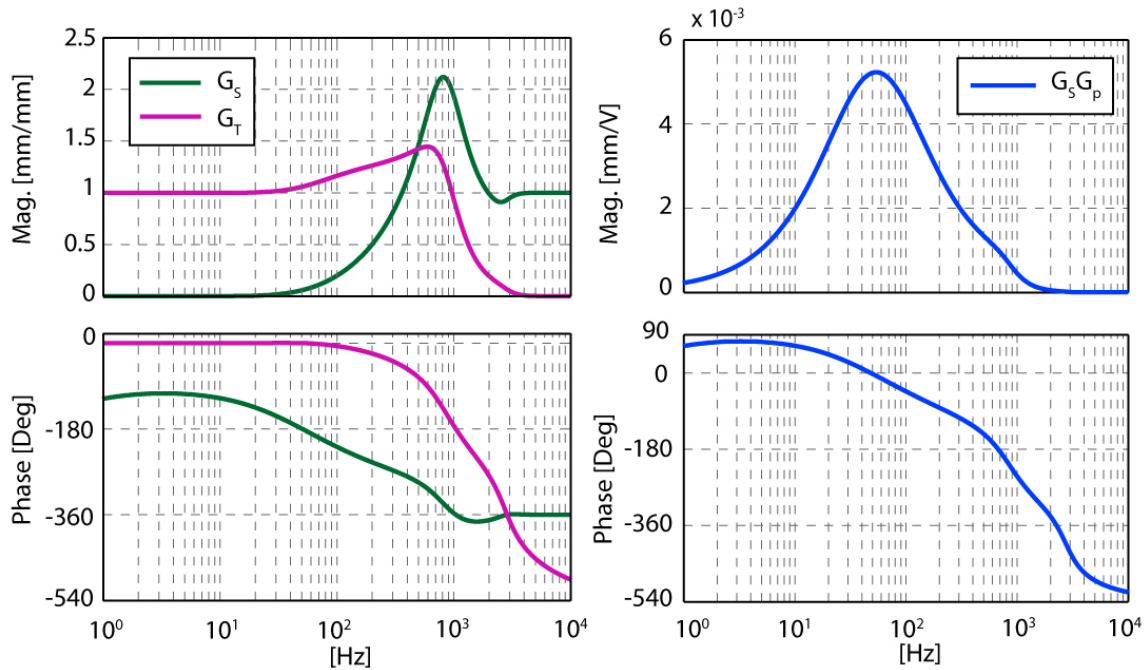


Fig. 5.10 Bode plots of transfer functions.

In the DEB method, contributions of each signal ( $r$ ,  $d$ ,  $v$ ) to the measured (control) and actual errors ( $e$ ,  $a$ ) are determined using their spectral models in terms of one-sided power spectral density (PSD) distributions. The one-sided PSD of a signal can be obtained from its Fast Fourier Transform ( $W(f)$ ) as [6],

$$S(f) = \frac{2 \cdot |W(f)|^2}{df} . \quad (5.8)$$

Above,  $df$  is the width of the frequency grid. Using linear time-invariant (LTI) system theory, transmissions of ( $r$ ,  $d$ ,  $v$ ) to ( $e$ ,  $a$ ) can be calculated as,

$$\begin{aligned} S_e(f) &= |G_S|^2 S_r(f) + |G_S G_p|^2 S_d(f) + |G_S|^2 S_v(f), \\ S_a(f) &= |G_S|^2 S_r(f) + |G_S G_p|^2 S_d(f) + |G_T|^2 S_v(f), \end{aligned} \quad (5.9)$$

where  $S_e(f)$ ,  $S_a(f)$ ,  $S_r(f)$ ,  $S_d(f)$ ,  $S_v(f)$ , are one-sided power spectral density distributions of  $e$ ,  $a$ ,  $r$ ,  $d$ ,  $v$ , respectively, vs. frequency ( $f$ ). The cumulative power spectrum (CPS) is evaluated from the discrete power spectral density as,

$$CPS(f_k) = \sum_{i=1}^k S_i df, \quad 1 < k < N, \quad (5.10)$$

The variance of a signal equals to the last element of CPS as,

$$\sigma^2 = CPS(f_N). \quad (5.11)$$

In DEB, this relationship is used to relate the cumulative contributions of individual PSD's to the variances of the analyzed signals ( $e$  and  $a$ ). The variance gives a solid quantification of signal magnitudes and allows comparisons between them.

Values for various spectral densities ( $S(f)$ ) are obtained in the following.  $S_v(f)$  corresponds to the encoder noise due to electrical and quantization noise. It is modeled as a broadband white noise. The encoder signal ( $\tilde{x}$ ) is recorded at the fixed middle stroke position with the air supply and power amplifiers turned off. Its CPS is obtained from its Fast Fourier Transform (FFT) as shown in Fig. 5.11.

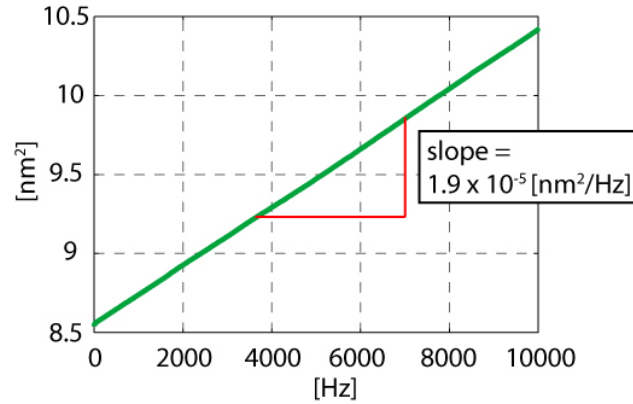


Fig. 5.11 CPS of encoder measurement at fixed position.

In CPS, the broadband component appears at high frequencies as a straight line with a slope of  $S_v(f)$  which can be expressed as,

$$S_v(f) = 1.9 \times 10^{-5} \text{ [nm}^2/\text{Hz]}, \quad 0 < f < 10 \text{ [kHz]}. \quad (5.12)$$

Above, the frequency limit  $f = 10 \text{ [kHz]}$  corresponds to half the sampling frequency, also known as the Nyquist frequency, which defines the frequency region where the FFT is valid. The jump near 0 [Hz] is due to the drift of the encoder. Using the least significant bit (LSB) of  $\delta_{enc} = 0.97 \text{ [nm]}$  for the encoder, the variance of the encoder quantization noise can be found as [75],

$$\sigma_{vq}^2 = \frac{\delta_{enc}^2}{12} = 0.0784 \text{ [nm}^2\text{]}. \quad (5.13)$$

Assuming a flat distribution, the encoder quantization noise PSD ( $S_{vq}$ ) can be calculated by using Eq. (5.10) in Eq. (5.11) as,

$$S_{vq} = \frac{\sigma_{vq}^2}{f_N} = 0.78 \times 10^{-5} \text{ [nm}^2/\text{Hz]}, \quad 0 < f < 10 \text{ [kHz]}. \quad (5.14)$$

Assuming that the encoder quantization noise ( $S_{vq}(f)$ ) and the electrical noise ( $S_{ve}(f)$ ) are uncorrelated, the encoder electrical noise component can be obtained by subtraction as,

$$S_{ve}(f) = S_v(f) - S_{vq}(f) = 1.12 \times 10^{-5} \text{ [nm}^2\text{/Hz]}, 0 < f < 10 \text{ [kHz]}. \quad (5.15)$$

The decomposition of  $S_v$  in Eq.'s (5.14) and (5.15) shows that the electrical and quantization noise components play comparable roles in the formation of the encoder noise.

The disturbance signal ( $d$ ) at the overall plant input is a voltage signal which interferes with the command applied by the controller to the power amplifiers. It can be due to the electrical and quantization noise of the DS2102 digital-to-analog converter (DAC) used in the interface. In this thesis, contribution of the DAC electrical noise is neglected. The  $\pm 10$  [V] range and 16-bit resolution of the DAC corresponds to a least significant bit (LSB) of  $\delta_{dac} = 0.305$  [mV]. Then, the variance of the quantization noise can be found as,

$$\sigma_{dac}^2 = \frac{\delta_{dac}^2}{12} = 7.8 \times 10^{-9} \text{ [V}^2\text{]}. \quad (5.16)$$

Assuming a flat power spectrum for  $S_{dac}(f)$ ,  $S_d$  can be calculated as,

$$S_d = S_{dac}(f) = \frac{\sigma_{dac}^2}{f_N} = 7.8 \times 10^{-13} \text{ [V}^2\text{/Hz]}, 0 < f < 10 \text{ [kHz]}. \quad (5.17)$$

PSD's  $S_e(f)$  and  $S_a(f)$  are estimated from the summation of individual contributions as shown in Eq. (5.9), and converted to CPS using Eq. (5.10). PSD of the control error ( $S_e(f)$ ) is also available from its recorded time history, and its cumulative spectrum can be denoted by  $CPS_e^*$ .

### 5.5.2. DEB results and discussion

In Fig. 5.12, the cumulative power spectrum of the control error ( $CPS_e^*$ ) is observed to follow the shape of the encoder noise ( $CPS_v$ ) at high frequencies, and the highest contributor to it is also  $CPS_v$ . Reference tracking ( $CPS_r$ ) seems to be mainly responsible for the initial bump at the low frequency

region. The effect of DAC quantization ( $CPS_d$ ) is observed to be negligible. The variance of  $e$  can be calculated from its recorded time history as  $(\sigma_e^2)^* = 2.482 \text{ [nm}^2\text{]}$ , which also corresponds to  $CPS_e^*(f_N)$  as shown in Fig. 5.13. The estimated variance of control error, on the other hand, is given as  $CPS_e(f_N) = \sigma_e^2 = 2.362 \text{ [nm}^2\text{]}$ . The 5% discrepancy can be due to additional unmodeled sources of disturbance, such as DAC electrical noise, floor vibrations, and power amplifier electrical noise.

The cumulative power spectrum of the actual error ( $CPS_a$ ) is calculated in Fig. 5.13. The control loop attenuates the contribution of encoder noise ( $v$ ) in actual positioning error ( $a$ ) through  $G_T$  which approaches to zero at high frequencies (Fig. 5.10). However, it is still observed to be the highest contributor to  $a$ . It is followed by the reference tracking ( $CPS_r$ ), and a negligible contribution from DAC quantization noise ( $CPS_d$ ).

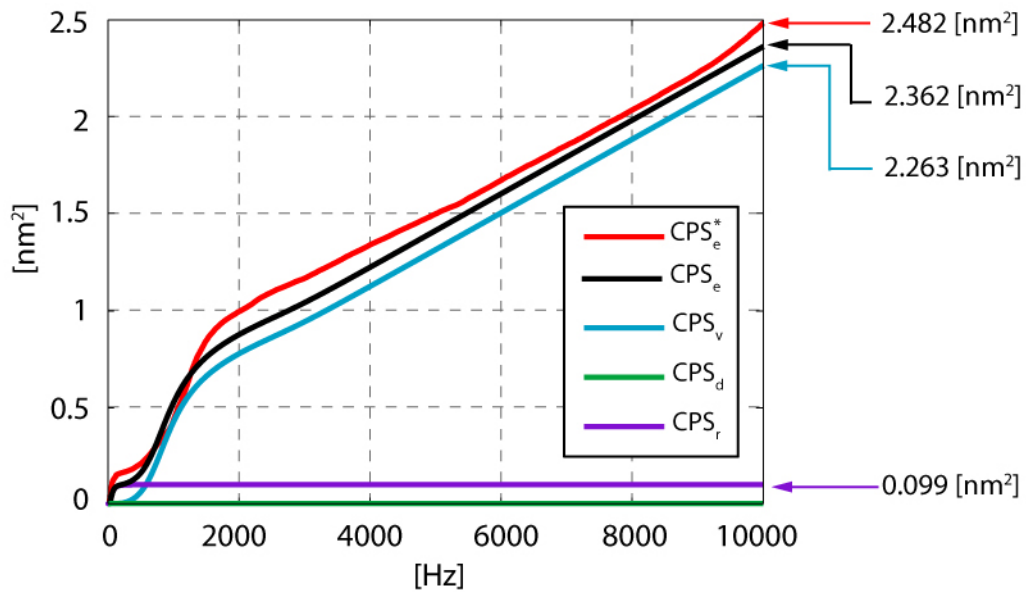


Fig. 5.12 Calculation of  $CPS_e$ .

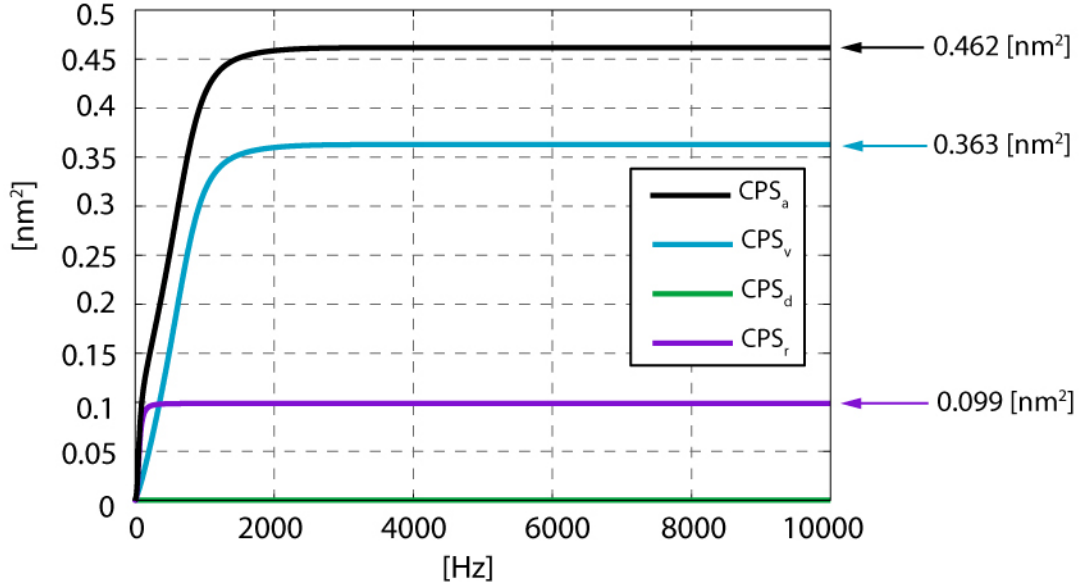


Fig. 5.13 Calculation of  $CPS_a$ .

The variance of the actual positioning error is calculated as  $CPS_a(f_N) = \sigma_a^2 = 0.462 \text{ [nm}^2\text{]}$ , as shown in Fig. 5.13. For the estimation of the actual positioning error ( $a$ ), comparison of the estimation with experimental results is not possible, as  $a$  cannot be measured. The 5% discrepancy in the estimation for  $e$  can be taken as an indicator that the actual positioning response can be predicted to an acceptable confidence level by the utilized methodology and signal models. If the actual positioning error ( $a$ ) is assumed to have zero mean, its root-mean-square (RMS) value is equal to its standard deviation, such that  $a_{RMS} = \sigma_a = 0.680 \text{ [nm]}$ . Positioning accuracy requirements in ultraprecision stage applications are often expressed in RMS error.

The DEB analysis shows that the actual positioning error of the motion stage is mainly formed by reference tracking and encoder noise errors (Fig. 5.13). Reference tracking can be improved by increasing the bandwidth of the controller, which would push peak sensitivity ( $\max\{G_S\}$ ) further right, and better attenuate the reference inputs at the low frequency region. However, this would also push complementary-sensitivity ( $G_T$ ) to the right, and transmit more of the high frequency encoder noise  $v$  towards  $a$  (Eq. (5.9)). Also, the bandwidth increase would transmit  $v$  to the control error ( $e$ ) through  $G_S$ , and increase the control effort ( $u = Ce$ ). This was already observed in the out of limit current demands of the experimentally tested 550 [Hz] control bandwidth. On the other hand,  $u$  due to noise can be suppressed by adding another pole to the controller ( $C$ ) beyond the cross-over

frequency. Such a pole would also positively affect  $G_S$  and  $G_T$ , by providing a sharper transition to the attenuation region. In the future, this additional pole will be implemented. However, bandwidth would most likely remain the same, as the contribution of encoder noise is already too high in  $a$  (Fig. 5.13). In fact, Fig. 5.13 suggests that the control bandwidth should be decreased, which would shift  $G_S$  and  $G_T$  left, in order to lift  $CPS_r$  up and push  $CPS_v$  down, respectively, for a lower combined contribution. However, the plots are obtained for a step trajectory, and lowering the bandwidth would increase the positioning errors for more demanding trajectories with larger spectral components at high frequencies by increasing the transmission of them to  $a$  through the left shifted  $G_S$ .

## 5.6. Trajectory following performance

During high feedrate trajectory following, the encoder quadrature detection errors due to encoder head misalignment become important. As these errors are periodic with the stage displacement, they result in high-frequency harmonics. For example, considering the 4 [ $\mu\text{m}$ ] measurement signal period, a 4 [mm/s] constant feed trajectory results in a 1000 [Hz] first harmonic in the error signal. As these harmonics can typically occur within the control bandwidth, audible, and potentially detrimental oscillations may get induced by the controller. A compensation scheme for these errors has been designed in Section 5.6.1 and an alternative to it is suggested in Section 5.6.3.

### 5.6.1. Compensation of encoder quadrature detection errors

The linear encoder system outputs two sinusoidal signals phased 90 [deg] apart, with 4 [ $\mu\text{m}$ ] period as was presented in Fig. 3.7. These signals can be expressed as follows:

$$\begin{aligned} A &= M \cos(\varphi), \\ B &= M \sin(\varphi), \end{aligned} \tag{5.18}$$

Above,  $M$  is the signal amplitude and  $\varphi$  is angular measurement of the instantaneous displacement. Heydemann [42] has proposed the following model for representing the distortions in sinusoidal encoder signals due to mechanical misalignment and electrical signal unbalance:

$$\begin{aligned} A' &= a \cos(\varphi) + A_o, \\ B' &= b \sin(\varphi - \theta) + B_o, \end{aligned} \tag{5.19}$$

In Eq. (5.19),  $a, b$  are distorted amplitudes,  $\theta$  is the phase error, and  $A_o, B_o$  are the offset errors. When arctangent interpolation is used with distorted encoder signals as the input, the calculated angular representation for the instantaneous displacement value will be erroneous, represented by:

$$\varphi_m = a \tan 2(B', A'). \quad (5.20)$$

The position measurement error can, then, be expressed as:

$$e_{pos} = [\varphi_m - \varphi] \times \left( \frac{4\mu m}{2\pi} \right). \quad (5.21)$$

In the experimental nano-positioning stage, the distorted A' and B' signals were recorded by translating the stage back and forth along the whole stroke length, several times. The Matlab® function 'lsqnonlin' in the Optimization Toolbox was used to fit the parameter set  $p = \{a, b, \theta, A_o, B_o\}$  to the signals [108]. The cost function used eliminates  $\varphi$  from the optimization objective as,

$$\cos(\varphi) = \frac{A' - A_o}{a}, \quad \sin(\varphi) = \frac{B' - B_o + \cos(\varphi) \sin(\theta)}{b \cos(\theta)}, \quad (5.22)$$

$$\beta = 1 - \sin^2(\varphi) - \cos^2(\varphi).$$

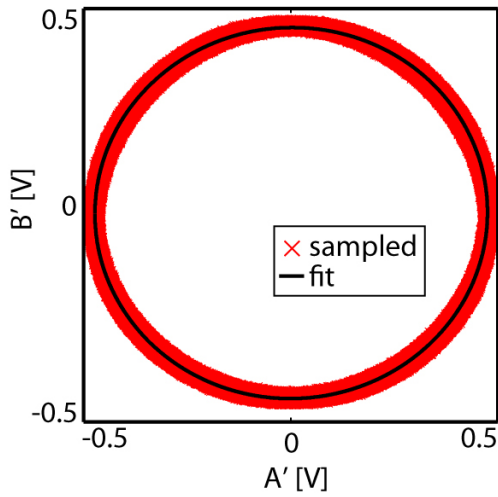
Above, the cost function ( $\beta$ ) is not squared as it is already done in the algorithm. The Lissajous figure [105] with recorded A' and B' points, along with the fitted parameters are presented in Fig. 5.14. While in the polar Lissajous graph, the individual phase errors may not appear to be too significant (ranging only in 0.2 - 1 % of the actual phase amplitudes) for A and B channels, it is verified in Section 5.6.2 that at the nanometer tracking level, left uncompensated these errors can significantly influence the dynamic accuracy of the positioning stage.

The resulting position measurement error prediction throughout one signal period is presented in Fig. 5.15. The one-sided FFT of the prediction ( $2|W_e|$ ) is also presented vs. angular frequency ( $\alpha$ ) in the figure. Temporal frequencies ( $f$ ) for constant feedrate motion can be obtained from  $\alpha$  as,



$$f = \frac{F\alpha}{4[\mu m]}, \quad (5.23)$$

where  $F$  is the feedrate and  $4 [\mu m]$  corresponds to the spatial period of the encoder signal. Values of  $2|W_e|$  at the first 4 harmonics are shown in Table 5.2. The model predicts that the measurement error is mainly clustered at the first two harmonics. Hence, it will exert corrections mainly at those frequencies. The magnitude of errors is observed to vary between  $-20$  to  $25$  [nm]. For the compensation of measurement error, a look-up table has been formed which maps  $\phi_m$  to  $e_{pos}$ . The compensator, shown in Fig. 5.16, obtains  $\phi_m$  from the erroneous position measurement and computes the required correction value.



a [V]	0.4741	$A_o$ [V]	0.0011
b [V]	0.4492	$B_o$ [V]	0.0052
$\theta$ [Deg]	-0.2320		

Fig. 5.14 Lissajous figure with recorded and fitted A' and B' signals.

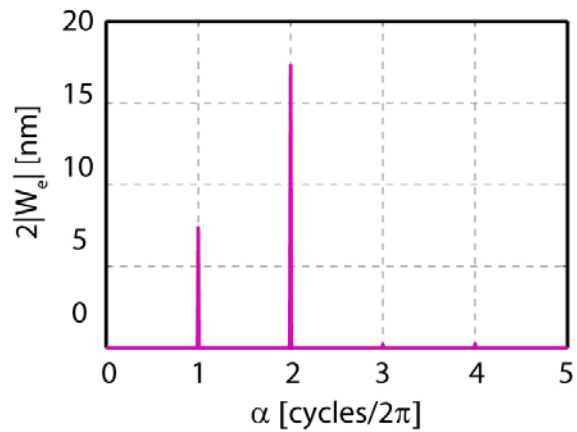
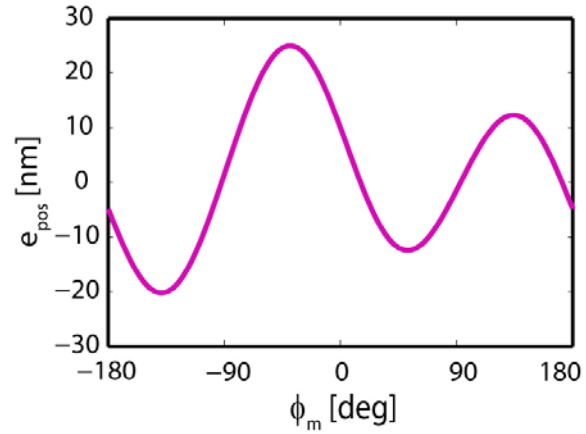


Fig. 5.15 Position measurement error in one signal period.

Table 5.2 Calculated and measured FFT's of sensor correction and error signals.

	1 <sup>st</sup> harmonic 750 [Hz] or 1 [cycles/2 $\pi$ ]	2 <sup>nd</sup> harmonic 1500 [Hz] or 2 [cycles/2 $\pi$ ]	3 <sup>rd</sup> harmonic 2250 [Hz] or 3 [cycles/2 $\pi$ ]	4 <sup>th</sup> harmonic 3000 [Hz] or 4 [cycles/2 $\pi$ ]
Sensitivity TF $ G_s $ [nm/nm]	2.088	1.260	0.933	0.949
FFT of correction ( $2 W_e $ ) [nm]	7.374	17.301	0.200	0.236
Transmitted FFT of correction ( $2 W_e^f  =  G_s  \times 2 W_e $ ) [nm]	15.396	21.800	0.187	0.224
Transmitted FFT of alternative correction ( $2 W_{e2}^f $ ) [nm]	14.028	23.350	2.746	2.758
FFT of uncompensated control error ( $2 W_u $ ) [nm]	12.247	26.599	3.257	1.868
FFT of compensated control error ( $2 W_c $ ) [nm]	2.218	2.818	3.005	2.296

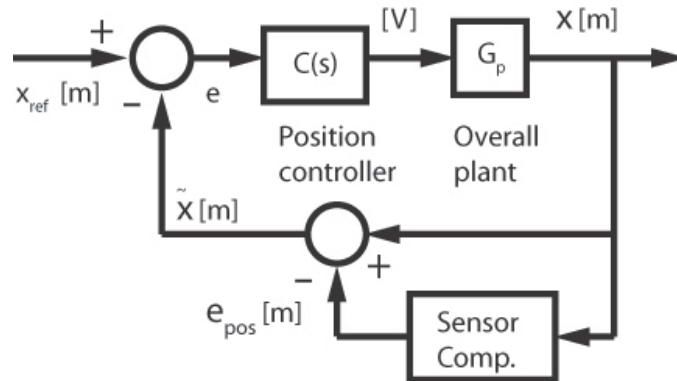


Fig. 5.16 Control block diagram showing sensor compensator.

### 5.6.2. Cubic acceleration profile trajectory test

A jerk limited cubic acceleration profile trajectory was commanded to the position control system with specified peak velocity (feedrate), acceleration, and jerk values of,  $F = 3$  [mm/s],  $A = 3$  [mm/s<sup>2</sup>], and  $J = 12$  [mm/s<sup>3</sup>], respectively (Fig. 5.17). The positioning reference and the resulting control errors with the sensor compensation turned off and on are shown in Fig. 5.18. It is observed that the

compensation is able to bring down the  $\pm 45$  [nm] constant feed tracking error down to  $\pm 15$  [nm]. Furthermore, the oscillations of control effort ( $u$ ) are suppressed, as it relates to the control error proportionally by  $u=C(s)e$ .

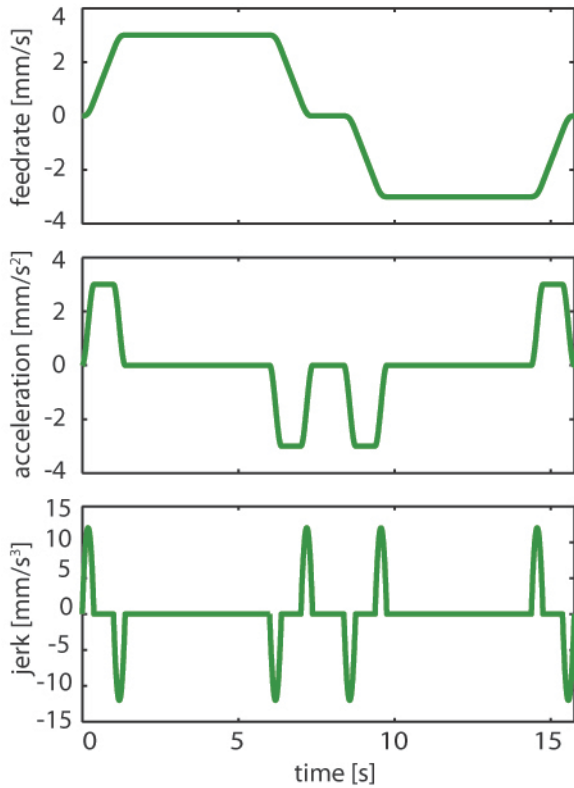


Fig. 5.17 Jerk limited cubic acceleration profile trajectory.

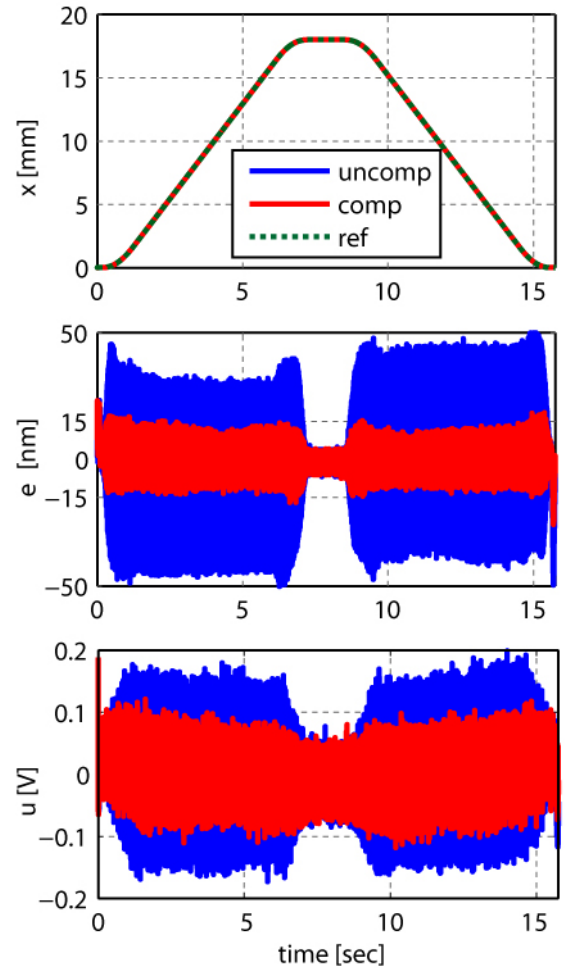


Fig. 5.18 Trajectory following results.

The FFT of the control error for the uncompensated and compensated sensor cases is presented in Fig. 5.19. It is observed that the first 2 harmonics (750 and 1500 [Hz]) of the error signal is matched considerably by the compensator. Higher harmonics are not compensated very well. The transmission of the correction signal to the control error can be expressed by  $|W_e^f| = |G_s| \times |W_e|$ . Values of  $|G_s|$  at the frequencies of the harmonics, and the transmitted correction  $|W_e^f|$  are presented in Table 5.2. The transmitted correction  $|W_e^f|$  is basically the prediction of the control errors by the correction scheme.

Comparing  $2|W_e^f|$  to the FFT of the uncompensated control error ( $2|W_u|$ ) it is observed that the first harmonic is overcompensated ( $2|W_e^f| = 15.396$  [nm] vs.  $2|W_u| = 12.247$  [nm]). The second harmonic is slightly matched with 18% difference. The third and fourth harmonics are almost totally neglected. FFT of the compensated control error ( $2|W_c|$ ) is in line with what could be expected from the level of match between  $|W_e^f|$  and  $|W_u|$ . The first harmonic of  $2|W_c|$  is formed as a result of overcompensation. Second, third, and fourth harmonics are present due to undercompensation. Nevertheless, nearly 3-fold improvement of the control error has been achieved by modeling and correcting for the periodic measurement errors.

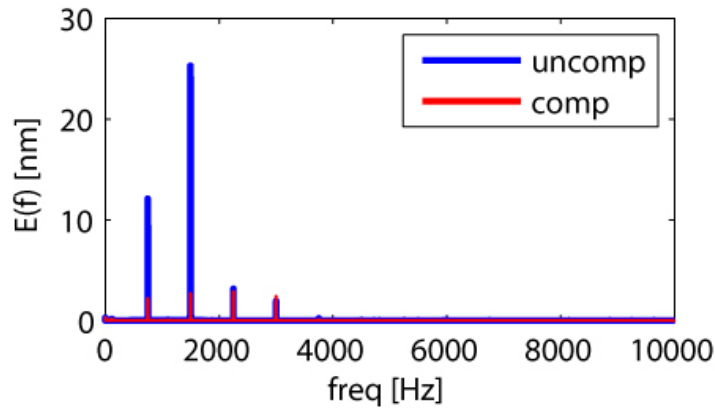


Fig. 5.19 FFT of the control error.

### 5.6.3. Alternative compensation scheme for the encoder quadrature detection errors

A possible alternative to the compensation scheme presented in Section 5.6.1 is to directly use encoder measurement errors to fit a number of harmonics to the required correction. The actual  $e_{pos}$  signal is not available, but the encoder measurement during motion can be high-pass filtered to approximate it. One such trajectory, excerpted from a manually generated motion, is presented in Fig. 5.20. The trajectory is high-pass filtered using Matlab® ‘filtfilt’ command which does zero-phase digital filtering. The filter is designed as an 8<sup>th</sup> order Butterworth filter using the ‘butter’ command, with cut-off frequency of 250 [Hz] [109]. A zoomed in view of the filtered signal is shown in Fig. 5.21.

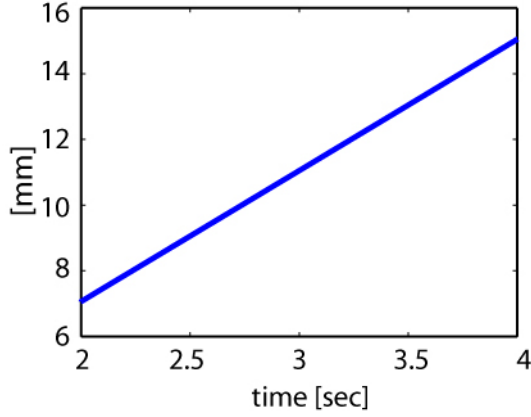


Fig. 5.20 Trajectory used to estimate measurement errors.

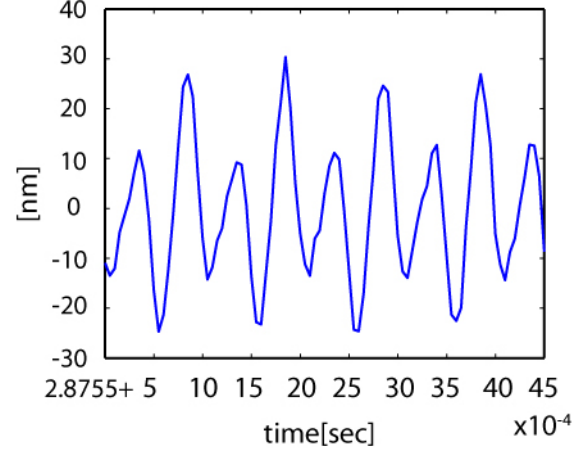


Fig. 5.21 High-pass filtered encoder signal.

The approximate measurement error ( $e_{pos}^*$ ) from the high-pass filtered encoder signal can be modeled as a function of the angular representation of measurement ( $\varphi_m$ ) as,

$$e_{pos}^* = a_1 \sin(\varphi_m + \kappa_1) + a_2 \sin(2\varphi_m + \kappa_2) + a_3 \sin(3\varphi_m + \kappa_3) + a_4 \sin(4\varphi_m + \kappa_4). \quad (5.24)$$

Then, a least squares fitting problem can be formulated as:

$$Y = \Phi \theta, \quad Y = \begin{bmatrix} e_{pos,1}^* \\ e_{pos,2}^* \\ \vdots \\ e_{pos,N}^* \end{bmatrix}, \quad \theta = \begin{bmatrix} a_1 \cos \kappa_1 \\ a_1 \sin \kappa_1 \\ a_2 \cos \kappa_2 \\ a_2 \sin \kappa_2 \\ \vdots \\ a_4 \cos \kappa_4 \\ a_4 \sin \kappa_4 \end{bmatrix}, \quad (5.25)$$

$$\Phi = \begin{bmatrix} \sin(\varphi_{m,1}) & \cos(\varphi_{m,1}) & \sin(2\varphi_{m,1}) & \cos(2\varphi_{m,1}) & \dots & \sin(4\varphi_{m,1}) & \cos(4\varphi_{m,1}) \\ \sin(\varphi_{m,2}) & \cos(\varphi_{m,2}) & \sin(2\varphi_{m,2}) & \cos(2\varphi_{m,2}) & \dots & \sin(4\varphi_{m,2}) & \cos(4\varphi_{m,2}) \\ \vdots & \vdots & \vdots & \vdots & \ddots & \vdots & \vdots \\ \sin(\varphi_{m,N}) & \cos(\varphi_{m,N}) & \sin(2\varphi_{m,N}) & \cos(2\varphi_{m,N}) & \dots & \sin(4\varphi_{m,N}) & \cos(4\varphi_{m,N}) \end{bmatrix}.$$

Above,  $e_{pos,k}^*$ ,  $\varphi_{m,k}$ , are filtered error signal, and instantaneous angle of measurement recorded at samples  $1 < k < N$ , respectively,. Variables of the model can be solved from the elements of  $\theta$  as,

$$\theta = \Phi^{-1}Y, \quad (5.26)$$

$$a_i = \sqrt{\theta_i^2 + \theta_{i+1}^2}, \quad \kappa_i = \tan^{-1}(\theta_{i+1}/\theta_i), \quad i = 1, 3, 5, 7.$$

Above,  $\Phi^{-1}$  stands for the pseudo-inverse. Samples of the whole 8 [mm] motion (Fig. 5.20) with 20 [kHz] sampling frequency are used. Fitted variables are listed in Table 5.3. Values of  $a_{1,\dots,4}$  also correspond to the predicted one-sided FFT amplitudes of first 4 harmonics of the measurement error, which can be denoted as  $2|W_{e2}|$ . The amplitudes are filtered through  $G_S$ , as was previously done for amplitudes obtained for the original compensation, and provided in Table 5.2 as  $2|W_{e2}^f|$ . Comparing  $2|W_{e2}^f|$  with  $2|W_u|$  reveals that the first harmonic is also overcompensated by the alternative correction scheme, but to a lesser degree. Second and third harmonics are predicted better than the original compensation ( $2|W_e^f|$ ). The fourth harmonic is overcompensated by the prediction of  $2|W_{e2}^f|$ . However, the severity of overcompensation is less than the undercompensation in the case of ( $2|W_e^f|$ ). Results show that the alternative approach can provide a better overall correction performance, which will be tested in experiments in the future.

Table 5.3 Least-squares fit to the approximate measurement error.

Variable	Fitted value [nm]	Variable	Fitted value [deg]
$a_1$	6.719	$\kappa_1$	110
$a_2$	18.531	$\kappa_2$	177
$a_3$	2.942	$\kappa_3$	-97
$a_4$	2.907	$\kappa_4$	176

## 5.6. Conclusion

A summary of the control system design process, as described in this chapter, can be presented as follows:

- Voice coil actuator dynamics has been identified using the frequency response technique. The deviations from an ideal first-order system have been verified in FE simulations to be rooted in eddy currents induced in the stage stator structure.
- A current controller has been designed and verified experimentally to deliver  $>907$  [Hz] bandwidth.
- A positioning controller has been designed with 450 [Hz] bandwidth, 40 [deg] phase margin and 1.96 gain margin.
- A positioning resolution of  $\pm 5$  [nm] has been achieved. Dynamic Error Budgeting (DEB) has been used to identify different factors contributing to the positioning error. The main source of error has been found to be the encoder measurement noise, followed by the reference tracking error.
- Trajectory following accuracy of  $\pm 15$  [nm] for high feedrates has been achieved using a sensor compensation scheme for encoder misalignment errors.

A number of items have been identified for future work and for consideration in designs to be made for similar ultraprecision motions systems. These can be listed as follows:

- Position controller design will be enhanced with more poles beyond the cross-over frequency for better attenuation of encoder noise.
- Better compensation schemes for the encoder signal will be investigated. Higher harmonics of the signal error, caused by the amplitude and phase mismatch of the A and B signals, will be better modelled. The proposed alternative correction schemes will be tested in experiments.
- Performance of the motion stage will be evaluated in the presence of dynamic disturbances, such as impact forces, and forces induced by micro-machining operations to verify disturbance rejection properties.

# Chapter 6

## Modal Testing

### 6.1. Introduction

Modal testing refers to measurement and analysis techniques for the determination of vibratory dynamics in mechanical systems. In ultraprecision motion stage design, the primary use of such information is in the design of the feedback control bandwidth. As a general rule, control bandwidth is set several times smaller than the first harmonic frequency of the system, in order not to excite vibrations. Vibrations are detrimental to accuracy and may even cause instability by growing in the feedback loop. Exceptions to this rule can be made if the mode shape associated with the harmonic (i.e. the motion pattern of oscillations) does not have significant components in the axes of actuation or position measurement. In that case, the control system is ‘blind’ to that mode, allowing bandwidths higher than the first harmonic. Hence, the influence of vibratory dynamics in a system depends equally on the natural frequencies and the mode shapes associated with them. Modal testing also constitutes a method for non-destructive testing. The static compliance of a point on a structure equals to the contributions of individual measured modes projected to 0 [Hz]. Similarly, the distribution of compliances in a system can be qualitatively judged from the natural frequencies associated with certain mode shapes. For example, if elements supporting the structure in the vertical direction do not have sufficient stiffness, a vertical translational mode with natural frequency lower than expected can be observed.

In this chapter, the application of modal testing to the nano-positioning stage is presented. Impact hammer testing is carried out using two different methods and the results are compared. In Section 6.2, an overview of the testing methods is presented. In Sections 6.3 and 6.4, methodology pertaining to method 1 (peak-picking), and method 2 (commercial software package) are presented, respectively. In Section 6.5, comparative modal testing results and discussion is presented. This chapter finishes with conclusions in Section 6.6.

### 6.2. Overview of the testing methods

The two independent methods used in the impact testing of the nano-positioner are summarized in Table 6.1. For both testing methods, feedback control is used to position the stage at the middle of the stroke length ( $x = 10$  [mm]). Using a low cross-over frequency of 2 [Hz] in this position controller,



the interference of it with vibration mode measurements is prevented. Details of how each method is employed are discussed in Sections 6.3 and 6.4.

Table 6.1. Comparison of the two independent methods used in modal testing.

Feature	Method 1 (Peak-picking)	Method 2 (Software package)
Frequency response function (FRF) acquisition system	CutPRO® MalTF module by Manufacturing Automation Laboratory (MAL), Inc.	LMS Test.Lab® by Siemens - PLM Software
Testing procedure	Roving hammer	Roving accelerometer
Accelerometer type	Dytran® 3035AG (1-channel)	PCB Electronics® 356A02 (3-channel)
Impact hammer type	Dytran® 5800SL	Dytran® 5800SL
Identification of natural frequencies and damping ratios	Peak-picking method	PolyMAX [85]
Identification of mode shape vectors	Peak-picking method	Least - Squares Frequency Domain (LSFD) [43]
Presentation of mode shapes	Manual 2D drawings	Automated 3D animations

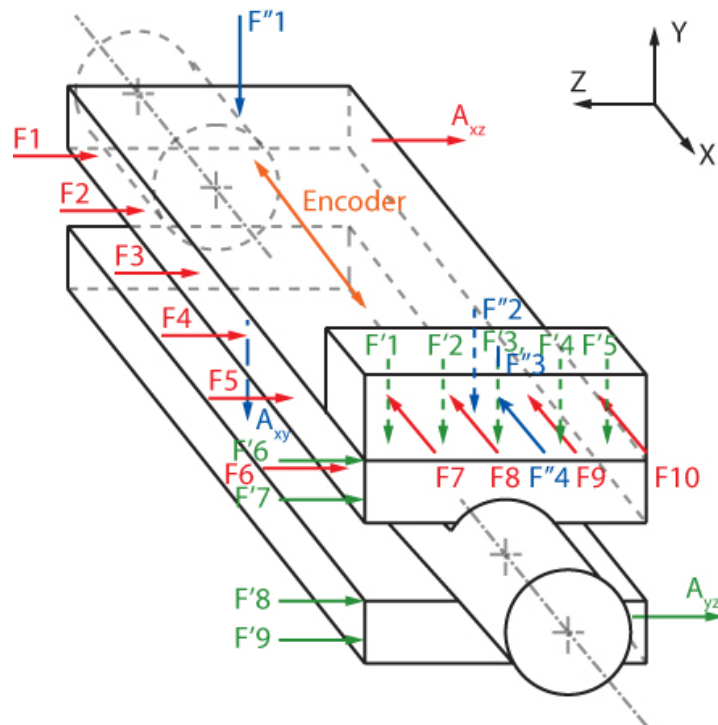


Fig. 6.1 Impact and measurement locations for method 1 (peak-picking).

### 6.3. Using method 1 (peak-picking)

#### 6.3.1 Impact and measurement points

For method 1 (peak-picking), FRF measurements were taken in 3 different planes: XY, YZ, and XZ (Fig. 6.1). For each measurement plane, accelerometer location and positive direction of acceleration measurement are indicated by  $A_{xz}$ ,  $A_{yz}$ , and,  $A_{xy}$ . In each measurement plane, impact locations and directions are indicated by  $F1$  to  $F10$  for  $A_{xz}$ ,  $F'1$  to  $F'9$  for  $A_{yz}$ , and  $F''1$  to  $F''4$  for  $A_{xy}$ .

#### 6.3.2. Method of analysis

In the first method, modal parameters, natural frequencies ( $\omega_n$ ) and damping ratios ( $\zeta$ ), are identified using the ‘peak-picking’ method. ‘Peak-picking’, in the general sense, refers to the usage of graphical features of the real and imaginary parts of the FRF to estimate modal parameters [22], [30], [95]. Different resources may refer to slightly varying formulations of the ‘peak-picking’ method, although they share the same basic idea. A brief description of it, as employed in this thesis, is presented here.

A single degree of freedom (SDOF) vibratory system, composed of linear mass, spring, and damper elements is presented in Fig. 6.2. The differential equation describing the system can be written as,

$$m\ddot{x} + c\dot{x} + kx = f(t), \quad (6.1)$$

where,  $m$  is the mass,  $c$  is the viscous damping coefficient, and  $k$  is the spring stiffness. The relationship between the excitation force,  $f(t)$  and the position of the mass,  $x(t)$  can be written in the frequency domain as,

$$\alpha(\omega) = \frac{X(\omega)}{F(\omega)} = \frac{1/k}{1 - \left(\frac{\omega^2}{\omega_n^2}\right) + j2\zeta\left(\frac{\omega}{\omega_n}\right)}, \quad \omega_n = \sqrt{\frac{k}{m}}, \quad \zeta = \frac{c}{2\sqrt{km}}, \quad (6.2)$$

where  $\omega_n$  is the natural frequency, and  $\zeta$  is the damping ratio. Above,  $\alpha(\omega)$  is termed as the ‘receptance’ of the system, and corresponds to the displacement response. It constitutes one of three common ways frequency response functions (FRF) can be expressed. The other two follow as ‘mobility’,  $v(\omega)$ , and ‘accelerance’,  $a(\omega)$ , which correspond to velocity and acceleration response, respectively, as:

$$\begin{aligned}
v(\omega) &= \frac{\dot{X}}{F} = j\omega \times \alpha(\omega), \\
a(\omega) &= \frac{\ddot{X}}{F} = j\omega \times v(\omega) = -\omega^2 \alpha(\omega).
\end{aligned}
\tag{6.3}$$

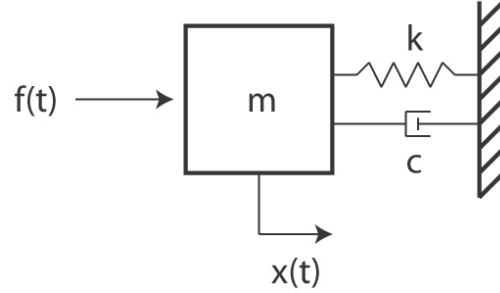


Fig. 6.2 The SDOF vibratory system.

Bode, real-imaginary, and Nyquist plots of all three FRF types, as well as the relationship between their graphical features and system properties are presented in Appendix C. As the transducer used in this thesis is an accelerometer, accelerance FRF can be directly obtained from the measurements, and the derived formulations of ‘peak-picking’ are based on it.

Accelerance FRF between two coordinates ( $i$  and  $k$ ) of a proportionally damped multi-degree of freedom system can be presented as a combination of vibratory modes as [30],

$$a^{ik}(\omega) = \sum_{r=1}^N \frac{-\omega^2 (1/k_r) \psi_r^i \psi_r^k}{1 - (\omega/\omega_r)^2 + j2\zeta_r (\omega/\omega_r)}.
\tag{6.4}$$

Above,  $N$  is the number of modes,  $\psi_r^i$  and  $\psi_r^k$  are the  $i$ -th and  $k$ -th elements of the  $r$ -th mode shape vector,  $\omega_r$  is the natural frequency,  $\zeta_r$  is the damping ratio, and  $k_r$  is the modal stiffness. In the case of a point FRF ( $i = k$ ),  $\psi_r^i \psi_r^k = 1$  can be set without loss of generality, which makes  $1/k_r$  equivalent to the static compliance contribution of each mode. Equation (6.4) can be also formulated using ‘mass normalized’ or ‘stiffness normalized’ mode shape vectors, but would not alter the presented method of analysis. The accelerance can be separated into real and imaginary parts as,

$$a^{ik}(\omega) = \sum_{r=1}^N (G_r^{ik}(\omega) + jH_r^{ik}(\omega)),$$

$$G_r^{ik}(\omega) = \frac{-\omega_r^2 z_r^2 (1 - z_r^2) (1/k_r) \psi_r^i \psi_r^k}{(1 - z_r^2)^2 + (2\zeta_r z_r)^2}, \quad (6.5)$$

$$H_r^{ik}(\omega) = \frac{2\zeta_r \omega_r^2 z_r^3 (1/k_r) \psi_r^i \psi_r^k}{(1 - z_r^2)^2 + (2\zeta_r z_r)^2},$$

where  $z_r = \omega/\omega_r$  represents the normalized frequency. If the modes are assumed to be separated from each other (i.e. having sufficiently distant natural frequencies), the real and imaginary plots of the FRF near each eigenfrequency  $\omega = \omega_r$  (or  $z_r = 1$ ) would resemble the characteristics of an SDOF system as presented in Fig. 6.3.

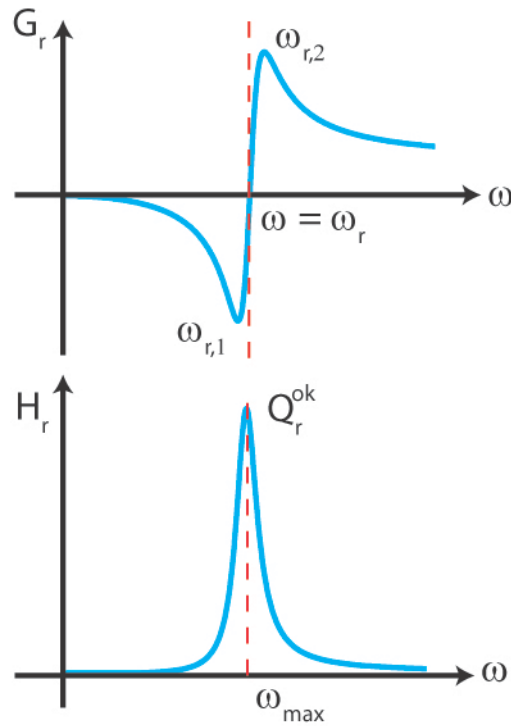


Fig. 6.3 Real and imaginary plots of a sample acceleration FRF.

Certain special points on the plots can be analytically defined as follows:

- i. Setting  $\frac{\partial G_r}{\partial \omega} = 0$  yields 2 positive roots as,  $\omega_{r,1} = \omega_r / \sqrt{1 + 2\zeta_r}$  and  $\omega_{r,2} = \omega_r / \sqrt{1 - 2\zeta_r}$ . Hence, minimum and maximum of the real accelerance plot around the natural frequency ( $\omega_r$ ) can be used to determine the damping ratio as,

$$\zeta_r = \frac{(\omega_{r,2}^2 - \omega_{r,1}^2)(\omega_r)^2}{4\omega_{r,1}^2\omega_{r,2}^2}, \quad (6.6)$$

- ii. Setting  $\frac{\partial H_r}{\partial \omega} = 0$  yields only  $\omega_{max} = \omega_r \sqrt{2\sqrt{\zeta_r^4 - \zeta_r^2 + 1} + 2\zeta_r^2 - 1}$  as the positive root. Assuming  $\zeta_r \ll 1$ ,  $\omega_r \approx \omega_{max}$  can be assumed. Hence, the imaginary peak/dip location can be used to identify the natural frequency ( $\omega_r$ ).
- iii. Limit  $\omega/\omega_r \rightarrow \infty$  yields  $G_r \rightarrow \frac{\omega_r^2 \Psi_r^i \Psi_r^k}{k_r}$  and  $H_r \rightarrow 0$ . Hence, real part has residues from lower modes, and using the vertical axis crossing of  $G_r$  for natural frequency estimation would be inaccurate.
- iv. Limit  $\omega/\omega_r \rightarrow 0$  yields  $G_r \rightarrow 0$  and  $H_r \rightarrow 0$ . Hence, higher frequency modes typically do not have an influence on their lower frequency counterparts.

For mode shapes to be identified, either the accelerometer location can be fixed and force impacts at different locations can be applied (roving hammer), or the impact location can be fixed while the accelerometer is placed at different points for each measurement (roving accelerometer). Due to the reciprocity rule ( $a^{ik} = a^{ki}$ ), results from the two cases are equivalent. Roving hammer measurements (for the same number of measurement points) can be carried out more quickly, as impacting at a point does not require any preparation. On the other hand, in the roving accelerometer case, more time is needed to properly mount the accelerometer at each measurement point, generally using wax. If one wants to determine mode shapes in three dimensions, which allows for a full three dimensional display of the vibratory motions, the response at every measurement point has to be measured in all three orthogonal axes. For the roving hammer case, this requires impacts in three orthogonal directions to be applied at each measurement point. This is very cumbersome; first, due to the difficulty of adjusting the orthogonal impact directions, second, due to the likelihood of some points being impossible to reach from all three directions. In such cases, it is much more advantageous to use a tri-axial accelerometer, which can output accelerations in all three axes at the same time, in roving accelerometer configuration. This way, both the problem of orienting measurement axes is

solved, and the possibility of being obstructed by the measured structure is minimized, as the accelerometer is both smaller, and stays in place during measurement. In this thesis, as the mode shapes are manually sketched in method 1, roving hammer configuration is used to obtain two dimensional mode shapes with hammer impacts from a single direction for each measurement point. On the other hand, due to the availability of three dimensional automated animation of mode shapes in method 2, roving accelerometer configuration is used with a tri-axial accelerometer.

Denoting the accelerometer location as 'o', the accelerance FRF is given by  $a^{ok}(\omega)$ . As the imaginary peak/dip approximately occurs at  $\omega_r$ , the value of the peak/dip can be expressed as:

$$H_r^{ok}(\omega_r) = Q_r^{ok} = \frac{\omega_r^2 \Psi_r^o \Psi_r^k}{2k_r \zeta_r}, \quad (6.7)$$

where  $Q_r^{ok}$  is the imaginary peak/dip. The value of the imaginary peak/dip measured for a number of impact points,  $k = 1 \dots m$ , can be related to the mode shape ( $\Psi_r$ ) as,

$$\begin{bmatrix} Q_r^{o1} \\ Q_r^{o2} \\ \vdots \\ Q_r^{om} \end{bmatrix} = \frac{\omega_r^2 \Psi_r^o}{2k_r \zeta_r} \begin{bmatrix} \Psi_r^1 \\ \Psi_r^2 \\ \vdots \\ \Psi_r^m \end{bmatrix}. \quad (6.8)$$

As the mode shapes, which are essentially eigenvectors of the system dynamics, can be scaled by any constant factor, the imaginary peak/dip values can be directly used as elements of the mode shape vector. An example case of how the modes are sketched using the imaginary peak/dip values is illustrated in Fig. 6.4, for the YZ measurement plane. The values of  $Q_r^{ok}$  can be carried on the undeformed sketch of the structure using a graphical scaling factor. The deformed body is sketched using the displaced points, matching the displacements in their respective axes. For the actual analysis, points F'6 to F'9 are also considered.

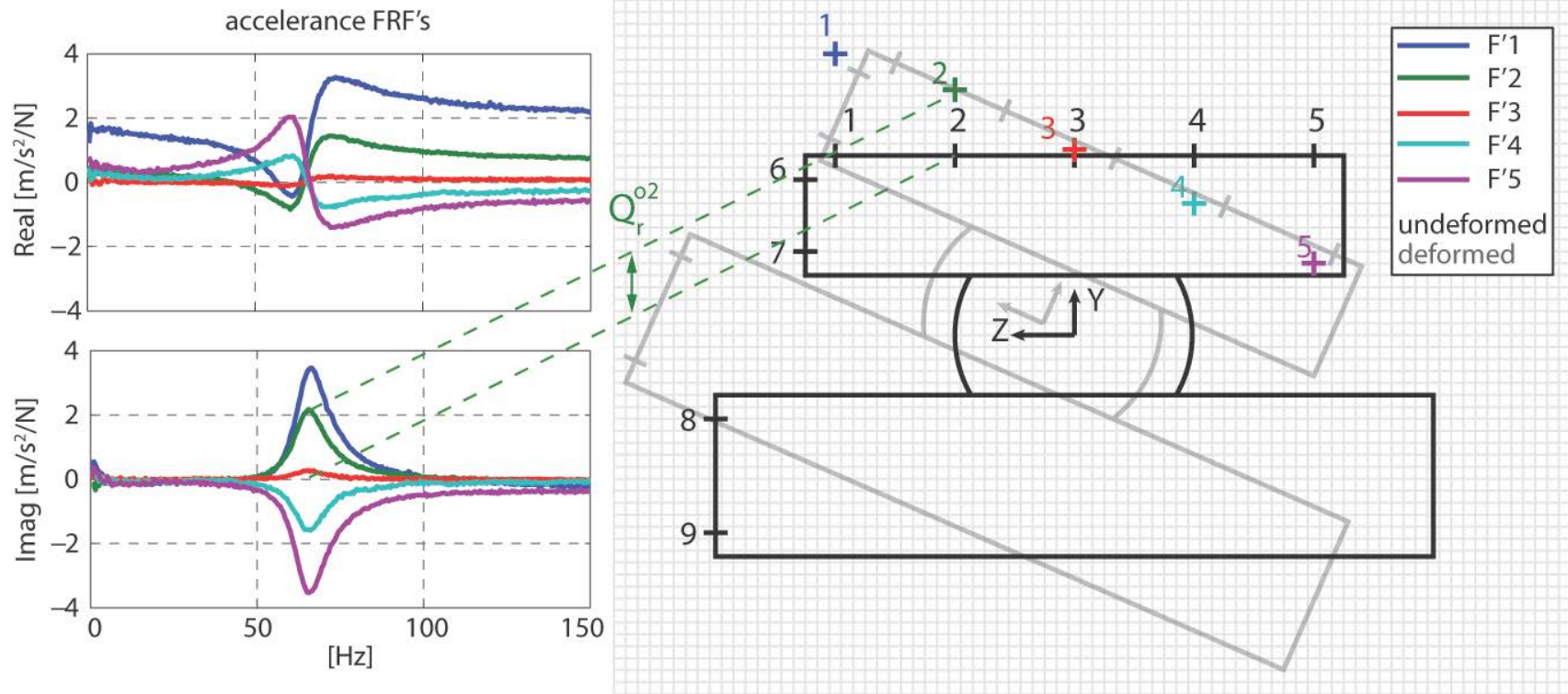


Fig. 6.4 Using imaginary peak/dip values to determine modal displacements.

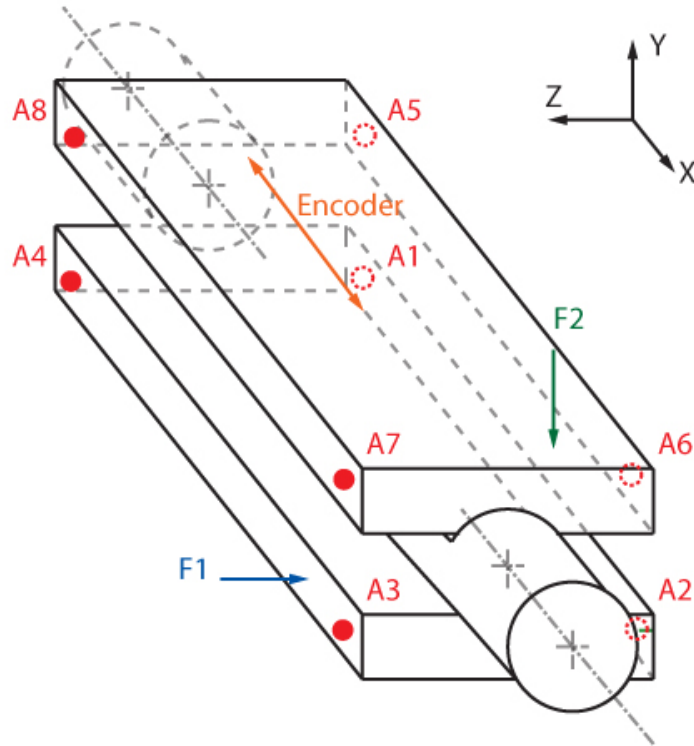


Fig. 6.5 Impact and measurement points for method 2 (software package).

#### 6.4. Using method 2 (software package)

##### 6.4.1. Impact and measurement points

For method 2 (software package), the stage is impacted at the locations  $F1$  and  $F2$ , as shown in Fig. 6.5. FRF's are measured from the 3-axis accelerometer roved through  $A1 - A8$ , which totals to 24 FRF's for each impact point. A related module of Test.Lab® was used to acquire and view the FRF's.

##### 6.4.2. Method of analysis

In method 2, modal identification has been carried out using automated algorithms that have been documented in literature, and implemented inside the commercially available vibration analysis software package. Natural frequencies and damping ratios were identified using the 'PolyMAX' module within LMS Test.Lab®. The proprietary 'PolyMAX' algorithm carries out a similar operation to the commonly used least-squares time domain complex exponential method in the frequency domain [85]. The resulting stabilization diagram is interpreted for natural frequencies and damping ratios. For mode shapes, these identified parameters are used in the least-squares frequency domain (LSFD) [43] algorithm, which finds the best fit to the modal displacement vector based on the agreement between the measured and fitted FRF's. The software package allows either complex or



real mode shapes to be fit. In this thesis, complex mode shapes are enabled to test the proportional damping assumption. Complexity of mode shapes are rated using ‘modal phase collinearity (*MPC*)’ and ‘mean phase deviation (*MPD*)’. *MPC* can be defined as [91],

$$MPC(\psi_r) = \frac{\|Re(\tilde{\psi}_r)\|_2^2 + \frac{1}{\varepsilon_{MPC}} Re(\tilde{\psi}_r^T) Im(\tilde{\psi}_r) (2(\varepsilon_{MPC}^2 + 1) \sin^2(\theta_{MPC}) - 1)}{\|Re(\tilde{\psi}_r)\|_2^2 + \|Im(\tilde{\psi}_r)\|_2^2},$$

$$\tilde{\psi}_r^k = \psi_r^k - \frac{\sum_{k=1}^m \psi_r^k}{m}, \quad \varepsilon_{MPC} = \frac{\|Im(\tilde{\psi}_r)\|_2^2 - \|Re(\tilde{\psi}_r)\|_2^2}{2 Re(\tilde{\psi}_r^T) Im(\tilde{\psi}_r)}, \quad (6.9)$$

$$\theta_{MPC} = \tan^{-1} \left( |\varepsilon_{MPC}| + \text{sign}(\varepsilon_{MPC}) \sqrt{1 + \varepsilon_{MPC}^2} \right).$$

*MPC* is based on a formulation which compares the eigenvalues of the variance - covariance matrix of real and imaginary parts of the complex mode shape to that of a real valued one [83]. *MPC* rates the complexity of the mode on a scale of 100% to 0%. *MPD* can be defined as [91],

$$MPD(\psi_r) = \frac{\sum_{\substack{k=1 \\ |\psi_r^k| > 0}}^m \cos^{-1} \left| \frac{Re(\psi_r^k) V_{22} - Im(\psi_r^k) V_{12}}{\sqrt{V_{12}^2 + V_{22}^2} |\psi_r^k|} \right|}{m},$$

$$MP(\psi_r) = \arg \min_{\theta} \frac{\|Im(\psi_r) - \tan(\theta) Re(\psi_r)\|_2^2}{1 + \tan \theta}, \quad (6.10)$$

$$MP(\psi_r) = \tan^{-1} \left( \frac{-V_{12}}{V_{22}} \right), \quad USV^T = [Re(\psi_r) \quad Im(\psi_r)].$$

Above, *MP* corresponds to the ‘mean phase’, and  $U \in R^{m \times 2}$ ,  $S \in R^{2 \times 2}$ ,  $V \in R^{2 \times 2}$  constitute a singular value decomposition. *MPD* is a measure of how much the phase of each mode shape entry (measurement point) is scattered from being either in-phase or out-of-phase with respect to each other, as in a real valued mode shape. *MPD* rates the complexity of the mode on a scale of 0-90 [deg]. Having a minimum *MPC* of 96.5%, and a maximum *MPD* of 12 [deg], in the set of identified mode shapes, the proportional damping assumption used in method 1 (Section 6.3.1) is observed to be

justifiable. Identified mode shapes have been played as a 3D video, and screenshots of the animated mode shapes are presented in the next section.

### **6.5. Comparative modal testing results and discussion**

Comparative modal testing results from method 1 (peak-picking) and method 2 (LMS Test.Lab®) are presented in Fig. 6.6 for the 0-1000 [Hz] range. Theoretical predictions of the natural frequencies made at the design stage using catalogue values for air bushing / bearing stiffness values are also presented. It is observed that the identified natural frequencies for methods 1 and 2 are rather close, except for a slightly larger deviation for the first mode. Damping ratios are also observed to be close. On the other hand, large discrepancies between the experimentally identified and initially predicted natural frequencies are noticed. This discrepancy is especially critical in the case of the first mode (roll), as the prediction of the first natural frequency is a determining factor for the choice of the control bandwidth. While methods 1 and 2 have predicted 65 [Hz] and 79 [Hz], respectively, the initial theoretical prediction was 672 [Hz]. The roll motion is only constrained by the air bearing, and air bearings are usually not rated for rotational stiffness. For the theoretical calculations, a simple model assuming a distributed stiffness for the air bearing was used. Apparently, the actual rotational stiffness of the air bearing is much lower than calculated, which can be attributed to the distortion of the air cushion in the bearing interface as a result of the out-of-plane rotations. In order to make more accurate predictions, more data on the rotational stiffness of the air bearing has to be collected.

Identified modes 2 (horizontal) and 3 (vertical) also imply deviation of the actual vibratory dynamics from the predicted ones. The fact that natural frequencies measured for these two modes are close suggests symmetry in the actual system in horizontal and vertical directions. On the other hand, such symmetry was not predicted due to the contribution of air bearing stiffness in the vertical direction. The effective normal stiffness of the air bearing also appears to be lower than the catalogue value, which may be due to an excessive gap in the final assembly. The air bearing still provides some stiffness, as evident from the slightly higher natural frequency identified for the vertical mode (mode 3).

Contrary to other modes, the natural frequency identified for mode 4 (pitch) is lower than the theoretical prediction. When the main compliances causing a vibratory mode shape are due to the bearings, mode shapes assume rigid-body motion like patterns, as assumed for the theoretical predictions. However, motions in each degree of freedom (linear and rotational axes) are not totally decoupled as it was assumed. This can be observed in modes 3 and 4, which have motions in both

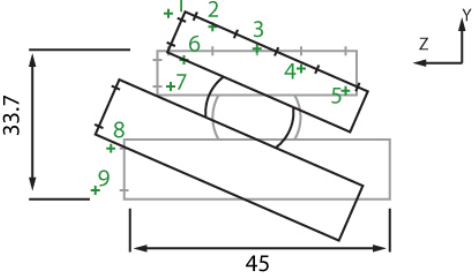
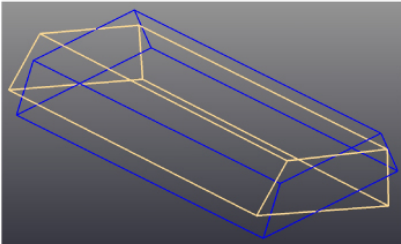
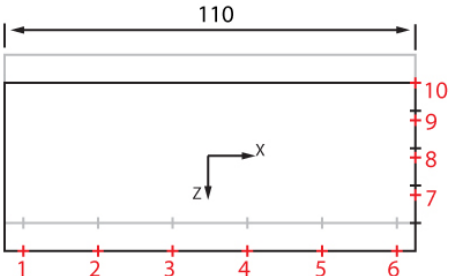
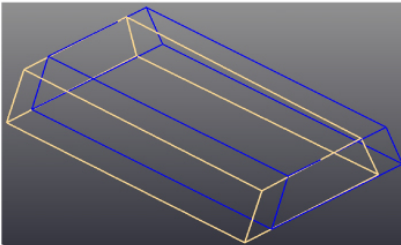
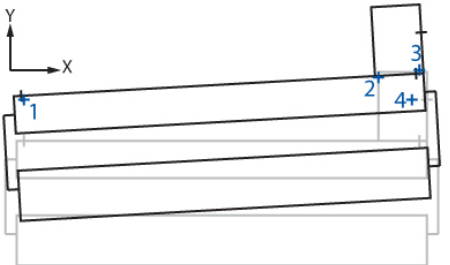
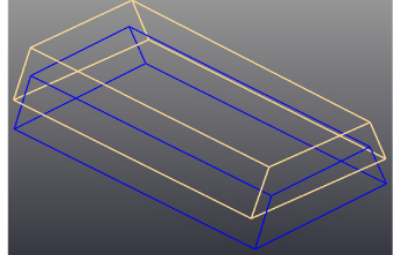
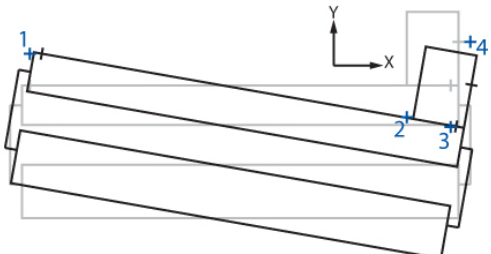
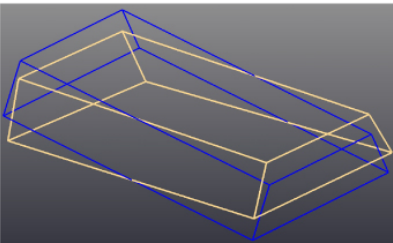
Method 1 - Peak-picking	Method 2 - Software package
Mode 1 (pred. $\omega_1 = 672$ [Hz])	
$\omega_1 = 65$ [Hz], $\zeta_1 = 0.10$	$\omega_1 = 79$ [Hz], $\zeta_1 = 0.11$
	
Mode 2 (pred. $\omega_2 = 940$ [Hz])	
$\omega_2 = 450$ [Hz], $\zeta_2 = 0.14$	$\omega_2 = 435$ [Hz], $\zeta_2 = 0.14$
	
Mode 3 (pred. $\omega_3 = 1248$ [Hz])	
$\omega_3 = 484$ [Hz], $\zeta_3 = 0.24$	$\omega_3 = 475$ [Hz], $\zeta_3 = 0.26$
	
Mode 4 (pred. $\omega_4 = 747$ [Hz])	
$\omega_4 = 960$ [Hz], $\zeta_4 = 0.10$	$\omega_4 = 938$ [Hz], $\zeta_4 = 0.12$
	

Fig. 6.6 Comparative modal testing results from the two methods and theoretical predictions at design stage. Dimensions are in [mm].

vertical and pitch directions. This can be the reason mode 4 attained a lower natural frequency than expected. Also, elastic deformations of the structural components couple with bearing compliances to alter vibratory dynamics. Mainly elastic modes were not identified in the 0 - 2000 [Hz] range, but a dominantly axial elastic mode was identified at 2765 [Hz] using method 1.

For the identification of axial modes in the X direction or modes which have significant displacement components along the stage's direction of sensitivity, measurements that are parallel to the encoder axis are needed. Such modes can also be critical for the position control stability, as they directly enter the control loop through the encoder measurement. In this regard, position readings from the encoder scale evaluated by the DSpace® DS3002 encoder interface board, were fed to CutPRO®'s MalTF interface, as a position measurement, using the DS2102 digital to analog converter. The boards (DS3002, DS2102) ran at sampling frequency of 20 [kHz]. The same impact points in three planes as in method 1 (Fig. 6.1) were used, with the accelerometer replaced by the encoder. Receptances acquired in this way did not yield any vibratory modes in the 0-2000 [Hz] range. Later on, positioning control bandwidth in the X-axis could be increased up to 550 [Hz] without experiencing any interactions with vibratory modes, in line with these results. The bandwidth was only limited by the current carrying capacity of the coil wires and the control command.

## **6.6. Conclusion**

In this chapter, modal testing of the ultraprecision motion stage has been carried out using impact hammer testing. Two independent methods for the analysis of vibratory dynamics are used and the results are compared. Identified natural frequencies are observed to be largely different from theoretical predictions. These discrepancies are attributed to the inaccuracy of certain assumptions used in the theoretical predictions, and also alterations of the system dynamics during assembly. The first natural frequency, which is critical for the selection of control bandwidth during design, was predicted to be 672 [Hz] in the roll direction. However, it is identified as 65 [Hz] and 79 [Hz] by methods 1 and 2, respectively, which indicates that it is much more critical than expected. Hence, the importance of measuring modal characteristics from the actual system is verified. On the other hand, none of the mode shapes identified had significant motions in the direction of the measurement axis. This was also verified by modal tests using the encoder measurement as the position sensor, which did not yield any modes in the 0 - 2000 [Hz] range. Later on, the control bandwidth could be increased up to 550 [Hz] without experiencing stability problems, which further evidenced this.

# Chapter 7

## Laser Interferometric Metrology

### 7.1. Introduction

A machine tool coordinate system and definitions for error motions are presented in Fig. 7.1, according to the ISO 2009 international standard [48]. The moving machine table is intended to move in a straight-line trajectory parallel to the X-axis.

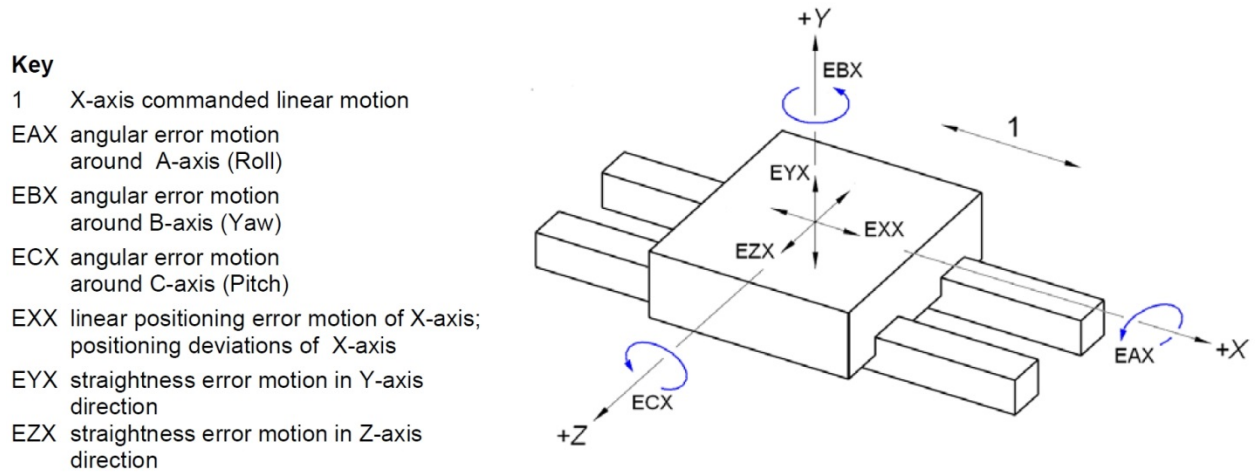


Fig. 7.1 Coordinate system and definitions for error motions of a linear stage [48].

In this chapter, laser interferometric metrology is used to determine each error component related to the developed ultraprecision stage. For each component, a different measurement setup is required. Geometric errors determined this way are combined with servo errors and estimated thermal errors to form the final error budget.

### 7.2. Methodology of measurements

The experimental procedure for obtaining linear positioning error (EXX) values is outlined in ISO 2006 [47], regarding the testing conditions, the number and separation of measurement points, presentation of results, etc. For the remainder of error measurements (EYX, EZX, EBX, ECX), the same procedure has also been applied. The laser interferometer used [89] generates two 90 [deg] phased sinusoidal measurement signals at a rate of two cycles per one wavelength of change in the length of the measurement beam, which are further interpolated using the 12-bit resolution encoder interface (DS3002). Under normal temperature and pressure (NTP), the wavelength of the He-Ne

laser is given by 632.82 [nm], resulting in a measurement resolution of 0.08 [nm]. On the other hand, the effective noise floor measured at static positions is observed to be  $\pm 40$  [nm]. Roll (EAX) measurements are not available, as rotations around the axis of motion cannot be measured with a laser interferometer [96]. Electronic levels used for such measurements are not available in the laboratory inventory. The experimental procedure is described in Section 7.2.1. Laser interferometric measurement setups used to measure different error components are presented in Section 7.2.2. The amplification of angular errors through a moment arm to generate linear errors is referred to as ‘Abbe errors’ in metrology [102]. Calculation of Abbe moment arms and the description of how Abbe errors are subtracted from linear measurements are presented in Section 7.2.3.

## 7.2.1. Experimental procedure

### 7.2.1.1. Measurement target positions

ISO standard [47] requires that a minimum of 5 target positions per meter and an overall minimum of 5 target positions to be selected for machine axes up to 2000 [mm]. In order to obtain very clear and detailed information about the developed stage’s volumetric errors, 18 measurement points were chosen over the stroke length of 20 [mm]. The general form of target positions is given by,

$$P_i = (i - 1)p + r, \quad (7.1)$$

where  $i$  is the index of the target position,  $p$  is the nominal interval, and  $r$  is the additional random component which should be within  $\pm 30\%$  of  $p$ . Using  $p = 1.0$  [mm] and choosing  $r$  within 5% of  $p$ , measurement target positions as shown in Table 7.1 are obtained. For all 5 types of errors measured, the same set of target positions has been used.

Table 7.1 Measurement target positions.

<b>Target index (<math>i</math>)</b>	1	2	3	4	5	6	7	8	9
<b>Target position (<math>P_i</math>) [mm]</b>	1.509	2.508	3.507	4.510	5.548	6.501	7.548	8.501	9.549
<b>Target index (<math>i</math>)</b>	10	11	12	13	14	15	16	17	18
<b>Target position (<math>P_i</math>) [mm]</b>	10.515	11.526	12.543	13.545	14.509	15.533	16.547	17.549	18.505

### 7.2.1.2. Trajectory used in the measurements

A smooth trajectory has been used for the translations between the measurement points. Feed, acceleration, and jerk limits of the trajectory are presented in Table 7.2. While approaching the first

point ( $i=1$ ) in the forward direction and the last point ( $i=18$ ) in the backward direction, the set of parameters for ‘Approach’ are used. In between, for positioning across the measurement points, ‘Measurement’ parameters are used. The stage rests for 2.0 [s] at each measurement point. This duration ensures that all dynamic transients have settled and the true positioning response can be viewed. A plot of the trajectory is presented in Fig. 7.2. When extracting data for measurement results, the measurement average of the 1.0 - 1.8 [s] portion of each rest period has been used.

Table 7.2 Feed, acceleration, and jerk limits of the measurement trajectory.

Case	Feed (F) [mm/s]	Acceleration (A) [mm/s <sup>2</sup> ]	Jerk (J) [mm/s <sup>3</sup> ]
Approach	1	2.5	75
Measurement	2	5	150

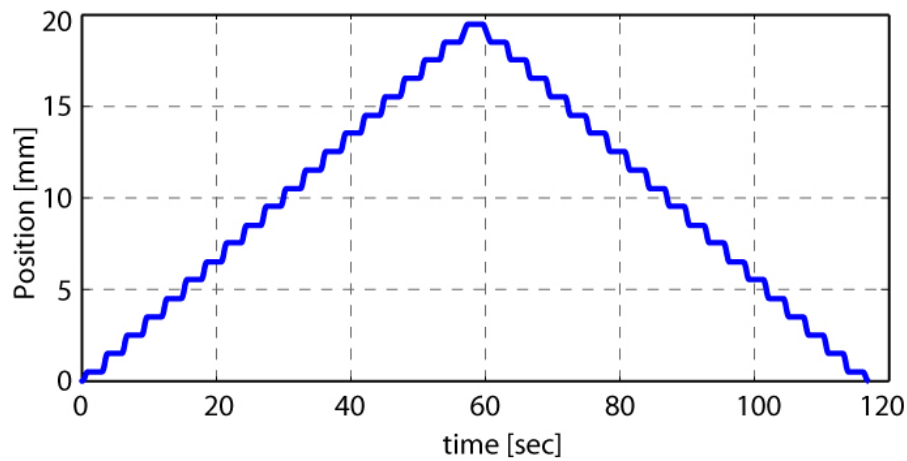


Fig. 7.2 Measurement trajectory.

### 7.2.1.3. Test environment and laser wavelength

Laser interferometric measurements are sensitive to changes in the ambient pressure, temperature and relative humidity, as these alter the light wavelength (and thus the laser beam). Ambient temperature and relative humidity are monitored using a data logger that is hung close to the experimental setup. Pressure readings are used from the U. Waterloo weather station, updated every 15 min. A 4 [mbar] uncertainty in the air pressure measurement results in a 1 [ppm] uncertainty in the refractive index of air, hence in the measured error [78]. As this uncertainty range is much lower than the uncertainties associated with the laser beam alignment and the air turbulence, the difference of the indoors air pressure from the atmospheric pressure is neglected. Vacuum values for wavelength of the laser are used as specified by the manufacturer [89]. Laser wavelengths used in the extraction of measurement results are calculated using the online tool provided by the National Institute of Standards and

Technology (NIST), which applies the Edlen equation [78]. The tested machine has to be immersed in the laboratory conditions for extended periods before the tests, in order for thermal equilibrium to be reached [47]. As the ultraprecision stage and measurement instrumentation were always kept in the laboratory, tests were initiated directly.

### 7.2.2. Experimental setups

For the investigation of each error component, a different setup with a different arrangement of optical elements is required. These will be briefly described in this section. Alignment of the laser beam to the measurement optics is done by monitoring the return beam intensity indicator lamp of the Renishaw® RLU10 system, as described in the manufacturer's guidelines [89]. The measurement optical instruments are mounted on the nano-positioner using special brackets manufactured for this purpose. Descriptions of each setup are presented in the following sections, and their photographs are presented in Appendix F. The photographs were shot at a different location in the laboratory than the initial location of the experiments, but they represent the same configuration.

#### 7.2.2.1. EXX setup

The laser interferometer setup used in EXX measurement is presented in Fig. 7.3. In this setup, the reference arm of the output laser beam travels inside the prisms built into the laser head (shown as a separate component in the drawing). Motion of the nano-positioner is detected using the varying fringe patterns formed at the interference point. The plane of actual laser beams is rotated 90 [deg] about the axis of motion in the figure for a simpler representation.

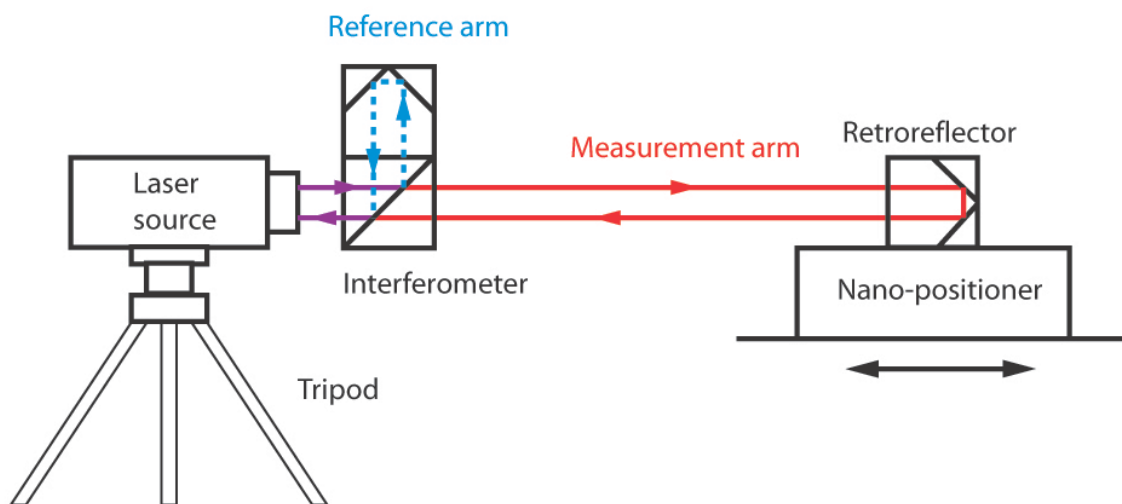


Fig. 7.3 EXX experimental setup.



### 7.2.2.2. EYX and EZX setup

The setup used in EYX and EZX measurements is presented in Fig. 7.4. The diagram presents the case for EYX measurements. For EZX measurements, the straightness retroreflector is rotated 90 [deg] about the motion axis. Due to the special shape of the retroreflector prism, Y (in EYX setup) or Z (in EZX setup) direction motions result in the elongation of one arm of the beam and the shortening of the other. As a result, variations in the fringe patterns at the interference point are observed. The difference of length between the laser arms ( $\delta_l$ ) becomes,

$$\delta_l = 4d = 4S \sin \theta, \quad (7.2)$$

where  $\theta=22.5$  [mrad] is a fixed parameter of the Wollaston prism. In the case of this thesis, Wollaston prism is the vertically displacing part instead of the retroreflector, but the relationship in Eq. (7.2) is still valid [90].

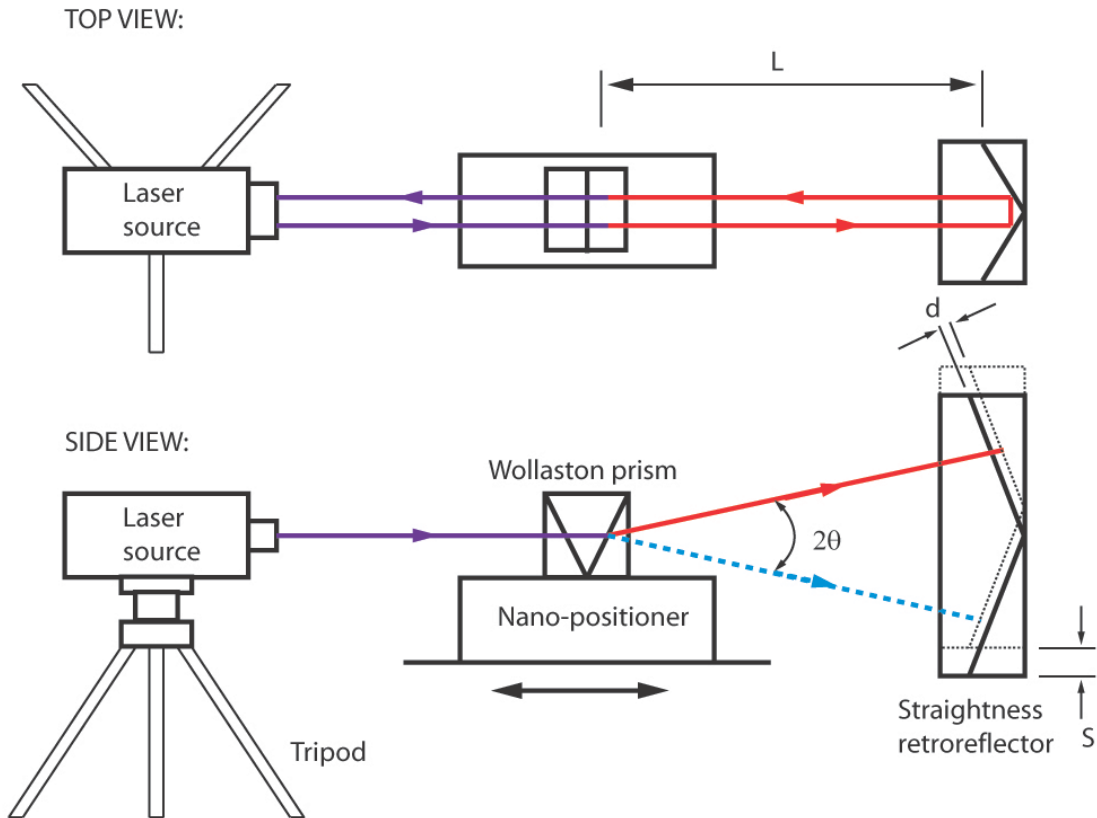


Fig. 7.4 EYX and EZX experimental setup.

### 7.2.2.3. EBX and ECX setup

The setup used in EBX and ECX measurements is presented in Fig. 7.5. The diagram depicts the case for pitch (ECX) measurements. For EBX, the angular interferometer and retroreflector have to be rotated 90 [deg] about the axis of motion. Rotation of the retroreflector can be related to the difference of the length of the laser arms ( $\delta_l$ ) as,

$$\theta = \sin^{-1}\left(\frac{\delta_l}{2h}\right), \quad \delta_l = 2d. \quad (7.3)$$

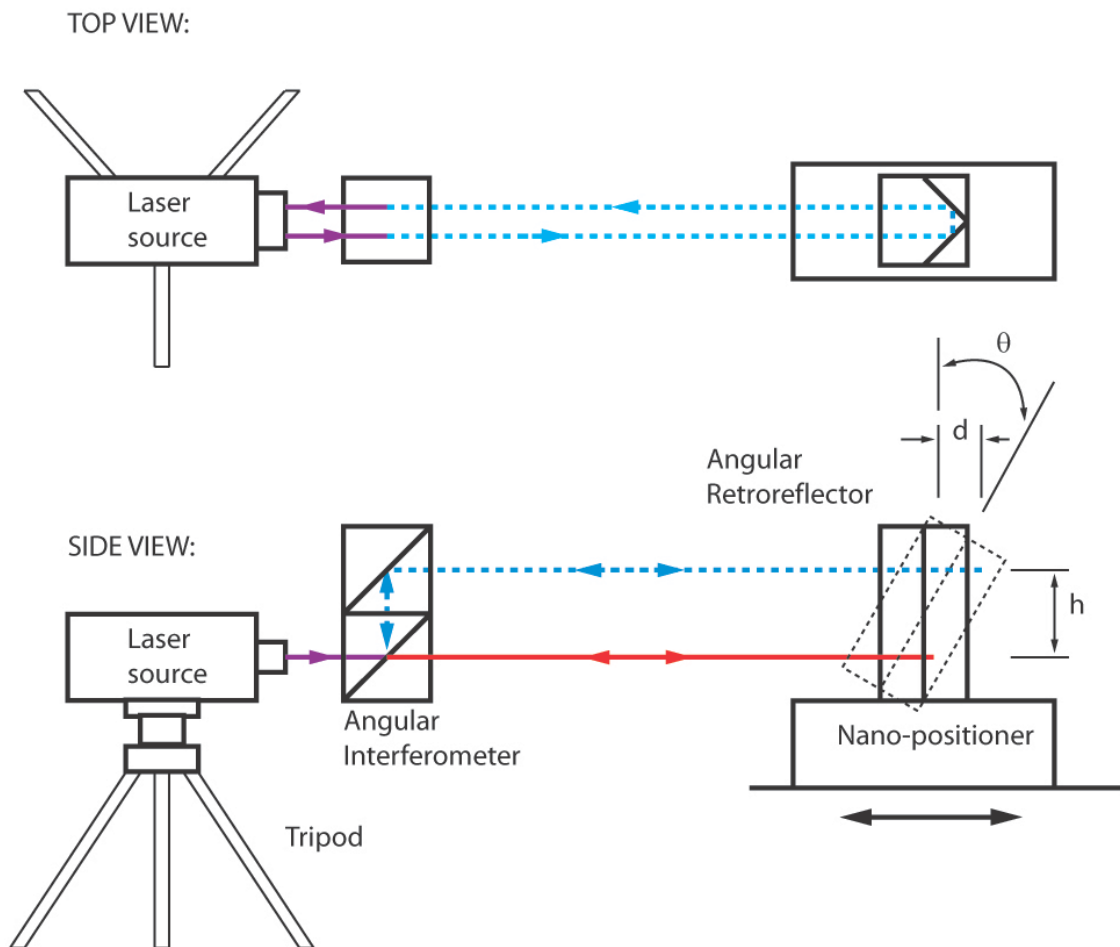


Fig. 7.5 EBX and ECX experimental setup.

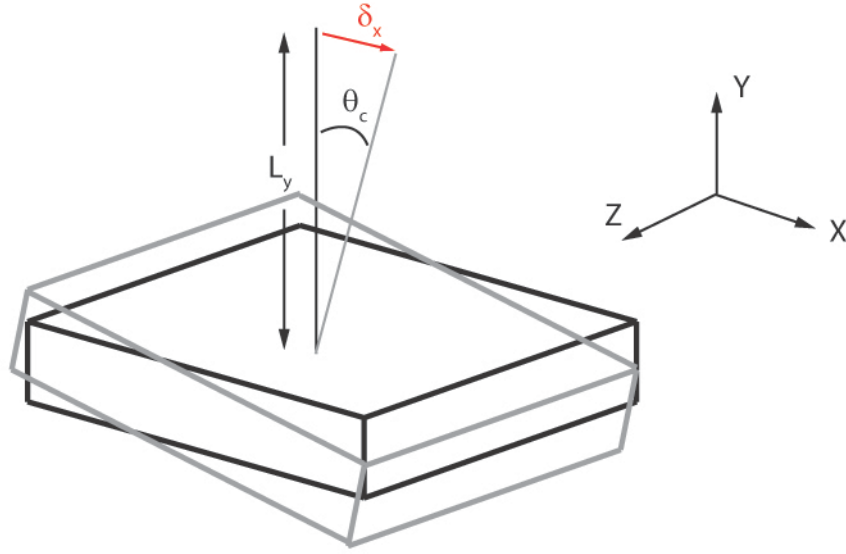


Fig. 7.6 Formation of Abbe errors.

### 7.2.3. Abbe errors

Abbe errors occur in linear axes due to motions in rotational axes, in the presence of a moment arm. Formation of Abbe errors is illustrated in Fig. 7.6. In the figure, the angular motion in the pitch axis represented by  $\theta_c$ , causes a linear deviation in X ( $\delta_x$ ), due to the vertical moment arm  $L_y$ , which can be expressed by  $\delta_x = L_y \theta_c$ . Linear errors in each axis can be expressed in terms of angular deviations and the 3-D rotation matrix simplified for small angular deviations as [54],

$$\begin{Bmatrix} \delta_x \\ \delta_y \\ \delta_z \end{Bmatrix} = \begin{bmatrix} 0 & -\theta_c & \theta_b \\ \theta_c & 0 & -\theta_a \\ -\theta_b & \theta_a & 0 \end{bmatrix} \begin{bmatrix} L_x \\ L_y \\ L_z \end{bmatrix}, \quad (7.4)$$

where  $\delta_{x,y,z}$  are linear errors,  $\theta_{a,b,c}$  are angular deviations in each rotation axis, and  $L_{x,y,z}$  are moment arms. The estimation of moment arms when compensating for Abbe errors is a source of uncertainty. The length of the moment arm can change along the axis of travel, due to varying centers of rotation. This effect is neglected for the case of this thesis. The estimation of moment arms for each linear measurement can be summarized as follows:

- i. For EXX,  $L_y$  is measured from the location of the position sensor. When there is no servo error, this estimation is actually exact, as the servo compensates for the rest of the errors. A

drawing of the relative position of the measurement optics to the linear encoder is presented in Fig. 7.7a.

- ii. For EYX and EZX, center of rotation is assumed to coincide with the center of mass of the stage, as the stage structure and the location of bearings are mostly symmetric. The drawing for this cases in which the measurement optics is the Wollaston prism, is depicted in Fig. 7.7b.

Moment arm estimations are summarized in Table 7.3.

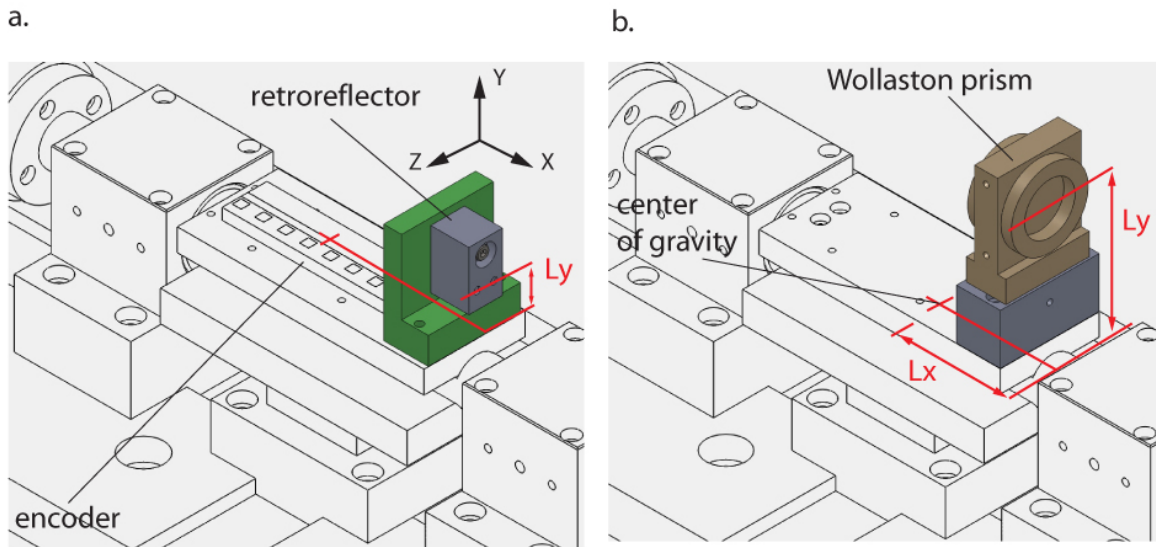


Fig. 7.7 Determination of Abbe moment arm lengths; a. EXX, b. EYX and EZX.

Table 7.3 Values of Abbe moment arms.

Linear deviation	$L_x$ [mm]	$L_y$ [mm]	$L_z$ [mm]
EXX	-	18.5	0
EYX	45.5	-	0
EZX	45.5	68.8	-

### 7.3. Metrology results

Metrology results in EXX are presented according to [47]. Other results (EYX, EZX, EAX, EBX, ECX) are presented in a similar fashion, although there is no mention of a preferred format for presenting this data in the standards. The experimental results in tabular format as suggested in [47] are given in Appendix E. In this section, only the last few summarizing rows are presented. Error plots are presented in Fig. 7.8 to Fig. 7.12. In the figures, measured deviations obtained for each of

the 18 positions, in 5 subsequent passes in both directions (forward and backward) ( $d_{ij} \updownarrow$ ), are represented by dots. The first three parameters plotted are forward ( $\bar{d} \uparrow$ ), backward ( $\bar{d} \downarrow$ ), and bidirectional ( $\bar{d}$ ) mean positional deviations [47], which can be expressed as:

$$\begin{aligned}\bar{d}_i \uparrow &= \frac{1}{n} \sum_{j=1}^n d_{ij} \uparrow, \\ \bar{d}_i \downarrow &= \frac{1}{n} \sum_{j=1}^n d_{ij} \downarrow, \\ \bar{d}_i &= \frac{\bar{d}_i \uparrow + \bar{d}_i \downarrow}{2},\end{aligned}\tag{6}$$

where  $i = 1 \dots 18$  is the index of measurement positions,  $j = 1 \dots 5$  is the index of pass, and  $d_{ij} \updownarrow$  are the deviations measured. In the case of the nano-positioner, the geometric errors in forward and backward directions are not expected to be different as the system is free from effects like backlash. On the other hand, the procedure suggested in the standard [47] is still applied. The estimator of standard uncertainty in forward direction ( $\uparrow$ ) is found as,

$$s_i \uparrow = \sqrt{\frac{1}{n-1} \sum_{j=1}^n (d_{ij} \uparrow - \bar{d}_i \uparrow)^2},\tag{7}$$

where the backward direction ( $\downarrow$ ) version is found by replacing ( $\uparrow$ ) by ( $\downarrow$ ). Parameters  $\bar{d} \uparrow \pm 2s \uparrow$  and  $\bar{d} \downarrow \pm 2s \downarrow$  are also plotted. Calculation of the accuracy and the related parameters are done according to [47], as presented in Appendix D. For the vertical and horizontal straightness errors (EYX and EZX), deviations are presented as normalized by the least-squares best fit line to the measurement data, as suggested in [107]. Results have the Abbe error subtracted, using mean bidirectional angular deviations ( $\bar{\alpha}$ ) and moment arms presented in Table 7.3. Later on, when the geometric errors for the point of interest are calculated, angular error contributions are added back to the linear errors, using the respective moment arms for that point.

### 7.3.1. EXX results

EXX plots are presented in Fig. 7.8. Accuracy results are presented in Table 7.4. The important feature that can be observed in the EXX plot is that the mean bidirectional positional deviation ( $\bar{d}$ ) does not start from zero. This is due to the ordered negative trend of forward and backward positional

deviations measured through the five measurement passes, which can be verified from the plot and also from Table E.1. Temperature measurements from the surface of the top plate of the motion stage were taken, but no significant change during the course of the measurement process was observed. Also, within the course of 10 minutes required to complete the measurement sequence, such a significant change in the system is not anticipated. As the error value does not return to its initial value at the beginning, this error cannot be due to erroneous laser wavelength or encoder signal period entered to the incremental encoder interface board. Additional measurements were taken, which sometimes had a similar trend, but sometimes did not. A possible reason for this error can be the mechanical relaxation of the tripod stage, causing a distortion of the laser alignment.

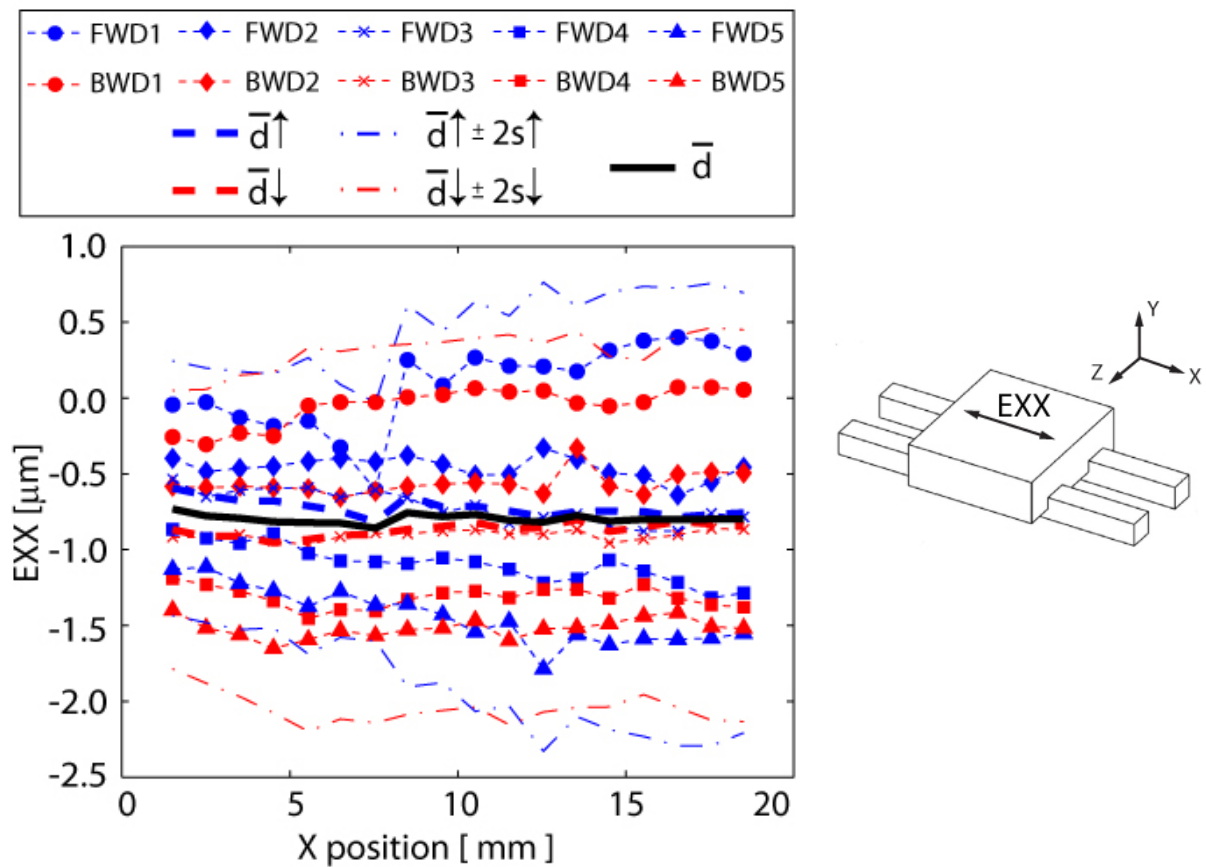


Fig. 7.8 EXX plots with the Abbe errors subtracted.

Table 7.4 EXX summary.

Axis deviation [ $\mu\text{m}$ ]	Unidirectional ↓	Unidirectional ↑	Bidirectional
Reversal value $B$	Not Applicable	Not Applicable	0.3
Mean reversal value $\bar{B}$	Not Applicable	Not Applicable	-0.1
Range mean bidirectional positional deviation $M$	Not Applicable	Not Applicable	0.1
Systematic positional deviation $E$	0.2	0.2	0.4
Repeatability of positioning $R$	2.6	3.1	3.1
Accuracy $A$	2.7	3.1	3.1

### 7.3.2. EYX results

EYX plots are presented in Fig. 7.9. Accuracy results are summarized in Table 7.5. The EYX error has much better repeatability compared to the EXX error. In the EXX error, the measurement arm of the laser is inside the laser head, and does not travel in air (Fig. 7.3). In the case of EYX and EZX setup (Fig. 7.4), both laser beams travel in air and then interfere at the return point. The improvement in repeatability may be due to the cancellation of random changes in laser beam alignment across the beams. The bidirectional mean deviation measured has a very linear trend with respect to the position of the motion stage. This can be due to the motion stage being mounted with a small angle with respect to the floor or the granite table, causing a proportional elevation of the point of interest during motion. The alignment of the Renishaw® RLU10 system is done based on the level of intensity at the interference point, according to manufacturer's recommendations [89]. The standard [47] predicts up to 15 [ $\mu\text{m}$ ] uncertainty in distance measurement for a motion range of 20 [mm], in such a case. This is mainly due to the stroke length being too small, and not allowing angular misalignment to be sufficiently noticed by translating the axis back and forth.

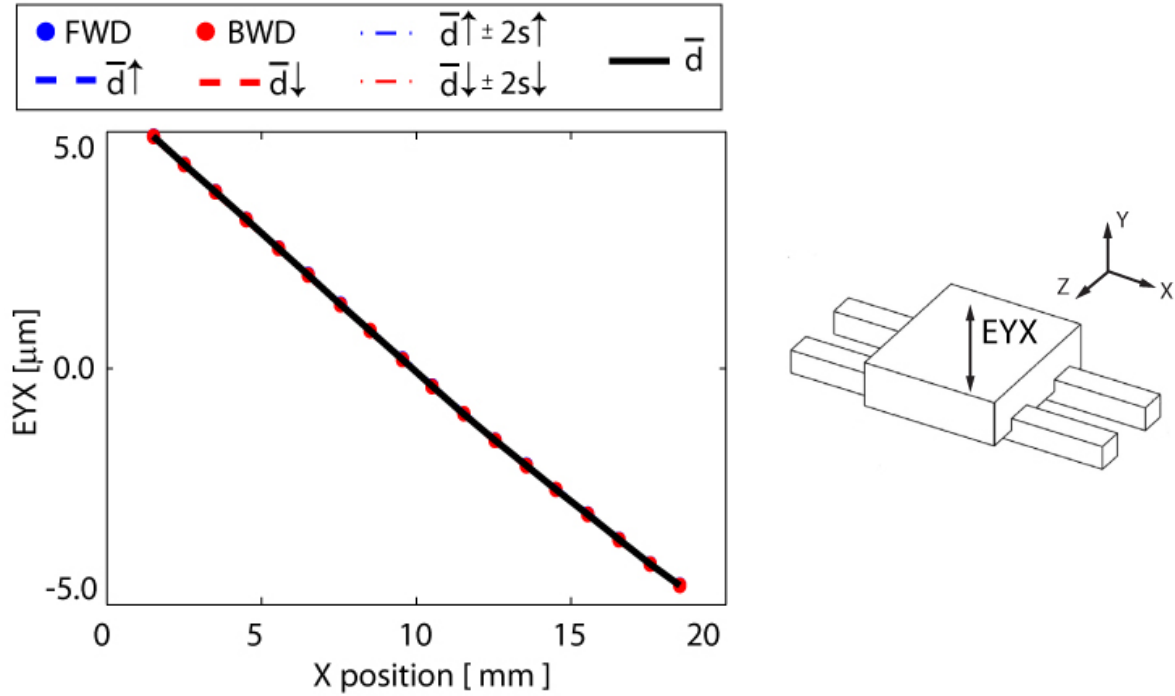


Fig. 7.9 EYX plots with the Abbe errors subtracted.

Table 7.5 EYX summary.

Axis deviation [μm]	Unidirectional ↓	Unidirectional ↑	Bidirectional
Reversal value $B$	Not Applicable	Not Applicable	0.003
Mean reversal value $\bar{B}$	Not Applicable	Not Applicable	-0.002
Range mean bidirectional positional deviation $M$	Not Applicable	Not Applicable	9.5
Systematic positional deviation $E$	9.5	9.5	9.5
Repeatability of positioning $R$	0.011	0.014	0.014
Accuracy $A$	9.5	9.5	9.5

### 7.3.3. EZX results

EZX plots are presented in Fig. 7.10. Accuracy results are summarized in Table 7.6. Like discussed in the EYX case, the EZX case also seems to have considerable measurement uncertainty due to misalignment. Both EYX and EZX measurements are used in the error budget as they are, nevertheless.



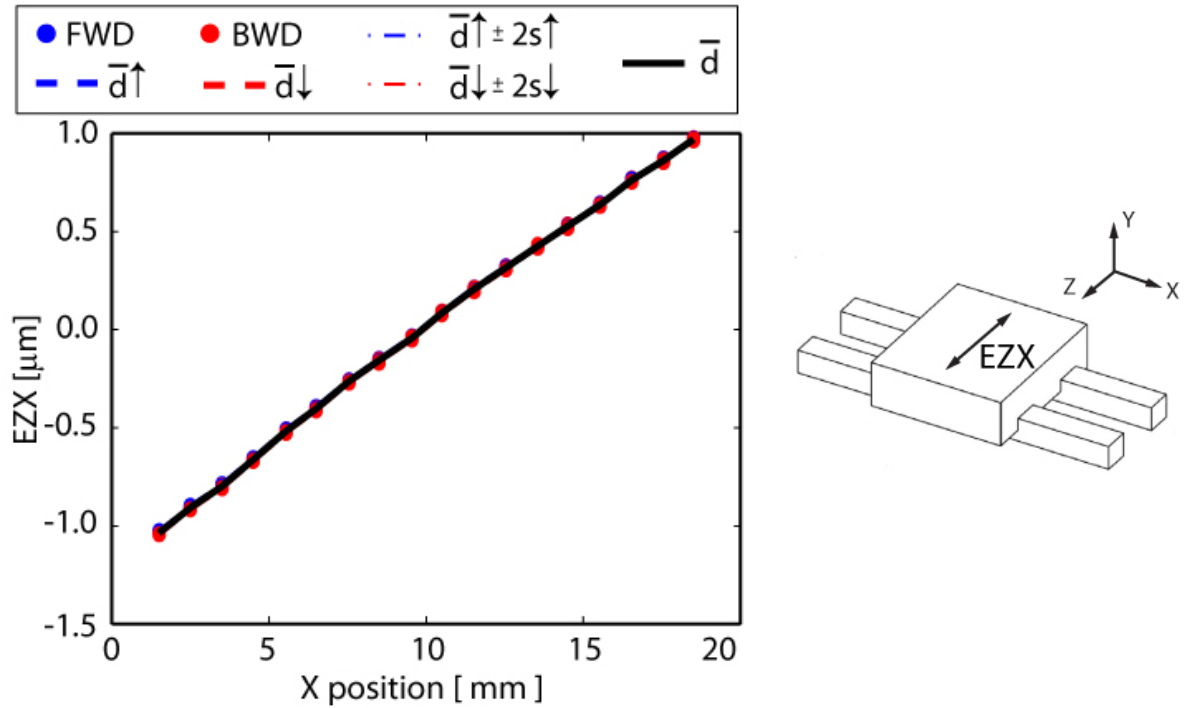


Fig. 7.10 EZX plots with the Abbe errors subtracted.

Table 7.6 EZX summary.

Axis deviation [μm]	Unidirectional ↓	Unidirectional ↑	Bidirectional
Reversal value $B$	Not Applicable	Not Applicable	0.004
Mean reversal value $\bar{B}$	Not Applicable	Not Applicable	-0.002
Range mean bidirectional positional deviation $M$	Not Applicable	Not Applicable	2.0
Systematic positional deviation $E$	2.0	2.0	2.0
Repeatability of positioning $R$	0.028	0.029	0.031
Accuracy $A$	2.0	2.0	2.0

#### 7.3.4. EBX results

EBX plots are presented in Fig. 7.11. Accuracy results are summarized in Table 7.7. The repeatability of positioning has similar values for the angular measurements EBX and ECX (Table 7.7 and Table 7.8), possibly due to being exposed to similar disturbances due to the positioning stage or the measurement procedure. Bidirectional yaw accuracy is  $A = 7.2$  [μrad], with unrepeatability errors constituting a significant portion of it ( $R = 3.4$  [μrad]).

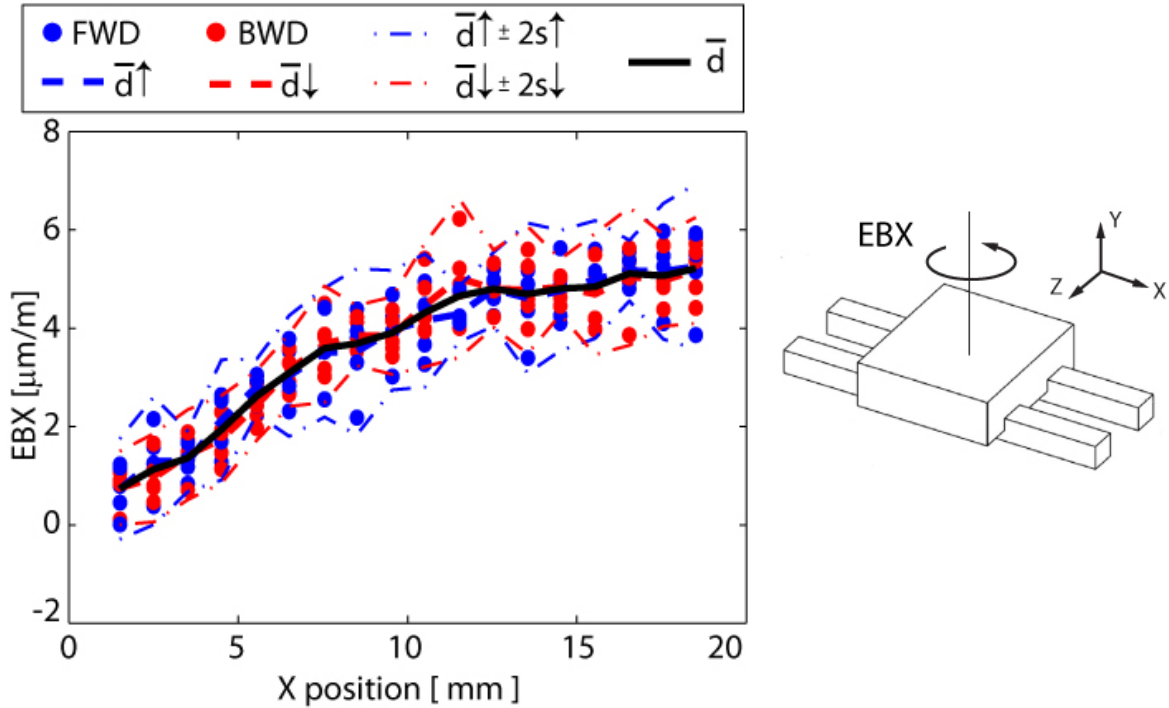


Fig. 7.11 EBX plots.

Table 7.7 EBX summary.

Axis deviation [ $\mu\text{m}/\text{m}$ ]	Unidirectional $\downarrow$	Unidirectional $\uparrow$	Bidirectional
Reversal value $B$	Not Applicable	Not Applicable	0.7
Mean reversal value $\bar{B}$	Not Applicable	Not Applicable	0.0
Range mean bidirectional positional deviation $M$	Not Applicable	Not Applicable	4.4
Systematic positional deviation $E$	4.4	4.5	4.5
Repeatability of positioning $R$	3.2	3.4	3.4
Accuracy $A$	6.6	7.2	7.2

### 7.3.5. ECX results

ECX plots are presented in Fig. 7.12. Accuracy results are summarized in Table 7.8. The pitch error (ECX) has a linear variation with respect to the position of the motion stage. The error measured is much higher than the one measured for yaw (EBX). The pitch error might be due to a curvature in the main shaft introduced during the machining of the flat surfaces which are used for mounting the top and bottom plates. It might have also formed during the assembly of the moving body.

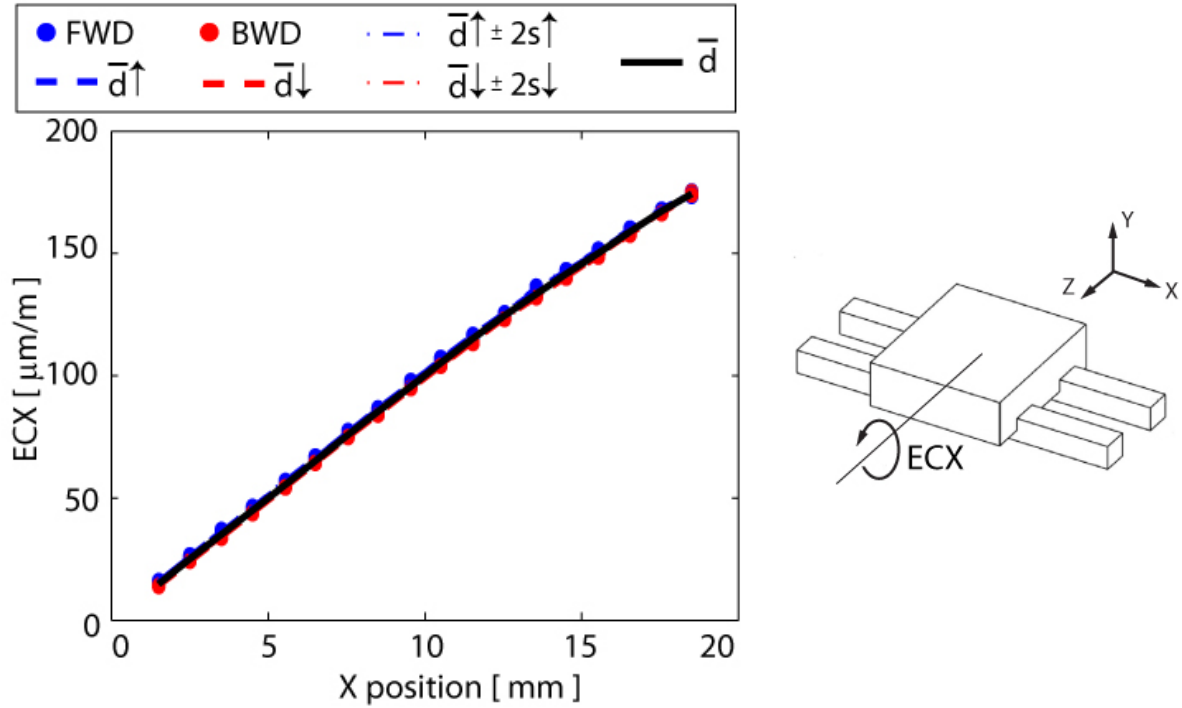


Fig. 7.12 ECX plots.

Table 7.8 ECX summary.

Axis deviation [ $\mu\text{m}/\text{m}$ ]	Unidirectional $\downarrow$	Unidirectional $\uparrow$	Bidirectional
Reversal value $B$	Not Applicable	Not Applicable	2
Mean reversal value $\bar{B}$	Not Applicable	Not Applicable	-1
Range mean bidirectional positional deviation $M$	Not Applicable	Not Applicable	160
Systematic positional deviation $E$	160	160	160
Repeatability of positioning $R$	3	5	5
Accuracy $A$	162	162	163

#### 7.4. Error budget

An error budget is a detailed breakdown of sources of errors in the positioning of a precision machine tool which enables design choices to be evaluated quantitatively by their respective influence on the accuracy. Different aspects of the concept of error budget have been studied in [98][102][110], however, there is no single established way of compiling error budgets.

### 7.4.1. Geometric components

The summary of geometric accuracies from error measurements is presented in Table 7.9. The repeatable portion of errors can be mapped and loaded into the position controller. The controller can compensate for these by shifting the position commands. Compensation of all the repeatable errors requires at least 5-axes to be controllable in the machine tool. Therefore, the linear positioner described in this thesis has to be coupled with actuators in the remaining 4 axes for such a scenario. Compensated accuracies assuming such ideal conditions using the mean bidirectional deviation ( $\bar{d}$ ) as the correction on the measured data are presented in Table 7.9.

Table 7.9 Summary of geometric accuracies.

Component	Accuracy		Units
	Uncompensated	Compensated	
Linear positioning (EXX)	3.1	3.1	[ $\mu\text{m}$ ]
Vertical straightness (EYX)	9.5	0.0	[ $\mu\text{m}$ ]
Horizontal straightness (EZX)	2.0	0.0	[ $\mu\text{m}$ ]
Yaw (EBX)	7.2	3.8	[ $\mu\text{m}/\text{m}$ ]
Pitch (ECX)	163	6.0	[ $\mu\text{m}/\text{m}$ ]

### 7.4.2. Thermal components

Thermal errors can be a major setback in trying to achieve high positioning accuracy in ultraprecision motion stages. Temperature variations cause thermal expansion and contraction of various components, which alters the geometric position of the point of interest. In this section, an analysis is presented which aims to take into account the major effects that would contribute to positioning errors due to thermal variations. The estimations can be used to judge the overall magnitude of thermal errors, but the results need to be verified in experiments. In Section 7.4.2.1, dimensional changes of components with respect to temperature variations is studied and resultant sensitivities of each linear axis are calculated. In Section 7.4.2.2, sources of heat are identified, and the range of temperature variations of the motion stage due to each of them is determined. The resulting positioning thermal errors are presented in Section 7.4.2.3.

#### 7.4.2.1. Thermal sensitivities

The linear nano-positioner moving body is made up of aluminum, steel, permanent magnet material, and encoder glass. A schematic diagram of the moving body of the positioning stage is presented in Fig. 7.13.

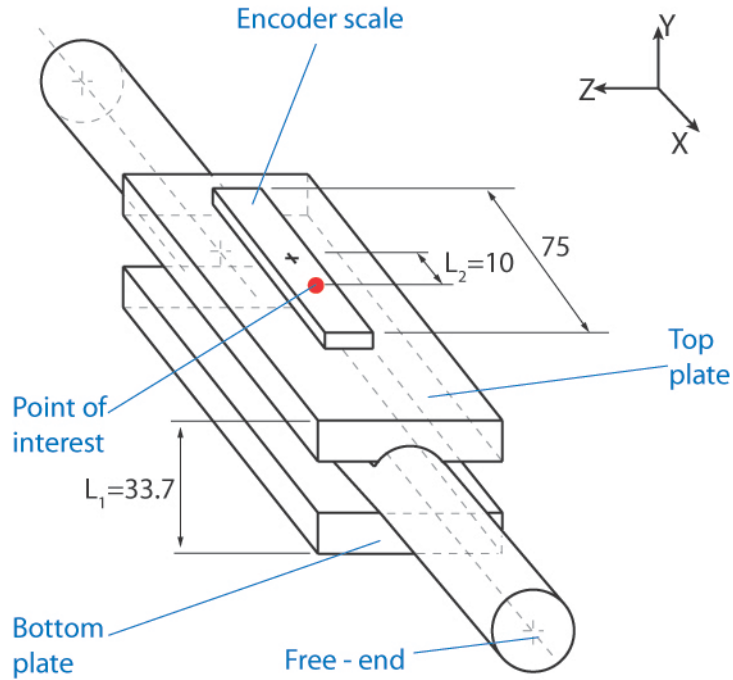


Fig. 7.13 Schematic diagram of the positioning stage. Dimensions in [mm].

The point of interest is defined at the center of the upper surface of the top plate as shown. The point of interest is sensitive to the following thermal disturbances:

- Along the Y-axis, thermal expansion of the stage would push the point of interest upwards by

$$\delta_y = \frac{\alpha_{al} \cdot L_1 \cdot \Delta T}{2}, \quad (7.5)$$

where  $\alpha_{al}$  is the coefficient of thermal expansion of Aluminum 6061,  $L_1$  is the thickness of the stage, and  $\Delta T$  is the temperature variation. If the moving body was only constrained by the air bearing at the bottom, the thermal expansion would be  $\delta_y = \alpha_{al} \cdot L_1 \cdot \Delta T$ . As the air bushings are expected to counteract this,  $L_1/2$  is used to approximate the equilibrium position.

- In the case of thermal expansion along the X axis, combined effect of the expansion of the encoder scale and the top plate needs to be considered. If the encoder scale is thought of as fixed at its center to the top plate, the deviation in X-positioning would be represented by

$$\delta_x = (\alpha_{al} - \alpha_{enc}) \cdot L_2 \cdot \Delta T, \quad (7.6)$$

where  $\alpha_{enc}$  is the coefficient of thermal expansion of the glass encoder scale specified by the manufacturer [28]. On the other hand, the encoder scale is held by clamps which do not exert a significant pressure on the scale and the scale can be thought of as decoupled from the top plate. In that case, X-axis positioning error needs to be revised as,

$$\delta_x = \alpha_{al} \cdot L_2 \cdot \Delta T, \quad (7.7)$$

which corresponds to a worse scenario due to  $\alpha_{al} > (\alpha_{al} - \alpha_{enc})$ .

- Thermal expansion along the Z axis does not affect the point of interest.

The thermal sensitivity in X and Y axes can be defined as,

$$\gamma_x = \frac{\delta_x}{\Delta T} = \alpha_{al} \cdot L_2, \quad \gamma_y = \frac{\delta_y}{\Delta T} = \frac{\alpha_{al} \cdot L_1}{2}. \quad (7.8)$$

The total linear thermal sensitivity of positioning can be expressed in root-mean-square as,

$$\gamma_T = \sqrt{\gamma_x^2 + \gamma_y^2}. \quad (7.9)$$

Values of the thermal sensitivities and parameters used in calculations are summarized in Table 7.10.

Table 7.10 Thermal sensitivities and parameters used in calculating them.

Quantity	Symbol	Value
Thermal expansion coefficient of Aluminum 6061	$\alpha_{al}$	23.5 [ppm/K]
Thermal expansion coefficient of the glass encoder scale	$\alpha_{enc}$	8 [ppm/K]
Thickness of the moving body	$L_1$	33.7 [mm]
Distance between the center of the top plate and the encoder scale	$L_2$	10 [mm]
Thermal sensitivity along the X-axis	$\gamma_x$	235 [nm/K]
Thermal sensitivity along the Y-axis	$\gamma_y$	396 [nm/K]
Total positioning thermal sensitivity	$\gamma_T$	460 [nm/K]

#### 7.4.2.2. Sources of thermal disturbance

The main sources of thermal disturbances identified in this thesis are heat dissipation from the VCA coils and the changes in the temperature of the ambient air. As the air bushings/bearings have near zero friction, heating due to friction is not considered.

##### *VCA thermal dissipation*

When the voice coil actuators (VCA) are operated at their current limit (0.58 [A]) each dissipate 1.19 [W] through the 3.57 [ $\Omega$ ] coil resistance (Table 4.3). The resulting thermal gradients of the moving body can be calculated using COMSOL® FEA. In this regard, first, the coefficients of convective heat transfer from the surfaces of the moving body need to be calculated. Heat transfer surfaces of the moving body are shown in Fig. 7.14. Surfaces 1 - 4 correspond to natural convective heat transfer surfaces. Surface 5 is the interface of the shaft and the air bushing, and corresponds to a forced convection surface [13].

Calculation of convective coefficient of heat transfer for Surfaces 1-4 is summarized in Table 7.11. Definitions of the symbols are provided in Table 7.12. The ambient temperature is taken as  $T_{\infty}=20$  [°C]. A temperature rise of 0.6 [°C] of the convective surfaces is assumed, and the properties of air at 1 [atm], at the film temperature  $T_f = 20.3$  [°C] are evaluated from tables [13] as presented in Table 7.13.

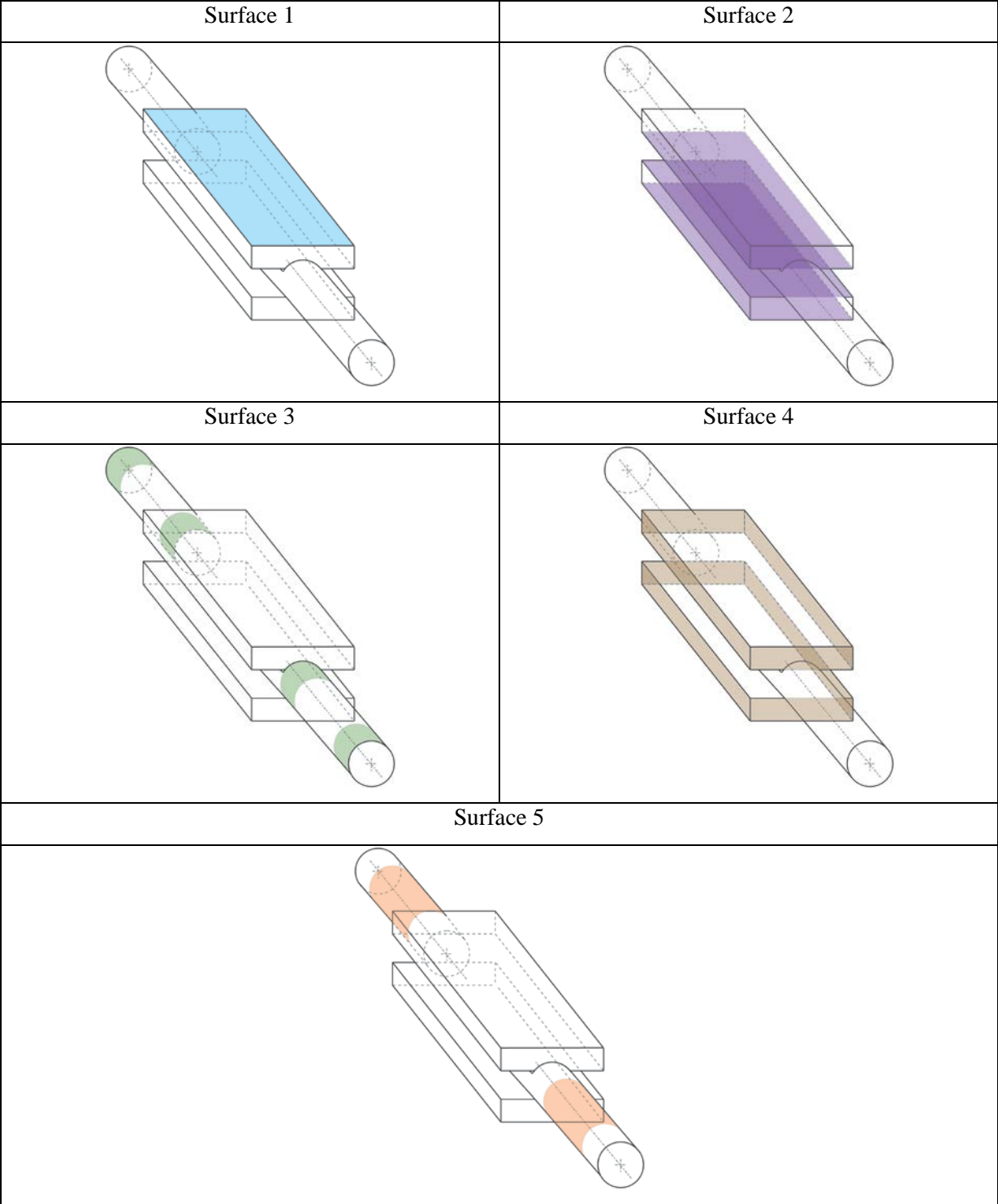


Fig. 7.14 Heat transfer surfaces.



Table 7.11 Calculation of coefficients of convective heat transfer for Surfaces 1-4.

Surface	Type	Characteristic length ( $L_c$ ) [mm]	Rayleigh number ( $Ra$ )	Nusselt number (Nu)	Convective coefficient of heat transfer (h) [W/m <sup>2</sup> .K]
1	Upper surface of horizontal plate	$L_c = \frac{A_s}{p}$	257.8 $Ra = \frac{g\beta(T_s - T_\infty)L_c^3 Pr}{\nu^2}$ (same formula for each) $\beta = 1/T_f$ [1/K], $T_f = (T_s + T_\infty)/2$	2.164 $Nu = 0.54 Ra_L^{1/4}$ (formula for $10^4 < Ra_L < 10^7$ , used as an approximation)	3.413 $h = \frac{kNu}{L_c}$ (same formula for each)
2	Lower surface of horizontal plate	$L_c = \frac{A_s}{p}$	463.1	1.252 $Nu = 0.54 Ra_L^{1/4}$ (formula for $10^5 < Ra_L < 10^{11}$ , used as an approximation)	1.625 (calculated for the lower surface of the bottom plate, used for the whole surface category)
3	Horizontal cylinder	$L_c = D$	506.5	2.277 $Nu = \left\{ 0.6 + \frac{0.387 Ra_D^{1/6}}{\left[ 1 + (0.559 / Pr)^{9/16} \right]^{8/27}} \right\}^2$	2.868
4	Vertical plate	$L_c = L$	63.3	2.173 $Nu = \left\{ 0.825 + \frac{0.387 Ra_L^{1/6}}{\left[ 1 + (0.492 / Pr)^{9/16} \right]^{8/27}} \right\}$	5.472 (calculated for the length of the top plate, used for the whole category)

Table 7.12 Definitions of variables used in the calculations of Table 7.11.

Symbol	Definition	Symbol	Definition
$A_s$	surface area	$T_f$	film temperature
$p$	perimeter	$T_s$	surface temperature
$D$	diameter	$T_\infty$	ambient temperature
$L$	vertical length	$Pr$	Prandtl number
$g$	gravitational acceleration	$\nu$	kinematic viscosity

Table 7.13 Properties of air at 1 [atm] pressure, at the film temperature  $T_f = 20.3$  [°C] [13].

Property	Value
Thermal conductivity, $k$	0.0252 [W/m.°C]
Kinematic viscosity, $\nu$	$1.5215 \times 10^{-5}$ [m <sup>2</sup> /s]
Prandtl number, $Pr$	0.7307

The surface of the air bushing interface with the shaft (Surface 5) is modeled using forced convection due to laminar flow in an annular duct [13]. Calculation of the forced convective heat transfer coefficient for this surface is presented in Table 7.14. The Reynolds number is calculated to be less than  $10^4$ , hence laminar flow is assumed with  $D_i \cong D_o$ . The coefficient of heat transfer is calculated to be very large due to the small gap in the interface.

COMSOL® FEA is carried out using the calculated convective heat transfer ( $h$ ) values as shown in Fig. 7.15. The average temperature of the top plate is calculated as 20.002 [°C]. The simulation shows that compressed air supply at the air bushings act as a heat sink and isolate the sensitive parts of the moving body from the heat dissipation of the coils. Maximum temperature is simulated as 20.4 [°C] at the ends of the shaft which are subject to coil heat dissipation.

Table 7.14 Calculation of the forced convective heat transfer coefficient at the air bushing interface.

Parameter	Symbol	Formula	Value
Air gap	$d_{gap}$	-	4 [μm]
Inner diameter	$D_i$	-	19.992 [mm]
Outer diameter	$D_o$	-	20.000 [mm]
Difference between inner and outer diameters of the annulus	$D_o - D_i$	-	8 [μm] ( $2d_{gap}$ )
Hydraulic diameter	$D_h$	$D_h = D_o - D_i$	8 [μm]
Nominal flow rate of air bushing	$\dot{V}_{bushing}$	-	4.15 normal liters per minute (average of min. and max. values)
Volumetric flow rate	$\dot{V}$	$\dot{V}_{bushing} / 2$ (average of the flow rate along the bushing length)	$3.729 \times 10^{-5}$ [m <sup>3</sup> /s]
Cross-sectional area of the duct	$A_c$	$\frac{\pi(D_o^2 - D_i^2)}{4}$	$1.256 \times 10^{-7}$ [m <sup>2</sup> ]
Linear flow rate	$v_m$	$v_m = \frac{\dot{V}}{A_c}$	296 [m/s]
Reynolds number	$Re$	$Re = \frac{v_m D_h}{\nu}$	77
Nusselt number	$Nu$	-	4.86
Coefficient of forced convective heat transfer	$h$	$h = \frac{kNu}{D_h}$	15300 [W/m <sup>2</sup> .K]

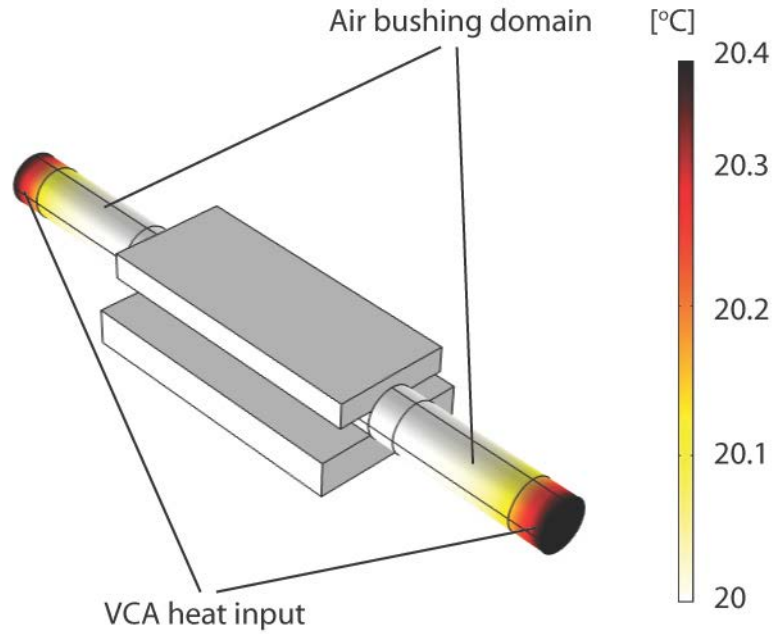


Fig. 7.15 COMSOL® FEA simulation of the temperature distribution.

#### *Variations of the ambient temperature*

Ambient temperature and relative humidity in the laboratory was recorded for a period of 2 weeks in December, right before the commencement of the tests. Temperature results are presented in Fig. 7.16. Temperature data is summarized in Table 7.15. The peak-to-valley thermal disturbance from the environment can be estimated as  $4\sigma = 0.70$  [°C], with 95% confidence [79].

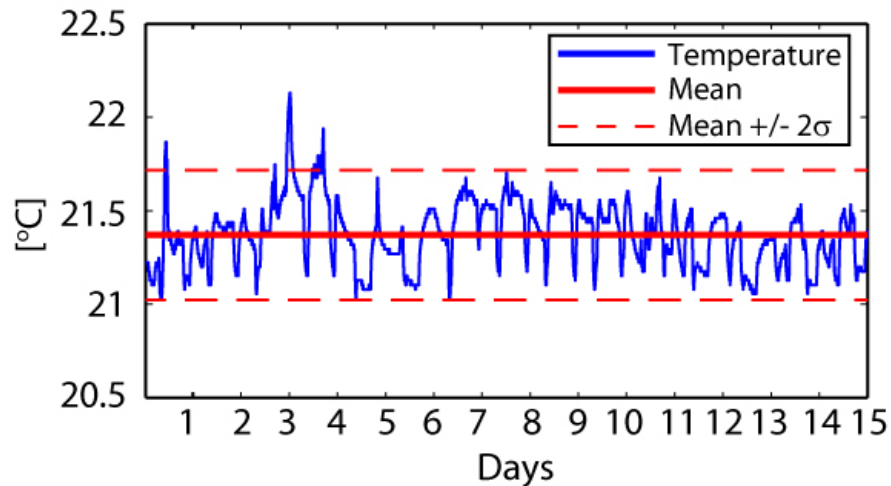


Fig. 7.16 Variations of the ambient temperature.

Table 7.15. Ambient temperature data.

	[°C]
Mean	21.37
Minimum	21.03
Maximum	22.13
Range	1.10
Standard deviation	0.174

#### 7.4.2.3. Thermal errors

The FEA simulation results in Section 7.4.2.2 showed that the average temperature of the top plate of the moving body follows the air supply temperature closely, with only 0.002 [°C] temperature rise at the equilibrium state. In the simulations, the air supply temperature is modeled equal to the ambient temperature. This assumption is due to the air supply piping being immersed in laboratory conditions. In the future, it can be tested in further experiments. As a result, the PV temperature variation of the top plate equals to the thermal uncertainty of the ambient air. Hence, total thermal error can be found using the thermal sensitivity (Table 7.10) as  $E_{thermal} = \gamma_T \Delta T = 322$  [nm], where  $\Delta T = 0.70$  [°C] is due to the variations of the ambient air conditions.

#### 7.4.3. Final error budget

The final error budget for the nano-positioner is presented in Table 7.16. The point of interest is the same as was presented in Fig. 7.13. It is located a vertical distance  $L_y = 15$  [mm] from the center of gravity, which is assumed to be the center of rotation. Therefore, EXX error is added a  $-L_y \cdot \theta_c$  term due to the Abbe error introduced by pitching. For the servo errors, the 30 [nm] PV error observed in Fig. 5.18 is used. As the servo error was already observed after a compensation scheme for sensor errors was implemented, no further reduction in errors is assumed in the table due to additional compensation. The arithmetic sum is obtained by a simple addition of each error term. For the root-mean-square (RMS) sum, first, peak-to-valley (PV) values given in the table need to be converted to RMS values. Assuming zero-mean uniform probability distribution, the following formula for RMS summation can be used [98],

$$E_{RMS} = \frac{1}{2\sqrt{3}} \left[ \sum_{i=1}^N (E_i)^2 \right]^{1/2}, \quad (7.10)$$

where  $E_i$  are the individual errors. The arithmetic sum of errors is considered to be an exaggerated worst-case scenario for how the individual errors may combine. On the other hand, the RMS sum is regarded as optimistic. A practical approach is to take the mean value of the two [110], as is done in Table 7.16. Cutting forces are estimated to contribute a peak-to-valley error of 0.34 [ $\mu\text{m}$ ] using calculations based on an example micro-milling case, as detailed in Appendix G. However, it is not included in the error budget.

Table 7.16. Error budget.

		PV Magnitude [nm]	
		Repeatable Errors Conserved	Repeatable Errors Subtracted
Linear (EXX)		4847	3090
Straightness			
	Vertical (EYX)	9503	15
	Horizontal (EZX)	2026	31
Angular		(included in Linear)	
Servo		30	30
Thermal		322	322
<b>Total Error</b>			
	Arithmetic Sum	16728	3488
	RMS Sum	3136	897
	<b>Mean</b>	9932	2192

### 7.5. Discussion

The error budget indicates a 9.9 [ $\mu\text{m}$ ] deviation with the repeatable errors conserved, and 2.2 [ $\mu\text{m}$ ] when 5 DOF compensation is assumed to be available. The largest error is associated with the vertical motion (EYX), followed by the linear positioning error (EXX). Vertical error is very repeatable, while the positioning error is mostly unrepeatable.

For the EXX case, the repeatable error might be due to encoder grating errors. The encoder calibration chart indicates a 1 [ $\mu\text{m}$ ] PV range for such errors. Also, the large error in ECX contributes to EXX through the Abbe moment arm. The ECX error might be due to a curvature in the shaft beyond the specified tolerances. This may have formed during the machining of the flat surfaces for the top and bottom plates, or during assembly. Servo and thermal errors are observed to contribute a small fraction of the overall error. Low thermal errors is associated with the compressed air discharge

at the air bushing interface, which acts as a heat sink and isolates thermally sensitive components of the stage from the heat dissipation of coils. If the overall motion error is assumed to be centered at zero, the machining tolerances corresponding to uncompensated and compensated cases of accuracy would be  $\pm 5.0$  [ $\mu\text{m}$ ] and  $\pm 1.1$  [ $\mu\text{m}$ ], respectively. In Chapter 3, at the design phase, tolerances deliverable by the machine were calculated as  $\pm 1.8$  [ $\mu\text{m}$ ], which included only the systematic components. This shows that the systematic error is almost double that of what was predicted.

Measurement uncertainty associated with the procedure is observed to be high. The most important systematic error in the measurements is estimated to be due to laser beam misalignment. As mentioned earlier, the standard [47] predicts up to 15 [ $\mu\text{m}$ ] uncertainty in distance measurement for a motion range of 20 [mm]. The same standard predicts it as 0.3 [ $\mu\text{m}$ ] over 1 [m]. This is due to the fact that, angular misalignment is harder to detect over short measurement lengths. Laser beam misalignment is thought to have influenced EYX and EZX considerably. Its influence in these cases is higher than EXX, as the variations in the laser arm length are amplified in straightness calculations (Eq. (7.2)). In EXX, EBX, and ECX measurements, random measurement errors are possibly responsible from at least part of the unrepeatable errors calculated. These can be due to air turbulence, ground vibrations, and ambient lights. However, the situation in EXX seems to be influenced also by some other factors, like the mechanical relaxation of the tripod stage. This additional trend is not observed in EBX and ECX, as angular measurement is more robust to random changes in laser alignment.

## 7.6. Conclusion

Laser interferometric metrology of the developed stage has been conducted to reveal the geometric errors. An error budget has been formed using these errors, the observed servo errors and modeled thermal errors. Stage accuracy was determined as  $\pm 5.0$  [ $\mu\text{m}$ ] and  $\pm 1.1$  [ $\mu\text{m}$ ] for uncompensated and 5 DOF assumed compensation cases, compared to the  $\pm 1.8$  [ $\mu\text{m}$ ] prediction at the design phase. Part of the repeatable error is concluded to be due to a curvature of the shaft beyond the specified tolerances. For the remaining repeatable errors, as well as the unrepeatable parts, influences of measurement uncertainty and actual geometric errors are not easily distinguishable. As part of future work, better ways to align the laser beam to the measurement optics can be investigated, so that the measurement uncertainty can be reduced and the true performance of the system can be more accurately quantified. Also, the thermal disturbance model can be tested in experiments.

## Chapter 8

### Conclusions and Future Work

#### 8.1. Thesis conclusions

In this thesis, a linear ultraprecision motion stage (nano-positioner) was designed, built and characterized. Design requirements of the stage were derived from a low-cost desktop precision micro machine tool concept. The mechatronic design of the nano-positioner was made in a holistic manner to integrate different components of actuation, control, sensing, and mechanical design towards high positioning performance. A stroke length of 20 [mm] was realized. Voice coil actuators were preferred for their non-contact, cog-free operation. They were utilized in moving-magnet mode in order to prevent the formation of parasitic forces due to lead cables. Also, the actuators were used in a complementary double configuration in order to generate uniform force response.

Voice coil actuators were designed from scratch based on a cylindrical design. Certain dimensions of the VCA were determined according to various factors such as the scale of required forces, availability of permanent magnets, stroke length, manufacturing/assembly tolerances, magnetic saturation of steel, and leakage flux. The remaining variables were set through an optimization procedure involving performance topologies using two optimization objectives. The finite element analysis method used in simulating the magnetic flux, and the formulations used in the calculation of performance objectives were verified in experiments.

Controller design was made for current control and the higher level positioning control systems. Frequency response measurements and finite element analyses were employed to model the system as close as possible to actuality, in order to ensure stability of the controllers. It was observed that eddy currents in the stator structure cause significant changes to the coil electrical dynamics at high frequencies. A current control bandwidth of greater than or equal to 907 [Hz] was achieved. The positioning controller was designed with 450 [Hz] bandwidth. Positioning tests were carried out, and the positioning resolution of the stage was determined as  $\pm 5$  [nm]. The positioning resolution was analyzed using Dynamic Error Budgeting (DEB), and the largest contributor to the error was identified to be the encoder electrical and quantization noise. Using DEB, actual positioning error of the nano-positioner for a step trajectory was estimated to be 0.680 [nm] RMS. A compensation



scheme was implemented to correct the two 90 [deg] phased measurement signals from the encoder, which had mismatch due to the misalignment of the encoder head. Control system was tested for trajectory tracking performance. Accuracies of  $\pm 45$  [nm] and  $\pm 15$  [nm] were recorded with the sensor correction turned off and on, respectively.

Vibratory modes of the motion stage were identified using two independent impact testing procedures. Method 1 employed the graphical ‘peak-picking’ approach, and Method 2 used automated algorithms in a commercially available software package, for analysis. Results from the two methods were observed to be similar. The first natural frequency which is a roll mode was observed to be at 65 [Hz] and 79 [Hz] by methods 1 and 2, respectively. This result was far lower than the 672 [Hz] prediction at the design phase. This discrepancy is attributed to the coarse estimation of the air bearing rotational (pitch) stiffness, using a formulation based on the catalogue value of the normal stiffness. The estimation neglected the loss of stiffness due to the distortion of air cushion at the bearing interface due to the out-of-plane rotations. However, this mode and two other modes identified within the bandwidth of the controller were not observed to interfere with the feedback control.

Laser interferometric metrology was applied to the nano-positioner to determine geometric accuracies. Thermal errors due to the voice coil actuators’ heat dissipation was estimated using a model for the convective heat transfer. An error budget was compiled using geometric, servo, and thermal errors. The accuracy of positioning was determined to be  $\pm 5.0$  [ $\mu\text{m}$ ], compared to the  $\pm 1.8$  [ $\mu\text{m}$ ] prediction at the design phase. Non-repeatable errors were found to be  $\pm 1.1$  [ $\mu\text{m}$ ]. The systematic part of the error was attributed to possible violations of production tolerances on the main shaft, deflections induced during assembly, and encoder grating errors. However, the uncertainty of measurement was also estimated to be a major contributor of the recorded errors.

## **8.2. Thesis contributions**

The design and development of the linear nano-positioner involved contributions in the following areas:

- The voice coil actuator design is optimized using two novel optimization objectives formulated independent of the coil wire gauge. Using the proposed formulations, the performance objectives, which are the maximization of the stage acceleration capacity and

the force produced per unit heat dissipation, are decoupled from the coil electrical specifications which are characterized through the coil wire gauge. Also, elimination of the coil current from the formulations made it possible to plot the performance topologies of each objective separately. This could not be achieved by certain former formulations which eliminate the coil current by combining expressions for different objectives.

- A self-aligning air-bushing/bearing arrangement has been used which reduces assembly and production costs associated with the proper alignment of the components. The often preferred double guideway design for constraining the roll motion has been discarded in favor of the single shaft design, thereby reducing the footprint of the stage. The discharge of compressed air from the air bushings is also observed to assist in the thermal stability of the sensitive components.
- The linear nano-positioner has been realized in a prototype from scratch and advanced analysis methods have been applied to assess its performance and evaluate the effectiveness of the design choices. A realistic Dynamic Error Budget (DEB) has been compiled, modal testing has been carried out, and laser interferometric metrology has been used. The motion stage's performance characteristics are verified to be similar or better than other stages in the relevant literature, while also retaining the reduced assembly cost and reduced footprint characteristics mentioned above.

### **8.3. Future research**

A number of future work items have been identified related to the proposed design and also as investigations related to the improvement of possible future designs, as follows:

- The position controller can be enhanced with an additional pole beyond the cross-over frequency to prevent the excessive oscillations of the control command signal around the set point due to the transmitted noise.
- Correction scheme for the encoder quadrature detection errors can be improved to compensate more harmonics of the measurement error with better accuracy.
- Uncertainty in laser interferometric measurements can be reduced by improving the alignment of the laser beam to the measurement optics, and minimizing the dead path errors.
- The thermal disturbance model used in the error budget can be verified in experiments.
- Experimental data may be collected on air bearings to characterize their pitching stiffness.

## References

- [1] Abramovitch, D., Hurst, T., and Henze, D., 1997, "Decomposition of Baseline Noise Sources in Hard Disk Position Error Signals Using the PES Pareto Method," *In Proceedings of the 1997 American Control Conference*, Albuquerque, NM, USA, pp. 2901–2905.
- [2] Abramovitch, D., Hurst, T., and Henze, D., 1997, "The PES Pareto Method: Uncovering the Strata of Position Error Signals in Disk Drives," *In Proceedings of the 1997 American Control Conference*, Albuquerque, NM, USA, pp. 2888–2895.
- [3] Aguirre, G., Gorostiaga, M., Buruaga, M., and Urreta, H, 2012, "Performance Analysis of Active Aerostatic Thrust Bearings with Dynamic Error Budgeting," *In Proceedings of the 28<sup>th</sup> Annual Meeting of the American Society for Precision Engineering ASPE2012*, San Diego, CA, USA.
- [4] Atsumi, T., Nakamura, S., Furukawa, M., Naniwa, I., and Xu, J., 2013, "Triple-Stage-Actuator System of Head-Positioning Control in Hard Disk Drives," *IEEE Trans. Magn.*, **49**(6), pp. 2738-2743.
- [5] Awtar, S., and Parmar, G., 2013, "Design of a Large Range XY Nanopositioning System," *J. Mechanisms Robotics*, **5**(2), #021008.
- [6] Bendat, J. S., and Piersol, A. G., 2010, *Random Data: Analysis and Measurement Procedures*, 4<sup>th</sup> ed, John Wiley & Sons, Hoboken, NJ.
- [7] Bishop, R. H., ed., 2002, *The Mechatronics Handbook, -2 Volume Set*. [e-book] CRC Press. Available through: University of Waterloo Library website < <http://www.lib.uwaterloo.ca/>> [Accessed 21 September 2016].
- [8] Bolton, W., 1999, *Mechatronics: Electronic Control Systems in Mechanical Engineering*, 2<sup>nd</sup> ed., Longman, Harlow.
- [9] Brandt, A., 2011, *Noise and Vibration Analysis: Signal Analysis and Experimental Procedures*, John Wiley & Sons, Hoboken, NJ.
- [10] Brauer, J. R., 2006, *Magnetic Actuators and Sensors*, John Wiley & Sons, Hoboken, NJ.
- [11] Brecher, C., Utsch, P., and Wenzel, C., 2009, "Five-Axes Accuracy Enhancement by Compact and Integral Design," *CIRP Annals-Manufacturing Technology*, **58**(1), pp. 355-358.
- [12] Buice, E. S., Otten, D., Yang, R. H., Smith, S. T., Hocken, R. J., and Trumper, D. L., 2009, "Design Evaluation of a Single-Axis Precision Controlled Positioning Stage," *Precision Engineering*, **33**(4), pp.418-424.

- [13] Cengel, Y. A., 2003, *Heat Transfer: A Practical Approach*, 2<sup>nd</sup> ed., McGraw-Hill, New York, NY.
- [14] Chae, J., Park, S. S., and Freiheit, T., 2006, "Investigation of Micro-Cutting Operations," *International Journal of Machine Tools and Manufacture*, **46**(3), pp. 313-332.
- [15] Chai, H.-D., 1998, *Electromechanical Motion Devices*, Prentice Hall, Upper Saddle River, NJ.
- [16] Chen, K. S., Trumper, D. L., and Smith, S.T., 2002, "Design and Control for an Electromagnetically Driven X–Y– $\Theta$  Stage," *Precision Engineering*, **26**(4), pp. 355-369.
- [17] Chen, S.-C., and Culpepper, M.L., 2006. "Design of a Six-Axis Micro-Scale Nanopositioner – Mhexflex," *Precision Engineering*, **30**(3), pp. 314-324.
- [18] Cheng, F., Fan, K.-C., Miao, J., Li, B.-K., and Wang, H.-Y., 2012, "A BPNN-PID Based Long-Stroke Nanopositioning Control Scheme Driven by Ultrasonic Motor," *Precision Engineering*, **36**(3), pp. 485-493.
- [19] Cheng, K., and Huo, D., ed., 2013, *Micro-cutting: Fundamentals and Application*, John Wiley & Sons, Hoboken, NJ.
- [20] Choi, Y.-M., Kim, J. J., Kim, J., and Gweon, D.-G., 2008. "Design and Control of a Nanoprecision XY $\Theta$  Scanner," *Rev. Sci. Instrum.*, **79**(4), #045109.
- [21] Chu, C. L., and Fan, S. H., 2006, "A Novel Long-Travel Piezoelectric-Driven Linear Nanopositioning Stage," *Precision Engineering*, **30**(1), pp. 85-95.
- [22] de Silva C. W., 1999, *Vibration: Fundamentals and Practice*. [e-book] CRC Press, Boca Raton. Available through: CRCnetBASE website <<http://www.crcnetbase.com/>> [Accessed 22 June 2016].
- [23] Donaldson, R. R., 1980, "Error Budgets," *Technology of Machine Tools*, 5, pp. 1-14.
- [24] Dong, W., Tang, J., and ElDeeb, Y., 2009, "Design of a Linear-Motion Dual-Stage Actuation System for Precision Control," *Smart Mater. Struct.*, **18**(9), #095035.
- [25] Donges, A., and Noll, R., 2015, *Laser Measurement Technology*. [e-book] Springer-Verlag, Berlin Heidelberg. Available through: University of Waterloo Library website < <http://www.lib.uwaterloo.ca/> > [Accessed 18 September 2016].
- [26] Dorf, R. C., 1997, *The Electrical Engineering Handbook*, 2<sup>nd</sup> ed., CRC Press, Boca Raton, FL.
- [27] Dornfeld, D., and Lee, D. E., 2008, *Machine Design for Precision Manufacturing*. [e-book] Springer, US. Available through: Springer Link website < <http://link.springer.com/> > [Accessed 21 September 2016].

- [28] Dr. Johannes Heidenhain GmbH, 2016, *Exposed Linear Encoders*. [online] Dr. Johannes Heidenhain GmbH. Available at: < [http://www.heidenhain.de/fileadmin/pdb/media/img/208960-2D\\_Exposed\\_Linear\\_Encoders\\_01.pdf](http://www.heidenhain.de/fileadmin/pdb/media/img/208960-2D_Exposed_Linear_Encoders_01.pdf) > [Accessed 18 August 2016]
- [29] Echeverria, D., Lahaye, D., Encica, L., Lomonova, E. A., Hemker, P.W., and Vandemput, A. J. A., 2006, "Manifold-Mapping Optimization Applied to Linear Actuator Design," *IEEE Trans. Magn.*, **42**(4), pp. 1183-1186.
- [30] Ewins, D.J., 1986, *Modal Testing: Theory and Practice*. RSP, Taunton:.
- [31] Fesperman, R., Ozturk, O., Hocken, R., Ruben, S., Tsao, T. C., Phipps, J., Lemmons, T., Brien, J., and Caskey, G., 2012, "Multi-Scale Alignment and Positioning System–MAPS," *Precision Engineering*, **36**(4), pp. 517-537.
- [32] Fitzgerald, A. E., Kingsley, Jr., C., and Umans, S. D., 1983, *Electric Machinery*, 4<sup>th</sup> ed. McGraw-Hill, USA.
- [33] Fleming, A. J., and Leang, K. K., 2014, *Design, Modeling, and Control of Nanopositioning Systems*, Springer.
- [34] Franklin, G. F., Powell, J. D., and Emami-Naeini, A., 2010, *Feedback Control of Dynamic Systems*, 6<sup>th</sup> ed., Pearson, Upper Saddle River, NJ.
- [35] Gao, W., Kim, S. W., Bosse, H., Haitjema, H., Chen, Y. L., Lu, X. D., Knapp, W., Weckenmann, A., Estler, W. T., and Kunzmann, H., 2015, "Measurement Technologies for Precision Positioning," *CIRP Annals-Manufacturing Technology*, **64**(2), 773-796.
- [36] Ghazaly, M. M., and Sato, K., 2013, "Characteristic Switching of a Multilayer Thin Electrostatic Actuator by a Driving Signal for an Ultra-Precision Motion Stage," *Precision Engineering*, **37**(1), pp. 107-116.
- [37] Gieras, J. F., 2002, *Permanent Magnet Motor Technology: Design and Applications*, CRC press.
- [38] Gorniak, J. M., 2010, *Design and Metrology of a Precision XY Planar Stage*. MASc. University of Waterloo, Waterloo, ON.
- [39] Gozen, B. A., and Ozdoganlar, O. B., 2012, "Design and Evaluation of a Mechanical Nanomanufacturing System for Nanomilling," *Precision Engineering*, **36**(1), pp. 19-30.
- [40] Hayt, Jr., W. H., Kemmerly, J. E., and Durbin, S. M., 2007, *Engineering Circuit Analysis*, 7<sup>th</sup> ed., McGraw-Hill, New York, NY.
- [41] Herrington, D., and Meacham, S., 1968, *Handbook Of Electronic Tables & Formulas*, 3<sup>rd</sup> ed., Howard W. Sams and Company, Inc., Indianapolis, IN.

- [42] Heydemann, P. L. M., 1981, "Determination and Correction of Quadrature Fringe Measurement Errors in Interferometers," *Applied Optics*, **20**(19), pp. 3382 - 3384.
- [43] Heylen, W., Lammens, S., Sas, P., 1995, *Modal Analysis Theory and Testing*, Department of Mechanical Engineering, Katholieke Universiteit Leuven, Leuven, Belgium.
- [44] Hiroshi, S., Gokan, T., Yoshioka, H., and Shinno, H., 2012, "A Newly Developed STM-Based Coordinate Measuring Machine," *Precision Engineering*, **36**(4), pp. 538-545.
- [45] Hurst, T., Abramovitch, D., and Henze, D., 1997, "Measurements for the PES Pareto Method of Identifying Contributors to Disk Drive Servo System Errors," *In Proceedings of the 1997 American Control Conference*, Albuquerque, NM, USA , pp. 2896–2900.
- [46] Ida, N., 2004, *Engineering Electromagnetics*, 2<sup>nd</sup> ed, Springer , New York, NY.
- [47] International Organization for Standardization, 2006, *ISO 230-2 Test Code for Machine Tools - Part 2: Determination of Accuracy and Repeatability of Positioning Numerically Controlled Axes*, ISO, Geneva.
- [48] International Organization for Standardization, 2009. *ISO/DIS 230-1 Test Code for Machine Tools - Part 1: Geometric Accuracy of Machines Operating Under No-Load or Quasi-Static Conditions*, ISO, Geneva.
- [49] Jabben, L., 2007, *Mechatronic Design of a Magnetically Suspended Rotating Platform*. PhD, Delft University of Technology.
- [50] Kang, D., Kim, K., Kim, D., Shim, J., Gweon, D. G., and Jeong, J., 2009, "Optimal Design of High Precision XY-Scanner with Nanometer-Level Resolution and Millimeter-Level Working Range," *Mechatronics*, **19**(4), pp. 562-570.
- [51] Kim, W. J., Verma, S., and Shakir, H., 2007, "Design and Precision Construction of Novel Magnetic-Levitation-Based Multi-Axis Nanoscale Positioning Systems," *Precision Engineering*, **31**(4), pp. 337-350.
- [52] Kim, S., Song, M. G., Park, N. C., Yoo, J., Park, Y. P., and Park, K. S., 2009, "Optimal Design of Moving-Magnet Type Actuators for Optical Disk Drives Considering Effect of Coil Electromagnet," *IEEE Transactions on Magnetics*, **45**(5), pp.2228-2231.
- [53] Kim, C.-G., Kim, K.-J., Yu, J.-S., and Cho, H.-W., 2013, "Dynamic Performance Evaluation of 5 DOF Magnetic Levitation and Guidance Device by Using Equivalent Magnetic Circuit Model," *IEEE Trans. Magn.*, **49**(7), pp. 4156-4159.
- [54] Kuipers, J. B., 1999, *Quaternions and Rotation Sequences: A Primer with Applications to Orbits, Aerospace, and Virtual Reality*, Princeton University Press, Princeton, NJ.

- [55] Kunzmann, H., Pfeifer, T., Flügge, J., 1993, "Scales vs. Laser Interferometers Performance and Comparison of Two Measuring Systems," *CIRP Annals-Manufacturing Technology*, **42**(2), pp. 753-767.
- [56] Lee, J., and Wang, S., 2012, "Topological Shape Optimization of Permanent Magnet in Voice Coil Motor Using Level Set Method," *IEEE Trans. Magn.*, **48**(2), pp. 931-934.
- [57] Leo Kumar, S. P., Jerald, J., Kumanan, S., and Prabakaran, R., 2014, "A Review on Current Research Aspects in Tool-Based Micromachining Processes," *Materials and Manufacturing Processes*, **29**(11-12), pp. 1291-1337.
- [58] Liu, Y. T., Higuchi, T., and Fung, R. F., 2003, "A Novel Precision Positioning Table Utilizing Impact Force of Spring-Mounted Piezoelectric Actuator - Part I: Experimental Design and Results," *Precision Engineering*, **27**(1), pp. 14-21.
- [59] Liu, Y.-T., Fung, R.-F., and Wang, C.-C., 2005, "Precision Position Control Using Combined Piezo-VCM Actuators," *Precision Engineering*, **29**(4), pp. 411-422.
- [60] Liu, C.-H., Jywe, W.-Y., Jeng, Y.-R., Hsu, T.-H., and Li, Y.-T., 2010, "Design and Control of a Long-Traveling Nano-Positioning Stage," *Precision Engineering*, **34**(3), pp.497-506.
- [61] Liu, Y., Zhang, M., Zhu, Y., Yang, J., and Chen, B., 2011, "Optimization of Voice Coil Motor to Enhance Dynamic Response Based on an Improved Magnetic Equivalent Circuit Model," *IEEE Trans. Magn.*, **47**(9), pp. 2247-2251.
- [62] Liu, Y. T., and Li, B. J., 2016, "A 3-Axis Precision Positioning Device Using PZT Actuators with Low Interference Motions," *Precision Engineering*, **46**, 118-128.
- [63] Lu, X. D., and Trumper, D. L., 2005, "Ultrafast Tool Servos for Diamond Turning," *CIRP Annals-Manufacturing Technology*, **54**(1), pp. 383-388.
- [64] Lu, X. D., and Trumper, D. L., 2007, "Self-Calibration of On-Axis Rotary Encoders," *CIRP Annals-Manufacturing Technology*, **56**(1), pp. 499-504.
- [65] Lu, X., and Usman, I., 2012, "6d Direct-Drive Technology for Planar Motion Stages," *CIRP Annals-Manufacturing Technology*, **61**(1), pp. 359-362.
- [66] Lu, X., Rao, N., and Usman, I., 2013, "Six-Axis Position Measurement System for Levitated Motion Stages," *CIRP Annals-Manufacturing Technology*, **62**(1), pp.507-510.
- [67] Lu, X., Dyck, M. and Altintas, Y., 2015, "Magnetically Levitated Six Degree of Freedom Rotary Table," *CIRP Annals-Manufacturing Technology*, **64**(1), pp. 353-356.
- [68] MacKenzie, I., 2015, *Design and Control Methods for High-Accuracy Variable Reluctance Actuators*. PhD, Massachusetts Institute of Technology Cambridge, MI.

- [69] Maeda, G. J., Sato, K., Hashizume, H., and Shinshi T., 2006, "Control of an XY Nano-Positioning Table for a Compact Nano-Machine Tool," *JSME International Journal Series C*, **49**(1), pp. 21-27.
- [70] Maia, N. M. M., and Silva, J. M. M., 1997, *Theoretical and Experimental Modal Analysis*, Research Studies Press, Baldock, Hertfordshire, England.
- [71] Manske, E., Jager, G., Hausotte, T., and Fussl, R., 2012, "Recent Developments and Challenges of Nanopositioning and Nanomeasuring Technology," *Measurement Science and Technology*, **23**(7), #074001.
- [72] McConnell, K. G., 1995, *Vibration Testing: Theory and Practice*, John Wiley & Sons, Hoboken, NJ.
- [73] Mekid, S. ed., 2008, *Introduction to Precision Machine Design And Error Assessment*. [e-book] CRC Press, Boca Raton. Available through: University of Waterloo Library website < <http://www.lib.uwaterloo.ca/> > [Accessed 18 September 2016].
- [74] Michellod, Y., Mullhaupt, P., and Gillet, D., 2006, "Strategy for the Control of a Dual-Stage Nano-Positioning System with a Single Metrology," *In Proceedings of IEEE Conference on Robotics, Automation and Mechatronics*, Bangkok, Thailand.
- [75] Monkhorst, W., 2004, *Dynamic Error Budgeting—A Design Approach*. Graduation, Delft University of Technology, Delft.
- [76] Mori, S., Hoshino, T., Obinata, G., and Ouchi, K., 2003, "Air-Bearing Linear Actuator for Highly Precise Tracking," *IEEE Trans. Magn.*, **39**(2), pp. 812-818.
- [77] National Electrical Manufacturers Association, 2014, *NEMA MW1000 – 2014 Magnet Wire*. [online] Available through: MWS Wire Industries, Westlake Village, CA website <[http://www.mwswire.com/pdf\\_files/mws\\_tech\\_book/page8\\_9\\_35.pdf](http://www.mwswire.com/pdf_files/mws_tech_book/page8_9_35.pdf)> [Accessed 03 October 2014]
- [78] National Institute of Standards and Technology (NIST), 2016, *Engineering Metrology Toolbox*. [online] Available at: <<http://emtoolbox.nist.gov/Wavelength/Edlen.asp>> [Accessed 11 April 2016].
- [79] National Institute of Standards and Technology (NIST), 2016, *What Do We Mean by "Normal" Data?* Available at: <<http://www.itl.nist.gov/div898/handbook/pmc/section5/pmc51.htm>> [Accessed 30 September 2016]
- [80] New Way Air Bearings, 2006, *Air Bearing Application and Design Guide*. [online] Aston, Pennsylvania: New Way Air Bearings. Available at: <<http://www.newwayairbearings.com/sites/>>



- default/files/new\_way\_application\_and\_design\_guide\_%20Rev\_E\_2006-01-18.pdf> [Accessed 12 August 2016]
- [81] New Way Air Bearings, 2016, *Catalogue*. [online] Available at: < [http://www.newwayairbearings.com / catalog / components](http://www.newwayairbearings.com/catalog/components) > [Accessed 24 September 2016].
- [82] Ouyang, P. R., Tjiptoprodjo, R. C., Zhang, W. J., and Yang, G. S., 2008, “Micro-Motion Devices Technology: The State of Arts Review,” *Int. J. Adv. Manuf. Technol.*, **38**(5-6), pp. 463-478.
- [83] Pappa, R. S., Elliott, K. B. and Schenk, A., 1992, *A Consistent-Mode Indicator for the Eigensystem Realization Algorithm*. Report NASA TM-107607. National Aeronautics and Space Administration, Vancouver.
- [84] Parmar, G., Barton, K., and Awtar, S., 2014, “Large Dynamic Range Nanopositioning Using Iterative Learning Control,” *Precision Engineering*, **38**(1), pp.48-56.
- [85] Peeters, B., Van der Auweraer, H., Guillaume, P., and Leuridan, J., 2004, “The Polymax Frequency-Domain Method: A New Standard for Modal Parameter Estimation?” *Shock Vib.*, **11**(3-4), pp. 395-409.
- [86] Quanser, 2002, *Linear Current Amplifier Module: User’s Guide*, version 2.0. [pdf].
- [87] Rahman, M. A., and Slemon, G. R., 1985, “Promising Applications of Neodymium Boron Iron Magnets in Electrical Machines,” *IEEE Trans. Magn.*, **21**(5), pp. 1712-1716.
- [88] Rakuff, S., and Cuttino, J. F., 2009, “Design and Testing of a Long-Range, Precision Fast Tool Servo System for Diamond Turning,” *Precision Engineering*, **33**(1), pp. 18-25.
- [89] Renishaw, 2015, *RLE Fiber Optic Laser Encoder*. [pdf] Renishaw. Available at: <<http://www.renishaw.com/media/pdf/en/7b583154fcef4f7eb772ab272c6d867c.pdf>> [Accessed 11 April 2016].
- [90] Renishaw, 2016, *Interferometric Straightness Measurement and Application to Moving Table Machines*. [pdf] Renishaw. Available at: < <http://resources.renishaw.com/en/details/white-paper-interferometric-straightness-measurement-and-application-to-moving-table-machines--48145>> [Accessed 30 September 2016]
- [91] Reynders, E., Houbrechts, J., and De Roeck, G., 2012, “Fully Automated (Operational) Modal Analysis,” *Mechanical Systems and Signal Processing*, **29**, pp.228-250.
- [92] Roters, H. C., 1941, *Electromagnetic Devices*, John Wiley & Sons, New York, NY.
- [93] Ruben, S. H., 2010, *Modeling, Control, and Real Time Optimization for a Nano-Precision System*. Ph.D, UCLA, Los Angeles, CA.

- [94] Schmidt, R. M., Schitter, G., and Rankers, A., 2014, *The Design of High Performance Mechatronics-: High-Tech Functionality by Multidisciplinary System Integration*, IOS Press.
- [95] Schmitz, T. L., Smith, K.S., 2009, *Machining Dynamics: Frequency Response to Improved Productivity*. [e-book] Springer, New York. Available through: SpringerLink website <<http://link.springer.com/>> [Accessed 22 June 2016]
- [96] Schwenke, H., Knapp, W., Haitjema, H., Weckenmann, A., Schmitt, R., and Delbressine, F., 2008, "Geometric Error Measurement and Compensation of Machines - An Update," *CIRP Annals - Manufacturing Technology*, **57**(2), pp. 660-675.
- [97] Shamoto, E., Murase, H. and Moriwaki, T., 2000, "Ultraprecision 6-Axis Table Driven by Means of Walking Drive," *CIRP Annals-Manufacturing Technology*, **49**(1), pp.299-302.
- [98] Shen, Y. L., 1993, "Comparison of Combinatorial Rules for Machine Error Budgets," *CIRP Annals - Manufacturing Technology*, **42**(1), pp. 619-622.
- [99] Shinno, H., Yoshioka, K., and Taniguchi, K., 2007, "A Newly Developed Linear Motor-Driven Aerostatic X-Y Planar Motion Table System for Nano-Machining," *CIRP Annals – Manufacturing Technology*, **56**(1), pp. 369-372.
- [100] Shinno, H., Yoshioka, H., and Sawano, H., 2011, "A Newly Developed Long Range Positioning Table System with a Sub-Nanometer Resolution," *CIRP Annals – Manufacturing Technology*, **60**(1), pp. 403-406.
- [101] Skogestad, S., and Postlethwaite, I., 1996, *Multivariable Feedback Control: Analysis and Design*, John Wiley & Sons, Chichester.
- [102] Slocum, A. H., 1992, *Precision Machine Design*, SME, Dearborn, MI.
- [103] Slocum, A., Basaran, M., Cortesi, R., Hart, A. J., 2003, "Linear Motion Carriage with Aerostatic Bearings Preloaded by Inclined Iron Core Linear Electric Motor," *Precision Engineering*, **27**(4); pp. 382-394.
- [104] Sriyotha, P., Nakamoto, K., Sugai, M., and Yamazaki, K., 2006, "Development of 5-Axis Linear Motor Driven Super-Precision Machine," *CIRP Annals-Manufacturing Technology*, **55**(1), pp. 381-384.
- [105] Tan, K. K., Lee, T. H., and Huang, S., 2008, *Precision Motion Control: Design and Implementation*, 2<sup>nd</sup> ed. [e-book] Springer Science & Business Media. Available through: University of Waterloo Library website < <http://www.lib.uwaterloo.ca/>> [Accessed 21 September 2016].

- [106] Teo, T. J., Yang, G., and Chen, I. M., 2015, "A Flexure-Based Electromagnetic Nanopositioning Actuator with Predictable and Re-Configurable Open-Loop Positioning Resolution," *Precision Engineering*, **40**, pp. 249-260.
- [107] The American Society of Mechanical Engineers, 2005, *ASME B5.54-2005 Methods for Performance Evaluation of Computer Numerically Controlled Machining Centers*, ASME, New York, NY.
- [108] The Mathworks Inc., 2011, *Optimization Toolbox<sup>TM</sup>, User's Guide*. [online] The Mathworks Inc. Available at: < [http://www.mathworks.com/help/releases/R2011b/pdf\\_doc/optim/optim\\_tb.pdf](http://www.mathworks.com/help/releases/R2011b/pdf_doc/optim/optim_tb.pdf) > [Accessed 17 August 2016].
- [109] The Mathworks Inc., 2016, *Signal Processing Toolbox, User's Guide*. [online] The Mathworks Inc. Available at: < [http://www.mathworks.com/help/pdf\\_doc/signal/signal\\_tb.pdf](http://www.mathworks.com/help/pdf_doc/signal/signal_tb.pdf) > [Accessed 27 September 2016].
- [110] Thompson, D. C., 1989, "The Design of an Ultra-Precision CNC Measuring Machine," *CIRP Annals - Manufacturing Technology*, **38**(1), pp. 501-504.
- [111] Wagner, C., and Harned, N., 2010, "EUV Lithography: Lithography Gets Extreme," *Nature Photonics*, **4**, pp. 24-26.
- [112] Wang, R., and Zhang, X., 2016, "A Planar 3-DOF Nanopositioning Platform with Large Magnification," *Precision Engineering*, **46**, pp. 221 -231.
- [113] Zhang, Z., and Menq, C.-H., 2007, "Six-Axis Magnetic Levitation and Motion Control," *IEEE Trans. Robotics*, **23**(2), pp. 196-205.
- [114] Zschaeck, S., Amthor, A., and Ament, C., 2011, "Decentralized High Precision Motion Control For Nanopositioning And Nanomeasuring Machines," *In Proceedings of the IEEE, 37th Annual Conference of the IEEE Industrial Electronics Society (IECON 2011)*, Melbourne, VIC, pp. 546-551.

## Appendix A

### Current Amplifier Circuit Diagram

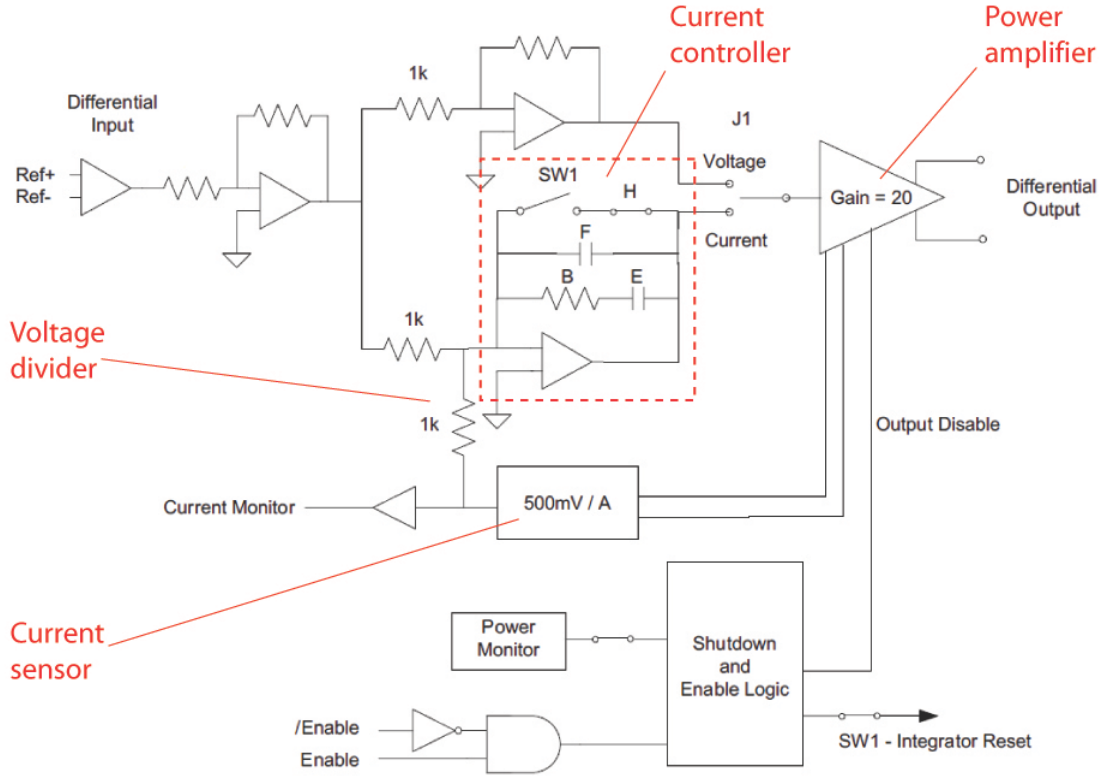


Fig. A.1 Simplified circuit diagram of the amplifier board [86].

The simplified circuit diagram of the current amplifier board is presented in Fig. A.1. In the figure, the J1 switch is used to select between voltage control and current control. The current control amplifier has a voltage divider at the input and B, E, F components for tuning the controller. SW1 switch and H are used to clear the integrator. The effective transfer function of the controller is an integrator + lead, which can be expressed as,

$$C_c(s) = K_c \frac{1}{s} \frac{T_c s + 1}{\alpha_c T_c s + 1}, \quad 0 < \alpha_c < 1. \quad (\text{A.1})$$

The current controller design is made in Chapter 5. The resulting controller parameters are matched to the passive components as shown in Table A.1. Values directly obtained from the controller design are implemented with slight deviations due to the availability of the actual physical components. Manufacturer's part numbers for the components are also provided.

Table A.1 Implementation of the current controller configuration using passive electronic components.

<b>Component</b>	<b>Expression</b>	<b>Value</b>	<b>Implementation</b>	<b>Part #</b>
Resistor B	$\frac{K_c T_c}{1 - \alpha_c}$	11.53 [k $\Omega$ ]	11.3 [k $\Omega$ ]	MRS25000C1132FRP00
Capacitor E	$\frac{1 - \alpha_c}{K_c}$	471.18 [nF]	470 [nF]	ECQ-E2474JB
Capacitor F	$\frac{\alpha_c}{K_c}$	28.82 [nF]	30 [nF]	ECW-F4303HL

## Appendix B

### Technical Drawing of the Main Shaft

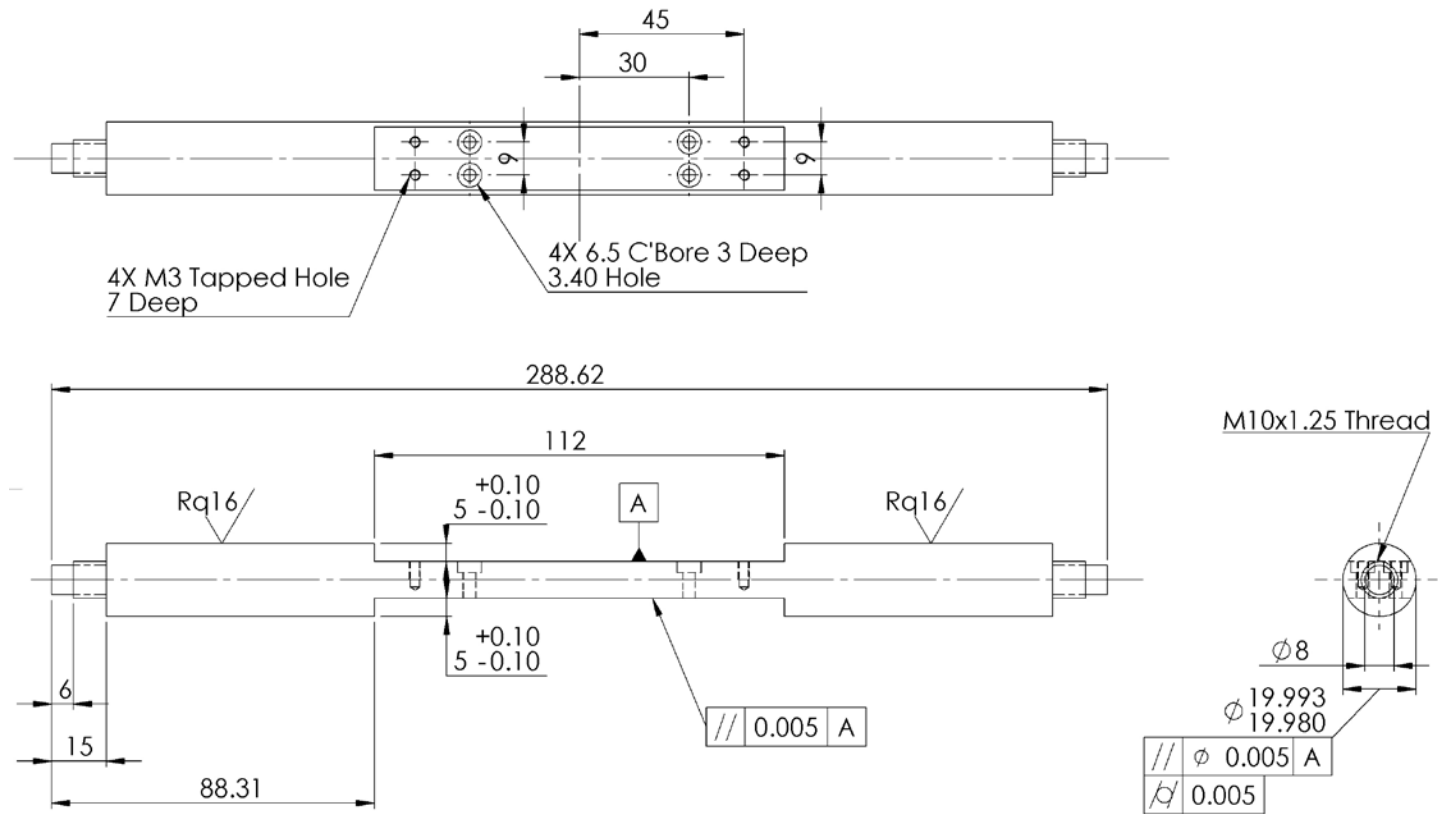


Fig. B.1 Technical drawing of the main shaft.

## Appendix C

### Frequency Response Functions for Modal Analysis

The receptance FRF can be rewritten in terms of the normalized frequency as,

$$\alpha(z) = \frac{1/k}{1 - z^2 + j2\zeta z}, \quad (\text{C.1})$$

where  $z = \omega/\omega_n$ . Mobility and accelerance FRF's can be derived from the receptance as,  $v(z) = jz\omega_n\alpha(z)$ , and  $a(z) = -z^2\omega_n^2\alpha(z)$ , respectively. Bode, real-imaginary, and Nyquist plots of the FRF's are presented in Fig. C.1 for a sample SDOF system with  $\omega_n = 10$  [rad/sec],  $\zeta = 0.07$ ,  $k = 1$  [N/m]. The SDOF system behaves like a pure spring at low frequencies and a pure mass at high frequencies. FRF's possess low and high frequency asymptotes accordingly, as presented in Table C.1.

Table C.1 Low and high frequency asymptotes of FRF's.

FRF	Low freq.	High freq.
Receptance, $\alpha(\omega)$	$1/k$	$1/m\omega^2$
Mobility, $v(\omega)$	$\omega/k$	$1/m\omega$
Accelerance, $a(\omega)$	$\omega^2/k$	$1/m$

Nyquist plot for mobility is a perfect circle, while it is a slightly flawed circle for receptance and accelerance. The diameter of the mobility plot is given by,

$$\phi_v = \frac{\omega_n}{2\zeta k}. \quad (\text{C.2})$$

For receptance and accelerance, the difference between the maximum and the minimum of the real parts ( $\phi_\alpha^*$ ,  $\phi_a^*$ ), which does not correspond to a well-defined diameter, relates to system properties as:

$$\begin{aligned}\phi_\alpha^* &= \frac{1}{2k(\zeta - \zeta^3)} \approx \frac{1}{2k\zeta} \text{ for } \zeta < 0.1, \\ \phi_a^* &= \frac{\omega_n^2}{2k(\zeta - \zeta^3)} \approx \frac{\omega_n^2}{2k\zeta} \text{ for } \zeta < 0.1.\end{aligned}\tag{C.3}$$



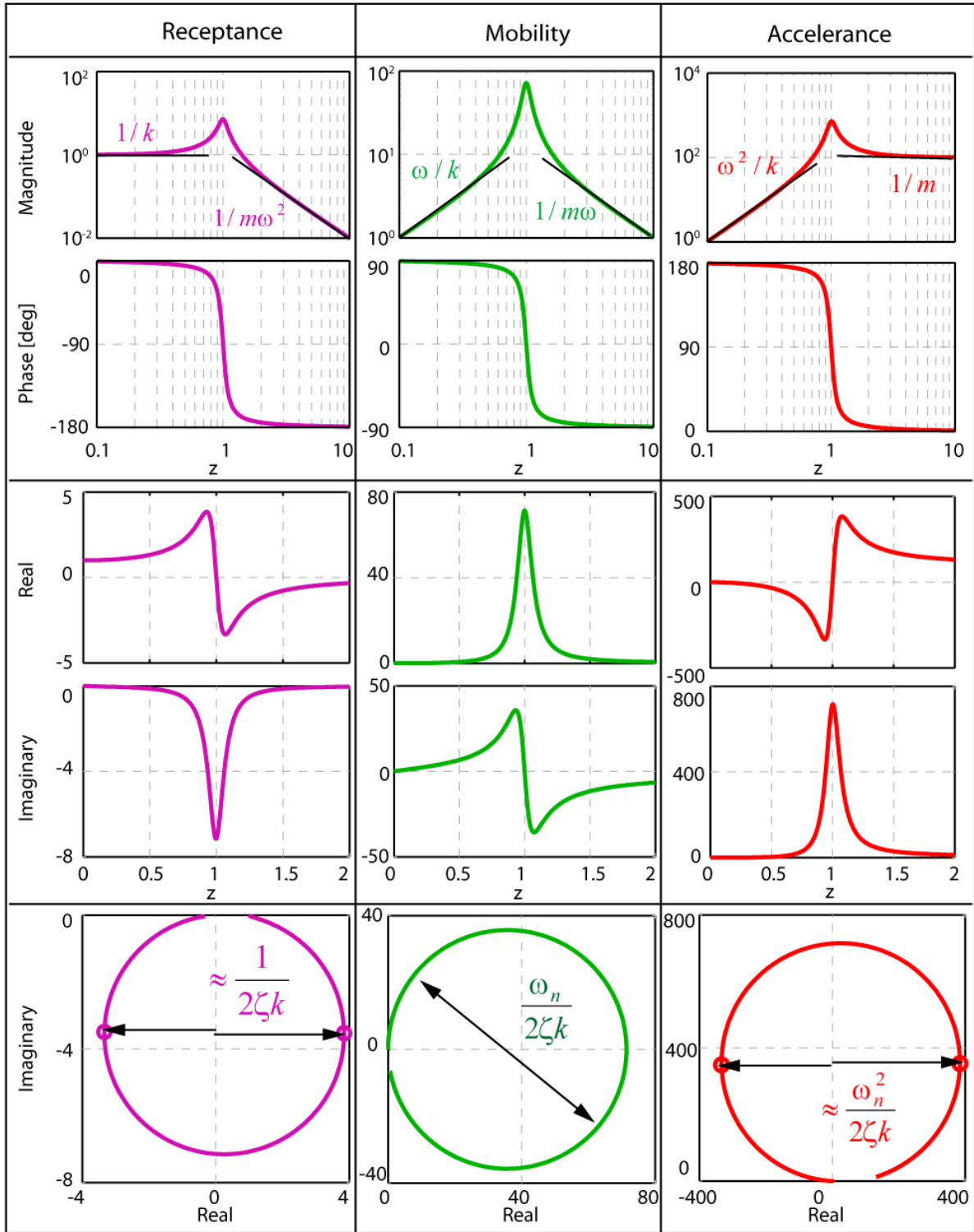


Fig. C.1 Bode, real - imaginary, and Nyquist plots of FRF's.

## Appendix D

### Formulas Used to Calculate Accuracy

Table D.1 Formulas used to calculate accuracy

Parameter	Definition	Formula
$B$	Reversal value	$B_i = \bar{d}_i \uparrow - \bar{d}_i \downarrow, B = \max\{ B_i \}$
$\bar{B}$	Mean reversal value	$\bar{B} = \frac{1}{m} \sum_{i=1}^m B_i$
$M$	Range mean bidirectional positional deviation	$M = \max\{\bar{d}_i\} - \min\{\bar{d}_i\}$
$E$	Systematic positional deviation	$E = \max\{\bar{d}_i \uparrow; \bar{d}_i \downarrow\} - \min\{\bar{d}_i \uparrow; \bar{d}_i \downarrow\}$
$R$	Repeatability of positioning	$R_i \uparrow = 4s_i \uparrow, R_i \downarrow = 4s_i \downarrow,$ $R_i = \max\{2s_i \uparrow + 2s_i \downarrow +  B_i ; R_i \uparrow; R_i \downarrow\},$ $R = \max\{R_i\}$
$A$	Accuracy	$A = \max\{\bar{d}_i \uparrow + 2s_i \uparrow; \bar{d}_i \downarrow + 2s_i \downarrow\} -$ $\min\{\bar{d}_i \uparrow - 2s_i \uparrow; \bar{d}_i \downarrow - 2s_i \downarrow\}$

**Appendix E**  
**Motion Errors in Standard Format**

Table E.1 Linear positioning error (EXX) results

$i$	1	2	3	4	5	6	7	8	9	10	11	12	13	14	15	16	17	18																			
<b>Target position <math>P_i</math> [mm]</b>	1.509	2.508	3.507	4.510	5.548	6.501	7.548	8.501	9.549	10.515	11.526	12.543	13.545	14.509	15.533	16.547	17.549	18.505																			
<b>Approach direction</b>	↓ ↑	↓ ↑	↓ ↑	↓ ↑	↓ ↑	↓ ↑	↓ ↑	↓ ↑	↓ ↑	↓ ↑	↓ ↑	↓ ↑	↓ ↑	↓ ↑	↓ ↑	↓ ↑	↓ ↑	↓ ↑																			
<b>Positional deviations <math>[\mu\text{m}]</math></b>	$j=1$	-0.3	0.0	-0.3	0.0	-0.2	-0.1	-0.2	-0.1	-0.1	0.0	-0.3	0.0	-0.6	0.0	0.3	0.0	0.1	0.1	0.3	0.0	0.2	0.0	0.2	0.0	0.2	0.0	0.3	0.0	0.4	0.1	0.4	0.1	0.4	0.1	0.3	
	2	-0.6	-0.4	-0.6	-0.5	-0.6	-0.5	-0.6	-0.5	-0.6	-0.4	-0.7	-0.4	-0.6	-0.4	-0.6	-0.4	-0.6	-0.4	-0.6	-0.5	-0.6	-0.5	-0.6	-0.3	-0.3	-0.4	-0.6	-0.5	-0.6	-0.5	-0.5	-0.6	-0.5	-0.6	-0.5	-0.5
	3	-0.9	-0.5	-0.9	-0.7	-0.9	-0.6	-0.9	-0.6	-1.0	-0.6	-0.9	-0.7	-0.9	-0.6	-0.9	-0.7	-0.9	-0.8	-0.9	-0.7	-0.9	-0.8	-0.9	-0.8	-0.9	-0.8	-1.0	-0.8	-0.9	-0.9	-0.9	-0.9	-0.9	-0.8	-0.9	-0.8
	4	-1.2	-0.9	-1.2	-0.9	-1.3	-1.0	-1.3	-0.9	-1.5	-1.0	-1.4	-1.1	-1.4	-1.1	-1.3	-1.1	-1.3	-1.1	-1.3	-1.1	-1.3	-1.1	-1.3	-1.2	-1.3	-1.2	-1.3	-1.1	-1.2	-1.1	-1.3	-1.2	-1.4	-1.3	-1.4	-1.3
	5	-1.4	-1.1	-1.5	-1.1	-1.6	-1.2	-1.6	-1.3	-1.6	-1.4	-1.5	-1.3	-1.6	-1.4	-1.5	-1.4	-1.5	-1.4	-1.5	-1.5	-1.6	-1.5	-1.5	-1.8	-1.5	-1.6	-1.5	-1.6	-1.4	-1.6	-1.4	-1.6	-1.5	-1.6	-1.5	-1.6
<b>Mean unidirectional positional deviation <math>\bar{d}_i</math> <math>[\mu\text{m}]</math></b>	-0.9	-0.6	-0.9	-0.6	-0.9	-0.7	-1.0	-0.7	-0.9	-0.7	-0.9	-0.7	-0.9	-0.8	-0.9	-0.6	-0.8	-0.7	-0.8	-0.7	-0.9	-0.7	-0.9	-0.8	-0.8	-0.7	-0.9	-0.7	-0.9	-0.7	-0.8	-0.8	-0.8	-0.8	-0.8		
<b>Estimator of standard uncertainty <math>s_i</math> <math>[\mu\text{m}]</math></b>	0.5	0.4	0.5	0.4	0.5	0.4	0.6	0.4	0.6	0.5	0.6	0.4	0.6	0.4	0.6	0.6	0.6	0.6	0.6	0.6	0.7	0.6	0.6	0.6	0.8	0.6	0.7	0.6	0.7	0.6	0.7	0.6	0.8	0.6	0.8	0.6	0.7
$2s_i$ $[\mu\text{m}]$	0.9	0.8	1.0	0.8	1.1	0.9	1.1	0.8	1.3	1.0	1.2	0.8	1.2	0.8	1.2	1.3	1.2	1.2	1.2	1.4	1.3	1.3	1.2	1.5	1.2	1.4	1.2	1.4	1.1	1.5	1.2	1.5	1.3	1.5	1.3	1.5	
$\bar{d}_i - 2s_i$ $[\mu\text{m}]$	-1.8	-1.4	-1.9	-1.5	-2.0	-1.5	-2.1	-1.5	-2.2	-1.7	-2.1	-1.6	-2.1	-1.6	-2.1	-1.9	-2.1	-1.9	-2.0	-2.1	-2.2	-2.0	-2.1	-2.3	-2.0	-2.1	-2.0	-2.2	-2.0	-2.2	-2.0	-2.3	-2.1	-2.3	-2.1	-2.2	
$\bar{d}_i + 2s_i$ $[\mu\text{m}]$	0.0	0.2	0.1	0.2	0.2	0.2	0.2	0.2	0.3	0.3	0.3	0.1	0.3	0.0	0.4	0.6	0.4	0.4	0.4	0.6	0.4	0.5	0.4	0.8	0.4	0.6	0.3	0.7	0.3	0.7	0.4	0.7	0.5	0.8	0.5	0.7	
<b>Unidirectional repeatability <math>R_i = 4s_i</math> <math>[\mu\text{m}]</math></b>	1.8	1.7	1.9	1.7	2.1	1.7	2.2	1.7	2.5	2.0	2.4	1.7	2.5	1.6	2.4	2.5	2.4	2.3	2.4	2.7	2.6	2.6	2.4	3.1	2.5	2.7	2.3	2.9	2.2	3.0	2.5	3.0	2.6	3.0	2.6	2.9	
<b>Reversal value <math>B_i</math> <math>[\mu\text{m}]</math></b>	-0.3	-0.3	-0.2	-0.3	-0.2	-0.2	-0.1	-0.2	-0.1	-0.1	-0.1	-0.1	-0.1	-0.1	-0.1	0.0	-0.1	-0.1	-0.1	-0.1	-0.1	-0.1	-0.1	-0.1	-0.1	-0.1	-0.1	-0.1	0.0	-0.1	-0.1	-0.1	-0.1	-0.1			
<b>Bidirectional repeatability <math>R_i</math> <math>[\mu\text{m}]</math></b>	2.0	2.1	2.1	2.2	2.5	2.4	2.5	2.7	2.5	2.7	2.7	3.1	2.7	2.9	3.0	3.0	3.0	3.0	3.0	3.0	3.0	3.0	3.1	2.7	2.9	3.0	3.0	3.0	3.0	3.0	3.0	3.0	3.0	3.0	2.9		
<b>Mean bidirectional positional deviation <math>\bar{d}_i</math> <math>[\mu\text{m}]</math></b>	-0.7	-0.8	-0.8	-0.8	-0.8	-0.8	-0.8	-0.9	-0.8	-0.8	-0.8	-0.8	-0.8	-0.8	-0.8	-0.8	-0.8	-0.8	-0.8	-0.8	-0.8	-0.8	-0.8	-0.8	-0.8	-0.8	-0.8	-0.8	-0.8	-0.8	-0.8	-0.8	-0.8	-0.8	-0.8		
<b>Axis deviation <math>[\mu\text{m}]</math></b>	Unidirectional ↓						Unidirectional ↑						Bidirectional																								
<b>Reversal value <math>B</math></b>	Not Applicable						Not Applicable						0.3 $[\mu\text{m}]$ (at $i = 1$ )																								
<b>Mean reversal value <math>\bar{B}</math></b>	Not Applicable						Not Applicable						-0.1																								
<b>Range mean bidirectional positional deviation <math>M</math></b>	Not Applicable						Not Applicable						0.1 $[\mu\text{m}]$ (- 0.7 3 - - 0.8 6)																								
<b>Systematic positional deviation <math>E</math></b>	0.2 (= - 0.8 0 - - 0.9 5)						0.2 (= - 0.5 9 - - 0.8 2)						0.4 $[\mu\text{m}]$ (- 0.5 9 - - 0.9 5)																								
<b>Repeatability of positioning <math>R</math></b>	2.6 (at $i = 17$ )						3.1 (at $i = 12$ )						3.1 $[\mu\text{m}]$																								
<b>Accuracy <math>A</math></b>	2.7 (0.4 6 - - 2.2 0)						3.1 (0.7 6 - - 2.3 3)						3.1 $[\mu\text{m}]$ (0.7 6 - - 2.3 3)																								
NOTE The values given in this table are rounded.																																					

Table E.2 Vertical straightness error (EYX) results

<i>i</i>	1	2	3	4	5	6	7	8	9	10	11	12	13	14	15	16	17	18																			
<b>Target position <math>P_i</math> [mm]</b>	1.509	2.508	3.507	4.510	5.548	6.501	7.548	8.501	9.549	10.515	11.526	12.543	13.545	14.509	15.533	16.547	17.549	18.505																			
<b>Approach direction</b>	↓ ↑	↓ ↑	↓ ↑	↓ ↑	↓ ↑	↓ ↑	↓ ↑	↓ ↑	↓ ↑	↓ ↑	↓ ↑	↓ ↑	↓ ↑	↓ ↑	↓ ↑	↓ ↑	↓ ↑	↓ ↑																			
<b>Positional deviations <math>[\mu\text{m}]</math></b>	<i>j</i> =1	4.9	4.9	4.3	4.3	3.7	3.7	3.1	3.2	2.5	2.5	2.0	2.0	1.4	1.4	0.8	0.8	0.2	0.2	-0.4	-0.4	-1.0	-1.0	-1.5	-1.5	-2.1	-2.1	-2.6	-2.6	-3.1	-3.1	-3.6	-3.6	-4.1	-4.1	-4.6	-4.6
	2	4.9	4.9	4.3	4.3	3.7	3.7	3.1	3.2	2.5	2.5	2.0	2.0	1.3	1.4	0.8	0.8	0.2	0.2	-0.4	-0.4	-1.0	-1.0	-1.5	-1.5	-2.1	-2.1	-2.6	-2.6	-3.1	-3.1	-3.6	-3.6	-4.1	-4.1	-4.6	-4.6
	3	4.9	4.9	4.3	4.3	3.7	3.7	3.1	3.1	2.5	2.5	2.0	2.0	1.3	1.4	0.8	0.8	0.2	0.2	-0.4	-0.4	-1.0	-1.0	-1.5	-1.5	-2.1	-2.1	-2.6	-2.6	-3.1	-3.1	-3.6	-3.6	-4.1	-4.1	-4.6	-4.6
	4	4.9	4.9	4.3	4.3	3.7	3.7	3.1	3.1	2.5	2.5	2.0	2.0	1.3	1.3	0.8	0.8	0.2	0.2	-0.4	-0.4	-1.0	-1.0	-1.5	-1.5	-2.1	-2.1	-2.6	-2.6	-3.1	-3.1	-3.6	-3.6	-4.1	-4.1	-4.6	-4.6
	5	4.9	4.9	4.3	4.3	3.7	3.7	3.1	3.1	2.5	2.5	2.0	2.0	1.3	1.3	0.8	0.8	0.2	0.2	-0.4	-0.4	-1.0	-1.0	-1.5	-1.5	-2.1	-2.1	-2.6	-2.6	-3.1	-3.1	-3.6	-3.6	-4.1	-4.1	-4.6	-4.6
<b>Mean unidirectional positional deviation <math>\bar{d}_i</math> <math>[\mu\text{m}]</math></b>	4.9	4.9	4.3	4.3	3.7	3.7	3.1	3.1	2.5	2.5	2.0	2.0	1.3	1.4	0.8	0.8	0.2	0.2	-0.4	-0.4	-1.0	-1.0	-1.5	-1.5	-2.1	-2.1	-2.6	-2.6	-3.1	-3.1	-3.6	-3.6	-4.1	-4.1	-4.6	-4.6	
<b>Estimator of standard uncertainty <math>s_i</math> <math>[\mu\text{m}]</math></b>	< 0.020																																				
<b><math>2s_i</math> <math>[\mu\text{m}]</math></b>	< 0.020																																				
<b><math>\bar{d}_i - 2s_i</math> <math>[\mu\text{m}]</math></b>	4.9	4.9	4.3	4.3	3.7	3.7	3.1	3.1	2.5	2.5	2.0	2.0	1.3	1.3	0.8	0.8	0.2	0.2	-0.4	-0.4	-1.0	-1.0	-1.5	-1.5	-2.1	-2.1	-2.6	-2.6	-3.1	-3.1	-3.6	-3.6	-4.1	-4.1	-4.6	-4.6	
<b><math>\bar{d}_i + 2s_i</math> <math>[\mu\text{m}]</math></b>	4.9	4.9	4.3	4.3	3.7	3.7	3.2	3.2	2.5	2.5	2.0	2.0	1.4	1.4	0.8	0.8	0.2	0.2	-0.4	-0.4	-1.0	-1.0	-1.5	-1.5	-2.1	-2.0	-2.6	-2.6	-3.1	-3.1	-3.6	-3.6	-4.1	-4.1	-4.6	-4.6	
<b>Unidirectional repeatability <math>R_i = 4s_i</math> <math>[\mu\text{m}]</math></b>	< 0.020																																				
<b>Reversal value <math>B_i</math> <math>[\mu\text{m}]</math></b>	< 0.020																																				
<b>Bidirectional repeatability <math>R_i</math> <math>[\mu\text{m}]</math></b>	< 0.020																																				
<b>Mean bidirectional positional deviation <math>\bar{d}_i</math> <math>[\mu\text{m}]</math></b>	4.9	4.3	3.7	3.1	2.5	2.0	1.4	0.8	0.2	-0.4	-1.0	-1.5	-2.1	-2.6	-3.1	-3.6	-4.1	-4.6																			
<b>Axis deviation <math>[\mu\text{m}]</math></b>	Unidirectional ↓					Unidirectional ↑					Bidirectional																										
<b>Reversal value <math>B</math></b>	Not Applicable					Not Applicable					0.003 (at <i>i</i> = 11)																										
<b>Mean reversal value <math>\bar{B}</math></b>	Not Applicable					Not Applicable					-0.002																										
<b>Range mean bidirectional positional deviation <math>M</math></b>	Not Applicable					Not Applicable					9.5 (= 4.9 0 - - 4.5 9)																										
<b>Systematic positional deviation <math>E</math></b>	9.5 (= 4.9 0 - - 4.5 9)					9.5 (= 4.9 0 - - 4.5 9)					9.5 (= 4.9 0 - - 4.5 9)																										
<b>Repeatability of positioning <math>R</math></b>	0.011 (at <i>i</i> = 17)					0.014 (at <i>i</i> = 11)					0.014																										
<b>Accuracy <math>A</math></b>	9.5 (= 4.9 0 - - 4.5 9)					9.5 (= 4.9 0 - - 4.5 9)					9.5 (= 4.9 0 - - 4.5 9)																										
NOTE The values given in this table are rounded.																																					

Table E.3 Horizontal straightness error (EZ<sub>X</sub>) results

<i>i</i>	1	2	3	4	5	6	7	8	9	10	11	12	13	14	15	16	17	18																			
<b>Target position <math>P_i</math> [mm]</b>	1.509	2.508	3.507	4.510	5.548	6.501	7.548	8.501	9.549	10.515	11.526	12.543	13.545	14.509	15.533	16.547	17.549	18.505																			
<b>Approach direction</b>	↓	↑	↓	↑	↓	↑	↓	↑	↓	↑	↓	↑	↓	↑	↓	↑	↓	↑	↓	↑																	
<b>Positional deviations <math>[\mu\text{m}]</math></b>	<i>j</i> = 1	-1.0	-1.0	-0.9	-0.9	-0.8	-0.8	-0.7	-0.7	-0.5	-0.5	-0.4	-0.4	-0.3	-0.3	-0.2	-0.1	0.0	0.0	0.1	0.1	0.2	0.2	0.3	0.3	0.4	0.4	0.5	0.5	0.6	0.6	0.8	0.8	0.9	0.9	1.0	1.0
	2	-1.0	-1.0	-0.9	-0.9	-0.8	-0.8	-0.7	-0.7	-0.5	-0.5	-0.4	-0.4	-0.3	-0.3	-0.2	-0.2	0.0	0.0	0.1	0.1	0.2	0.2	0.3	0.3	0.4	0.4	0.5	0.5	0.6	0.6	0.8	0.8	0.9	0.9	1.0	1.0
	3	-1.0	-1.0	-0.9	-0.9	-0.8	-0.8	-0.7	-0.7	-0.5	-0.5	-0.4	-0.4	-0.3	-0.3	-0.2	-0.2	0.0	0.0	0.1	0.1	0.2	0.2	0.3	0.3	0.4	0.4	0.5	0.5	0.6	0.6	0.8	0.8	0.9	0.9	1.0	1.0
	4	-1.0	-1.0	-0.9	-0.9	-0.8	-0.8	-0.7	-0.7	-0.5	-0.5	-0.4	-0.4	-0.3	-0.3	-0.2	-0.2	0.0	0.0	0.1	0.1	0.2	0.2	0.3	0.3	0.4	0.4	0.5	0.5	0.6	0.6	0.8	0.8	0.9	0.9	1.0	1.0
	5	-1.0	-1.0	-0.9	-0.9	-0.8	-0.8	-0.7	-0.7	-0.5	-0.5	-0.4	-0.4	-0.3	-0.3	-0.2	-0.2	-0.1	0.0	0.0	0.1	0.1	0.2	0.2	0.3	0.3	0.4	0.4	0.5	0.5	0.6	0.6	0.8	0.8	0.9	0.9	1.0
<b>Mean unidirectional positional deviation <math>\bar{d}_i</math> <math>[\mu\text{m}]</math></b>	-1.0	-1.0	-0.9	-0.9	-0.8	-0.8	-0.7	-0.7	-0.5	-0.5	-0.4	-0.4	-0.3	-0.3	-0.2	-0.2	0.0	0.0	0.1	0.1	0.2	0.2	0.3	0.3	0.4	0.4	0.5	0.5	0.6	0.6	0.8	0.8	0.9	0.9	1.0	1.0	
<b>Estimator of standard uncertainty <math>s_i</math> <math>[\mu\text{m}]</math></b>	< 0.030																																				
<b><math>2s_i</math> <math>[\mu\text{m}]</math></b>	< 0.030																																				
<b><math>\bar{d}_i - 2s_i</math> <math>[\mu\text{m}]</math></b>	-1.0	-1.0	-0.9	-0.9	-0.8	-0.8	-0.7	-0.7	-0.5	-0.5	-0.4	-0.4	-0.3	-0.3	-0.2	-0.2	-0.1	-0.1	0.1	0.1	0.2	0.2	0.3	0.3	0.4	0.4	0.5	0.5	0.6	0.6	0.7	0.8	0.8	0.8	0.8	1.0	1.0
<b><math>\bar{d}_i + 2s_i</math> <math>[\mu\text{m}]</math></b>	-1.0	-1.0	-0.9	-0.9	-0.8	-0.8	-0.7	-0.7	-0.5	-0.5	-0.4	-0.4	-0.3	-0.3	-0.1	-0.1	0.0	0.0	0.1	0.1	0.2	0.2	0.3	0.3	0.4	0.4	0.5	0.5	0.6	0.6	0.8	0.8	0.9	0.9	1.0	1.0	
<b>Unidirectional repeatability <math>R_i = 4s_i</math> <math>[\mu\text{m}]</math></b>	< 0.030																																				
<b>Reversal value <math>B_i</math> <math>[\mu\text{m}]</math></b>	-0.002	-0.003	-0.003	-0.002	-0.002	-0.002	-0.001	-0.002	-0.002	-0.001	-0.001	-0.001	-0.001	-0.001	-0.001	-0.002	-0.002	0.000	0.000																		
<b>Bidirectional repeatability <math>R_i</math> <math>[\mu\text{m}]</math></b>	0.022	0.029	0.031	0.021	0.028	0.026	0.021	0.028	0.025	0.022	0.027	0.022	0.022	0.022	0.028	0.021	0.026	0.028	0.019																		
<b>Mean bidirectional positional deviation <math>\bar{d}_i</math> <math>[\mu\text{m}]</math></b>	-1.0	-0.9	-0.8	-0.7	-0.5	-0.4	-0.3	-0.2	0.0	0.1	0.2	0.3	0.4	0.5	0.6	0.8	0.9	1.0																			
<b>Axis deviation <math>[\mu\text{m}]</math></b>	Unidirectional ↓					Unidirectional ↑					Bidirectional																										
<b>Reversal value <math>B</math></b>	Not Applicable					Not Applicable					0.004 (at <i>i</i> = 2)																										
<b>Mean reversal value <math>\bar{B}</math></b>	Not Applicable					Not Applicable					-0.002																										
<b>Range mean bidirectional positional deviation <math>M</math></b>	Not Applicable					Not Applicable					2.0 (= 0.9 7 - - 1.0 4)																										
<b>Systematic positional deviation <math>E</math></b>	2.0 (= 0.9 7 - - 1.0 4)					2.0 (= 0.9 7 - - 1.0 3)					2.0 (= 0.9 7 - - 1.0 4)																										
<b>Repeatability of positioning <math>R</math></b>	0.028 (at <i>i</i> = 14)					0.029 (at <i>i</i> = 3)					0.031																										
<b>Accuracy <math>A</math></b>	2.0 (= 0.9 8 - - 1.0 5)					2.0 (= 0.9 7 - - 1.0 5)					2.0 (= 0.9 8 - - 1.0 5)																										
NOTE The values given in this table are rounded.																																					

Table E.4 Yaw error (EBX) results

$i$	1	2	3	4	5	6	7	8	9	10	11	12	13	14	15	16	17	18	
<b>Target position <math>P_i</math> [mm]</b>	1.509	2.508	3.507	4.510	5.548	6.501	7.548	8.501	9.549	10.515	11.526	12.543	13.545	14.509	15.533	16.547	17.549	18.505	
<b>Approach direction</b>	↓ ↑	↓ ↑	↓ ↑	↓ ↑	↓ ↑	↓ ↑	↓ ↑	↓ ↑	↓ ↑	↓ ↑	↓ ↑	↓ ↑	↓ ↑	↓ ↑	↓ ↑	↓ ↑	↓ ↑	↓ ↑	
<b>Angular deviations <math>[\mu\text{m}/\text{m}]</math></b>	$j=1$	0.1 0.8	0.8 0.4	1.3 1.4	1.5 1.3	2.2 2.7	2.7 3.2	3.5 2.2	3.4 3.0	4.0 3.3	4.0 4.2	4.2 4.2	4.0 4.4	4.4 4.4	4.3 4.0	4.0 4.0	3.9 4.8	5.0 4.1	4.8 3.9
	2	1.1 0.0	0.5 1.1	1.5 1.2	1.9 1.7	2.0 2.4	2.9 2.3	3.0 3.0	2.6 3.6	3.3 3.6	3.9 3.7	4.9 4.1	4.8 4.6	4.6 3.4	4.6 4.1	4.2 5.1	5.4 5.2	4.4 5.5	4.4 5.8
	3	0.9 0.5	0.8 1.2	1.7 0.8	1.1 2.6	2.4 3.0	3.6 3.5	4.5 3.5	4.1 3.8	3.7 3.9	4.2 4.5	4.7 4.1	4.9 4.9	5.6 5.2	5.0 4.9	5.0 5.1	5.4 4.9	4.8 5.0	5.4 5.2
	4	0.8 1.2	1.1 2.2	0.7 1.7	2.3 2.6	2.9 3.1	3.3 3.8	3.9 3.5	3.7 4.4	4.1 4.2	5.4 4.4	6.2 4.8	4.8 5.2	4.5 4.9	5.0 5.0	4.9 5.2	5.0 5.4	5.7 5.3	5.7 5.5
	5	0.8 1.2	1.7 1.6	1.9 1.3	1.9 2.5	2.6 2.9	3.3 2.8	3.8 3.8	4.4 4.2	3.9 4.4	4.7 4.8	4.9 5.2	4.2 5.3	5.0 5.3	5.2 5.1	5.6 5.5	5.6 5.6	4.9 6.0	5.6 5.9
<b>Mean unidirectional positional deviation <math>\bar{d}_i</math> [<math>\mu\text{m}</math>]</b>	0.7 0.7	1.0 1.3	1.4 1.3	1.7 2.1	2.4 2.8	3.1 3.0	3.7 3.5	3.8 3.5	3.9 4.0	4.5 4.2	5.0 4.3	4.8 4.8	4.8 4.6	4.8 4.8	4.7 5.0	5.1 5.2	5.0 5.2	5.2 5.3	
<b>Estimator of standard uncertainty <math>s_i</math> [<math>\mu\text{m}</math>]</b>	0.4 0.5	0.5 0.6	0.5 0.3	0.4 0.6	0.4 0.3	0.4 0.6	0.6 0.7	0.3 0.8	0.4 0.6	0.6 0.7	0.8 0.3	0.4 0.4	0.6 0.8	0.3 0.6	0.6 0.6	0.7 0.3	0.5 0.7	0.5 0.8	
$2s_i$ [ $\mu\text{m}$ ]	0.7 1.0	0.9 1.3	0.9 0.6	0.9 1.2	0.7 0.6	0.7 1.2	1.2 1.3	0.6 1.7	0.8 1.2	1.3 1.4	1.6 1.6	0.6 0.8	0.7 1.3	1.5 0.6	1.2 1.2	1.2 1.4	0.6 0.9	1.4 1.1	
$\bar{d}_i - 2s_i$ [ $\mu\text{m}$ ]	0.0 -0.3	0.1 0.0	0.5 0.7	0.9 0.9	1.7 2.2	2.4 1.8	2.5 2.2	3.2 1.8	3.1 2.7	3.2 2.8	3.4 3.7	4.0 4.0	3.5 3.1	4.3 3.5	3.5 3.8	3.7 4.6	4.0 3.8	4.1 3.6	
$\bar{d}_i + 2s_i$ [ $\mu\text{m}$ ]	1.5 1.8	1.9 2.6	2.3 1.9	2.6 3.4	3.1 3.4	3.9 4.3	4.9 4.8	4.5 5.2	4.6 5.2	5.7 5.5	6.6 4.9	5.6 5.5	6.1 6.1	5.4 6.0	5.9 6.2	6.5 5.8	5.9 6.5	6.3 6.9	
<b>Unidirectional repeatability <math>R_i = 4s_i</math> [<math>\mu\text{m}</math>]</b>	1.5 2.0	1.8 2.6	1.8 1.2	1.8 2.4	1.4 1.1	1.5 2.5	2.4 2.6	1.2 3.4	1.6 2.4	2.5 2.7	3.2 1.1	1.6 1.5	2.6 3.1	1.1 2.4	2.5 2.4	2.8 1.2	1.9 2.8	2.2 3.4	
<b>Reversal value <math>B_i</math> [<math>\mu\text{m}</math>]</b>	0.0	-0.3	0.1	-0.4	-0.4	0.1	0.2	0.3	-0.1	0.3	0.7	0.0	0.2	0.1	-0.3	-0.1	-0.2	-0.1	
<b>Bidirectional repeatability <math>R_i</math> [<math>\mu\text{m}</math>]</b>	2.0	2.6	1.8	2.5	1.7	2.5	2.7	3.4	2.4	2.9	3.2	1.6	3.1	2.4	2.7	2.8	2.8	3.4	
<b>Mean bidirectional positional deviation <math>\bar{d}_i</math> [<math>\mu\text{m}</math>]</b>	0.7	1.1	1.4	1.9	2.6	3.1	3.6	3.7	3.9	4.3	4.7	4.8	4.7	4.8	4.8	5.1	5.1	5.2	
<b>Axis deviation [<math>\mu\text{m}</math>]</b>	Unidirectional ↓					Unidirectional ↑					Bidirectional								
<b>Reversal value <math>B</math></b>	Not Applicable					Not Applicable					0.7 (at $i = 11$ )								
<b>Mean reversal value <math>\bar{B}</math></b>	Not Applicable					Not Applicable					0.0								
<b>Range mean bidirectional positional deviation <math>M</math></b>	Not Applicable					Not Applicable					4.4 (= 5.2 1 - 0.7 4)								
<b>Systematic positional deviation <math>E</math></b>	4.4 (= 5.1 8 - 0.7 5)					4.5 (= 5.2 6 - 0.7 3)					4.5 (= 5.2 6 - 0.7 3)								
<b>Repeatability of positioning <math>R</math></b>	3.2 (at $i = 11$ )					3.4 (at $i = 8$ )					3.4								
<b>Accuracy <math>A</math></b>	6.6 (= 6.6 4 - 0.0 0)					7.2 (= 6.9 3 - - 0.2 9)					7.2 (= 6.9 3 - - 0.2 9)								
NOTE The values given in this table are rounded.																			

Table E.5 Pitch error (ECX) results

$i$	1	2	3	4	5	6	7	8	9	10	11	12	13	14	15	16	17	18	
<b>Target position <math>P_i</math> [mm]</b>	1.509	2.508	3.507	4.510	5.548	6.501	7.548	8.501	9.549	10.515	11.526	12.543	13.545	14.509	15.533	16.547	17.549	18.505	
<b>Approach direction</b>	↓ ↑	↓ ↑	↓ ↑	↓ ↑	↓ ↑	↓ ↑	↓ ↑	↓ ↑	↓ ↑	↓ ↑	↓ ↑	↓ ↑	↓ ↑	↓ ↑	↓ ↑	↓ ↑	↓ ↑	↓ ↑	
<b>Angular deviations <math>[\mu\text{m}/\text{m}]</math></b>	$j=1$	15 16	25 27	35 37	45 46	55 57	65 67	75 77	84 87	95 98	105 107	114 117	124 126	132 136	142 143	149 151	158 160	167 168	175 175
	2	14 16	24 26	34 36	44 46	54 56	64 65	74 77	84 86	95 96	104 106	114 116	124 125	132 134	141 143	149 152	159 159	167 168	174 175
	3	14 15	24 26	34 36	44 45	54 57	64 66	76 77	84 86	95 96	104 106	114 115	125 125	132 134	141 142	150 151	159 159	167 168	175 174
	4	14 14	24 25	34 35	44 45	54 55	64 65	75 76	85 86	95 96	104 106	114 117	124 126	132 133	140 142	149 151	158 160	166 168	174 174
	5	14 15	24 25	34 35	44 45	55 55	64 65	75 76	84 86	95 96	104 106	113 116	123 125	132 135	140 142	149 151	158 159	167 168	174 174
<b>Mean unidirectional positional deviation <math>\bar{d}_i</math> [<math>\mu\text{m}</math>]</b>	14 15	24 26	34 36	44 46	55 56	64 66	75 76	84 86	95 96	104 106	114 116	124 125	132 134	141 143	149 151	158 159	167 168	174 174	
<b>Estimator of standard uncertainty <math>s_i</math> [<math>\mu\text{m}</math>]</b>	0 1	0 1	1 1	1 1	1 0	1 0	1 0	1 0	0 1	0 1	1 1	0 1	0 0	1 1	1 0	0 0	1 0	0 1	1 1
$2s_i$ [ $\mu\text{m}$ ]	1 2	0 1	1 2	1 1	1 2	1 2	1 1	1 1	1 0	2 1	1 1	1 1	1 0	2 1	1 1	1 1	1 1	1 0	1 2
$\bar{d}_i - 2s_i$ [ $\mu\text{m}$ ]	13 14	24 25	33 34	43 44	54 54	64 64	74 75	84 85	95 94	103 105	113 115	123 124	132 132	139 142	148 150	157 158	166 168	173 173	
$\bar{d}_i + 2s_i$ [ $\mu\text{m}$ ]	15 17	25 27	35 37	45 47	55 58	65 67	76 78	85 87	95 98	105 107	115 117	125 126	133 137	142 144	150 152	159 161	167 168	175 176	
<b>Unidirectional repeatability <math>R_i = 4s_i</math> [<math>\mu\text{m}</math>]</b>	2 3	1 2	2 3	2 3	1 4	1 3	2 3	1 2	1 4	1 2	2 2	2 2	1 5	3 3	2 2	1 2	2 2	1 2	3 3
<b>Reversal value <math>B_i</math> [<math>\mu\text{m}</math>]</b>	-1	-1	-2	-1	-1	-1	-1	-2	-1	-2	-2	-1	-2	-2	-2	-1	-1	0	
<b>Bidirectional repeatability <math>R_i</math> [<math>\mu\text{m}</math>]</b>	3	3	4	4	4	3	4	3	4	4	4	3	5	4	3	3	2	3	
<b>Mean bidirectional positional deviation <math>\bar{d}_i</math> [<math>\mu\text{m}</math>]</b>	15	25	35	45	55	65	76	85	96	105	115	125	133	142	150	159	167	174	
<b>Axis deviation [<math>\mu\text{m}</math>]</b>	Unidirectional ↓					Unidirectional ↑					Bidirectional								
<b>Reversal value <math>B</math></b>	Not Applicable					Not Applicable					-2 (at $i = 13$ )								
<b>Mean reversal value <math>\bar{B}</math></b>	Not Applicable					Not Applicable					-1								
<b>Range mean bidirectional positional deviation <math>M</math></b>	Not Applicable					Not Applicable					160 (= 174.3 - 14.8)								
<b>Systematic positional deviation <math>E</math></b>	160 (= 174.3 - 14.3)					160 (= 174.4 - 15.2)					160 (= 174.4 - 14.3)								
<b>Repeatability of positioning <math>R</math></b>	3 (at $i = 14$ )					5 (at $i = 13$ )					5								
<b>Accuracy <math>A</math></b>	162 (= 175.4 - 13.3)					162 (= 176.0 - 13.7)					163 (= 176.0 - 13.3)								
NOTE The values given in this table are rounded.																			



## Appendix F

### Photographs of the Laser Interferometric Measurement Setups

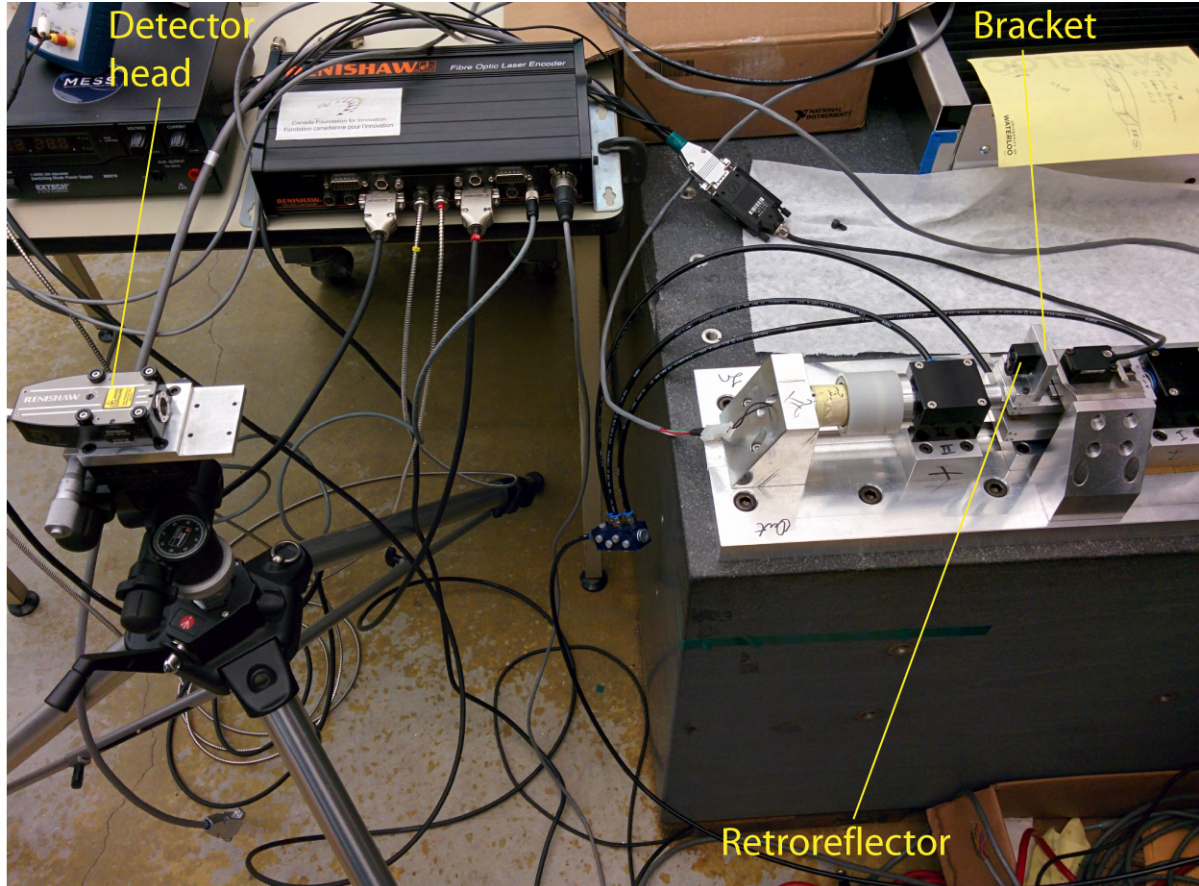


Fig. F.1 Linear error (EXX) setup.

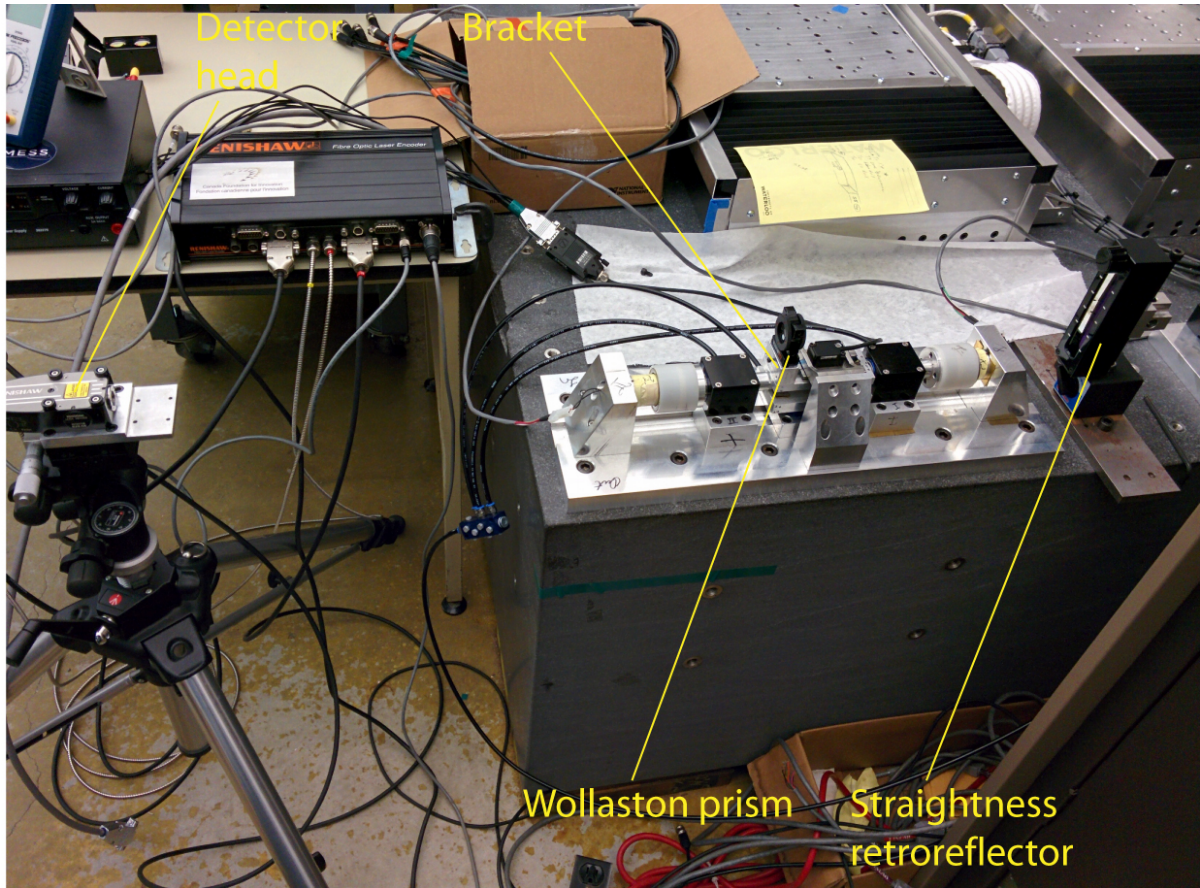


Fig. F.2 Straightness error (EYX and EZX) setup.

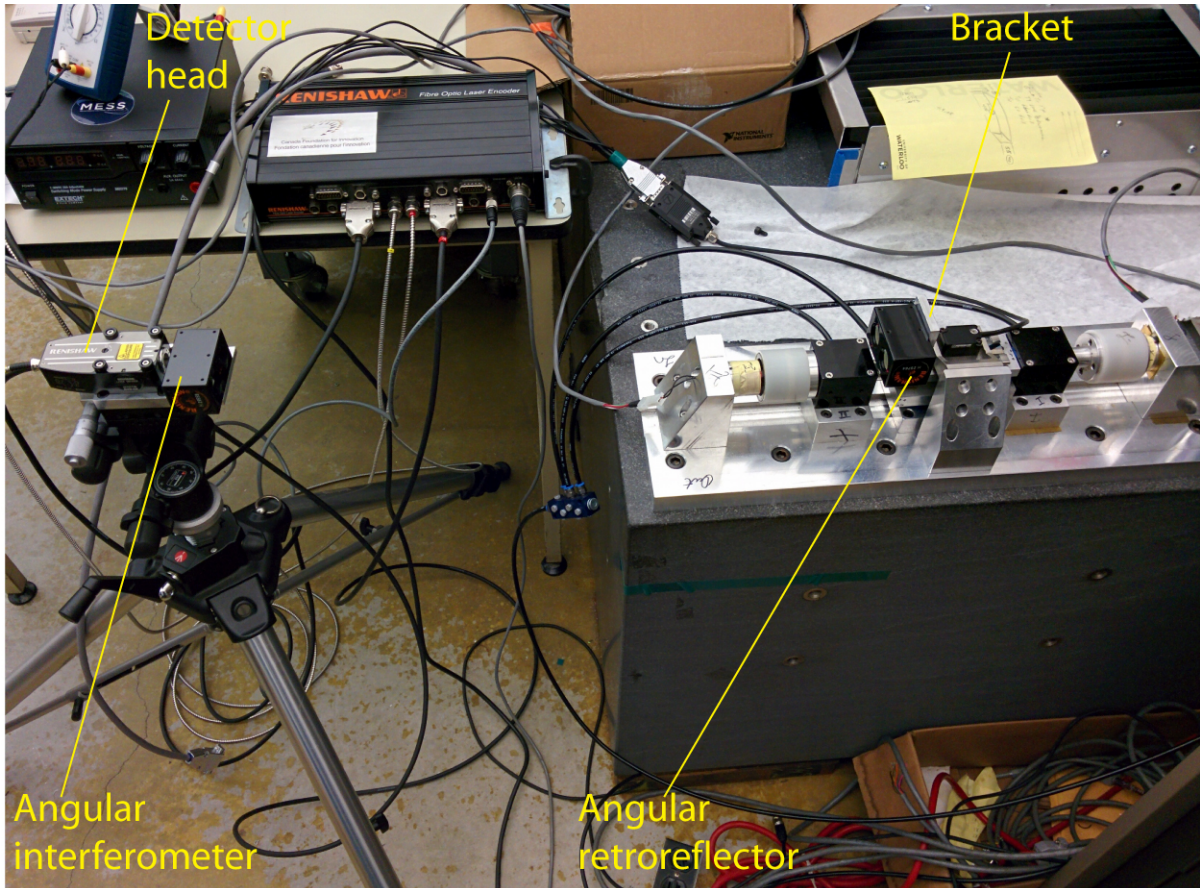


Fig. F.3 Angular error (EBX and ECX) setup.

## Appendix G

### Estimated Deflections Due to Machining Forces

The application of micro-milling for which the linear nano-positioner is designed within the framework of the preliminary design for a precision micro-milling machine involves disturbances due to cutting forces. These cutting forces result in deflections of the tool and the workpiece through the frequency dependent compliance of each, which also corresponds to the receptance frequency response function (FRF) measured at the locations of interest. As the design of the micro-milling machine is in its preliminary stage, the extent these deflections affect the tolerances on the machined part cannot be fully determined. However, deflections of the already built linear nano-positioner which corresponds to the X positioning axis of the micro-milling machine can be quantified from the available FRF data. As the milling forces act on the workpiece in all three directions, point FRF's have to be obtained from the workpiece for each direction, as shown in Fig. G.1a by  $F_x$ ,  $F_y$  and  $F_z$ . As the experimental prototype of the X positioning axis has the encoder in the prospective location of the workpiece, these cannot be directly measured. On the other hand, FRF's have been obtained during the modal testing studies (Method 1, Section 6.3) in directions parallel to the cutting forces. In this regard, referring to Fig. G.1b, FRF obtained from  $F''1 - A_{xy}$  can be used to estimate compliance in the Y-direction, while the FRF obtained from  $F1 - A_{xz}$  can be used to estimate the compliance in the Z-direction.

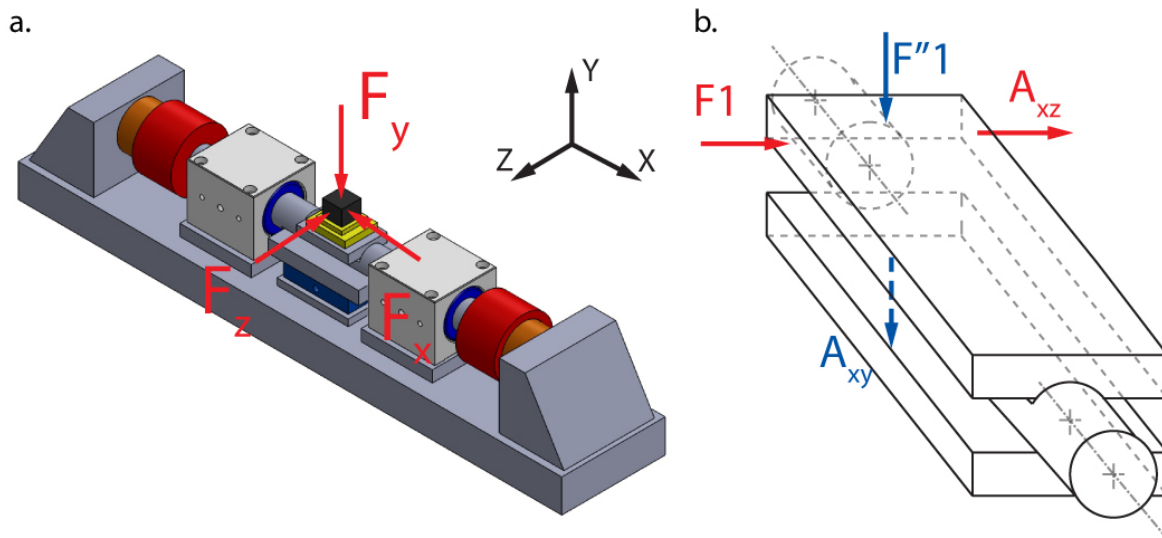


Fig. G.1 Forces due to milling operation; a. Location of forces on the workpiece, b. Impact testing points used in estimation of the compliances.

Actually, these FRF's represent a worse scenario than FRF's measured on the workpiece which is centered on the stage, as they involve additional compliances due to pitch and yaw modes, respectively.

In the case of the X axis, the compliance of the stage is determined by the disturbance transfer function of the position controller. The control block diagram with the force disturbance input in X direction is presented in Fig. G.2. The disturbance transfer function between the position output ( $x$ ) and the disturbance force ( $F_x$ ) can be expressed as:

$$G_F = \frac{x}{F_x} = \frac{1/ms^2}{1+CG_p} = \frac{G_S}{ms^2}, \quad (G.1)$$

where  $G_S$  is the sensitivity transfer function.

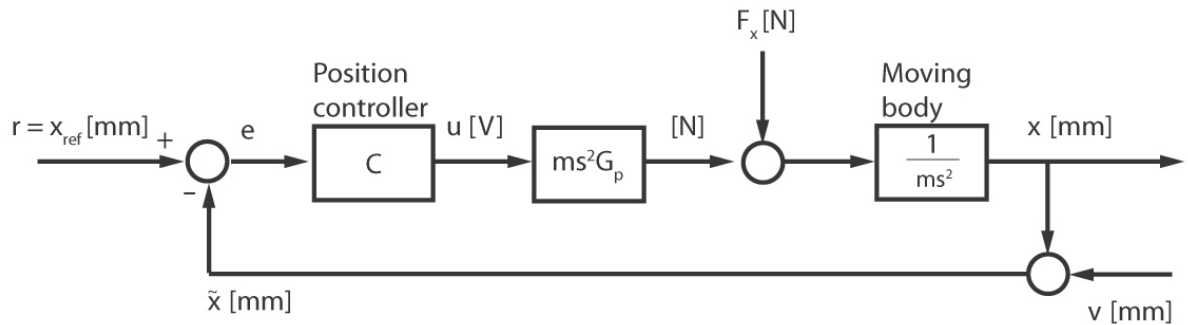


Fig. G.2 Control block diagram with cutting force disturbance.

In micro-milling, due to the compliance of the tools used, the machining forces are limited to 1-2 [N] in order to obtain the desired tolerances in the finished part. This is achieved by limiting the chip load using high spindle speeds commonly in excess of 100,000 [rpm] [19]. As an example case,  $F_x = 1$  [N] and  $F_z = 1$  [N] can be assumed in the tangential directions, and  $F_y = 0.2$  [N] can be assumed for the axial force. Slotting operation can be considered with a two teeth cutter at the spindle speeds of 3,000 [rpm] and 30,000 [rpm], which can be assumed to generate a single harmonic of the cutting force at 100 [Hz] and 1000 [Hz], respectively.

The frequency dependent compliance in X direction,  $\alpha_x = G_F$  is presented in Fig. G.3a. The compliances in Y and Z axes ( $\alpha_y$  and  $\alpha_z$ ), which are given by the receptances in the same directions are presented in Fig. G.3b-c.

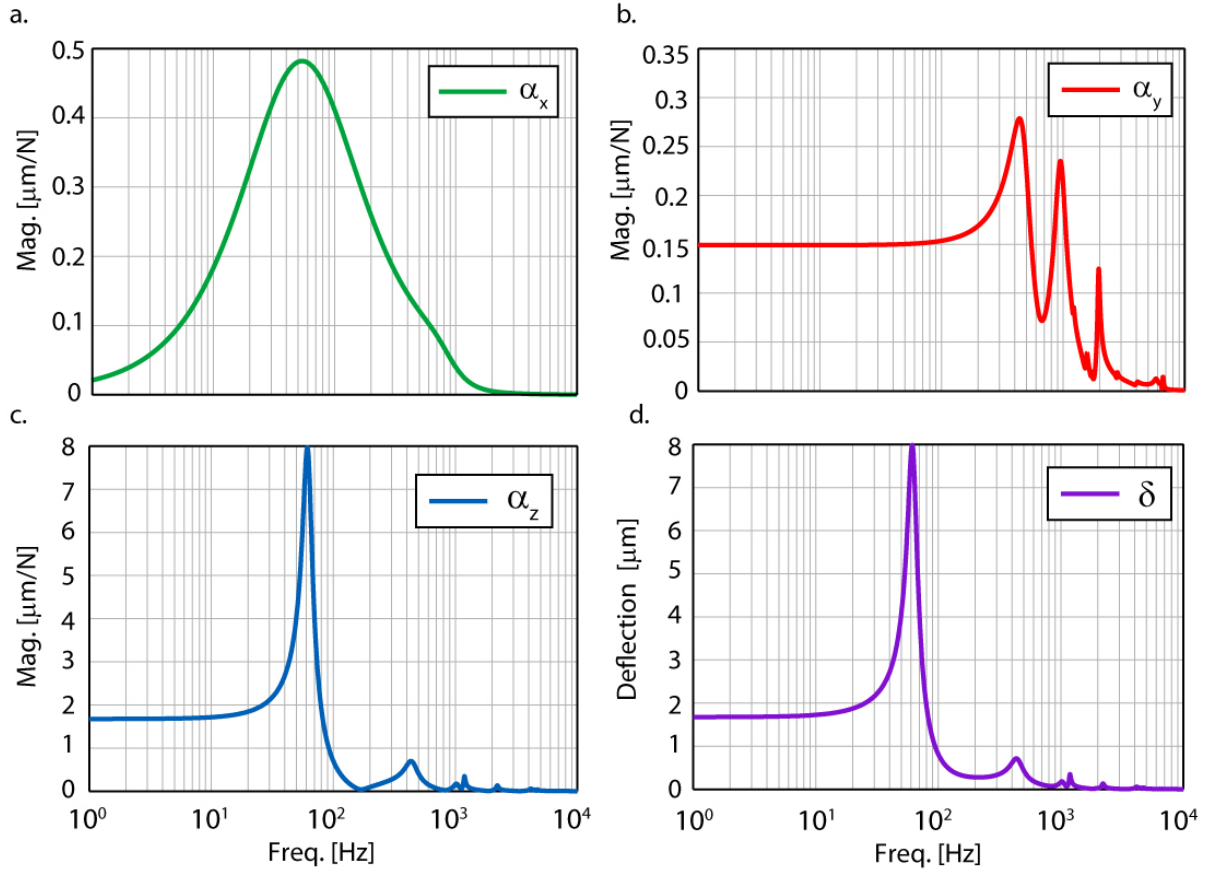


Fig. G.3 Receptances and total deflection due to cutting forces; a. Receptance in X direction, b. Receptance in Y direction, c. Receptance in Z direction, d. Total deflection.

The receptances are derived from the measured accelerances from impact tests. As the acceleration transfer function is affected by noise, mathematically deriving the receptance directly from it yields inaccurate results. Instead, modes have been fitted to the accelerance using the peak-picking method, and the receptance is derived as a superposition of modes. Deflections in each axes and the total deflection are presented in Table G.1.

Table G.1 Deflections due to cutting forces.

Direction	Force amplitude [N]	Deflection ( $\delta$ ) at 100 [Hz], [ $\mu\text{m}$ ]	Deflection ( $\delta$ ) at 1000 [Hz], [ $\mu\text{m}$ ]
X	1	0.41	0.04
Y	0.2	0.03	0.04
Z	1	0.70	0.16
Total ( $\sqrt{\delta_x^2 + \delta_y^2 + \delta_z^2}$ )	-	0.81	0.17

It is observed that a total deflection of 0.81 [ $\mu\text{m}$ ] occurs at 100 [Hz], corresponding to a relatively low spindle speed of 3,000 [rpm] for micro-milling. When the spindle speed is increased to 30,000 [rpm], a much lower deflection of 0.17 [ $\mu\text{m}$ ] is predicted. Examination of plots in Fig. G.3 shows that the major contributor to the overall compliance of the stage is the roll mode at 65 [Hz]. However, its effect diminishes quickly as the spindle speed is increased. Cutting forces are also expected to possess a static part which would be influential due to the higher compliances towards 0 [Hz], but the magnitude estimation of it requires further deliberation of the cutting process.